# Reinventing infrared optical systems with advanced materials and engineering methods

By

Hongyan Mei

A dissertation submitted in partial fulfillment of the requirements for the degree of

Doctor of Philosophy

(Electrical and Computer Engineering)

at the

UNIVERSITY OF WISCONSIN–MADISON

2024

Date of final oral examination: 05/03/2024

The dissertation is approved by the following members of the Final Oral Committee:

Mikhail A. Kats, Associate Professor, Electrical and Computer Engineering

Irena Knezevic, Professor, Electrical and Computer Engineering

Zongfu Yu, Professor, Electrical and Computer Engineering

Victor Brar, Associate Professor, Physics

Jennifer Choy, Assistant Professor, Electrical and Computer Engineering

# Abstract

This thesis is about the precision characterization and engineering of optical properties within the infrared spectrum, aiming to push the boundaries of current optical technologies. Using advanced techniques like Fourier Transform Infrared (FTIR) spectroscopy and spectroscopic ellipsometry, we have refined our understanding of material interactions with infrared light.

Chapter Two highlights our development of a robust protocol for the measurement of reflection, transmission, and thermal emission, facilitating precise analysis of both macroscale and microscale samples.

In Chapter Three, we extend these methodologies to identify and characterize a new class of infrared optical materials, $A_{1+x}BX_3$, which demonstrate exceptional broadband optical anisotropy. This breakthrough has potential applications in the creation of ultrathin polarization optics such as polarizers and waveplates, which surpass the performance of traditional materials in controlling infrared polarization. Our collaborative investigations reveal that the remarkable properties of these materials stem from their unique and unexpected, providing a foundation for future material design aimed at achieving even greater optical anisotropy.

Chapter Four introduces a novel application of focused ion beam (FIB) technology for selective modulation of material properties, in particular of zinc oxide and vanadium

dioxide. This technique allows for precise, lithography-free position-dependent engineering of materials, enabling the fabrication of complex optical components. The applications demonstrated include tunable frequency-selective optical elements, which showcase the versatility and adaptability of this approach.

Finally, Chapter Five summarizes our findings and outlines prospective research directions, emphasizing the ongoing importance of optical studies and the potential for these new materials to revolutionize the field of optics. The thesis ultimately underscores the critical role of tailored refractive indices in meeting the challenges and harnessing the opportunities of future technological landscapes.

# Acknowledgements

As I reflect on the years spent pursuing my PhD at UW Madison, I am overwhelmed with gratitude for the myriads of people who have supported, inspired, and motivated me along this incredible journey. Each of you has contributed immensely to my growth, both personally and professionally, and it is with a deep sense of appreciation that I write these acknowledgments.

Firstly, I would like to acknowledge my PhD advisor, Prof. Mikhail Kats. My decision to join UW-Madison was significantly influenced by Mikhail. After a two-hour Skype interview during midnight in China, I was convinced that he was the PhD mentor I was seeking and the scientist with whom I desired to work. Truly, I could not have asked for a better advisor. His steadfast support and mentorship have been the foundation of my doctoral journey. I have always admired his boundless enthusiasm and dedication to science, which has profoundly inspired me and shown me that science is vibrant and intriguing, not merely dry or mundane. His infectious passion has made the pursuit of research both joyful and meaningful. He is incredibly meticulous with every detail in research, maintaining an unwavering commitment to excellence, which has inspired me to surpass my own expectations. This meticulousness ensures our confidence in our research findings; even though we sometimes make mistakes, self-correction is always encouraged. Our countless discussions and brainstorming sessions have been crucial in refining my ideas and

broadening my perspectives. Mikhail has a remarkable ability to provide constructive feedback while recognizing and appreciating my efforts. His belief in my capabilities, especially during times of self-doubt, has been an immense source of encouragement. Moreover, Mikhail genuinely cares about people. I greatly respect his commitment to nurturing talent, training, and preparing his mentees for professional success, which he regards as one of his most significant life goals. More than just a mentor, he has been a pivotal figure in both my personal and professional growth. Personally, as I aspire to pursue a career in academia, Mikhail is the role model and advisor I aim to emulate. He sets a wonderful example for me on how to be an effective advisor.

Then, I would also like to express my gratitude to my committee members, Prof. Zongfu Yu, Prof. Jennifer Choy, Prof. Irena Knezevic, and Prof. Victor Brar. Their diverse insights and rigorous evaluations of my work have been instrumental in refining my dissertation. Their questions during my defense brought a necessary depth and breadth to my research, challenging me to think more broadly and critically. I am deeply appreciative of their commitment to my academic and personal development.

A heartfelt thank you goes to all my research collaborators at UW Madison and beyond. The opportunity to work alongside such talented and driven individuals has been both inspiring and enlightening. Our collaborations across different disciplines have not only enhanced my dissertation but have also broadened my understanding and appreciation of interconnected scientific fields.

I am grateful to Prof. Carsten Ronning, Alexander Koch, Martin Hafermann, and Jura Rensberg from the University of Jena for their collaboration on the focused ion beam and ion irradiation work. I also extend my thanks to Prof. Shriram Ramanathan and Zhen Zhang from Purdue University for our collaborative work on $VO_2$-related projects.

Special thanks to Prof. Rohan Mishra, Guodong Ren, and Gwan-Yeong Jung from Washington University in St. Louis, and Prof. Jayakanth Ravichandran, Boyang Zhao, Huandong Chen, and Shantanu Singh from the University of Southern California, for their collaboration on projects related to anisotropic materials. I have gained invaluable knowledge related to DFT and STEM from Rohan, Guodong, and Gwan-Yeong. The insights from Jayakanth and Boyang on XRD and structural analysis have been particularly enlightening. Rohan and Jayakanth are brilliant materials physicists from whom I have learned tremendously, offering me diverse perspectives from fields outside optics and photonics. Boyang and Guodong have been wonderful peers; graduating together this year has been a highlight. They are exceptional collaborators, and I feel incredibly fortunate to have worked alongside them.

I am also thankful to Prof. Georgia Papadakis and Maxime Giteau from ICFO for their constructive and helpful discussions on thermal emitter designs and thermal emission measurements.

I would love to acknowledge my close collaborators at UW, Prof. Filiz Yesilkoy, Yuber Samir Sanchez Rosas, Wihan Adi, and Aidana Beisenova. It has been a pleasure to

contribute to their innovative projects in biomedical science and infrared spectroscopy.

Additionally, I enjoy working with Prof. Eric Tervo and his students Titilope Dada, Parth Solanki, and Vida Nooshnab for all kinds of measurements with the FTIR system. Thank you, Eric, for enhancing our lab's capabilities with new accessories and measurement tools.

A special thank you to my undergraduate research advisors, Prof. Lei Zhang and Prof. Limin Tong from Zhejiang University, along with Prof. Jimin Bao and Prof. Tianfu Wu from the University of Houston. Their encouragement and guidance during the early stages of my academic career were pivotal in navigating my path toward this PhD. Their belief in my potential laid the foundation for my academic journey.

I am immensely thankful for the support provided by the Department of Electrical and Computer Engineering. A special mention goes to our department chair, Prof. Susan Hagness, for making ECE feel like home—a vibrant, diverse, and equitable community with a friendly environment.

I want to express my deepest appreciation to the wonderful ECE Administrative Staff: Kathy Hall, Delight Hensler, Katrina M. Olson, Allyson Crowley, and Lisa Harrington, to name just a few. The department would not function nearly as well without your amazing work. I also want to extend a heartfelt thank you to Alex Conrad, the best graduate program coordinator one could ask for. Alex knows everything, and her angelic support has been indispensable in every way possible.

I want to express my heartfelt thanks to Prof. Zhenqiang (Jack) Ma, Prof. Haihan Sun, Prof. Luke Mawst, and Prof. Dakotah Thompson from UW-Madison. Their invaluable teaching, instruction, and discussions have profoundly shaped my understanding and skills. Additionally, their support in various capacities has been instrumental to my success and growth throughout my academic journey.

I am also deeply grateful to the staff from the Wisconsin Centers for Nanoscale Technology (WCNT). Special thanks to Julie Morasch and Richard Keith Noll from the Nanoscale Imaging and Analysis Center (NIAC) for their training on SEM and AFM; Don Savage for XRD training and support; and John Jacobs for XPS training and support. I also appreciate the efforts of Kurt Kupcho, Quinn Leonard, and Frank Flack from the Nano Fabrication Center (NFC) who trained me on photolithography, e-beam lithography, and various deposition and etching tools. Additionally, thanks to Mike Efremov and Anna Kiyanova from the Soft Materials Characterization Lab (SMCL) for their initial training and support in spectroscopic ellipsometry.

I want to thank David A. Czaplewski and Alan M. Dibos from Argonne National Laboratory for their support and training on cleanroom fabrications at the Center for Nanoscale Materials (CNM).

Next, I would like to extend my heartfelt thanks to all friends and colleagues from the Kats group. First, a huge shoutout to Jad Salman; in my mind, Jad is truly almighty. He not only possesses extensive knowledge but is also an incredibly kind person to interact with. He was a real mentor to me in research, teaching me the intricacies of

ellipsometry fitting, various material properties, and semiconductor knowledge. He invested considerable time in training me to become an independent researcher. I owe him a ton for his guidance and support!

I am also immensely grateful to Chenghao Wan, the actual “boss” of the Kats Group. As the lab manager and a meticulous researcher, Chenghao, like Jad, seems to know everything. If you ever need help, Chenghao is the person to ask, not just about lab stuff. I deeply appreciate his teaching me numerous FTIR tricks and everything related to $VO_2$.

Yuzhe Xiao has been a wonderful role model for me as a researcher. His productivity, punctuality, and balanced approach to work and life are truly admirable. He is not only a friendly collaborator and scientist but also eager to teach without reservation. I thoroughly enjoyed working with Yuzhe on managing the FTIR system and admire his leadership in thermal emission measurement work, where he developed many techniques using the FTIR.

Zhaoning (April) Yu is truly an angel. She has a gentle and loving heart and has been especially considerate as the first female in the group, taking extra care to support and encourage me throughout my PhD. I am profoundly thankful for her encouragement, support, and help. We have also become great friends, and I cherish our friendship deeply.

I also want to acknowledge Bryan E. Rubio Perez, with whom I entered the group as first-year students. We spent a lot of time taking classes together, exploring potential

research projects, learning to navigate the resources and opportunities, and trying to establish ourselves in the group. I felt a deep sadness when Bryan first changed groups during our PhD journey, but I am now thrilled for him, landing a fantastic job in San Diego—a place I frequently enjoy visiting. Having Bryan as a friend when I first joined the group was truly fortuitous.

I also want to extend my gratitude to other friends and colleagues from the Kats Group for their tremendous help and support: Alireza Shahsafi, Raymond Wambold, Purva Bhumkar, Jonathan King, Demeng Feng, Graham Joe, Michel Frising, Jin-Woo Cho, Yeonghoon Jin, Sanket Deshpande, Rabeeya Hamid, Tanuj Kumar, Chengyu Fang, Shenwei (Erick) Yin, Minjeong Kim, Justin Edwards, Chunhui (Kevin) Yao, and Fiona Evelyne Uwase. Working with each one of you has been an absolute pleasure. Thank you all for making the Kats Group a perfect, heaven-like place for conducting research and learning. I truly appreciate the group's vibe—everyone is incredibly nice, friendly, and consistently supportive, always ready to help, support, and respect each other. The collaborative spirit of our group has not only facilitated my research but has also created memorable friendships that I treasure. This environment has profoundly enriched my PhD experience.

To my friends at UW-Madison—Ming Zhou, Qing Chen, Lei Ying, Boyuan Liu, Yurui Qu, Jin Xiang, Zhu Wang, Dianjing Liu, Guoming Huang, Erfan Khoram, Yulu Mao, Yunhan Hu, Zhenyang Xia, Wenxin (Sabrina) Wu, Maryam Zahedian, Xuting Yang, Ricardo Vidrio, Shuguang Wei, Jingrui Wei, Jun Meng, Minyi Dai, Mojue Zhang, Chen Shen,

Nuohao Liu, Xuanxin Hu, Yuhao Kang, and Yuguang Duan—thank you for filling these years with laughter, adventure, and solace. I have cherished our times skiing, ice skating, playing badminton, spikeball, and pickleball. Your friendship has been a source of joy and comfort amidst the pressures of PhD life. You have made Madison not just a place of study, but a home.

To my friends outside of UW, Cheng Guo and Qiushi Guo, your words of encouragement and our escapes from the academic bubble have been refreshing and cherished. Meeting Cheng at CLEO and Qiushi at MRS, I was surprised and delighted by how quickly our circles overlapped, allowing us to become instant friends, both professionally and socially. Cheng, a serious physicist with a knack for explaining complex concepts in an intuitive, easy-to-understand manner, has always been willing to share his knowledge. I deeply appreciate his affirmation of my work and his support and encouragement during my moments of uncertainty. Qiushi, already an accomplished scientist and a rising star when I met him, has been incredibly generous with his knowledge and support. His readiness to share his extensive expertise and his approachable nature have made him a remarkable colleague and friend. Qiushi's work is solid, and his ascent in academia as an assistant professor continues to inspire me. I am fortunate to have received so much support and help from both Cheng and Qiushi, making my journey outside the UW confines all the more enriching.

Over the past six years, I've had several rounds of roommates—Yan Li, Zheng Zhang, Wei Zeng, Cheng Li, Yunheng Xue, Peiyu Yang, Zige Liu, and Yixin Ren. Living with you

has been one of the highlights of my time in Madison. Your friendship, support, and understanding, especially during the most stressful times, have helped keep everything in perspective. The warmth and laughter in our home provided the perfect balance to the rigors of PhD life.

I am also grateful to my friends from my undergraduate years—Xueji Wang, Rui Chen, Yijie Zhang, Yuanjun Zhu, Qiyu Hu, Chengyu Qiao, Haokun Luo, Tian Tong, Bowen Cui, Xiaojiong Chen, Dawei Cai, Yi Kang, and Sida Peng—who have cheered me on from different corners of the world. Your enduring support and occasional reminders of life outside academia have been refreshing and greatly appreciated.

Lastly, to my family—my parents, my elder brother, and my grandparents—and to my significant other, Zhicheng (Peter) Wu, words cannot adequately express my gratitude. Your unconditional love, unwavering support, and endless patience have been the foundation of my achievements. Thank you for believing in me, for cheering me on, and for standing by me through every challenge and triumph.

# Table of Contents

# List of Figures

# List of Tables

# Chapter 1

# Introduction

## 1.1 Overview and motivation

Optics, the science of light, encompasses the behavior and properties of light, including its interactions with matter. As a cornerstone of physics, optics has an illustrious history that dates back to ancient civilizations Euclid[1], Ptolemy[2], Alhazen[3], et al., who grappled with the fundamental nature of light and vision. The field has since evolved dramatically during the Renaissance, fueled by pivotal contributions from figures such as Kepler[4] and Newton[5], whose research expanded on the understanding of the eye, vision and spectrum of colors. The 19th century heralded the wave theory of light, propelled by Thomas Young's double-slit experiment[6] which illustrated light's wave-like interference patterns. Augustin-Jean Fresnel furthered this wave theory through his mathematical treatment of light's behavior[7]. Simultaneously, the electromagnetic theory developed by James Clerk Maxwell[8] unequivocally described light as an electromagnetic wave, a monumental

breakthrough that unified optics with electromagnetism. Entering the 20th century, the development of quantum mechanics introduced new dimensions to optics. Scientists like Albert Einstein, who explained the photoelectric effect[9], and Niels Bohr, whose model of the hydrogen atom incorporated quantum phenomena[10], contributed profoundly.

Today, optics continues to be at the forefront of technological innovation, including research that focuses on understanding and engineering light-matter interactions and developing sophisticated materials and devices to further manipulate light in novel ways.

Electromagnetic energy travels in waves and spans a broad spectrum from very long radio waves to very short gamma rays, as shown in Fig. 1.1 from NASA[11]. The human eye can only detect a small portion of this spectrum within 380-700 nm, called visible light. The infrared (IR) spectrum, which lies beyond the visible range of light, is of profound importance in both fundamental science and practical applications. This spectral range, typically defined from about 700 nm to 1 mm in wavelength, offers unique opportunities for exploration and innovation due to its distinctive interaction with matter. IR radiation is inherently linked to the vibrational resonances and thermal energy of objects; thus, materials that can interact with infrared light are critical in a multitude of applications ranging from environmental monitoring[12] and medical imaging[13] to security[14] and telecommunications[15].

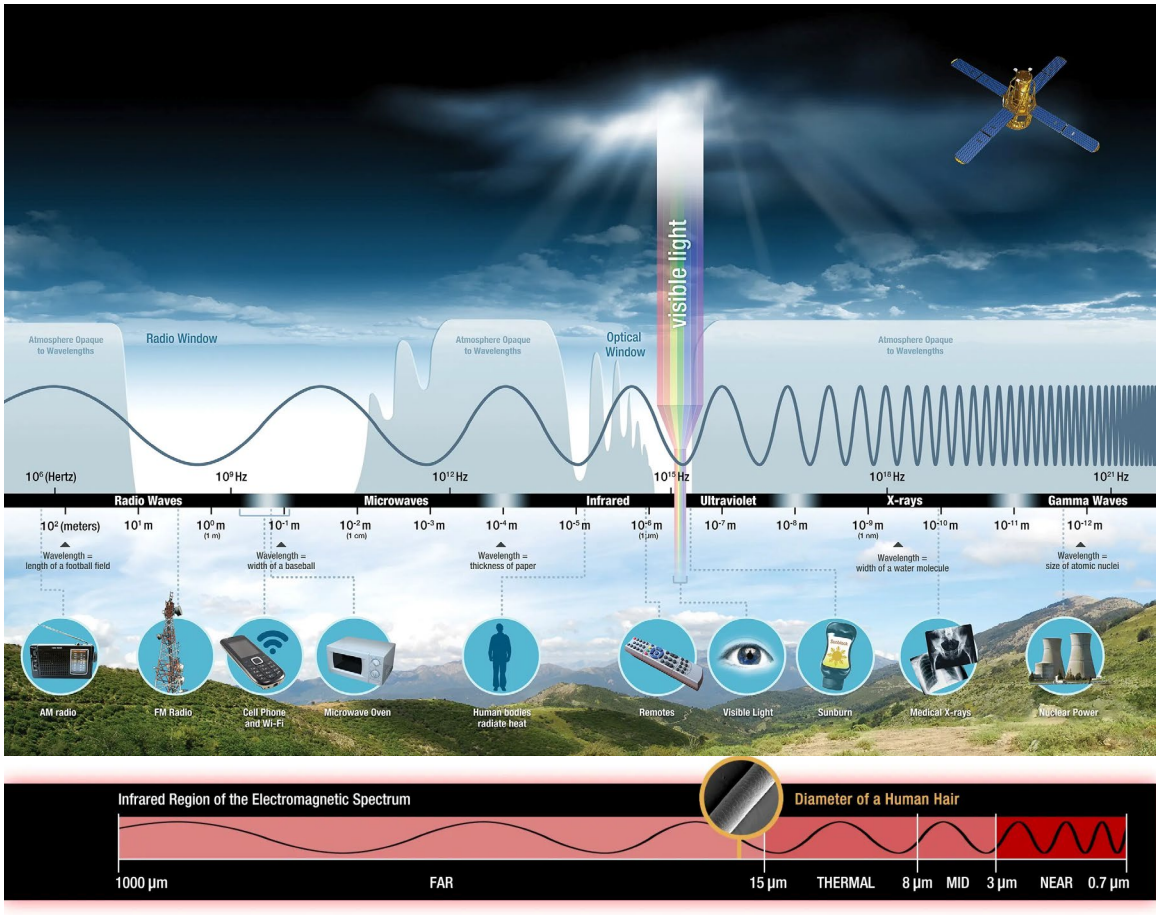


**Figure 1.1** Complete diagram of the electromagnetic spectrum (top) and infrared region of the electromagnetic spectrum (bottom). Figures from NASA science website[11].

One of the pivotal reasons the IR range is so valuable stems from its ability to penetrate materials that are opaque in the visible spectrum, providing a powerful tool for non-invasive inspection techniques. This capability is indispensable in fields such as astronomy, where infrared observations can peer through cosmic dust clouds to reveal the structure of the universe[16]. Infrared light is also important in security, where IR technology enables night vision and thermal imaging[14,17,18]. Materials that are responsive to infrared light play a central role in these technologies. The

development of accurate characterization methods for IR materials is crucial for understanding the physics inside the materials. These materials can be engineered to have specific optical properties, such as tailored refractive indices, to optimize their interaction with IR light. This tailoring allows for the creation of more efficient detectors and emitters, which are essential components of devices ranging from simple environmental sensors[12] to complex communication systems that use IR wavelengths for signal transmission[15].

In this thesis, the focus will be on precision characterization and engineering of optical properties of materials within the infrared spectrum. By advancing our understanding of these materials and their interactions with IR light, we aim to contribute to the development of next-generation optical devices and systems that are more efficient, versatile, and capable of addressing the evolving challenges and opportunities in science and technology.

## 1.2 Outline of the dissertation

In Chapter Two, I overview the state-of-the-art characterization techniques for optical materials including infrared spectroscopy and spectroscopic ellipsometry. Specifically, I introduce the use of our FTIR system for precision measurement of reflection, transmission, and thermal emission. Our group summarizes a generalized protocol for precision measurement of emission of different samples at various

scenarios. We also investigate the nonlinearity of the detector response and provide methods for calibration. For the spectroscopic ellipsometry, I in collaboration with other members of the group combine extensive measurement and modelling to prove the ability for characterization of various groups of materials.

In Chapter Three, I and my colleague in the group leverage and expand upon the spectroscopic characterization techniques introduced in Chapter two to characterize new optical materials. First, we describe our approach in merging Fourier-transform spectroscopy, spectroscopic ellipsometry, and optical modelling to discover new class of infrared optical materials $A_{1+x}BX_3$ with broadband and record-breaking optical anisotropy in the form of very large birefringence. These new materials can be used to create ultrathin polarization optics such as polarizers and waveplates at infrared wavelengths for which other natural, bulk material are not nearly as efficient at controlling polarization. Second, in collaboration with XRD experts, TEM experts, and materials theorists, we figured out even in the same group of materials with the same quasi-1D nature in their structures, the origin of their exotic large birefringence is different, in which the giant optical anisotropy in $BaTiS_3$ and $BaTiSe_3$ comes from correlated structural disorders, and for $Sr_{1+x}TiS_3$, it comes from non-stoichiometry induced structural modulation. The different mechanisms allow us to think about possible design rules for achieving even larger optical anisotropy and for realizing tunability and modulation of optical anisotropy. Finally, we showcase two applications based on these materials with giant birefringence for ultrathin

waveplate and for planar polarized narrowband thermal emitters, and we envision the future use of these materials to advance the development of optical components.

In Chapter Four, I, together with my collaborators from the University of Jena, develop a simple but straightforward technique by using a commercial focused ion beam (FIB) system to realize selective modulation of material properties. We demonstrate it in two semiconductor material systems, zinc oxide (ZnO), a representative transparent conducting oxide, and vanadium dioxide ($VO_2$), a strong-correlated phase change material. Such area-selective modification of materials properties by direct writing using a FIB provides a simple, lithography-free, and mask-less route to the fabrication of complicated optical structures that enable multifunction, especially when multiple or continuous levels of doping or defect density are required. Additionally, we demonstrated two promising applications using the FIB-ZnO and FIB-$VO_2$ platforms, showcasing their capabilities for tunable frequency-selective reflection, transmission, and thermal emission. These examples illustrate the potential of our approach to facilitate sophisticated optical functionalities tailored for advanced material applications.

Finally, Chapter Five concludes by summarizing the insights gained and proposing future research avenues. It underscores the significance of continuing research on optical characterization techniques and highlights the transformative potential of these novel materials and engineering methods in advancing the field of optics.

The continued advancement in optical materials and devices underscores the enduring importance of optics as a field of study. As researchers push the boundaries of what is possible, the integration of new materials and technologies continues to expand the frontier of optics, driving forward both theoretical understanding and practical applications. This thesis aims to explore these developments, with a particular focus on how the refractive index can be tailored to meet the challenges and opportunities of the future.

## 1.3 List of previously published work

The significant portions of the work in this thesis have been previously published in peer-reviewed journals or open-access repository of preprints (*arXiv*). Here, a list of all authored works is presented.

**Chapter 2**

C. Yao, **H. Mei**, Y. Xiao, A. Shahsafi, W. Derdeyn, J. L. King, C. Wan, R. O. Scarlat, M. H. Anderson, M. A. Kats, "Correcting thermal-emission-induced detector saturation in infrared spectroscopy", *Optics Express*, 30, 38458 (2022)

Y. Xiao, C. Wan, A. Shahsafi, J. Salman, Z. Yu, R. Wambold, **H. Mei**, B. E. Rubio Perez, W. Derdeyn, C. Yao, M. A. Kats, "Precision measurements of temperature-dependent and nonequilibrium thermal emitters", *Laser & Photonics Reviews*, 14, 1900443 (2020)

**Chapter 3**

B. Zhao, **H. Mei**, Z. Du, S. Singh, T. Chang, N. Settineri, S. J. Teat, Y. Chen, S. B. Cronin, M. A. Kats, and J. Ravichandran, "Infrared optical anisotropy in quasi-1D hexagonal chalcogenide $BaTiSe_3$", *arXiv:*2402.02323, https://doi.org/10.48550/arXiv.2402.02323 (2024)

H. Chen, S. Singh, **H. Mei**, G. Ren, B. Zhao, M. Surendran, Y. Wang, R. Mishra, M. A. Kats, J. Ravichandran, "Molten flux grown single crystals of hexagonal chalcogenide $BaTiS_3$", *arXiv:*2403.05869, https://arxiv.org/abs/2403.05869 (2024)

B. Zhao*, G. Ren*, **H. Mei**, V. C. Wu, S. Singh, G. Y. Jung, H. Chen, R. Giovine, S. Niu, A. S. Thind, J. Salman, N. S. Settineri, B. C. Chakoumakos, M. E. Manley, R. P. Hermann, A. R. Lupini, M. Chi, J. A. Hachtel, A. Simonov, S. J. Teat, R. J. Clément, M. A. Kats, J. Ravichandran and R. Mishra, "Giant Modulation of Refractive Index from Picoscale Atomic Displacements", *Advanced Materials*, 2311559 (2024)

**H. Mei***, G. Ren*, B. Zhao*, J. Salman*, G. Y. Jung, H. Chen, S. Singh, A. S. Thind, J. Cavin, J. A. Hachtel, M. Chi, S. Niu, G. Joe, C. Wan, N. Settineri, S. J. Teat, B. C. Chakoumakos, J. Ravichandran, R. Mishra, M. A. Kats, "Colossal optical anisotropy from atomic-scale modulations", *Advanced Materials*, 2303588 (2023)

B. Zhao, M. S. B. Hoque, G. Y. Jung, **H. Mei**, S. Singh, G. Ren, M. Milich, Q. Zhao, N. Wang, H. Chen, S. Niu, S. J. Lee, C. T. Kuo, J. S. Lee, J. A. Tomko, H. Wang, M. A. Kats, R. Mishra, P. E. Hopkins, J. Ravichandran, "Orientation controlled anisotropy in single crystals of quasi-1D $BaTiS_3$", *Chemistry of Materials*, 34, 5680 (2022)

## Chapter 4

**H. Mei***, A. Koch*, C. Wan*, J. Rensberg, Z. Zhang, J. Salman, M. Hafermann, M. Schaal, Y. Xiao, R. Wambold, S. Ramanathan, C. Ronning, M. A. Kats, "Tuning carrier density and phase transitions in oxide semiconductors using focused ion beams", *Nanophotonics*, 11, 3923 (2022)

A. Koch, **H. Mei**, J. Rensberg, M. Hafermann, J. Salman, C. Wan, R. Wambold, D. Blaschke, H. Schmidt, J. Salfeld, S. Geburt, M. A. Kats, and C. Ronning, "Heavily doped zinc oxide with plasma frequencies in the telecommunication wavelength range", *Advanced Photonics Research*, 2200181 (2022)

## Other co-authored works

Y. Xiao, Z. Yu, R. Wambold, **H. Mei**, G. Hickman, R. Goldsmith, M. Saffman, M. A. Kats, "Efficient generation of optical bottle beams", *Nanophotonics*, 10, 2893 (2021)

S. Rosas, K. A. Schoeller, E. Chang, **H. Mei**, M. A. Kats, K. W. Eliceiri, X. Zhao, F. Yesilkoy, "Metasurface-enhanced mid-infrared spectrochemical imaging of tissues", *Advanced Materials* 2301208 (2023)

D. Feng*, T. Kumar*, S. Yin, M. Mah, P. Lin, M. Fortman, G. R. Jaffe, C. Wan, **H. Mei**, Y. Xiao, R. Synowicki, R. J. Warzoha, V. W. Brar, J. J. Talghader, M. A. Kats, "Self-referencing photothermal common-path interferometry to measure absorption of $Si_3N_4$ membranes for laser-light sails", *arXiv:*2404.04449, https://arxiv.org/abs/2404.04449 (2024)

X. Yang, P. Mukherjee, M. Kim, **H. Mei**, C. Fang, S. Choi, Y. Tong, S. Perlowski, D. A. Czaplewski, A. M. Dibos, M. A. Kats, and J. T. Choy, "Atomic magnetometry using a metasurface polarizing beamsplitter in silicon on sapphire", *arXiv:*2404.02102, https://arxiv.org/abs/2404.02102 (2024)

# Chapter 2

## Optical characterization techniques in infrared

In this Chapter, two optical characterization techniques are discussed. One is Fourier-transform infrared (FTIR) spectroscopy that allows us to perform precision measurement of reflection, transmission and thermal emission. The other is spectroscopic ellipsometry that we can combine with modelling to characterize composition, crystallinity, roughness, doping concentration, and other material properties associated with a change in optical response.

Specific to the work presented on the thermal emission measurement, I want to acknowledge Dr. Yuzhe Xiao (now an assistant professor at the University of North Texas), who led the initial thermal emission measurement in our FTIR system and demonstrated general procedures. The section on emission measurement protocols has been adapted from our publication in *Laser Photonics & Review*[19]. For the detector saturation issues and calibration methods, I want to acknowledge Chunhui Yao, who was my mentee during his research internship in Kats Group. Relevant sections have been adapted from our publication in *Optical Express*[20].

## 2.1 Infrared spectroscopy

Infrared spectroscopy is an analytical technique that involves the interaction of infrared radiation with matter to identify and study chemicals. It's based on the principle that molecules absorb infrared light at specific frequencies that are characteristic of their structure. More specifically, when infrared radiation is absorbed by a material, it causes molecular vibrations (rotational, vibrational, or both). This absorption can be used to identify functional groups, characterize chemical bonds, and understand the composition and structure of substances. By measuring the absorption of infrared light at different wavelengths, infrared spectroscopy provides a "fingerprint" of the material, which can be used to identify and quantify various components.

### 2.1.1 Classification

Infrared spectrometers can be categorized based on the region of the infrared spectrum they analyze: near-infrared (NIR), mid-infrared (MIR), and far-infrared (FIR). The NIR spectrometers (800 to 2500 nm) are often used in quality control and clinical diagnostics due to their ability to probe overtone and combination modes of molecular vibrations, which is ideal for quantitative analysis of organic compounds, especially in agricultural, pharmaceutical, and food industries[21]. MIR instruments (2.5 to 25 μm) are typically employed to study fundamental vibrations and their associated rotational-vibrational structure, which is commonly used for qualitative analysis and identifying functional groups in organic compounds[22]. FIR

spectrometers (25 to 1000 μm) are useful for rotational spectroscopy and low-frequency vibrations, which is usually used for studying inorganic compounds and low energy lattice vibrations[23].

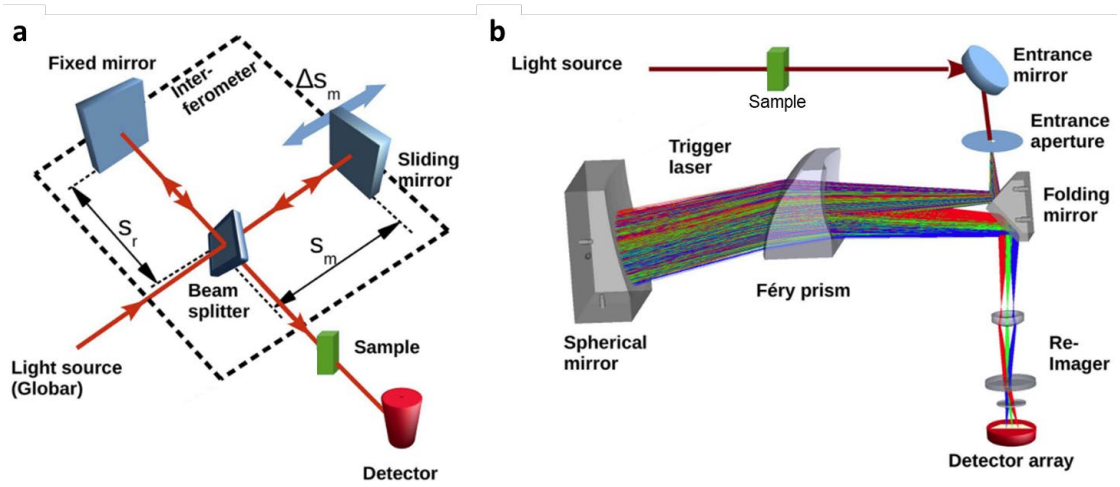


**Figure 2.1:** Fourier-transform type vs. dispersive type spectrometers. Adapted from Ref [24].

Another classification is based on the technology used and system configuration. Infrared spectrometers can be divided into dispersive and Fourier-transform (FTIR) types. Dispersive spectrometers use dispersive elements such as prisms or diffraction gratings to separate the broadband IR light into its component wavelengths, measuring one wavelength at a time, also called "scanning monochromator" method, as shown in Fig. 2.1(a).

In contrast, FTIR spectrometers use an interferometer to collect all wavelengths simultaneously [Fig. 2.1(b)]. More specifically, infrared light is guided through a Michelson interferometer and then through the sample (or vice versa). A moving mirror inside the apparatus alters the distribution of infrared light that passes

through the interferometer. The signal directly recorded by the detector, called an "interferogram", represents light output as a function of mirror position. And then, Fourier transform processing turns the interferogram into the spectrum (light output as a function of wavelength or frequency). One reason that FTIR is favored is called “Fellgett's advantage” or the “multiplex advantage”: The information at all frequencies is collected simultaneously, improving both speed and signal-to-noise ratio. Another is called “Jacquinot's advantage” or the “throughput advantage”: there are fewer optics and no slits as with a grating, the total power of each data point is much higher. FTIR also has better accuracy of the frequencies in the spectrum, called “Conne’s advantage”[25].

Overall, the dispersive method is more common in UV-Vis spectroscopy, and FTIR is more commonly and practically used in the infrared due to its fast speed, high sensitivity and resolution.

### 2.1.2 Infrared measurement based on FTIR systems

During my PhD studies in the Kats Group, I, together with other members in the group developed a detailed protocol for measuring reflection, transmission, and emission of both macroscale and microscale samples using our FTIR system, which includes the Bruker Vertex 70, Hyperion 2000 microscope, and associated accessories (as illustrated in Fig. 2.2). Table 1.1 lists the main components of our FTIR system. By carefully choosing the right combination of sources, beam splitters, and detectors, we

are able to comprehensively cover the spectral range required for specific analytical needs.


**Figure 2.2:** A typical FTIR system: Bruker Vertex 70 + Hyperion 2000 microscope. Photo from Bruker Co.

**Table 2.1:** Main component of our FTIR system

| Components | Model | Notes |
|---|---|---|
| Internal laser | He-Ne gas laser | 632 nm |
| Source | Tungsten lamp Q428 | 20 W, 25000-1000 $cm^{-1}$ |
| | Tungsten lamp Q502 | 150 W, 25000-1000 $cm^{-1}$, water cooled |
| | Globar Q328 | 10000-50 $cm^{-1}$ |
| Beam splitter | Quartz | 28000-4000 $cm^{-1}$ |
| | Ge on KBr substrate | 7800-370 $cm^{-1}$ |
| | Multilayer | 680-30 $cm^{-1}$ |

| | | |
|---|---|---|
| Detector | Silicon diode | 25000-9000 $cm^{-1}$, room temperature |
| | InGaAs diode | 12500-5800 $cm^{-1}$, room temperature |
| | PC-MCT | 12000-600 $cm^{-1}$, Liquid $N_2$ cooled |
| | PV-MCT | 10000-850 $cm^{-1}$, Liquid $N_2$ cooled |
| | DTGS w/PE window | 700-10 $cm^{-1}$, room temperature |

#### 2.1.2.1 Reflection and transmission measurement

Reflection and transmission measurements can be conducted using a Hyperion 2000 microscope, where objectives with varying numerical apertures (NA) are selectable to suit different requirements. By utilizing a reference material with known reflectance or transmittance values, the reflectance and transmittance of the sample can be accurately determined. For larger, macroscale samples, transmission measurements can also be performed in the sample compartment on the bench, which involves nearly collimated incident light with a low NA, providing a more straightforward configuration for such analyses. Both configurations of bench measurement and microscope measurement are illustrated in Fig. 2.3.

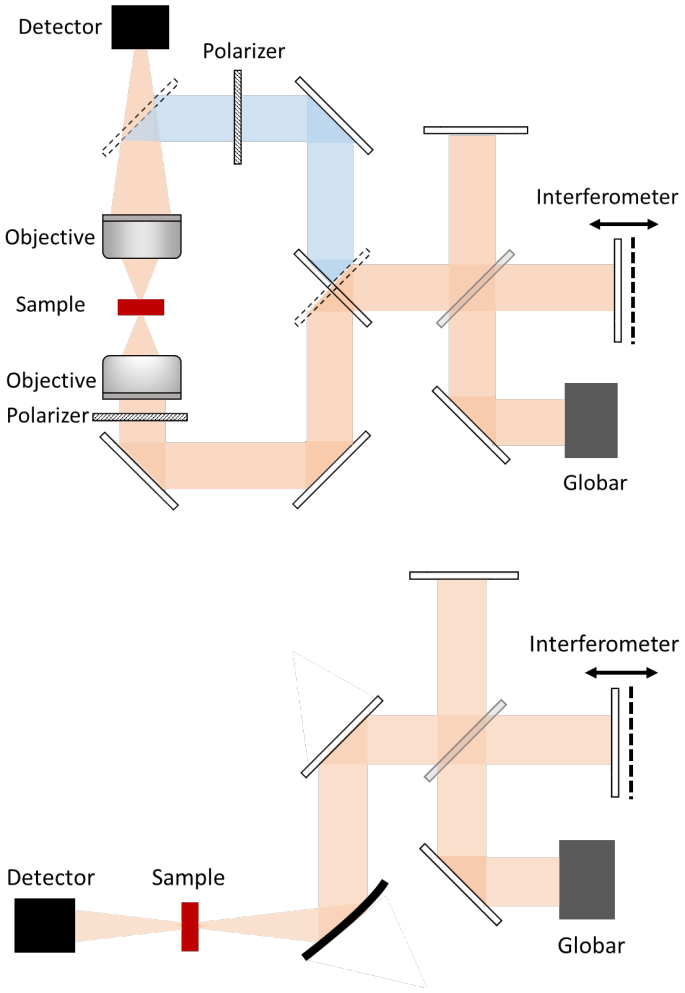


**Figure 2.3:** Schematics for reflection and transmission measurement with the Bruker FTIR system outfitted with the infrared microscope.

### 2.1.2.2 Direct emission measurement

Thermal emission refers to the radiation of electromagnetic waves from any object with a temperature higher than absolute zero. The potential of thermal-emission engineering spans multiple practical applications in solar-energy harvesting[26], thermal light sources[27], passive radiative cooling[28], infrared camouflage[29,30],

thermophotovoltaics, and environmental sensing, making it an essential point for contemporary scientific research[31]. The exploration of these applications demonstrates the wide-ranging impact of thermal-emission engineering across various industries, including renewable energy, environmental technology, and military defense.

The thermal emission from a perfect blackbody (an ideal thermal emitter) only depends on its temperature, as described by Planck's law[32].

$$B(\lambda, T) = \frac{2hc^2}{\lambda^5} \frac{1}{e^{hc/(\lambda k_B T)} - 1} \quad (2.1)$$

Where $B(\lambda, T)$ is the spectral radiance (energy radiated per unit area per unit time per unit wavelength), $\lambda$ is the wavelength of the electromagnetic radiation, $T$ is the absolute temperature of the black body, $h$ is Planck's constant, $c$ is the speed of light in a vacuum, $k_B$ is the Boltzmann constant.

For a non-ideal thermal emitter, i.e., a grey body, thermal emission also depends on how effectively the emitter can radiate, quantified as its emissivity $\epsilon(\lambda, T)$.

$$I(\lambda, T) = \epsilon(\lambda, T) \cdot \frac{2hc^2}{\lambda^5} \frac{1}{e^{hc/(\lambda k_B T)} - 1} \quad (2.2)$$

For reciprocal emitters in thermal equilibrium, the emissivity is exactly equal to its absorptivity, as described by Kirchhoff's law[33].

$$\alpha(\lambda) = \epsilon(\lambda) \quad (2.3)$$

In this case, emission can be indirectly obtained by measuring absorption (i.e., by measuring transmission, reflection and scattering). However, there are scenarios where direct emission measurement must be performed, for example nonreciprocal emitters where Kirchhoff's law is violated[34,35] and emitters not in equilibrium[36,37].

Unlike reflection and transmission measurement, direct thermal-emission measurement can be challenging due to various sources of background radiation, even from the instrument itself[38]. Our group has been working on direct thermal-emission measurement using a commercial Fourier-transform spectroscopy system integrated with an infrared microscope and a temperature control system [Fig. 2.4(a, b)]. The development of the guidelines of these direction emission measurement was led by Dr. Yuzhe Xiao, with contributions from me and other members in the group, and we summarize general guidelines for thermal-emission measurements for a variety of conditions[19], including characterization of emitters not in equilibrium or with temperature-dependent emissivity [Fig. 2.4(c)].

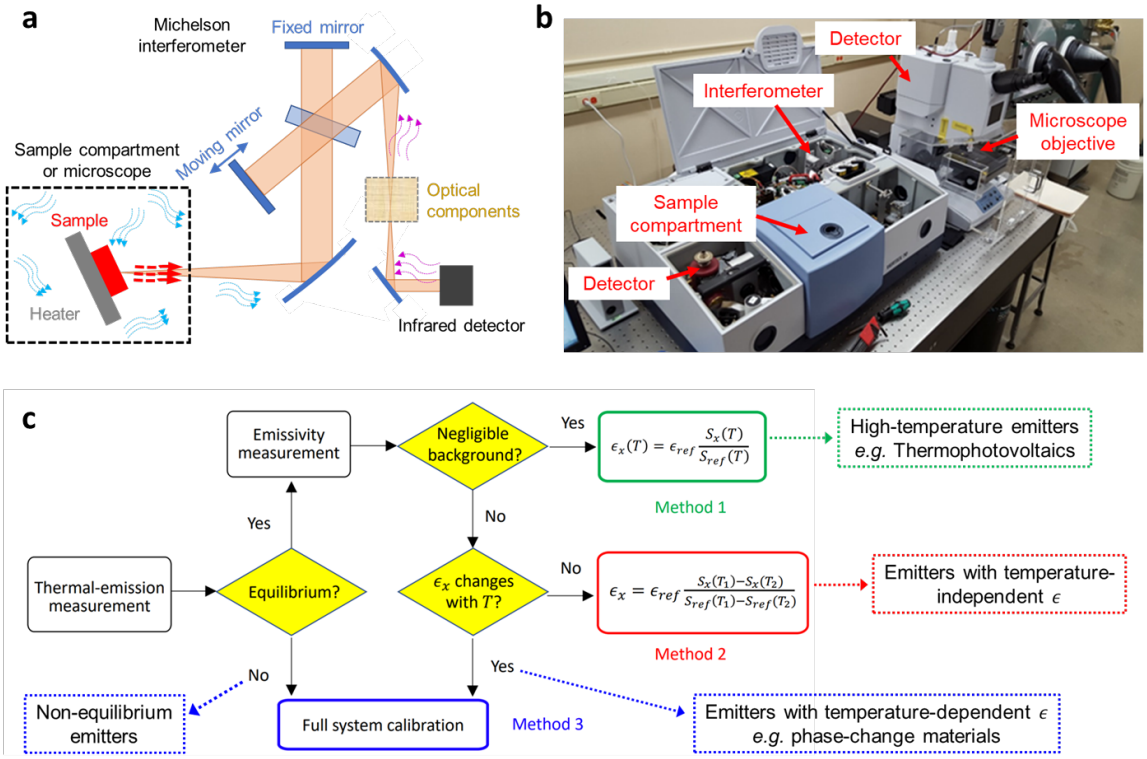


**Figure 2.4: (a, b)** Thermal-emission measurement system based on a Fourier-transform spectrometer. **(c)** Flowchart for direct emission measurements. Adapted from Ref[19].

In general, the measured signal, $S_x(\lambda, T)$, from an emitter $x$ at temperature $T$, can be expressed as:

$$S_x(\lambda, T) = m(\lambda)[\epsilon_x(\lambda, T)I_{BB}(\lambda, T) + B_x(\lambda, T)] \qquad (2.4)$$

where $m(\lambda)$ is the system-response function that quantifies the collection efficiency and the detector response, $\epsilon_x(\lambda, T)$ is the emissivity, $I_{BB}(\lambda, T)$ is the blackbody-radiation distribution, and $B_x(\lambda, T)$ is background distribution. We proposed a guideline for measurement of thermal emission and Fig. 2.4(c) shows the flowchart that can help to decide which method can be used.

***Method 1*** applies to the simplest case with (i) negligible background and (ii) temperature-independent emissivity, for example, high-temperature emitters for thermophotovoltaics[39–41]. When $B_x(\lambda,T) \ll \epsilon_x(\lambda,T)I_{BB}(\lambda,T)$, In this case, Eq. (2.4) can be well approximated by

$$S_x(\lambda,T) = m(\lambda)\epsilon_x(\lambda,T)I_{BB}(\lambda,T) \quad (2.5)$$

Therefore, $\epsilon_x(\lambda,T)$ can be obtained simply by measuring the thermal-emission signal for both the sample $x$ and a known reference, and taking the ratio:

$$\epsilon_x(\lambda,T) = \epsilon_{ref}(\lambda,T)\frac{S_x(\lambda,T)}{S_{ref}(\lambda,T)} \quad (2.6)$$

If the background $B_x(\lambda,T)$ cannot be neglected, the emissivity for temperature-independent emitters can be obtained via

$$\epsilon_x(\lambda,T) = \epsilon_{ref}(\lambda,T)\frac{[S_x(\lambda,T_1)-S_x(\lambda,T_2)]}{[S_{ref}(\lambda,T_1)-S_{ref}(\lambda,T_2)]} \quad (2.7)$$

which we denote as ***Method 2***. The background $B_x(\lambda,T)$ is cancelled out by taking the difference of two measurements at different temperatures. This is a commonly used method for the measurement of emissivity, especially in the remote sensing community[42–44], where remote emission measurements can be used to sense, *e.g.*, temperature and atmospheric humidity.

Measurement noise can become an issue when using ***Method 2***, if the difference between $T_1$ and $T_2$ are is not sufficient. If the emissivity does not change with temperature at all, then $T_1$ and $T_2$ should be chosen far away from each other so that

the denominator in Equ 2.7 is sufficiently large. If, on the other hand, the emissivity only remains constant within a narrow temperature window, then $T_1$ and $T_2$ must be chosen accordingly. In this case, the difference between temperatures will be small, which can amplify the measurement noise and may yield unreliable results. If the sample emissivity changes considerably with temperature even we pick $T_1$ and $T_2$ close to each other, ***Method 2*** will fail.

To validate ***Method 2*** using our setup, we characterized the emissivity of polished sapphire and fused-silica wafers as shown in Fig. 2.5. Here, a laboratory blackbody (approximately 500-μm tall vertically aligned carbon nanotube (CNT) forest[45] grown on a silicon substrate) with a constant emissivity of ~0.97 was used as the reference. Using the spectra in Fig. 2.5(a) and Eq. 2.7, we calculated the emissivity of sapphire and fused silica, and plotted them in Fig. 2.5(b).

To confirm the results of ***Method 2***, we also calculated the emissivity of the fused-silica wafer indirectly using Kirchhoff's law. Because the fused-silica wafer is opaque for $\lambda > 5$ μm and our sample is non scattering (the wafer is polished), Kirchhoff's law yields:

$$\epsilon(\lambda) = \alpha(\lambda) = 1 - R(\lambda) \qquad (2.8)$$

where $\alpha(\lambda)$ is the sample absorptivity. We measured the optical properties ($n$ and $\kappa$) of the fused-silica wafer using spectroscopic ellipsometry and then calculated its reflectance using Fresnel equations. The indirectly calculated emissivity via Eq. 2.8 is

plotted in Fig. 2.5(b) and is in excellent agreement with direct measurement ***Method 2***.

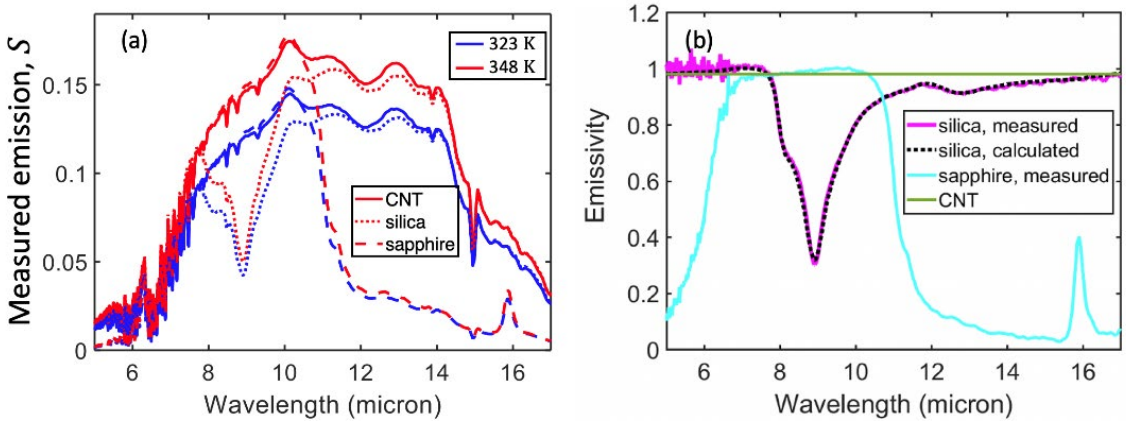


**Figure 2.5: (a)** Measured thermal-emission signal (in arbitrary units) from a CNT blackbody (solid), a fused-silica wafer (dotted), and a sapphire wafer (dashed), at 323 (blue) and 348 K (red). The measurements were unpolarized, at an angle of 10°. **(b)** Measured emissivity of the fused-silica (solid purple) and sapphire (solid cyan) wafers using the data in **(a)**, extracted ***Method 2***. The emissivity of the CNT blackbody is plotted using the solid-green curve. The calculated emissivity of fused silica using $n$ and $\kappa$ measured with spectroscopic ellipsometry is plotted using the dotted-black curve, showing excellent agreement with ***Method 2***. Figures adapted from Ref[19].

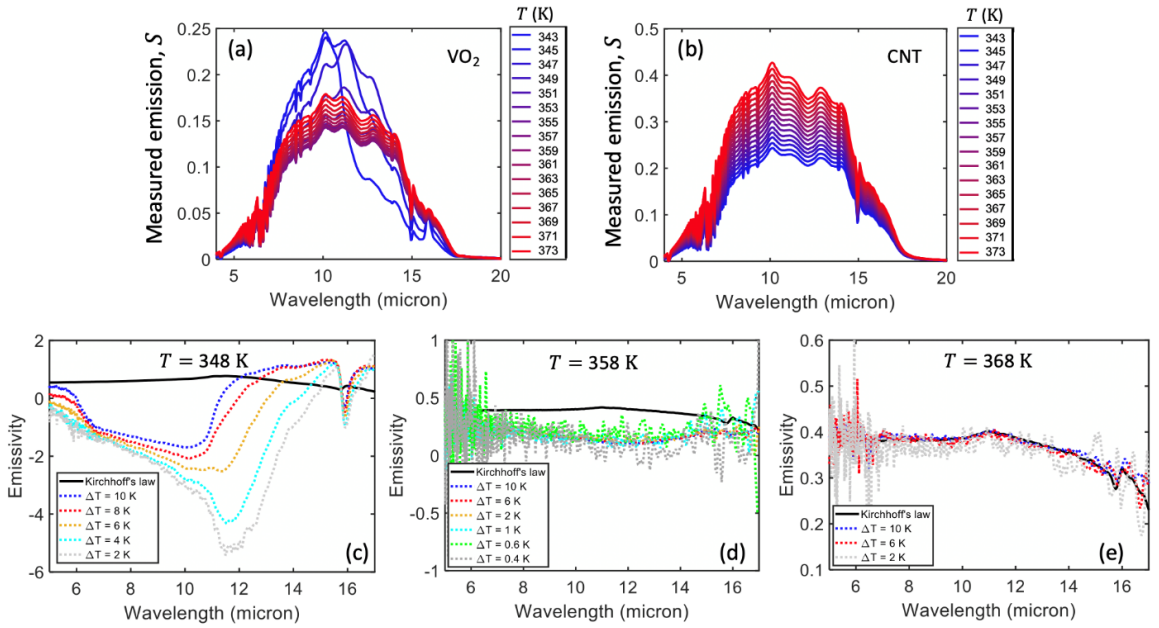


**Figure 2.6: (a, b)** Measured thermal-emission signal (in arbitrary units) from the $VO_2$-based emitter and the blackbody from 343 to 373 K. The measurements were unpolarized, at an angle of 10°. **(c-e)** Comparison of the measured emissivity of the $VO_2$-based emitter using Kirchhoff's law (solid black, here assumed to be correct) and direct emission measurements analyzed with ***Method 2*** (dotted curves, Eq. 2.7) around $T = 348$ K **(c)**, 358 K **(d)**, and 368 K **(e)** for different values of $\Delta T$. The results in **(c)** and **(d)** show that ***Method 2*** cannot be applied to emitters with temperature-dependent emissivity. The agreement in **(e)** comes from the fact that the emissivity of the $VO_2$-based emitter no longer changes with temperature beyond 360 K. Figure adapted from Ref[19].

For cases where the background cannot be neglected and the emissivity changes with temperature, full system calibration is needed, which we denote as ***Method 3***. This method applies to almost all situations, including emitters not in equilibrium or with temperature-dependent emissivity. This method allows for the extraction of the true

emission $I_x(\lambda, T)$ by first fully characterizing the system response $m(\lambda)$ and the background $B_x(\lambda, T)$:

$$I_x(\lambda, T) = \epsilon_x(\lambda, T) I_{BB}(\lambda, T) = \frac{S_x(\lambda,T)}{m(\lambda)} - B_x(\lambda, T) \quad (2.9)$$

If the emitter is in thermal equilibrium, its emissivity can be determined via:

$$\epsilon_x(\lambda, T) = \frac{\frac{S_x(\lambda,T)}{m(\lambda)} - B_x(\lambda,T)}{I_{BB}(\lambda,T)} \quad (2.10)$$

The response function $m(\lambda)$ can be obtained from Eq. 2.11 by using the thermal-emission signal measured from a known reference whose optical properties do not change with temperature at two different temperatures $T_1$ and $T_2$:

$$m(\lambda) = \frac{S_{ref}(\lambda, T_1) - S_{ref}(\lambda, T_2)}{\epsilon_{ref}(\lambda)[I_{BB}(\lambda, T_1) - I_{BB}(\lambda, T_2)]} \quad (2.11)$$

The characterization of $B_x(\lambda, T)$ is more complicated. Depending on both the optical properties of the emitter and the specific experimental setup, there are several ways that the emitter $x$ could have an impact on $B_x(\lambda, T)$, such as via reflection, transmission, or scattering. Therefore, different types of emitters, such as opaque and non-scattering emitters in thermal equilibrium or non-equilibrium, semi-transparent and non-scattering emitters, and the more complex scattering emitters, require distinct considerations. For a more comprehensive analysis of these cases, detailed discussions are available in Ref[19].

In summary, the methods for directly measuring thermal emission can vary significantly, contingent upon the optical properties and temperature-dependence of

the emitter, as well as the relevance of background emission in the instrument. We have outlined various methods designed to capture the nuances of thermal emission across a spectrum of increasingly complex scenarios. Note that all of the demonstrations of these methodologies are realized using the Fourier-transform infrared (FTIR) spectrometer in our laboratory.

Our extensive analysis highlights that a measurement apparatus can be characterized to facilitate the accurate measurement of temperature-dependent emissivity, and emitters that are not in thermal equilibrium. By employing rigorous calibration procedures and advanced analytical techniques, our lab has effectively characterized the specific emissivity characteristics of diverse materials. The development and refinement of these measurement methods pave the way for new insights in thermal physics and enhanced applications in technology and industrial processes. Our results affirm the robustness of the FTIR spectrometer in handling complex measurements and underscore the importance of precise instrument calibration to achieve reliable data. As we continue to refine these techniques, we anticipate even more sophisticated analyses and applications emerging from the study of thermal emission.

### 2.1.3 Issues and challenges: detector nonlinearity

While FTIR spectrometers excel in measurements such as reflection, transmission, and emission, they are not without challenges. We found that temperature-dependent

(especially at high temperature) infrared spectroscopy measurements (i.e., reflectance or transmittance) using a Fourier-transform spectrometer can have substantial errors, especially for elevated sample temperatures and collection using an objective lens. These errors can arise as a result of partial detector saturation due to thermal emission from the measured sample reaching the detector, resulting in nonphysical apparent reduction of reflectance or transmittance with increasing sample temperature. In the session, we demonstrate that these temperature-dependent errors can be corrected by implementing several levels of optical attenuation that enable convergence testing of the measured reflectance or transmittance as the thermal-emission signal is reduced, or by applying correction factors that can be inferred by looking at the spectral regions where the sample is not expected to have a substantial temperature dependence.

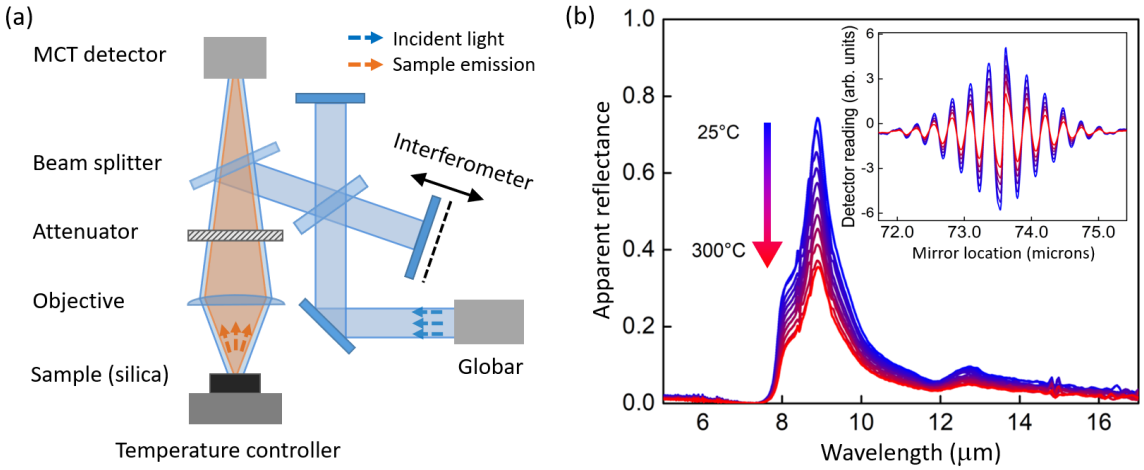


**Figure 2.7:** Nonlinearity in temperature-dependent reflectance measurements. **(a)** The optical path of our Fourier-transform spectrometer (FTS). An infrared microscope is placed after the interferometer with a reflective objective that illuminates the sample and then

collects the reflected light and sends it to the MCT detector. The photons that hit the detector mainly come from two components: (1) the light from the Globar, which passes through the interferometer and is therefore modulated, and (2) the thermal emission from the sample, which does not pass through the interferometer and is therefore not modulated. **(b)** Measured apparent reflectance of a flat fused-silica wafer from 25 to 300 °C, in intervals of 25 °C, using a gold mirror (at room temperature) as a reference. We observe a (mostly) nonphysical decrease in reflectance as a function of temperature over the entire wavelength range. Inset: the center-burst regions of selected interferogram traces corresponding to the spectra in the main panel. Figure adapted from Ref[20].

Figure 2.7(a) shows a standard FTS setup we used for temperature-dependent reflectance measurements. The sample is placed on a temperature-controlled stage, so that its reflectance can be measured as a function of temperature. An infrared microscope is positioned after the interferometer, such that the sample is illuminated using a reflective objective with NA = 0.4, with the reflected light collected using the same objective, and then sent to a liquid-nitrogen-cooled mercury-cadmium-telluride (MCT) detector. The light incident on the detector can be broken down into two components: (1) light from the FTS source, which passes through the interferometer and is reflected by the sample, and (2) thermal emission from the sample which does not pass through the interferometer, and thus is not modulated by the scanning mirror [Fig. 2.7(a)]. We refer to the reflected light as the AC contribution, and the thermal emission from the sample as the DC contribution [Fig. 2.8(a)]. Because of the standard AC coupling of the detector amplifier, the DC contribution is not be directly

measured by the instrument. Nevertheless, this DC contribution still hits the detector, thus "invisibly" contributing to detector saturation.

In Fig. 2.7(b), we plotted the measured temperature-dependent reflectance spectra of a polished fused-silica wafer (about 0.5 mm thick) from 25 to 300 °C, normalized to a gold mirror measured at room temperature. The measured reflectance is dramatically reduced for increasing temperature (more than 50% reduction from 25 to 300 °C), which is nonphysical for silica[46], and points to the presence of detector nonlinearity. The fused-silica measurement is somewhat complicated by the fact that a reflectance reduction with temperature is actually expected at frequencies near the vibrational resonance of this material[46,47], but the expected reduction is much smaller than what is observed in Fig. 2.7(b). Note that this anomaly includes only a reduction in the amplitude of the interferogram, but no interferogram phase shift (inset of Fig. 2.7(b)), such as the one we previously observed in certain thermal-emission measurements near room temperature[38]. We also note that it has been reported that a portion of light thermally emitted by the sample may enter the interferometer and be reflected back to the sample, adding extra distortions to the interferogram[48,49]; we believe this path to be at most a minor effect in our setup, in particular because the reduction in reflectance in Fig. 2.7(b) appears to be wavelength-independent. To the best of our knowledge, though the nonlinear effects in FTS measurements have been widely reported, the wavelength-independent reduction in the measured interferogram for temperature-dependent microscope-based infrared reflectance and transmittance measurements has not been appropriately addressed.

The saturation effort can be found in different types of infrared detectors, including InSb, InGaAs, and MCT detectors[50–53], when the intensity of incident light exceeds a certain threshold. In our experiments, an MCT detector is used. Note that DLaTGS and DTGS detectors are known to have less nonlinearity and hence may help during temperature-dependent measurements, but at the cost of a significantly lower signal-to-noise ratio[54]. In the detectors and their associated electronics, there can be a nonlinear relationship between the recorded voltage signal and the incident photon intensity. To understand the effect of the detector nonlinearity (specifically, the nonlinear relationship between the recorded voltage signal and the incident photon intensity) on temperature-dependent measurements, we first summarize how an interferogram is generated in an FTS: the motion of a mirror in one arm of a Michelson interferometer modifies the interference condition at the detector, resulting in a variation of incident photon flux (we refer to this mirror-position-dependent photon flux as the AC contribution). In the measurement described in Fig. 2.7(a), photon flux on the detector also includes a DC contribution from thermal emission from the sample that does not pass through the interferometer and is therefore mirror-position-independent. For the same sample at different temperatures, the AC contribution is expected to be approximately the same, since the optical properties of most materials have a weak dependence on temperature. However, the DC contribution can change substantially due to the temperature dependence of thermal emission [Fig. 2.8(a)]. Figure 2.8(b, c) schematically shows the mapping from photon flux to voltage and how the nonlinear detector responsivity affects these conversion

processes. The physical position-dependent voltage (before being processed by the detector amplifier) consists of an AC part, $V^{AC}(x,T)$, and a DC part, $V^{DC}(T)$[51], where $x$ represents the location of the moving mirror in the interferometer and $T$ is the temperature of the sample. In practice, the AC-coupled detector amplifier filters out the DC part $V^{DC}(T)$, so only the AC part $V^{AC}(x,T)$ is recorded as the measured interferogram $I_m(x,T)$. However, the DC contribution of the incident photon, though typically not recorded, can nevertheless have an impact on the measurement due to detector nonlinearity. Since the detector responsivity curve is expected to be concave down with increasing photon flux (partial saturation) [Fig. 2.8(b)], the large DC contribution from a high-temperature sample can lead to a suppression in the amplitude of its recorded AC contribution [Fig. 2.8(c)]. Therefore, we introduce a sample-dependent distortion factor $d(T)$ to describe the reduction in amplitude, so that the measured interferogram can be expressed as:

$$I_m(x,T) = d(T)V^{AC}(x,T) \quad (2.12)$$

We expect that $d(T) = 1$ when the sample is at room temperature, but gradually decreases with increasing sample temperature, which explains the wavelength-independent decrease in our measured spectra. Note that the AC contribution can result in additional mirror-position-dependent detector saturation, especially in the center-burst region[55,56], but this effect does not influence the mirror-position-independent amplitude suppression in the recorded interferograms induced by the DC contribution and is also not noticeable in our experiments, therefore, is not the focus of this manuscript.

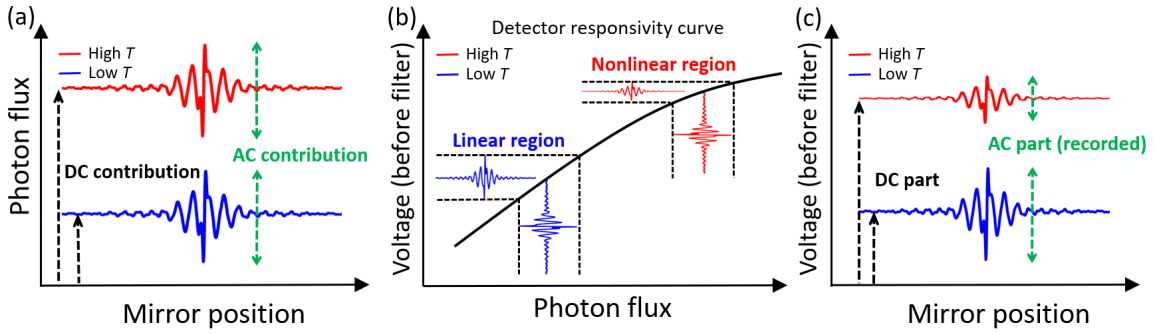


**Figure 2.8:** The effect of detector nonlinearity on high-temperature spectroscopy measurements. **(a)** For high-temperature measurements in our FTS, the photon flux on the detector includes (1) the AC contribution which is mirror-position-dependent and (2) the DC contribution from the thermal emission, which is temperature-dependent. Therefore, when a sample is heated to a higher temperature, the DC contribution increases while the AC contribution remains basically unchanged. **(b)** Beyond a certain threshold, the slope of the responsivity curve (voltage vs. photon flux) decreases with increasing incident photon flux. **(c)** The voltage (before the high-pass filter) also includes the AC and DC parts, while only the AC part is recorded as the measured interferogram. Due to the decreasing slope of the responsivity curve, the unrecorded DC contribution from a high-temperature sample can cause a reduction in the amplitude of its recorded AC contribution. Figure adapted from Ref[20].

Here we introduce two nonlinearity correction methods: one based on "convergence testing" using increasing levels of optical attenuation, and a second based on data processing, where we use prior knowledge about the material to correct the temperature-dependent measurement data. The two methods can be used independently or in tandem.

First, since the nonlinearity is attributed to the overlarge photon flux that strikes the detector, the most intuitive way to minimize the nonlinearity is to introduce attenuation into the beam path[49], increasing the attenuation level until the detector

response is approximately linear; we refer to this approach as ***Method 1***. In our setup, we use an aluminum foil with evenly spaced holes (each several millimeters in diameter) as a mesh-type attenuator. Note that it is rather common to implement attenuations in FTS-based measuring systems to limit the intensity of incident beam from the light source. In most cases, the attenuator or optical aperture is placed between the source and the interferometer[57]. However, this attenuator placement will not work in our case because it is the thermal emission from the sample that does not pass through the interferometer that results in the nonlinearity. Therefore, our attenuator is positioned right above the objective (Fig. 2.7(a)), such that it reduces both the reflected light (not necessarily desired) and the thermal radiation from the sample.

Figure 2.9(a-c) shows the measured apparent reflectance of fused silica from 25 to 300 °C using different levels of attenuation (no attenuation, attenuation to about 25% of the original photon flux and attenuation to about 15%, respectively) to perform a "convergence test". As the attenuation increases, the nonphysical reduction in the apparent reflectance begins to vanish. When the intensity is substantially attenuated, the measured reflectance of silica becomes mostly independent of temperature except for the spectral region between 8 to 9 μm, where the actual (physical) reflectance is affected by the temperature-dependent vibrational resonances of $SiO_2$[47].

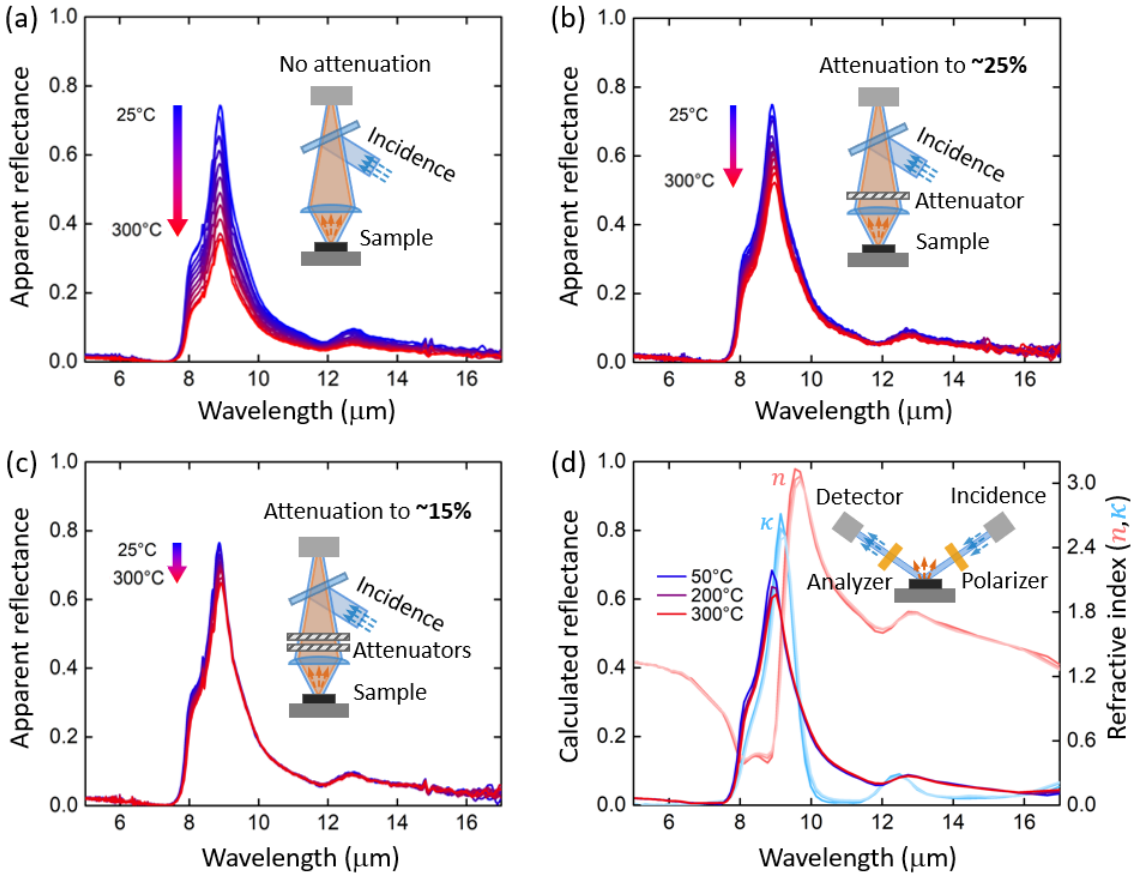


**Figure 2.9:** Convergence testing using increasing attenuation. **(a-c)** Measured apparent reflectance of a fused-silica wafer from 25 to 300 °C using our FTS with **(a)** no attenuation, **(b)** attenuation to about 25%, and **(c)** attenuation to about 15%, respectively. **(d)** Temperature-dependent real ($n$) and imaginary ($\kappa$) parts of the complex refractive index of fused silica extracted from ellipsometry measurements, and the calculated reflectance based on the ellipsometry data. The inset shows the schematic of the ellipsometer used in our measurements with incident angles of 60 and 70°. Figure adapted from Ref[20].

For comparison, we also measured and fitted the complex refractive index ($n$ and $\kappa$) of the same fused-silica sample at 50, 200 and 300 °C using infrared variable-angle spectroscopic ellipsometry (IR-VASE) and then calculated its reflectance using

Fresnel coefficients, as shown in Fig. 2.9(d). Note that the ellipsometry measurements were much-less affected by temperature compared to our microscope-based reflectance measurements, because the beam in the ellipsometer was well collimated, and therefore most of the thermal emission (emitted into a large solid angle) could be filtered out by a small aperture in front of the detector which is placed about 25 centimeters away from the sample. Note also that a large solid angle in a microscope measurement is necessary to isolate thermal emission from a small sample, and thus the approach we took with ellipsometry is only applicable to large sample areas. The calculated reflectance is consistent with the FTS reflectance measurements at the highest level of attenuation [i.e., Fig. 2.9(c)].

We also explored a second method for extracting the true temperature-dependent reflectance from the apparent reflectance based entirely on data processing, denoted as ***Method 2***. This method can be inferred from Eq. 2.12: we can correct the measured interferogram by inferring the mirror-position-independent distortion factor $d(T)$ from experimental data. To demonstrate this approach, we used both the fused-silica wafer we previously used in Figs. 2.7 and 2.9, and also a polished sapphire wafer (also about 0.5 millimeter thick). Figure 2.10(a, d) shows the apparent reflectance of these samples measured with no attenuation (i.e., the data in Fig. 2.10(a) are the same as Fig. 2.7(b) and Fig. 2.9(a)). In Fig. 2.10(b, e), we show the ratio $r(\lambda, T)$ of the reflectance measured at temperature $T$ to the reflectance measured at $T_{room} = 25$ °C:

$$r(\lambda, T) = \frac{R(\lambda,T)}{R(\lambda,T_{room})} \quad (2.13)$$

For both samples, $r(\lambda, T)$ has several features. There exist wavelength regions where $r(\lambda, T)$ is temperature-dependent, such as 15 – 16 μm in Fig. 2.10(e); this temperature dependence is expected to be physical. Other regions are noisy, such as 5 – 8 μm and 15 – 17 μm in Fig. 2.10(b), resulting from a division by zero where $R(\lambda, T_{room})$ is very small. However, there are also regions within the mid-infrared atmospheric-transparency window where the ratios are almost flat, suggesting that the decrease in $R(\lambda, T)$ is wavelength-independent, and therefore likely nonphysical. We interpret this wavelength-independent region of $r(\lambda, T)$ as representative of the distortion factor $d(T)$ in Eq. 2.12. Note that the "flat ratio" in Fig. 2.10(b) includes a distortion around 12 μm due to the presence of a secondary vibrational resonance; nevertheless, the distortion is small, so we fitted $d(T)$ to the entire 9 – 14 μm region. Thus, we fit these "flat ratios" into constants based on the least-squares method[58], and then the true interferogram can then be calculated by:

$$I_t(x, T) = \frac{I_m(x,T)}{d(T)} \qquad (2.14)$$

where $I_t(x, T)$ and $I_m(x, T)$ represent the true and measured interferogram, respectively. For example, the fitted $d(300\ ℃)$ for silica and samphire is 0.49 and 0.57, respectively. Based on Eq. 2.14, we corrected the apparent reflectance of the fused-silica and sapphire wafers, as shown in Fig. 2.10(c, f). The corrected spectra are mostly temperature-independent, except for the spectral regions corresponding to vibrational resonances. The insets in Fig. 2.10(c, f) show the vibrational-resonance regions of silica and sapphire, respectively, where their optical properties are

expected to be temperature-dependent. These characteristic peaks gradually change in value and shift in wavelength with increasing temperatures.

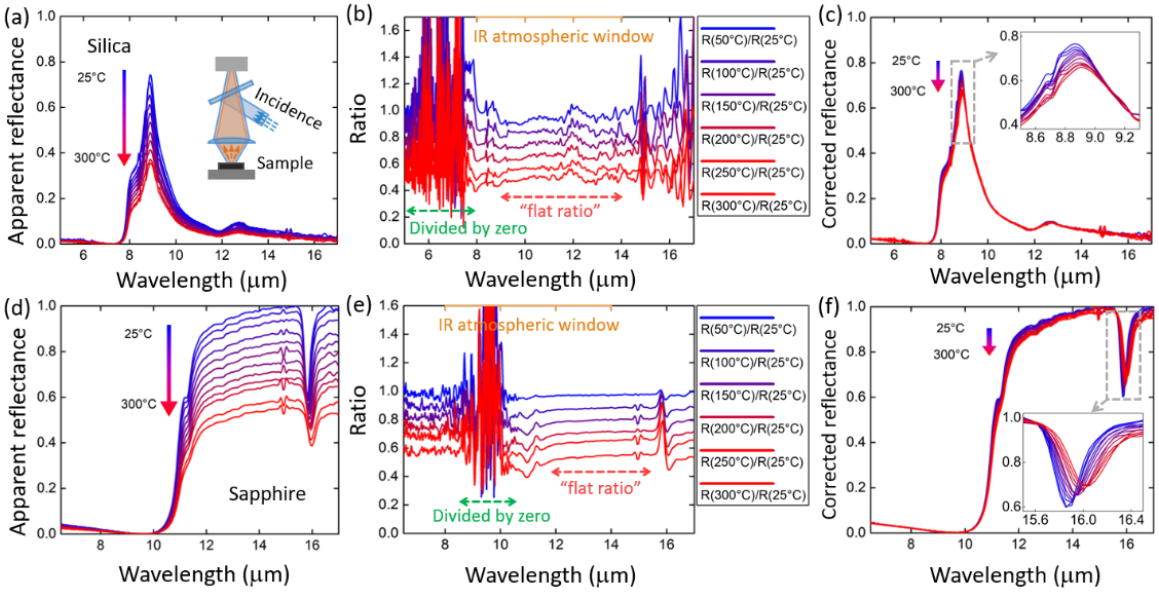


**Figure 2.10:** Correction of the apparent reflectance assuming the existence of temperature-independent wavelength ranges. **(a, d)** Measured apparent reflectance of flat **(a)** fused-silica and **(d)** sapphire wafers from 25 to 300 °C using an FTS with no attenuation. **(b, e)** Ratios of spectra measured at different temperatures, i.e., the ratio between the spectrum at high temperature and the spectrum at 25 °C, for **(b)** fused silica and **(e)** sapphire. There exist spectral regions where the ratios are approximately wavelength-independent, and other regions where the ratio is noisy because the reflectance values are very low (resulting in divide-by-zero errors). **(c, f)** Corrected reflectance of **(c)** fused-silica and **(f)** sapphire wafers from 25 to 300 °C, calculated by multiplying the apparent reflectance spectra in **(a, d)** by the fitted constant ratios in **(b, e)**. The insets show spectral regions near vibrational resonances where the temperature-dependent changes in reflectance are expected to be physical. Figure adapted from Ref[20].

In Fig. 2.11, we plot the reflectance spectra of both fused silica and sapphire corrected using ***Method 1*** (solid lines) and ***Method 2*** (dashed lines) at 50 and 300 °C, respectively. The reflectance of silica obtained via ellipsometry measurements and the indirectly calculated reflectance of sapphire via Kirchhoff's law based on our previous direct emissivity measurements[19] are also plotted (dotted lines) for comparison; note that below 7 μm, the sapphire sample becomes partially transparent, and therefore this simple expression for Kirchhoff's law does not apply, resulting in a minor discrepancy. The spectra corrected using ***Method 1*** and ***Method 2*** are very consistent for both samples, as evaluated using mean-absolute-percent discrepancies (defined as $\Delta = \frac{1}{n}\sum_{i=1}^{n}\left|\frac{A_i - B_i}{A_i}\right|$, where $A_i$ and $B_i$ denote the reflectance spectra corrected using Method 1 and Method 2, respectively). For silica, $\Delta = 1.4\%$ at 50 °C and 2.6% at 300 °C, and for sapphire $\Delta = 1.6\%$ at 50 °C and 3.1% at 300 °C. We note that different references are used for the reflectance and direct-emission measurements (gold for reflectance, carbon-nanotube forest for emission[19]), so imperfect knowledge of the reflectance and emissivity of these references may lead to minor differences in the extracted reflectance spectra. The reflectance of silica based on the ellipsometry measurements is also close to the corrected spectra, though there are some minor differences ($\Delta = 7.6\%$ and 8.7% for silica at 50 and 300°C, respectively) that we attribute to errors in the fitting of $n$ and $\kappa$ and also to the difference in numerical aperture between the ellipsometry and FTS measurements.

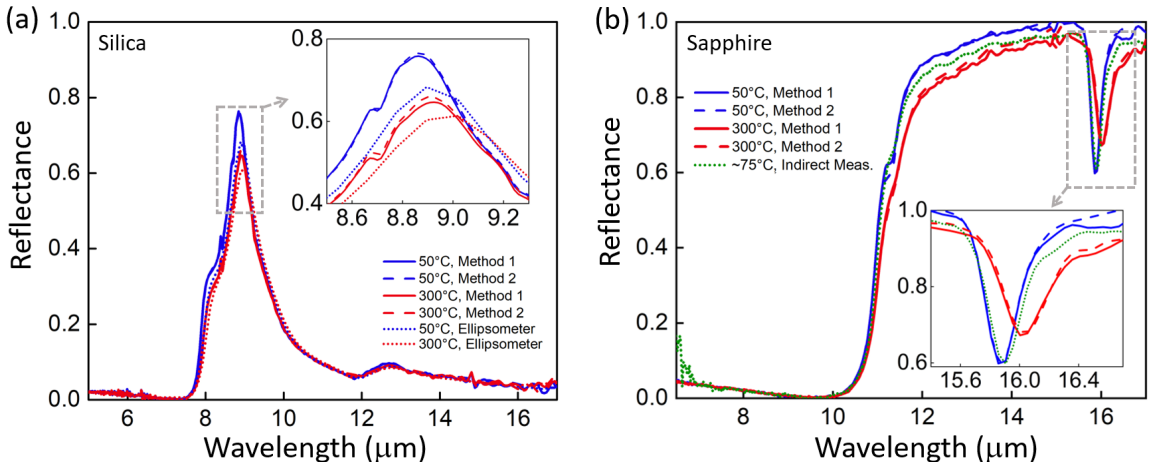


**Figure 2.11:** Verification of the two correction methods. **(a)** Solid lines, dashed lines and dotted lines represent the reflectance of fused silica at 50 and 300 °C obtained based on method 1, method 2, and ellipsometry measurements, respectively. **(b)** Solid lines and dashed lines represent the reflectance of sapphire at 50 and 300 °C obtained based on method 1 and method 2, respectively. The dotted green line represents the indirectly calculated reflectance of sapphire at around 75 °C via Kirchhoff's law based on our previous direct emissivity measurements[19]. The insets show the spectral regions where the temperature-dependent changes in reflectance are expected due to the vibrational resonances. Figure adapted from Ref[20].

In summary, we observed a nonphysical reduction in the reflectance of samples measured using a Fourier-transform spectrometer (FTS) and infrared microscope for increasing sample temperature. We figured out that this reduction, which is expected in both reflection and transmission measurements, results from partial detector saturation due to significant thermal emission from the heated samples. The effect is expected to be particularly large for measurement using a large numerical aperture, such as in microscope-based experiments that can be used for small samples, because

of the collection of thermal emission over a large solid angle. We proposed and verified two methods to measure or recover the true reflectance (or transmittance) spectra even when the detector saturation is substantial. ***Method 1*** is a "convergence testing" approach using several levels of attenuation in the setup to reduce detector saturation until it is negligible. The attenuators are placed after the sample to suppress the thermal emission from the sample, though the attenuation can also compromise the signal-to-noise ratio of the measurement, which if needed can be boosted using a lock-in amplifier[59]. ***Method 2*** applies correction factors by looking at reflectance/transmittance data within spectral regions where the sample has minimal temperature dependence. ***Method 2*** requires the materials to be measured to have weak temperature dependence in at least some portion of the spectrum where the reflectance/transmittance is not close to zero, such that the correction factor can be properly fitted. Hence, ***Method 2*** cannot be used for samples with strong temperature-dependent characteristics where no "flat region" over a substantial wavelength range exists. In practice, the two correction methods can be used independently or in combination, where the latter means implementing sufficient attenuation during the measurements and then fitting the correction factors (expected to be close to 1) to verify or correct the measured spectra.

Addressing the issue of detector nonlinearity in infrared measurements using FTS is crucial for enhancing the accuracy of data across various scientific fields. Nonlinear responses can lead to significant errors in quantifying sample characteristics,

especially in complex analyses involving subtle spectral features. Developing robust calibration methods to correct these nonlinearities is therefore essential. It ensures that FTIR spectrometry remains a reliable tool for precise measurements, whether in research, quality control, or diagnostic applications, ultimately leading to more consistent and trustworthy results.

## 2.2 Generalized Spectroscopic Ellipsometry

### 2.2.1 Working principle of ellipsometry

Spectroscopic ellipsometry is a sophisticated optical technique used to measure the dielectric properties (refractive index $n$ and extinction coefficient $\kappa$) of materials and/or thickness of thin film structures[60]. It is highly precise and non-destructive, and is broadly used in materials science, semiconductor manufacturing, and optical coatings. Ellipsometers measure the change in the polarization of light reflected from the surface of a sample, given an incident beam with well-known polarization state. The change in polarization of light interacting with the measured sample is quantified in the complex valued Fresnel coefficients, which are the ratios between the reflected and the incident field amplitudes with respect to light polarized parallel ($p$-polarized) and perpendicular ($s$-polarized) to the plane of incidence, as shown in Fig. 2.12.

$$r_{pp} = \frac{E_{p_{out}}}{E_{p_{in}}}, \qquad r_{ss} = \frac{E_{s_{out}}}{E_{s_{in}}} \qquad (2.15)$$

$$r_{ps} = \frac{E_{s_{out}}}{E_{p_{in}}}, \quad r_{sp} = \frac{E_{p_{out}}}{E_{s_{in}}} \qquad (2.16)$$

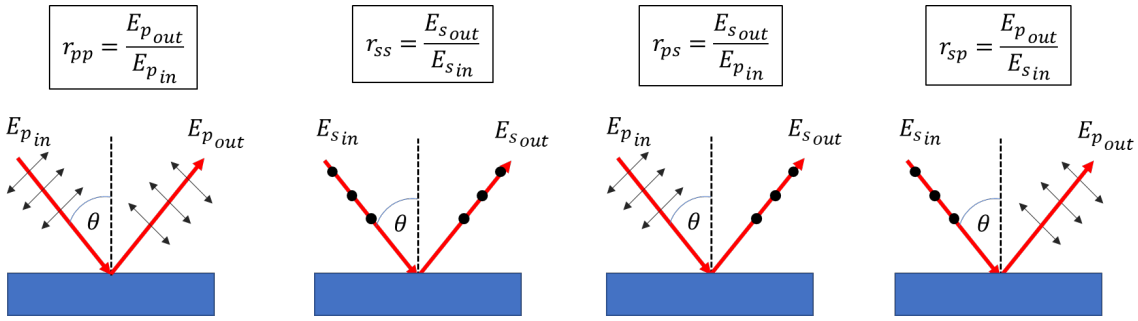


**Figure 2.12:** Schematics showing the ratios between the incident field and reflected field (Fresnel coefficients).

Ellipsometry measures the ratio between the two complex Fresnel coefficients in the case of a bulk (approximated as semi-infinite) sample, or, for single and multi-layered samples, the ratio of the pseudo Fresnel coefficients, which is defined as the ratio between the total reflected or transmitted field amplitude to the incident field. This complex ratio is described by $A_{ne}, A_{ps}, A_{sp}$. $A_{ne}$ is the ratio between the two Fresnel coefficients $r_{pp}$ and $r_{ss}$, and $A_{ps}$ and $A_{sp}$ are the "$p$ into $s$" ratio and "$s$ into $p$" to capture the cross-polarization interaction.

$$A_{ne} = \rho = \frac{r_{pp}}{r_{ss}} = \tan\left(\Psi_{A_{ne}}\right) e^{i\Delta_{A_{ne}}} \qquad (2.17)$$

$$A_{ps} = \frac{r_{ps}}{r_{pp}} = \tan\left(\Psi_{A_{ps}}\right) e^{i\Delta_{A_{ps}}} \qquad (2.18)$$

$$A_{sp} = \frac{r_{sp}}{r_{ss}} = \tan\left(\Psi_{A_{sp}}\right) e^{i\Delta_{A_{sp}}} \qquad (2.19)$$

where Ψ and Δ are the two quantities (in degrees) measured by the ellipsometer, and tan(Ψ) is related to the magnitude of the ratio and Δ is related to the phase difference between the two coefficients. The term $A_{ne}$ is also referred to as the normal ellipsometric coefficients and alone can be used to quantify isotropic optical materials. For anisotropic materials, a more generalized ellipsometry approach is used to capture all cross-polarization interactions and $A_{ps}$ and $A_{sp}$ terms are needed. Other than $A_{ne}, A_{ps}, A_{sp}$, one can also use Mueller matrix elements to describe how the sample transforms the Stokes vector of the incident light. More details of Mueller matrix measurement and fitting will be discussed in Chapter 3.

Since the ratio between the two polarization states is all that is measured, capturing the absolute magnitude of the reflected light is not necessary for accurate measurements. This makes ellipsometry insensitive to fluctuations in light intensity and partial scattering due to macroscopic dust or surface defects, and allows for use of a beam larger than the sample size.

The quantities of interest from the measurement of a sample, however, are not the raw data channels Ψ and Δ but rather the optical properties—$n$ and $\kappa$—and/or thickness if the material is a thin film structure. In the simplest case of a uniform, semi-infinite substrate the optical properties can be directly calculated via[61,62]:

$$n + i\kappa = n_o \sin(\theta_i) \sqrt{1 + \tan^2(\theta_i) \left(\frac{1-\rho}{1+\rho}\right)^2} \quad (2.20)$$

where $n_o$ is the refractive index of the medium surrounding the sample (typically air, $n$ = 1), $\theta_i$ is the angle of incidence of the light incoming to the sample, and $\rho$ are the measured ratios of the Fresnel coefficients from Eq. 2.17. For more complicated structures such as thin films structures or a rough surface, Eq. 2.20 only represents pseudo refractive index, *i.e.*, the refractive index assuming the entire structure is a semi-infinite substrate with all reflected light being from the first reflection.

Thus, to extract the true refractive indices of a more complex structure, a model must be built to solve for the inverse problem: find $n$, $\kappa$, and thickness that will fit the measured Ψ and Δ. In the context of ellipsometry, the model is one that can represent the materials' optical response to light. Each layer in the model is given a thickness and optical constants ($n$ and $\kappa$) that can be varied. The optical constants are not independent arbitrary values, however. They are determined by using optical oscillator functions (*e.g.*, Lorentz, Sellmeier, Drude, etc.) to provide a physically-grounded basis, that is, the optical oscillator are consistent with the Kramers-Kronig relation where the real and imaginary parts of the optical constants are coupled and correlated[63,64].

Then, the ellipsometry fitting process involves iteratively adjusting model parameters to best match the experimental data obtained from ellipsometric measurements. This typically starts with an initial guess for the parameters and then refined using optimization algorithms to minimize the difference between the measured ellipsometric parameters (Ψ and Δ) and those calculated by the model,

often employing methods like least squares fitting. Figure 2.13 outlines the complete flow of performing ellipsometry analysis. In this work, the building of optical models, fitting of model parameters, and calculation of optical properties were performed using the WVASE32 software suite provided by J.A. Woollam Company[63].

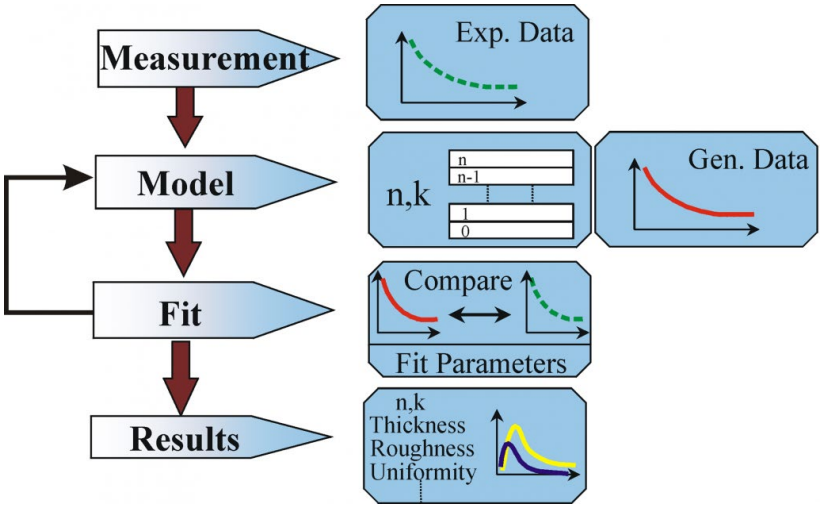


**Figure 2.13:** A flow chart describing the ellipsometry data fitting process for extracting optical parameters of a material, typically the complex refractive index, but also thickness, nonuniformity, surface roughness, and anisotropy among others. Adapted from J. A. Woollam[63].

## 2.2.2 Instrumentation

The primary tools for collecting ellipsometry data all include the following: light source, polarization generator, sample stage, polarization analyzer, and detector. Light Source provides a continuous spectrum of light, usually from the ultraviolet through the visible to the near-infrared, broadband infrared sources such as Globar can also be used for mid- and far-infrared measurement. The polarization generator

and analyzer are constructed of optical components that manipulate the polarization: polarizers, compensators, and phase modulators. Sample stage holds the sample and can often rotate to change the angle of incidence. Polarization analyzer analyzes the state of polarization after reflection from the sample. Detectors working at different spectral range can be used for measuring the intensity of the light and outputs data that can be analyzed to determine Ψ and Δ. Common ellipsometer configurations include rotating analyzer (RAE), rotating polarizer (RPE), rotating compensator (RCE), and phase modulation (PME)[65]. The RAE configuration is shown in Figure 2.14. A light source produces unpolarized light which is then sent through a polarizer. The polarizer allows light of a preferred electric field orientation to pass. The polarizer axis is oriented between the $p$- and $s$- planes, such that both arrive at the sample surface. The linearly polarized light reflects from the sample surface, becomes elliptically polarized, and travels through a continuously rotating polarizer (referred to as the analyzer). The amount of light allowed to pass will depend on the polarizer orientation relative to the electric field "ellipse" coming from the sample. The detector converts light to electronic signal to determine the reflected polarization. This information is compared to the known input polarization to determine the polarization change caused by the sample reflection. This is the ellipsometry measurement of Ψ and Δ.

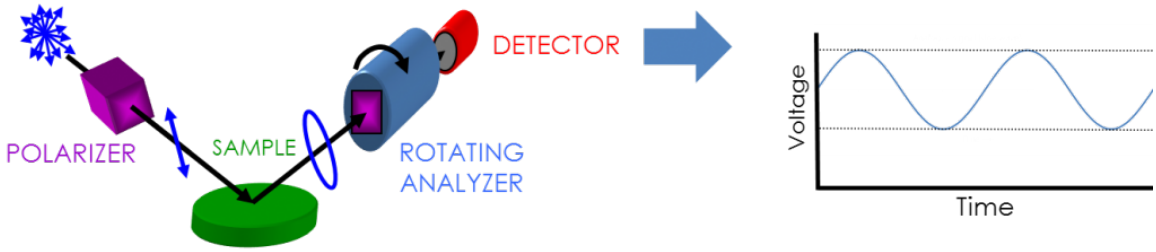


**Figure 2.14:** Schematics of a typical ellipsometer. Adapted from J. A. Woollam Co.

### 2.2.3 Applications

Overall, spectroscopic ellipsometry is used extensively in material science for measuring film thickness and optical properties. It's a non-destructive technique with high precision and can analyze multi-layer structures, providing detailed insights into each layer separately. However, data interpretation and analysis of ellipsometry can be complex and generally requires advanced knowledge of optical modeling. Also, it's most effective for thin, transparent or semi-transparent films; thick or highly absorbing films are more challenging to analyze. Usually it's sensitive to sample alignment so precise alignment and calibration for accurate measurements are required.

It's critical in industries such as semiconductors for quality control and layer verification during manufacturing. Additionally, it finds applications in photovoltaics for optimizing solar cells, in biotechnology for studying thin bio-layers, and in optical coatings to enhance product performance. Its non-destructive nature and high precision make it ideal for both research and industrial applications, providing detailed insights into material properties.

# Chapter 3

## Advanced materials with exotic optical anisotropy

The advancement of infrared spectroscopy and spectroscopic ellipsometry has led to our discovery of advanced materials with unique optical properties. This chapter introduces a novel quasi-one-dimensional (1D) material system, $A_{1+x}BX_3$ ($A$ = alkaline metal like Ba, Sr, $B$ = transition metal like Ti, $X$ = anion like S, Se), which exhibits significant infrared birefringence with low loss. This chapter is divided into three parts: the first focuses on characterizing these materials, such as $BaTiS_3$ (BTS), $BaTiSe_3$ (BTSe), and $Sr_{1+x}TiS_3$ (STS), using polarized infrared spectroscopy and generalized spectroscopic ellipsometry to fully determine their anisotropic refractive index tensors. The second part explores the origins of their substantial optical anisotropy, attributing it to non-stoichiometry induced structural modulation in $Sr_{1+x}TiS_3$ and correlated disorder in $BaTiS_3$ and $BaTiSe_3$. The final section discusses practical applications like ultrathin waveplates and polarized narrowband thermal emitters, including the development of anti-reflection (AR) coatings for enhancing their practical usability.

This work was performed in close collaboration with Prof. Jayakanth Ravichandran's group at University of Southern California, who performed the synthesis and X-ray characterization, and with Professor Rohan Mishra's group at Washington University in St. Louis, who performed the STEM studies and theoretical DFT calculations, and with Professor Sun-Kyung Kim's group at Kyung Hee University, who conducted the deposition of the AR coatings.

Specific to the work presented on $Sr_{1+x}TiS_3$, I want to acknowledge Dr. Jad Salman, who led the initial optical characterization of this material and with whom I worked in close collaboration on this portion of the project. Sections on $BaTiS_3$ has been adapted from our publications in *Chemistry of Materials*[66], *Advanced Materials*[67], and *arXiv* preprint[68]. Sections on $BaTiSe_3$ has been adapted from our publication in *arXiv* preprint[69]. Sections on $Sr_{1+x}TiS_3$ has been adapted from our publication in *Advanced Materials*[70]. Sections on AR coatings and narrowband thermal emitter applications have not yet been published.

## 3.1 introduction of quasi-1D hexagonal chalcogenide $A_{1+x}BX_3$

Anisotropic material is a fundamental and essential building block for polarization control (e.g. in wave plates, polarizing beam splitters, etc.[71–73]), nonlinear optics and quantum optics (e.g. for phase matching[74,75] and production of entangled photons[76]), micromanipulation[77], and as a platform for unconventional light-matter coupling, such as Dyakonov-like surface polaritons[78] and hyperbolic phonon polaritons[79–81].

Birefringence (quantified by $\Delta n$) is the dependence of the refractive index on the polarization of light travelling through a material. The observation of birefringence in calcite as early as 1669[82]—called Iceland spar at the time—eventually led to Fresnel's insight in 1821 that light is a transverse wave[7,83]. Calcite's record as the most birefringent material stood for over a century, with $\Delta n = |n_e - n_o| = 0.17$ in the visible, as analyzed and explained by Bragg[84,85]; here, $n_e$ and $n_o$ are respectively the extraordinary and ordinary refractive index. In calcite ($CaCO_3$) and other calcite-type carbonates ($RCO_3$; $R$ = Mg, Zn, Fe, Mn, and others), the anisotropy primarily results from the interaction of dipole excitations around the oxygen atoms within the planar carbonate ions ($CO_3^{2-}$), which are all oriented perpendicular to the optic axis within the crystal[84–87]. Achieving much larger optical birefringence is expected to require much larger structural anisotropy, and often rely on artificial anisotropic micro/nano-structures (form birefringence).

The revolution of layered (two-dimensional or 2D) materials has led to the demonstration of many crystals with very large optical anisotropy due to strong intra-layer bonding (covalent or ionic) and weak inter-layer bonding (van der Waals), resulting in, *e.g.*, $\Delta n \sim 0.7$ in hexagonal boron nitride (h-BN)[88–92] in the visible and near infrared and $\Delta n \sim 1.5$ in molybdenum disulfide ($MoS_2$)[89] in the near infrared. However, the giant anisotropy found in (usually thin) layered crystals is difficult to exploit for either bulk optics or micro-optics because their optic axis is out of the

plane of the layers and the layers are weakly bonded. Therefore, there is a need to discover or engineer bulk materials with giant anisotropy, especially in the infrared.

Our groups have been studies on quasi-one-dimensional (quasi-1D) hexagonal perovskite chalcogenides $A_{1+x}BX_3$ and we found that this family of narrow-bandgap and bulk single-crystalline materials can feature some of the largest infrared birefringence. Specifically, three main representative materials $BaTiS_3$, $BaTiSe_3$, and $Sr_{1+x}TiS_3$ have been investigated.

Single crystals of $BaTiS_3$, $BaTiSe_3$, and $Sr_{1+x}TiS_3$ were grown by chemical vapor transport (CVT) method with iodine as transporting agent, with varying starting materials[66,93]. For example, barium sulfide powder (Sigma-Aldrich, 99.9%), titanium powder (Alfa Aesar, 99.9%), sulfur pieces (Alfa Aesar, 99.999%) and iodine pieces (Alfa Aesar 99.99%) were used for synthesis of $BaTiS_3$, while strontium sulfide powder (Alfa Aesar, 99.9%) was used for synthesis of $Sr_{1+x}TiS_3$, and barium selenide powder (Materion, 99.9%) and selenium powder (Alfa Aesar, 99%) were used for synthesis of $BaTiSe_3$. As shown in Fig. 3.1, Stoichiometric quantities of precursor powders were mixed and loaded into a quartz tube along with iodine inside the glove box. In the synthesis, precursors were heated to reaction temperature at a certain heating rate and held for some time before a slow cooling down rate. All of these temperature (both heating and cooling) profiles are optimized for synthesizing different materials, and also for controlling different orientation and/or stoichiometry in the same material. More details for the materials synthesis and

controlling orientation can be found in Ref[66] and CVT method for controlling stoichiometry has not yet been published.

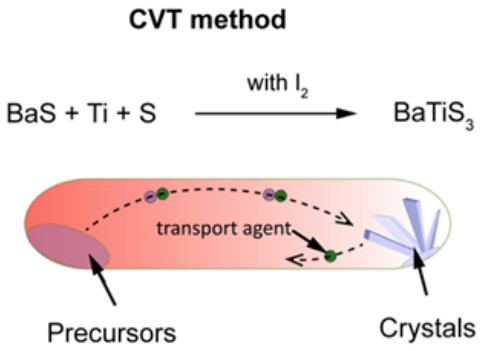


**Figure 3.1:** Schematic illustration of $BaTiS_3$ crystal growth from precursors using CVT method. Adapted from Ref[68].

Figs. 3.2(a-c) visualize the crystal structure of CVT-grown (100) $BaTiS_3$ resolved by single crystal X-ray diffraction (XRD), showing quasi-1D chains of face-shared $TiS_6$ octahedra that are aligned along a 6-fold rotational axis (commonly the *c*-axis), viewed along the *c*-axis, suggesting hexagonal symmetry.

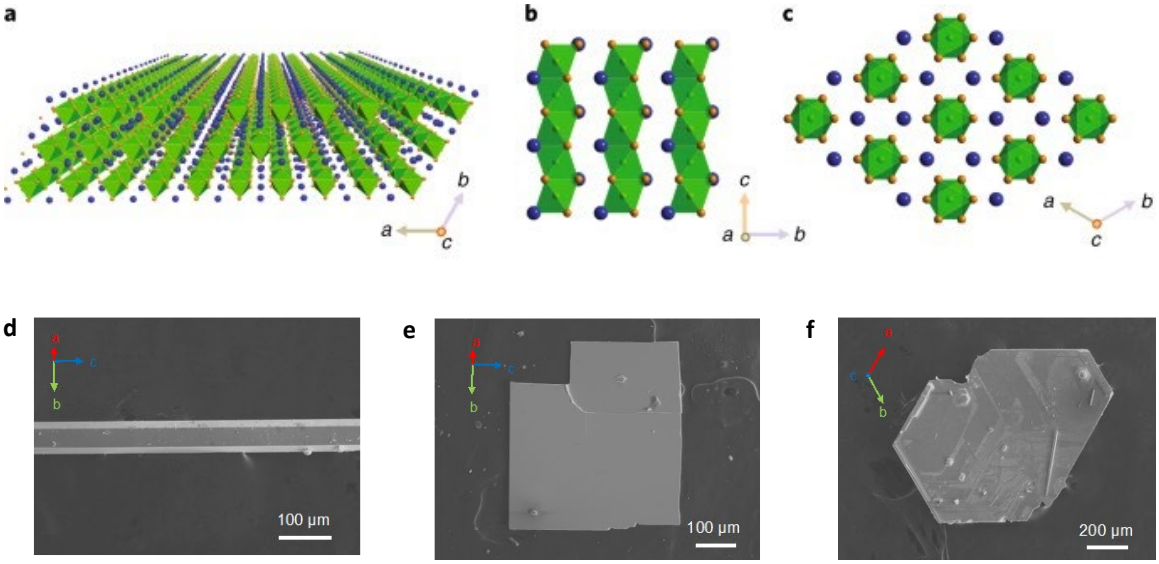


**Figure 3.2:** BTS crystal structure. **(a)** Perspective view of a $BaTiS_3$ crystal plate with blue and orange spheres representing barium and sulfur atoms, respectively. $TiS_6$ octahedra are highlighted in green. **(b)** $BaTiS_3$ crystal structure viewed along the *a* axis, showing $TiS_6$ chains parallel to the *c* axis. Green spheres represent titanium atoms. **(c)** $BaTiS_3$ crystal structure viewed along the *c* axis, showing hexagonal symmetry. Scanning electron microscopy (SEM) images and crystal orientations of **(d)** BTS needle, **(e)** (100)-oriented BTS platelet, and **(f)** (001)-oriented BTS platelet. Crystal shape and surface terraces can be used to distinguish them. Adapted from Ref[66,93].

Figs 3.2(c-e) show the SEM image of $BaTiS_3$ needle, and (100)- and (001)-oriented $BaTiS_3$ platelets, respectively. Compared to the needle and rectangular platelet-shaped $BaTiS_3$ (100) crystals, $BaTiS_3$ (001) crystals show distinct hexagonal faceting, suggesting hexagonal symmetry for this face. The typical thickness of the platelets was ~ 5-20 $\mu m$, while needles were ~ 20-50 $\mu m$ thick.

We performed a systematic investigation of the effect of growth parameters on the orientation and size of the crystals [Table 3.1]. We observed a sensitive dependence of the orientation of the crystals on the growth temperature, suggesting a subtle temperature-dependence of the surface energy for the different facets. Further, the

surfaces that possess large surface energies (enthalpic component) tend to be more stable at higher temperatures as the entropy plays a more dominant role. Based on this argument, a temperature below 1020 ℃ is too low to strike a balance between nucleation and growth to form large-area crystalline surfaces, thus making polycrystalline powders the dominant product. As the growth temperature is raised above 1020 ℃, the (100) surface becomes most favored amongst all the terminations, and the (100) orientation of BTS crystal nuclei becomes more stable and sustains appreciable growth rate, forming BTS needles. When the temperature goes up above 1055 ℃, the (001) orientation is also favored. Between 1020 ℃ and 1055 ℃, certain amount of growth along <001> is allowed to form a larger (100) surface, enabling BTS platelets with (100) orientation. We usually find larger crystals at higher temperatures, where crystals of both morphologies coexist, but sintering is found to be dominant at temperatures higher than 1060 ℃ where free-standing crystals were not observed.

**Table 3.1:** $BaTiS_3$ of Different Shapes and Orientations, adapted from Ref[66].

| Crystal | Reaction Temperature | Crystal Morphology | Surface Orientation |
|---|---|---|---|
| BTS needle | 1020 – 1060 ℃ | Needle-like | {100} |
| (100)-oriented BTS | 1040 – 1060 ℃ | Rectangular platelet | (100) |
| (001)-oriented BTS | 1055 – 1060 ℃ | Hexagonal platelet | (001) |

Recently, our groups have reported a new method to synthesize $BaTiS_3$ crystals utilizing a molten salt flux of either potassium iodide, or a mixture of barium chloride and barium iodide. The crystals obtained through this method exhibit a substantial increase in volume compared to those synthesized via the CVT method, while preserving their intrinsic optical and electronic properties, as shown in Fig. 3.3. Our flux growth method provides a promising route towards the production of high-

quality, large-scale single crystals of $BaTiS_3$, which will greatly facilitate advanced characterizations of $BaTiS_3$ and its practical applications that require large crystal dimensions. Additionally, our approach offers an alternative synthetic route for other emerging complex chalcogenides.

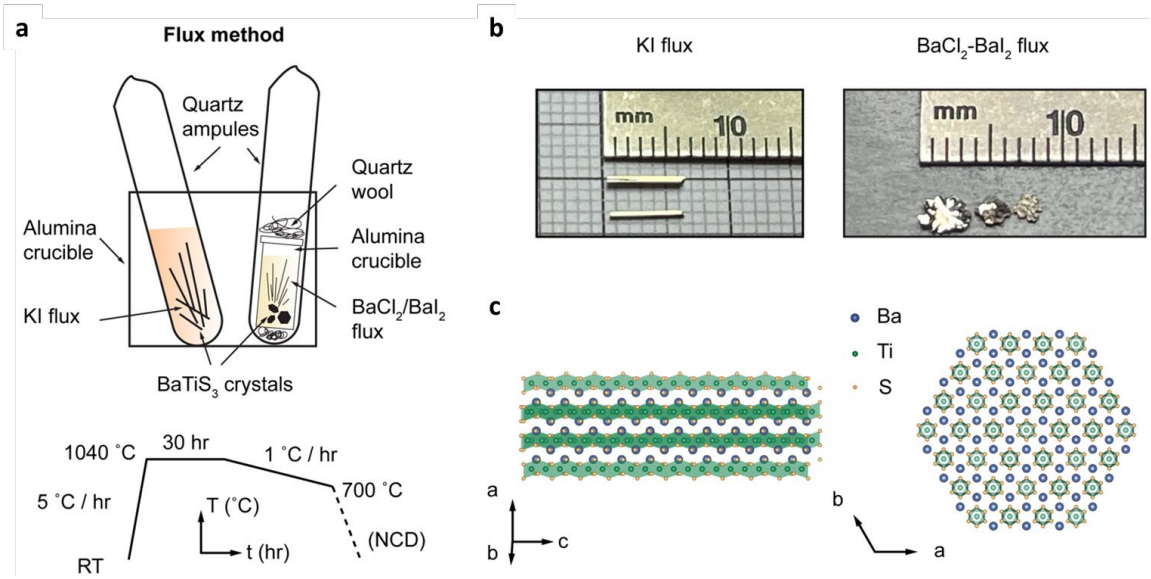


**Figure 3.3:** Flux growth methods of $BaTiS_3$ single crystals. **(a)** Schematic illustration of molten flux growth of $BaTiS_3$ crystals using a vertical geometry (top) and the temperature profile used for the flux growth of $BaTiS_3$ (bottom). **(b)** Optical image of representative $BaTiS_3$ crystals grown with KI and $BaCl_2$-$BaI_2$ fluxes, respectively. KI flux growth yielded crystals with ~ 6 mm length and half a millimeter in both width and thickness. $BaTiS_3$ thick-plate-like crystals with 3 mm lateral dimensions and up to 250 μm thickness were obtained from $BaCl_2$-$BaI_2$ flux growth. **(c)** Flux-grown $BaTiS_3$ crystal structure viewed towards the *a*-*c* plane and along the *c*-axis resolved by XRD. Adapted from Ref[68].

## 3.2 Broadband characterization of anisotropic material $A_{1+x}BX_3$

Complex refractive index tensor can be reliably extracted using spectroscopic ellipsometry combined with modeling of the optical oscillators of the material in

question, and spectroscopic ellipsometers can cover a broad spectral range spanning the ultraviolet through the far infrared, which is limited by their optical components and detectors. In an ideal scenario, a single sample with large geometries (on the order of several millimeters or more) can be measured across multiple instruments with a single optical model fit to the entire data range. However, due to limitations in our equipment capabilities to measure very small samples (geometries of 1 mm or less), ellipsometry in the infrared was not feasible. This issue is common for most commercialized infrared spectroscopic ellipsometers. Therefore, in order to extract the optical properties of anisotropic material $A_{1+x}BX_3$, we employed generalized spectroscopic ellipsometry (VASE + focusing optics, J. A. Woollam Co.) to cover the spectral range from 190 nm to 2500 nm, and polarized reflection/transmission infrared spectroscopy (Bruker VERTEX 70 + Hyperion 2000 with MCT IR detector) to cover the spectral range from 1.5 μm to 17 μm. The VASE ellipsometer and the focusing probes can provide a 200 μm beam diameter at normal incidence, with the beam diameter increasing as a function of $1/\cos(\theta_i)$ in the horizontal direction ($\theta_i$ is the angle of incidence). FTIR integrated with infrared microscope can also be used for measuring micron-scale samples. Thus, we are able to build a single optical model to fit both the ellipsometry data and polarized reflectance/transmittance data which can cover a broad wavelength range. Details for the modelling and fitting of the three materials $BaTiS_3$, $BaTiSe_3$, and $Sr_{1+x}TiS_3$ are summarized below.

### 3.2.1 Extraction of the anisotropic complex refractive index of $Sr_{9/8}TiS_3$

The $Sr_{9/8}TiS_3$ crystal was suspended over air with no substrate during the measurement. As shown in Figure 3.4 the crystal plate has a thickness of ~3.2 μm. Three ellipsometry measurements were made under Mueller Matrix Mode with three different crystal orientations: with the crystal *c*-axis perpendicular to the plane of incidence; parallel to the plane of incidence; and at off-axis angles (~30°). The three measurements were all made at 55° from the surface normal.

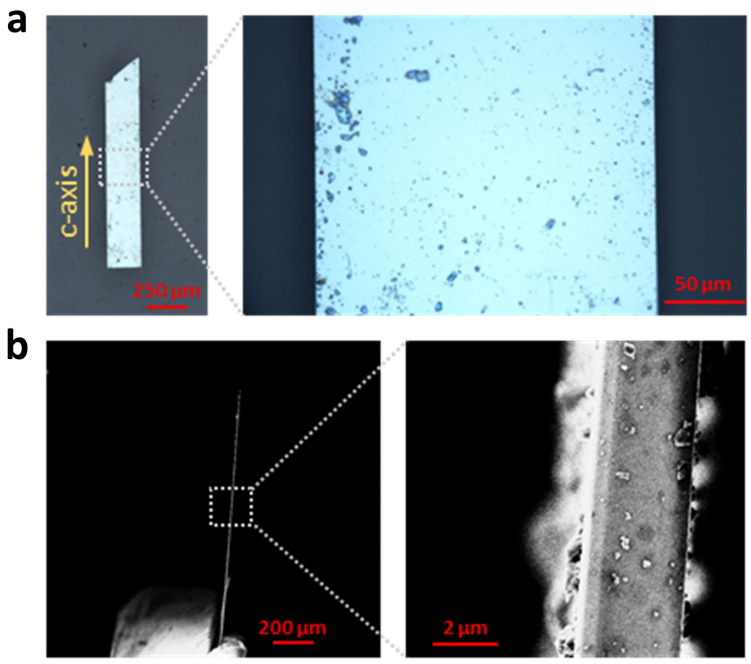


**Figure 3.4: (a)** optical image of a $Sr_{9/8}TiS_3$ crystal plate. **(b)** SEM cross-section image of a $Sr_{9/8}TiS_3$ crystal plate, showing the thickness of ~3.2 μm. Figure from Ref[70].

Figure 3.5 shows the raw measured ellipsometry data (in green) and the corresponding model fitted data (in red) for the three measurements for $Sr_{9/8}TiS_3$,

consisting of the generalized ellipsometry data types $A_{ne}, A_{ps}, A_{sp}$ and Mueller matrix elements $mm_{12}, \ldots, mm_{34}$. $A_{ne}, A_{ps}, A_{sp}$ correspond to three related complex ratios. Mueller matrix elements describe how the sample transforms the Stokes vector of the incident light. The $m_{11}$ element represents the total intensity of the reflection or transmission of the sample and the VASE ellipsometer records other Mueller matrix elements normalized to $m_{11}$, so the quantities range between -1 and +1[63].

$$S = \begin{bmatrix} I \\ Q \\ U \\ V \end{bmatrix} = M \begin{bmatrix} I^{in} \\ Q^{in} \\ U^{in} \\ V^{in} \end{bmatrix} \quad (3.1)$$

$$M = \begin{bmatrix} m_{11} & m_{12} & m_{13} & m_{14} \\ m_{21} & m_{22} & m_{23} & m_{24} \\ m_{31} & m_{32} & m_{33} & m_{34} \\ m_{41} & m_{42} & m_{43} & m_{44} \end{bmatrix} = m_{11} \begin{bmatrix} 1 & m_{12}' & m_{13}' & m_{14}' \\ m_{21}' & m_{22}' & m_{23}' & m_{24}' \\ m_{31}' & m_{32}' & m_{33}' & m_{34}' \\ m_{41}' & m_{42}' & m_{43}' & m_{44}' \end{bmatrix} \quad (3.2)$$

All three datasets were fit simultaneously using a single optical model with uniaxial birefringence. Here, optical properties perpendicular and parallel to the *c*-axis contain independent oscillators. By incorporating the polarization-resolved reflectance and transmittance of $Sr_{9/8}TiS_3$ into the ellipsometry data, the optical model could be extended up to the detection limit of the FTIR MCT detector (17 μm). Thus, seven independent optical measurements (three ellipsometry measurements, two polarized reflectance measurements, and two polarized transmittance measurements) could all be fit simultaneously to a single anisotropic optical model to yield a full set of refractive indices for the samples spanning the 190 nm through 17 μm.

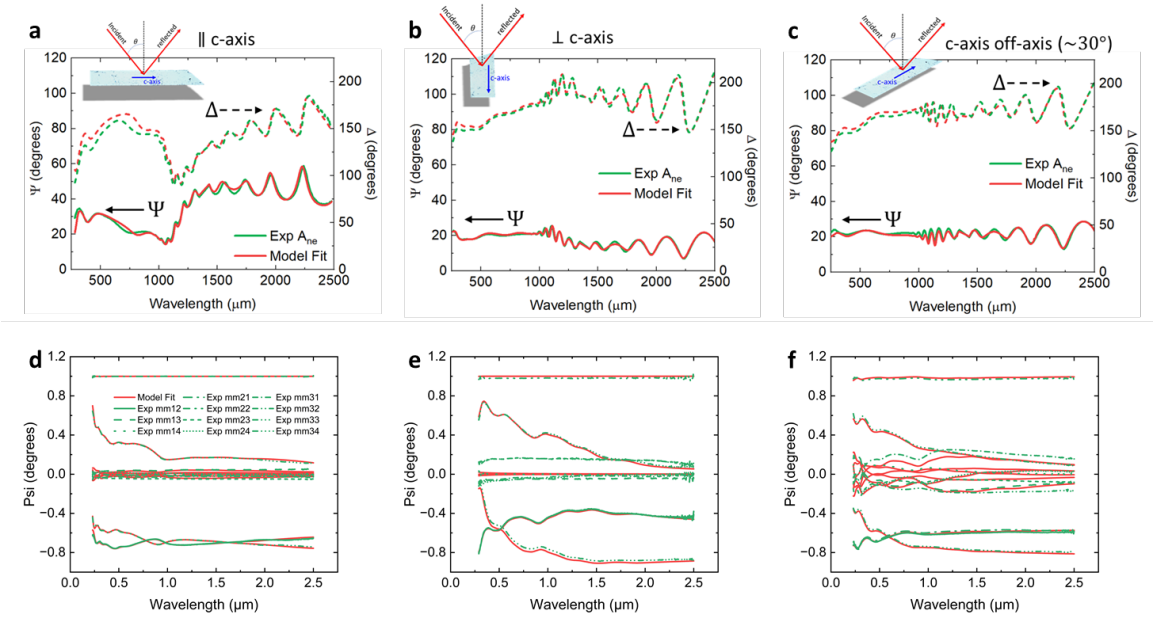


**Figure 3.5:** Raw ellipsometry data (Ψ and Δ of $A_{ne}$ **(a-c)**, Mueller matrix elements **(d-f)**) for $Sr_{9/8}TiS_3$ at $\theta_i = 55°$ with the crystal *c*-axis parallel to the plane of incidence **(a)**, perpendicular to the plane of incidence **(b)**, and at an off-axis angle ~30° **(c)**, showing good consistence between the experimental data (green lines) and model fit data (red lines). Figure adapted from Ref[70].

Figure 3.5 shows that the ellipsometry data Ψ and Δ and Mueller matrix elements acquired by experimental measurement match well with the model fitted data and Figure 3.6 shows the good agreement between the experimental polarization-resolved FTIR reflectance and transmittance data and model fitted data.

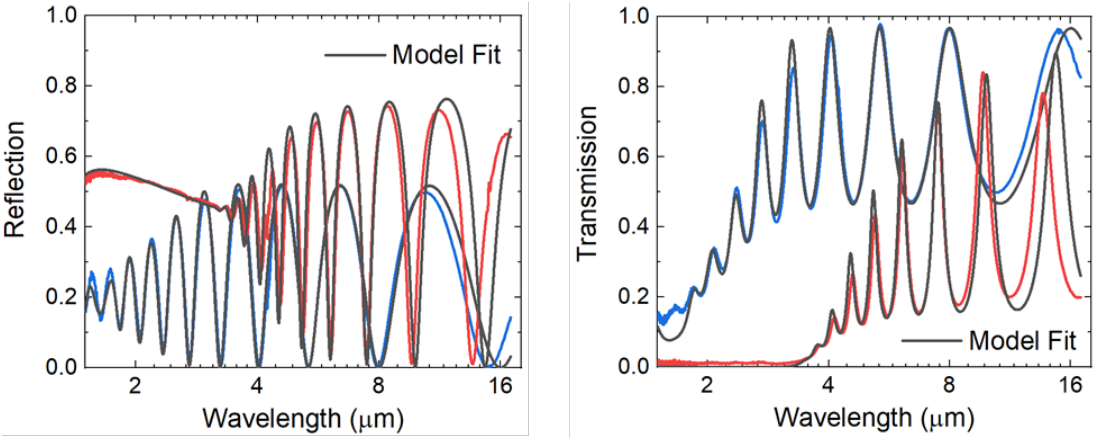


**Figure 3.6:** Final fitted model data of $Sr_{9/8}TiS_3$, in black, compared to measured polarization-resolved FTIR reflectance and transmittance data, in red and blue. Figure adapted from Ref[70].

The total oscillator model for each direction is the sum of individual Kramers-Kronig-consistent oscillators as shown in Figure 3.7. Table 3.2 lists the oscillators used in the anisotropic optical model for both the ordinary and extraordinary directions.

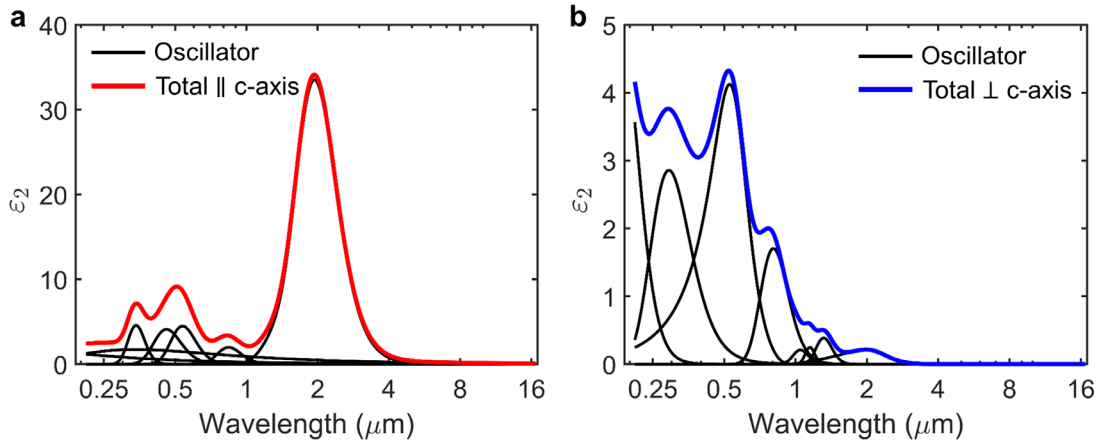


**Figure 3.7:** The $\varepsilon_2$ values were calculated from the final optical oscillator model used to fit the ellipsometry data of $Sr_{9/8}TiS_3$. The optical oscillator model is built on Kramers-Kronig consistent oscillators as listed in Table 3.2. Figure adapted from Ref[70].

**Table 3.2:** Oscillators and the fitted parameters of the $Sr_{9/8}TiS_3$ crystal.

| **Oscillator** | **Parameters (eV)** | | |
|---|---|---|---|
| Gaussian<br>$\varepsilon_{Gaus} = \varepsilon_1 + i\varepsilon_2$<br>$\varepsilon_2 = A_n e^{\left(\frac{E-E_n}{\sigma}\right)^2} - A_n e^{-\left(\frac{E+E_n}{\sigma}\right)^2}$<br>$\varepsilon_1 = \frac{2}{\pi} P \int_0^{\infty} \frac{\xi \varepsilon_2(\xi)}{\xi^2 - E^2} d\xi$<br>Where, $\sigma = \frac{Br_n}{2\sqrt{\ln(2)}}$, $P$ is the Cauchy Principal Value | Ordinary | Ordinary | Ordinary |
| | $A_1$ = 1.2389 | $E_1$ = 1.537 | $Br_1$ = 0.48721 |
| | $A_2$ = 2.8591 | $E_2$ = 4.2407 | $Br_2$ = 1.9164 |
| | $A_3$ = 4.5825 | $E_3$ = 6.5818 | $Br_3$ = 2.2495 |
| | $A_4$ = 0.25625 | $E_4$ = 0.75646 | $Br_4$ = 0.12458 |
| | $A_5$ = 0.21926 | $E_5$ = 0.94097 | $Br_5$ = 0.2041 |
| | $A_6$ = 0.4238 | $E_6$ = 0.00065 | $Br_6$ = 0.17878 |
| | Extraordinary | Extraordinary | Extraordinary |
| | $A_7$ = 4.1011 | $E_7$ = 2.6967 | $Br_7$ = 0.82102 |
| | $A_8$ = 4.4872 | $E_8$ = 2.3077 | $Br_8$ = 0.65113 |
| | $A_9$ = 1.709 | $E_9$ = 1.3753 | $Br_9$ = 0.26131 |
| | $A_{10}$ = 2.8654 | $E_{10}$ = 1.8896 | $Br_{10}$ = 8.1843 |
| | $A_{11}$ = 4.5852 | $E_{11}$ = 3.6265 | $Br_{11}$ = 0.69007 |
| | $A_{12}$ = 1.404 | $E_{12}$ = 8.3814 | $Br_{12}$ = 9.8278 |
| Tauc-Lorentz<br>$\varepsilon_{TL} = \varepsilon_1 + i\varepsilon_2$<br>$\varepsilon_2 = \frac{A_n E o_n C_n (E - E g_n)^2}{(E^2 - E o_n^2)^2 + C_n^2 E^2} \cdot \frac{1}{E}$, $for\ E > E g_n$<br>$\varepsilon_2 = 0$, $for\ E \leq E g_n$<br>$\varepsilon_1 = \frac{2}{\pi} P \int_{E g_n}^{\infty} \frac{\xi \varepsilon_2(\xi)}{\xi^2 - E^2} d\xi$ | Ordinary<br>$A_1$ = 26.696, $Eo_1$ = 2.2384, $C_1$ = 1.142, $Eg_1$ = 1.3129 | | |
| Parametric Semiconductor<br>See WVASE manual by J.A. Woollam Co.[63] | Ordinary (Psemi-M0)<br>$A_1$ = 0.31885, $Eo_1$ = 0.51766, $B_1$ = 0.088998, $WR_1$ = 0.86135, $PR_1$ = 0.62087, $AR_1$ = 0.35457, $O2R_1$ = 1<br>Extraordinary (Psemi-Tri)<br>$A_1$ = 135.04, $Ec_1$ = 0.5936, $B_1$ = 0.1323, $WL_1$ = 0.10456, $WR_1$ = 0.55047, $AL_1$ = 0.0021511, $AR_1$ = 0.043094 | | |

Figure 3.8 shows the complete extracted complex refractive index of $Sr_{9/8}TiS_3$, with a birefringence ($\Delta n$) up to 2.1 in the low-loss region of $\lambda > 6$ μm. This is by far the largest birefringence among reported anisotropic crystals, to the best of our knowledge [summary plot in Fig. 3.23]. As we discuss in a later section, this extreme birefringence is a result of the enhancement of the extraordinary index ($n_e$) from the expected $\lesssim 3.4$ in a hypothetical unmodulated stoichiometric crystal to ~4.5 in $Sr_{9/8}TiS_3$.

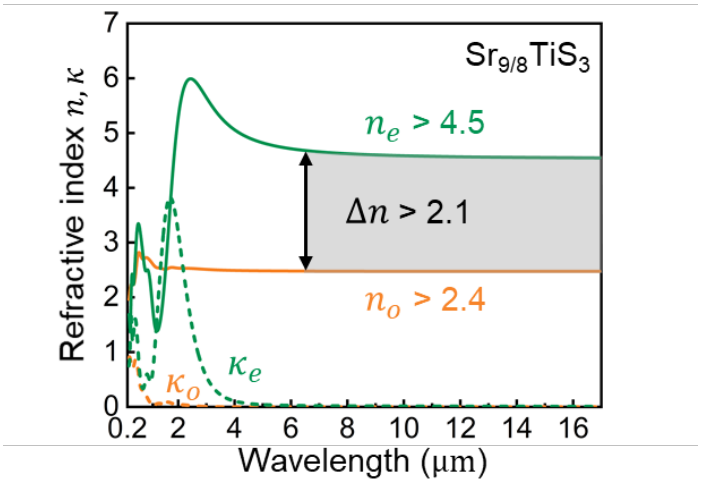


**Figure 3.8:** Extracted complex refractive-index values of uniaxial $Sr_{9/8}TiS_3$ for the ordinary (perpendicular to *c*-axis, orange) and extraordinary (parallel to *c*-axis, green) directions spanning the visible through the mid infrared, based on a combination of spectroscopic ellipsometry and transmittance/reflectance measurements. For wavelengths longer than ~6 μm, the material is highly transparent and maintains a large birefringence, $\Delta n > 2.1$ (gray shaded region). Figure adapted from Ref[70].

## 3.2.2 Extraction of the anisotropic complex refractive index of $BaTiS_3$

### 3.2.2.1 CVT-grown $BaTiS_3$

Similar ellipsometry and FTIR measurements and modelling have been performed in the CVT-grown single crystalline $BaTiS_3$ sample. As shown in the SEM image in Fig. 3.9, the surface is smooth and uniform across a fairly big region, where we performed the ellipsometry and FTIR measurements.

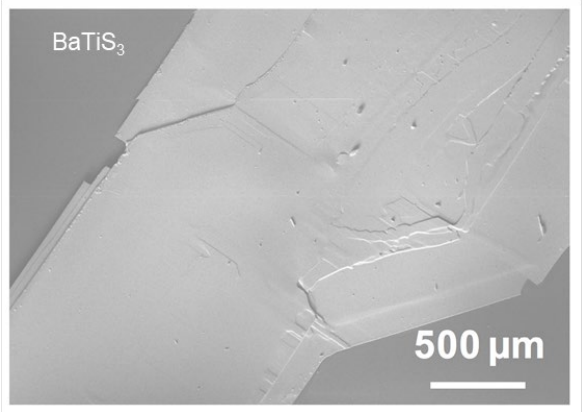


**Figure 3.9:** $BaTiS_3$ SEM image with the *c*-axis in plane showing a fairly smooth surface of the materials grown using chemical vapor transport (CVT) method. Adapted from Ref[93].

Similar fitting procedures were conducted and the final fitting results are shown in Figure 3.10 and 3.11, showing a good agreement between the experimental data and model fitted data. Table 3.3 summarizes the oscillators and the final fitted parameters of both ordinary and extraordinary axis for the CVT-grown $BaTiS_3$ crystals. Figure 3.12 shows the extracted complex refractive index of CVT-grown $BaTiS_3$, with a birefringence ($\Delta n$) up to 0.76 in the low-loss region of $\lambda > 5$ µm. In a later section, we'll discuss the birefringence originates from correlated disorders in the *a*-*b* plane.

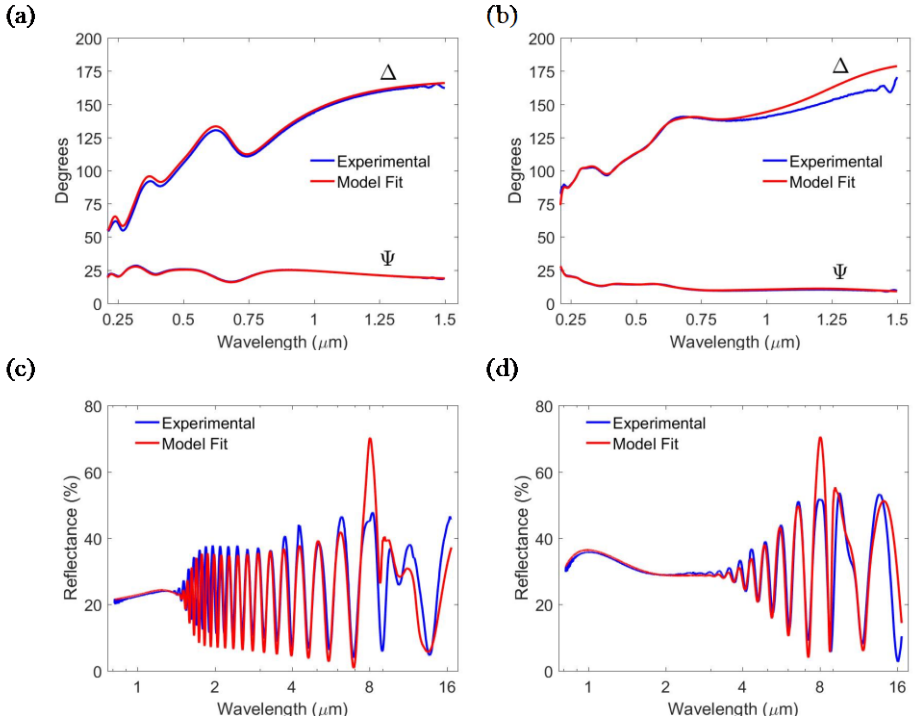


**Figure 3.10:** Optical index extraction. Ellipsometry measurement $A_{ne}$ data and fit for plane of incidence parallel to **(a)** and perpendicular to **(b)** optic axis. Reflection spectra and fitting for normal incidence with polarization parallel to **(c)** and perpendicular to **(b)** optic axis. Adapted from Ref[93].

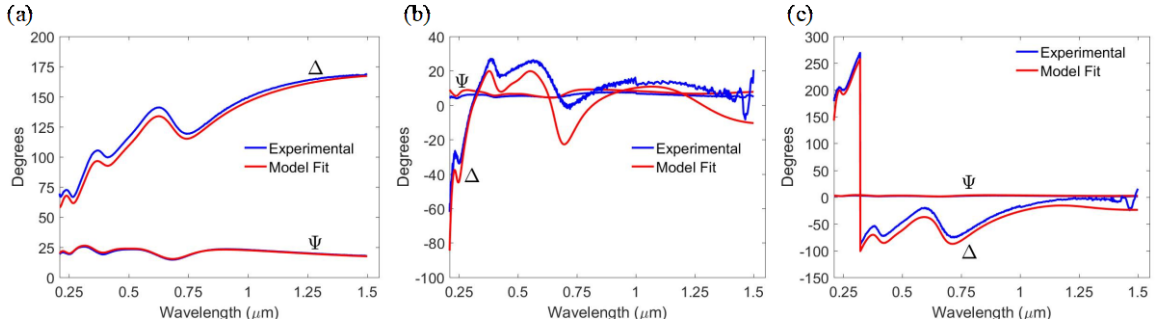


**Figure 3.11:** Additional ellipsometry fitting data. Ellipsometry measurement and fitting for plane of incidence 14° to optic axis. $A_{ne}$ data **(a)**, $A_{ps}$ data **(b)** and $A_{sp}$ **(c)** and their fitted results, showing good consistency. Adapted from Ref[93].

**Table 3.3:** Oscillators and the fitted parameters of the CVT-grown $BaTiS_3$ crystal**.** Adapted from Ref[93].

| Oscillator | Type | Ordinary Polarization | | | Extraordinary Polarization | | |
|---|---|---|---|---|---|---|---|
| | | Amplitude | Center Energy (eV) | Broadening (eV) | Amplitude | Center Energy (eV) | Broadening (eV) |
| 1 | Parametric Semiconductor Type M0 | 13.114 | 0.46544 | 0.19839 | 2.8028 | 0.93957 | 0.10527 |
| | Additional Parameters | WR = 0.37589<br>PR = 0.50781<br>AR = 0.13736<br>02R = -0.35684 | | | WR = 1.7071<br>PR = 0.45783<br>AR = 1.0843<br>02R = -0.41881 | | |
| 2 | Gaussian | 10.806 | 1.2482 | 0.60813 | 0.09194 | 0.46441 | 0.85569 |
| 3 | Gaussian | 2.1971 | 2.0928 | 0.31515 | 1.5358 | 2.1143 | 0.34348 |
| 4 | Gaussian | 1.0562 | 2.2213 | 0.4364 | 3.4748 | 2.6078 | 0.85381 |
| 5 | Gaussian | 6.0646 | 2.3037 | 1.2508 | 4.097 | 3.8571 | 1.6043 |
| 6 | Gaussian | 1.7897 | 3.4254 | 0.65011 | 0.33953 | 4.3222 | 0.40208 |
| 7 | Gaussian | 2.6001 | 3.7998 | 1.3305 | 1.7616 | 5.1471 | 1.0746 |
| 8 | Gaussian | 1.6933 | 5.2252 | 1.1674 | 1.1192 | 5.6369 | 0.64256 |
| 9 | Lorentzian | 4.6109 | 7.2782 | 1.263 | 5.8287 | 8.1991 | 1.7749 |

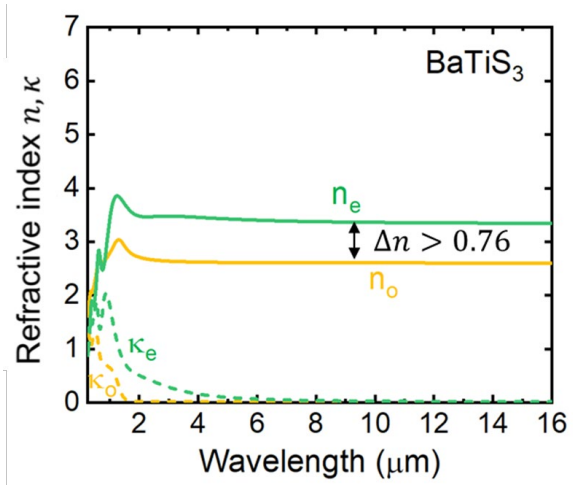


**Figure 3.12:** Extracted complex refractive-index values of uniaxial CVT-grown $BaTiS_3$ for the ordinary and extraordinary directions spanning the visible through the mid infrared. For

wavelengths longer than ~5 μm, the material is highly transparent and maintains a large birefringence, $\Delta n > 0.76$. Adapted from Ref[93].

### 3.2.2.2 KI flux-grown $BaTiS_3$

The KI flux-grown $BaTiS_3$ crystal was suspended over air with no substrate during the measurement, as shown in Figure 3.13. Three ellipsometry measurements were made under Mueller Matrix Mode with three different crystal orientations: with the crystal *c*-axis perpendicular to the plane of incidence; parallel to the plane of incidence; and at off-axis angles (~48°) and the three measurements were made with an angle of incidence of 55° from the surface normal.

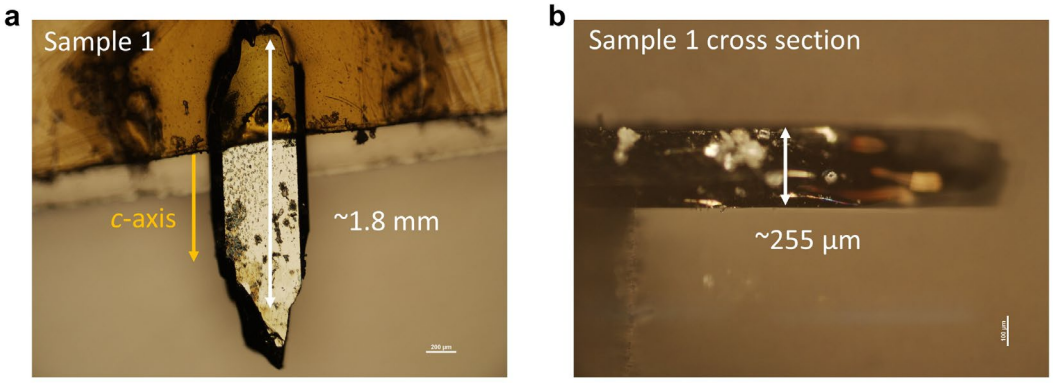


**Figure 3.13: (a)** optical images of a KI flux grown $BaTiS_3$ crystal plate, with dimension along *c*-axis larger than 1.8 mm. **(b)** cross-section image of a KI flux grown $BaTiS_3$ crystal plate, showing the thickness of ~255 μm. Figure adapted from Ref[68].

All three datasets were fitted simultaneously using a single optical model with uniaxial birefringence. By integrating the polarization-resolved reflectance of KI flux grown $BaTiS_3$ into the ellipsometry data, three ellipsometry measurements and two

reflectance measurements could all be fit simultaneously to a single anisotropic optical model to yield a full set of refractive indices spanning 210 nm through 17 μm. As shown in Figure 3.14, the measured data match well with the model fitted data.

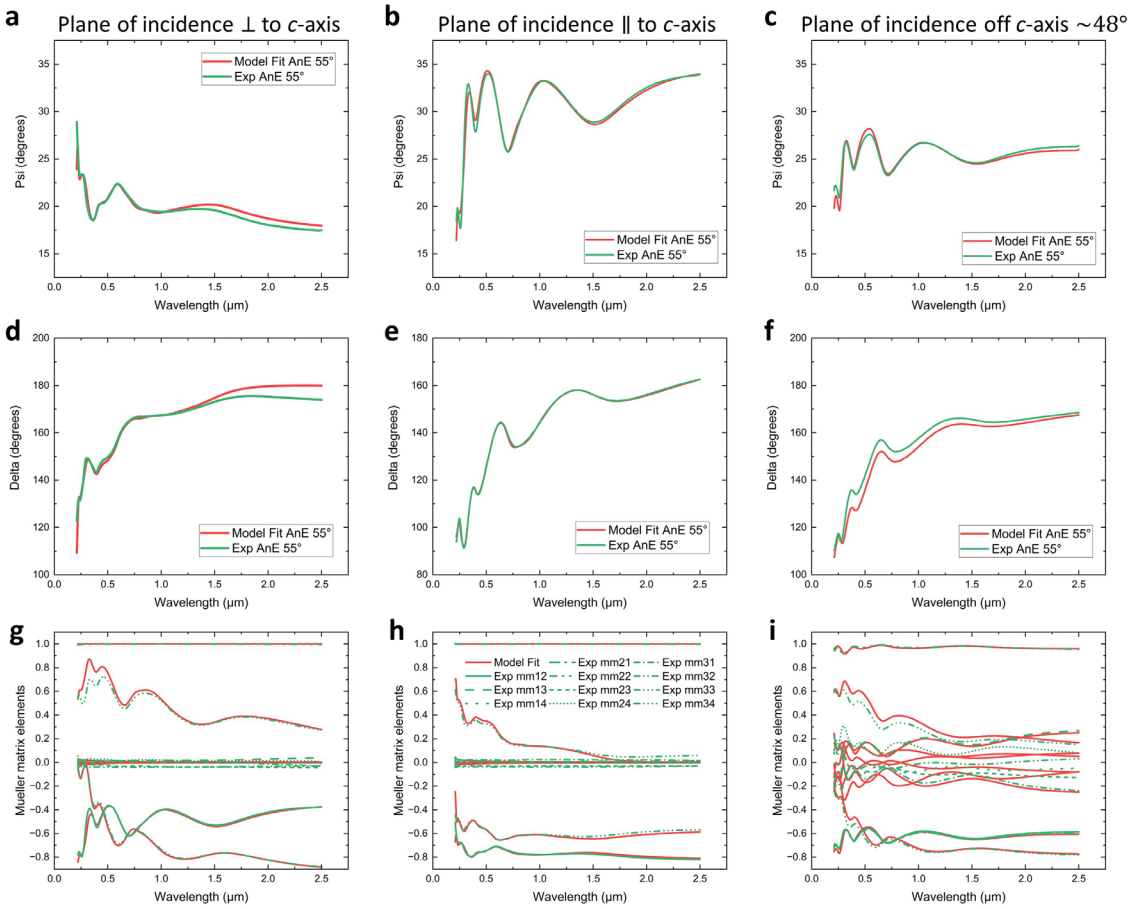


**Figure 3.14:** Raw ellipsometry data (Ψ **(a-c)** and Δ **(d-f)** of $A_{ne}$, Mueller matrix elements **(g-i)**) for KI flux grown $BaTiS_3$ at $\theta_i = 55°$ with the crystal *c*-axis perpendicular, parallel, and at an off-axis angle ~48° to the plane of incidence, showing good consistence between the experimental data (green lines) and model fit data (red lines). Figure adapted from Ref[68].

The total oscillator model for each direction is the sum of individual Kramers-Kronig-consistent oscillators as shown in Figure 3.15. Table 3.4 lists the oscillators used in the anisotropic optical model for both the ordinary and extraordinary directions.

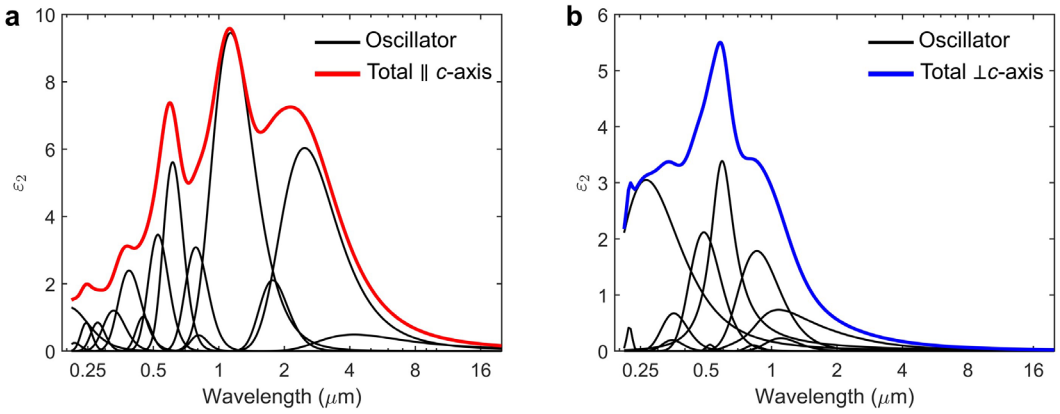


**Figure 3.15:** The $\varepsilon_2$ values calculated from the final optical oscillator model used to fit to the ellipsometry data of KI flux grown $BaTiS_3$. The optical oscillator model is built on Kramers-Kronig consistent oscillators. Figure adapted from Ref[68].

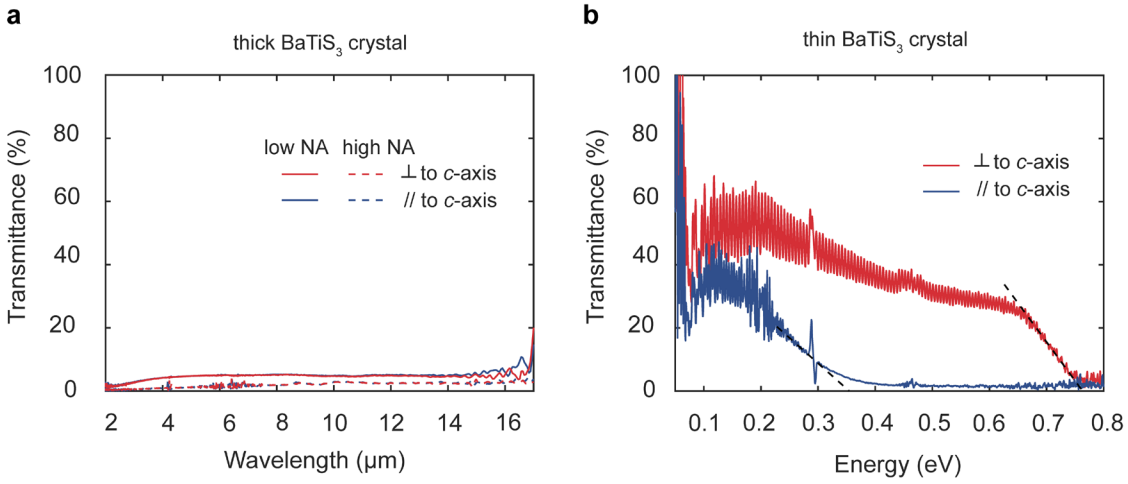


**Figure 3.16: (a)** Infrared transmission spectra of a thick KI flux-grown $BaTiS_3$ crystal with incident light polarized at 0˚ and 90˚, with respective to the *c*-axis. Two different objective lenses (low NA: 15×, NA=0.4, Casegrain reflective objective; high NA: 5×, NA=0.17, Ge IR

refractive objective) have been used for the measurements. **(b)** Infrared transmission spectra of a relatively thin KI flux-grown $BaTiS_3$ crystal (~ 40 μm thick) with incident light polarized perpendicular and parallel to the *c*-axis. Two absorption edges at ~ 0.35 eV and ~ 0.77 eV are clearly revealed. Energy scale was used for the ease of analysis. Figure adapted from Ref[68].

**Table 3.4:** Oscillators and the fitted parameters of the KI flux-grown $BaTiS_3$ crystal**.**

| **Oscillator** | **Parameters (eV)** | | |
|---|---|---|---|
| Gaussian<br>$\varepsilon_{Gaus} = \varepsilon_1 + i\varepsilon_2$<br><br>$\varepsilon_2 = A_n e^{-\left(\frac{E-E_n}{\sigma}\right)^2} - A_n e^{-\left(\frac{E+E_n}{\sigma}\right)^2}$<br><br>$\varepsilon_1 = \frac{2}{\pi} P \int_0^\infty \frac{\xi \varepsilon_2(\xi)}{\xi^2 - E^2} d\xi$<br><br>Where $\sigma = \frac{Br_n}{2\sqrt{\ln(2)}}$, the $1/2\sqrt{In(2)}$ factor defines $Br_n$ = FWHM. *P* is the Cauchy Principal Value. | Ordinary | Ordinary | Ordinary |
| | $A_1$ = 0.22881 | $E_1$ = 1.1236 | $Br_1$ = 0.4612 |
| | $A_2$ = 1.7844 | $E_2$ = 1.4476 | $Br_2$ = 0.73465 |
| | $A_3$ = 0.10508 | $E_3$ = 1.5034 | $Br_3$ = 0.27766 |
| | $A_4$ = 0.11355 | $E_4$ = 2.3794 | $Br_4$ = 0.23803 |
| | $A_5$ = 2.117 | $E_5$ = 2.5385 | $Br_5$ = 0.97834 |
| | $A_6$ = 0.67282 | $E_6$ = 3.4884 | $Br_6$ = 1.1235 |
| | $A_7$ = 0.19641 | $E_7$ = 3.5532 | $Br_7$ = 0.91346 |
| | $A_8$ = 3.0509 | $E_8$ = 4.6747 | $Br_8$ = 3.3703 |
| | $A_9$ = 0.44297 | $E_9$ = 5.5807 | $Br_9$ = 0.36085 |
| | Extraordinary | Extraordinary | Extraordinary |
| | $A_1$ = 0.49005 | $E_1$ = 0.29574 | $Br_1$ = 0.31132 |
| | $A_2$ = 6.0344 | $E_2$ = 0.5 | $Br_2$ = 0.3465 |
| | $A_3$ = 2.1032 | $E_3$ = 0.70144 | $Br_3$ = 0.24885 |
| | $A_4$ = 9.455 | $E_4$ = 1.0952 | $Br_4$ = 0.56054 |
| | $A_5$ = 0.47327 | $E_5$ = 1.5367 | $Br_5$ = 0.32465 |
| | $A_6$ = 3.0859 | $E_6$ = 1.5826 | $Br_6$ = 0.445 |
| | $A_7$ = 5.616 | $E_7$ = 2.2017 | $Br_7$ = 0.49401 |
| | $A_8$ = 3.4602 | $E_8$ = 2.3637 | $Br_8$ = 0.5914 |
| | $A_9$ = 1.0241 | $E_9$ = 2.7584 | $Br_9$ = 0.5183 |
| | $A_{10}$ = 2.3982 | $E_{10}$ = 3.2084 | $Br_{10}$ = 0.91344 |
| | $A_{11}$ = 1.2056 | $E_{11}$ = 3.7787 | $Br_{11}$ = 1.0342 |
| | $A_{12}$ = 0.85088 | $E_{12}$ = 4.4721 | $Br_{12}$ = 0.79528 |
| | $A_{13}$ = 0.84736 | $E_{13}$ = 5.0477 | $Br_{13}$ = 0.69215 |
| | $A_{14}$ = 0.24468 | $E_{14}$ = 5.7131 | $Br_{14}$ = 0.86262 |
| | $A_{15}$ = 1.3047 | $E_{15}$ = 6.0456 | $Br_{15}$ = 2.6429 |
| Lorentz<br>$\varepsilon_L = \varepsilon_1 + i\varepsilon_2$ | Ordinary | | |

| | |
|---|---|
| $\varepsilon_2 = \frac{A_n Br_n E_n}{E_n^2 - E^2 - iBr_n E}$<br><br>$\varepsilon_1 = \frac{2}{\pi} P \int_0^\infty \frac{\xi \varepsilon_2(\xi)}{\xi^2 - E^2} d\xi$<br>Where P is the Cauchy Principal Value. | $A_1$ = 3.3693 $E_1$ = 2.1165 $Br_1$ = 0.64235 |
| <u>Parametric Semiconductor</u><br>Psemi-(M0, M1, M2, M3 & Tri)<br><br>See WVASE manual by J.A. Woollam Co. | <u>Ordinary (Psemi-Tri)</u><br>$A_1$ = 1.7299 $Ec_1$ = 1.233 $B_1$ = 0.18861<br>$WL_1$ = 1.0042 $WR_1$ = 1.0207<br>$AL_1$ = 0.86247 $AR_1$ = 0.1880 |

Figure 3.17(b) plots the corresponding dispersion of the real ($n$) and imaginary part ($\kappa$) of the refractive index for the ordinary (perpendicular to *c*-axis) and extraordinary (parallel to *c*-axis) directions. In the region with wavelengths of ~ 4 μm and above, the flux-grown $BaTiS_3$ shows a large birefringence of ~ 0.8, which is consistent with the reported values. The model fits well for the reflectance spectra, as shown in Figure 3.17(a).

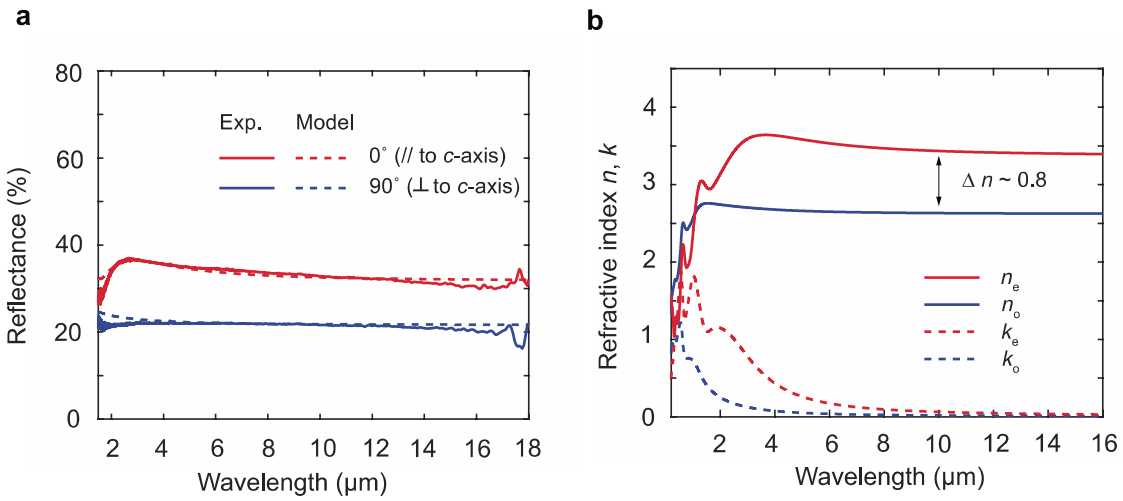


**Figure 3.17:** Optical anisotropy of flux-grown $BaTiS_3$. **(a)** Infrared reflectance spectra of a KI flux-grown $BaTiS_3$ crystal with incident light polarized at 0° and 90°, with respect to the *c*-axis. **(b)** Extracted complex refractive-index values of flux-grown $BaTiS_3$ for the ordinary (perpendicular to *c*-axis) and extraordinary (parallel to *c*-axis) from visible to mid-infrared region. Figure adapted from Ref[68].

### 3.2.3 Extraction of the anisotropic complex refractive index of $BaTiSe_3$

The $BaTiSe_3$ crystal was suspended over the air with no substrate during the measurement. As shown in Figure 3.18 the crystal plate has a thickness of ~22 μm with some rough features on the back side, resulting in a sub-micron thick interface, which explains the scattering feature in the transmission spectra in Figure 3.20(c, d).

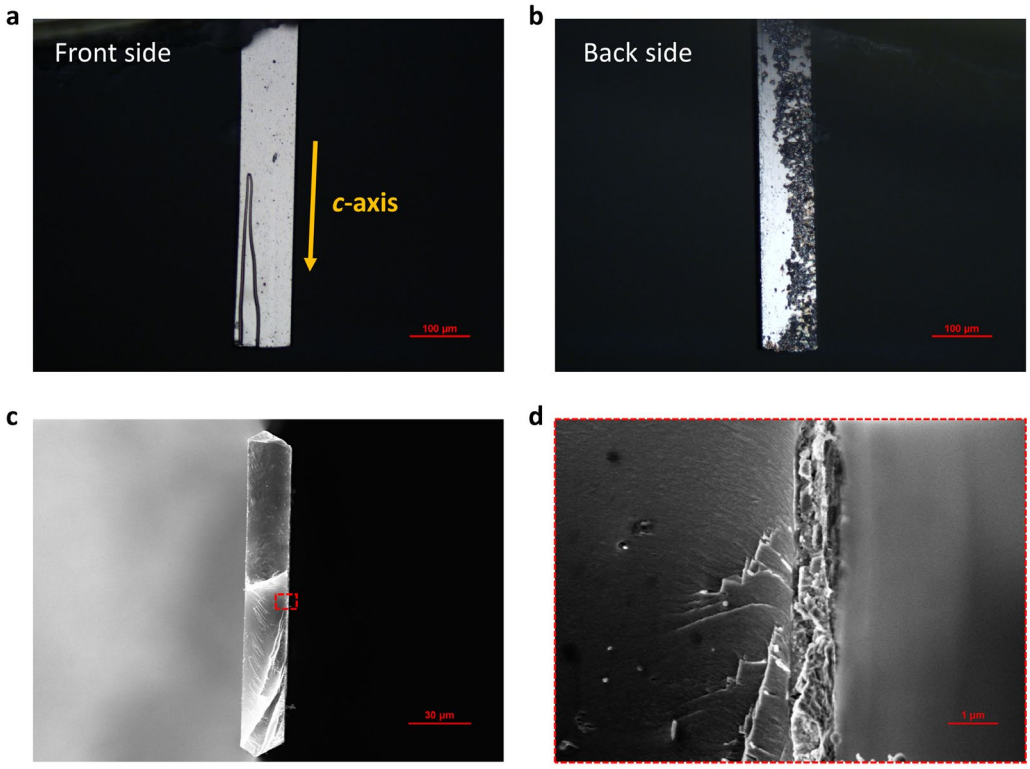


**Figure 3.18: (a, b)** optical images of a $BaTiSe_3$ crystal plate. **(c, d)** SEM cross-section image of a $BaTiSe_3$ crystal plate, showing the thickness of ~22 µm, dashed square showing the sub-micron thick interface with rough features on the back side in **(d)**. Figure adapted from Ref[69].

Four ellipsometry measurements were made under Mueller Matrix Mode with four different crystal orientations: with the crystal *c*-axis perpendicular to the plane of incidence; parallel to the plane of incidence; and at off-axis angles (~40° and ~18°). The four measurements were all made at 55° from the surface normal.

Figure 3.19 shows the raw measured ellipsometry data (in green) and the corresponding model fitted data (in red) for the four measurements for $BaTiSe_3$,

consisting of the generalized ellipsometry data types $A_{ne}, A_{ps}, A_{sp}$ and Mueller matrix elements $mm_{12}, \ldots, mm_{34}$, showing good agreement with the model fitted data.

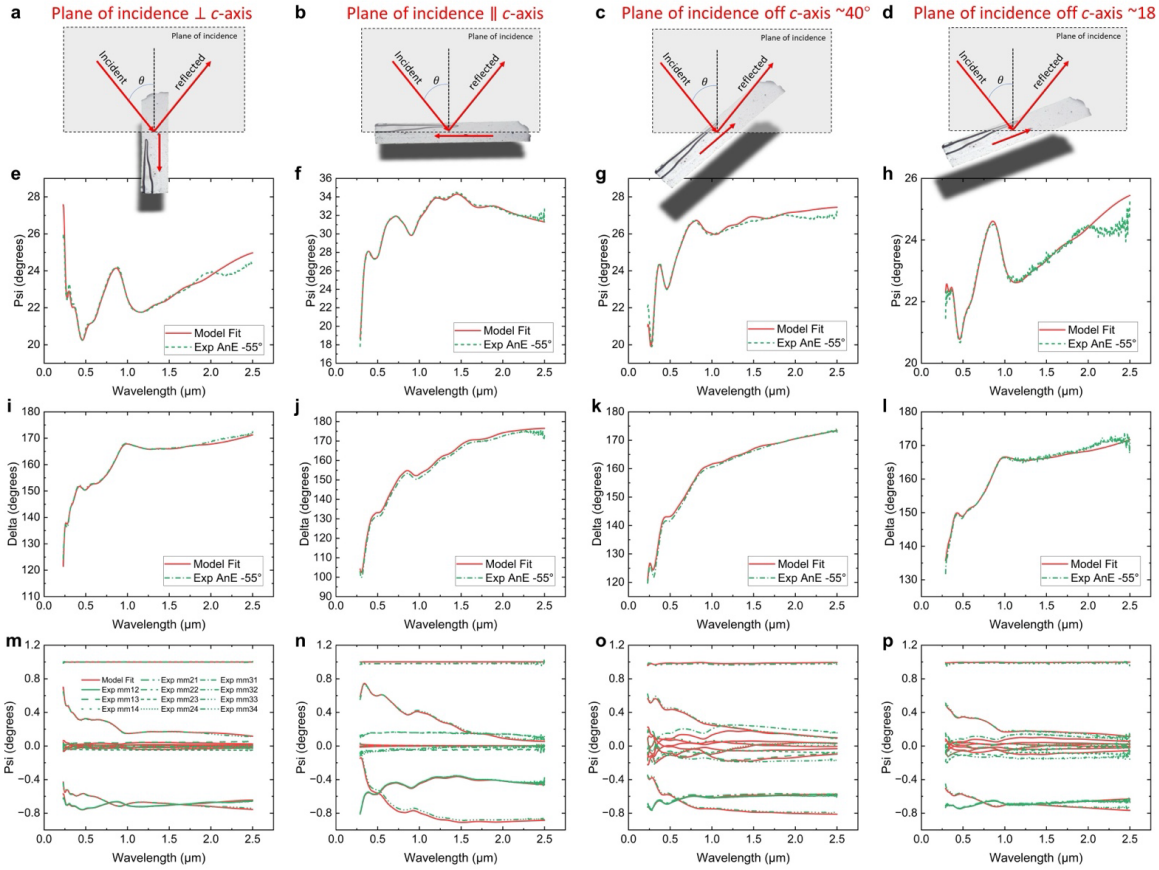


**Figure 3.19:** Raw ellipsometry data (Ψ **(e-h)** and Δ **(i-l)** of $A_{ne}$, Mueller matrix elements **(m-p)**) for $BaTiSe_3$ at $\theta_i$ = 55° with the crystal *c*-axis perpendicular to the plane of incidence **(a)**, parallel to the plane of incidence **(b)**, and at an off-axis angle ~ 40° **(c)**, and ~ 18° **(d)**, showing good consistency between the experimental data (green lines) and model fit data (red lines). Figure adapted from Ref[69].

Figure 3.20 shows the good agreement between the experimental polarization-resolved FTIR (reflection and transmission) data and model-fitted data.

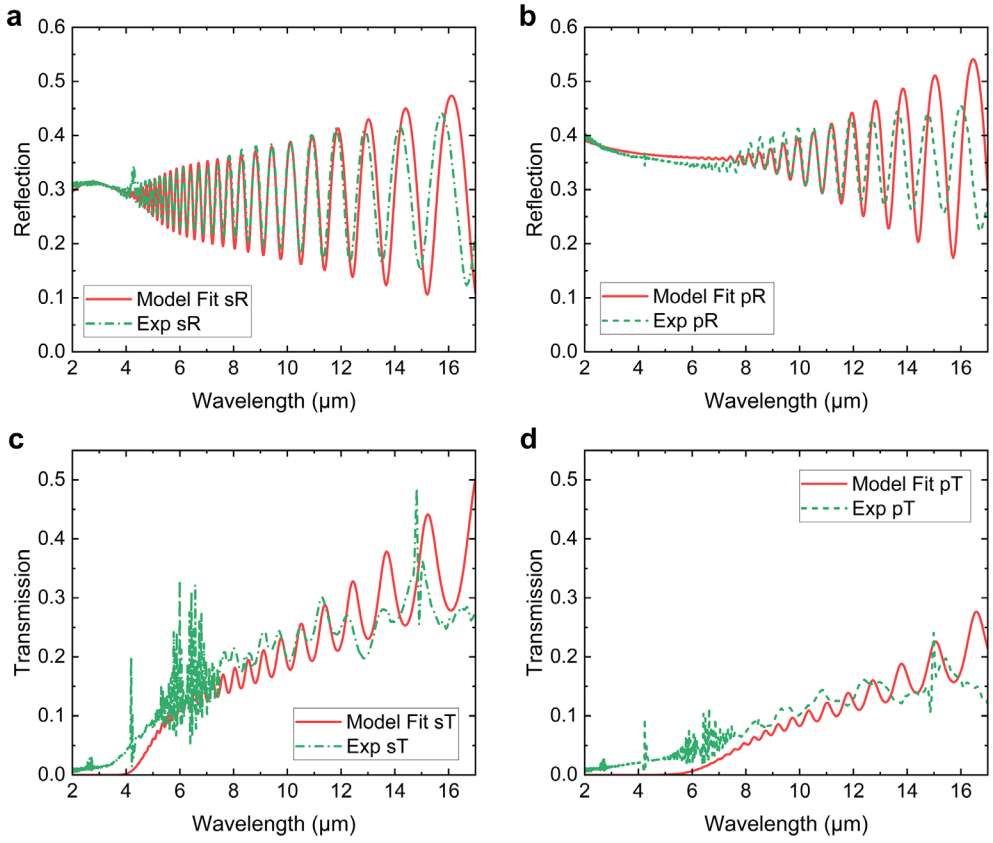


**Figure 3.20:** Final fitted model data of $BaTiSe_3$, in red, compared to measured polarization-resolved FTIR reflectance **(a, b)** and transmittance **(c, d)** data, in green. Figure adapted from Ref[69].

The total oscillator model for each direction is the sum of individual Kramers-Kronig-consistent oscillators as shown in Figure 3.21. Table 3.5 lists the oscillators and fiting parameters used in the anisotropic optical model for both the ordinary and extraordinary directions.

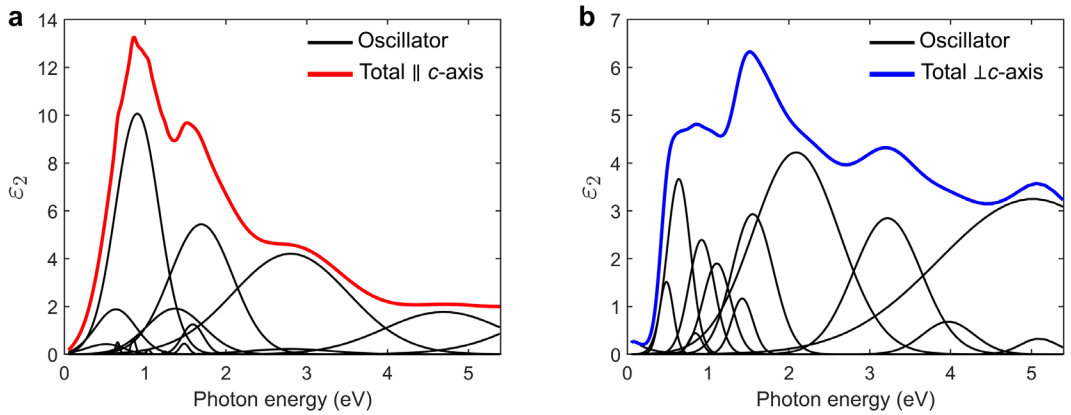


**Figure 3.21:** The $\varepsilon_2$ values were calculated from the final optical oscillator model used to fit the ellipsometry data of $BaTiSe_3$. The optical oscillator model is built on Kramers-Kronig consistent oscillators. Figure adapted from Ref[69].

**Table 3.5:** Oscillators and the fitted parameters of $BaTiSe_3$.

| **Oscillator** | **Parameters (eV)** | | |
|---|---|---|---|
| | Ordinary | Ordinary | Ordinary |
| | $A_1$ = 1.5124 | $E_1$ = 0.4836 | $Br_1$ = 0.20058 |
| | $A_2$ = 3.6653 | $E_2$ = 0.63718 | $Br_2$ = 0.33828 |
| | $A_3$ = 0.44005 | $E_3$ = 0.84283 | $Br_3$ = 0.19294 |
| Gaussian | $A_4$ = 2.3937 | $E_4$ = 0.91936 | $Br_4$ = 0.37249 |
| $\varepsilon_{Gaus} = \varepsilon_1 + i\varepsilon_2$ | $A_5$ = 1.9005 | $E_5$ = 1.1077 | $Br_5$ = 0.40201 |
| | $A_6$ = 1.1659 | $E_6$ = 1.4221 | $Br_6$ = 0.30895 |
| $\varepsilon_2 = A_n e^{-\left(\frac{E-E_n}{\sigma}\right)^2} - A_n e^{-\left(\frac{E+E_n}{\sigma}\right)^2}$ | $A_7$ = 2.933 | $E_7$ = 1.5513 | $Br_7$ = 0.59778 |
| | $A_8$ = 4.2238 | $E_8$ = 2.0893 | $Br_8$ = 1.2554 |
| $\varepsilon_1 = \frac{2}{\pi} P \int_0^\infty \frac{\xi \varepsilon_2(\xi)}{\xi^2 - E^2} d\xi$ | $A_9$ = 2.8485 | $E_9$ = 3.2188 | $Br_9$ = 0.98692 |
| | $A_{10}$ = 0.68236 | $E_{10}$ = 3.9728 | $Br_{10}$ = 0.7448 |
| Where $\sigma = \frac{Br_n}{2\sqrt{\ln(2)}}$, the $1/2\sqrt{In(2)}$ | $A_{11}$ = 3.249 | $E_{11}$ = 5.0192 | $Br_{11}$ = 2.744 |
| factor defines $Br_n$ = FWHM. $P$ is the | $A_{12}$ = 0.32826 | $E_{12}$ = 5.0945 | $Br_{12}$ = 0.5377 |
| Cauchy Principal Value. | | | |
| | Extraordinary | Extraordinary | Extraordinary |
| | $A_1$ = 1.8778 | $E_1$ = 0.63771 | $Br_1$ = 0.58605 |
| | $A_2$ = 0.50041 | $E_2$ = 0.66015 | $Br_2$ = 0.060581 |
| | $A_3$ = 0.65533 | $E_3$ = 0.85329 | $Br_3$ = 0.069399 |

| | | | |
|---|---|---|---|
| | $A_4$ = 10.068 | $E_4$ = 0.90245 | $Br_4$ = 0.63456 |
| | $A_5$ = 0.19622 | $E_5$ = 1.042 | $Br_5$ = 0.05498 |
| | $A_6$ = 0.12273 | $E_6$ = 1.2436 | $Br_6$ = 0.052481 |
| | $A_7$ = 1.9092 | $E_7$ = 1.3704 | $Br_7$ = 0.82993 |
| | $A_8$ = 0.44403 | $E_8$ = 1.4835 | $Br_8$ = 0.1329 |
| | $A_9$ = 1.2484 | $E_9$ = 1.5903 | $Br_9$ = 0.30869 |
| | $A_{10}$ = 5.4351 | $E_{10}$ = 1.6945 | $Br_{10}$ = 0.91403 |
| | $A_{11}$ = 0.22097 | $E_{11}$ = 2.795 | $Br_{11}$ = 1.1966 |
| | $A_{12}$ = 4.204 | $E_{12}$ = 2.801 | $Br_{12}$ = 1.6834 |
| | $A_{13}$ = 1.7699 | $E_{13}$ = 4.6936 | $Br_{13}$ = 1.7231 |
| | $A_{14}$ = 3.5774 | $E_{14}$ = 7.0005 | $Br_{14}$ = 2.2483 |
| Tauc-Lorentz<br>$\varepsilon_{TL} = \varepsilon_1 + i\varepsilon_2$<br>$\varepsilon_2 = \frac{A_n Eo_n C_n (E - Eg_n)^2}{(E^2 - Eo_n^2)^2 + C_n^2 E^2} \cdot \frac{1}{E}$, $for\ E > Eg_n$<br>$\varepsilon_2 = 0$, $for\ E \leq Eg_n$<br>$\varepsilon_1 = \frac{2}{\pi} P \int_{Eg_n}^{\infty} \frac{\xi \varepsilon_2(\xi)}{\xi^2 - E^2} d\xi$<br>Where P is the Cauchy Principal Value. | Ordinary<br>$A_1$ = 0.088984 $Eo_1$ = 0.19328 $C_1$ = 0.55236 $Eg_1$ = 0.0001 | | |
| Parametric Semiconductor<br>Psemi-(M0, M1, M2, M3 & Tri)<br>See WVASE manual by J.A. Woollam Co. | Extraordinary (Psemi-M0)<br>$A_1$ = 30.512 $E0_1$ = 0.44453 $B_1$ = 0.26265<br>$WR_1$ = 0.28723 $PR_1$ = 0.58753 $AR_1$ = 0.000635 $O2R_1$ = 0 | | |

The resulting complex refractive ($n$ and $\kappa$), birefringence ($\Delta n = n_e - n_o$), and dichroism ($\Delta\kappa = \kappa_e - \kappa_o$) are then plotted in Figure 3.22. The dichroism becomes largest near 1 eV, within the short-wave infrared (SWIR) spectrum range, and the birefringence is as large as 0.9 across MWIR and LWIR. As the low-loss regime of $BaTiSe_3$ occurs below 0.20 eV, red spheres marked its spectral range in Figure 3.22(b).

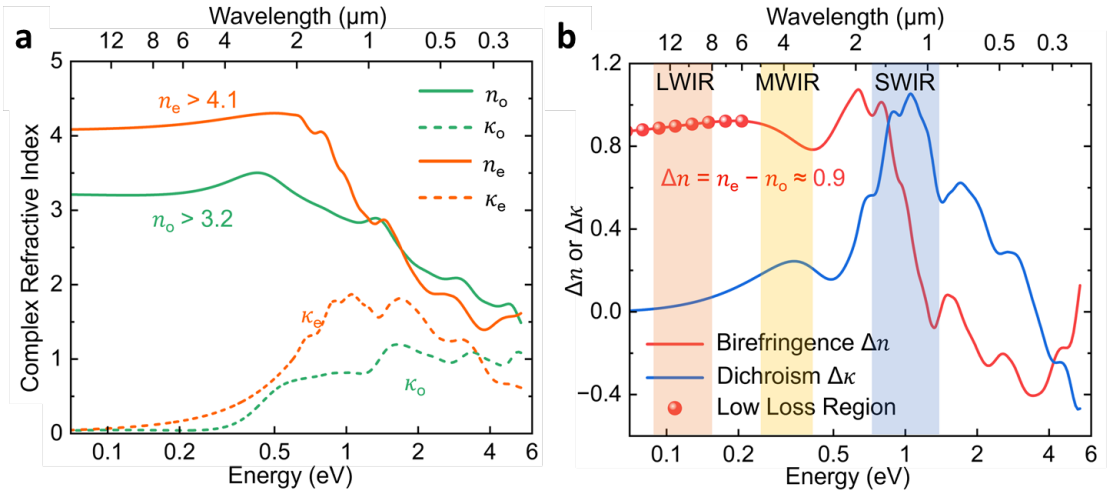


**Figure 3.22: (a)** Optical properties obtained from combining FTIR and ellipsometry, both real ($n$) and imaginary ($\kappa$) parts for ordinary and extraordinary linear polarization. **(b)** The large dichroism ($\Delta\kappa = \kappa_e - \kappa_o$) peak across SWIR leaves behind a giant birefringence ($\Delta n = n_e - n_o$) up to 0.9 across the MWIR to LWIR wavelengths. Figure adapted from Ref[69].

The imaginary part of the refractive index (or extinction coefficient), $\kappa_o$ and $\kappa_e$, of $BaTiS_3$, $BaTiSe_3$, and $Sr_{9/8}TiS_3$ are compared with each other in Figure 3.23. Contrary to the $\kappa$ peak featuring a sharp drop of absorption that decays to ~ 0 near 4 μm in in $Sr_{1+x}TiS_3$, $BaTiS_3$ and $BaTiSe_3$ have $\kappa$ peaks at shorter wavelengths but decay gradually to zero until ~5 μm and ~ 6 μm. Such absorption characteristic of $BaTiS_3$ and $BaTiSe_3$ leads to dichroism of a broader spectrum range but also cause more loss (reflectance + transmittance < 100%) in the LWIR region compared to $Sr_{9/8}TiS_3$.

The room temperature birefringence ($\Delta n$) and the low loss regions (after the absorption edge) of $BaTiS_3$, $BaTiSe_3$, and $Sr_{9/8}TiS_3$ are then listed for wavelengths from 1 μm to 17 μm in Figure 3.23, along with a variety of IR birefringent crystals[94–102]. $BaTiS_3$ and $BaTiSe_3$ share similar structural features, especially the existence of the $a$-

*b* plane Ti displacements and the disorder of such in-plane distortions (more discussions related to the in-plane disorders in $BaTiS_3$ and $BaTiSe_3$ can be found in the following sections). $BaTiSe_3$, up to 0.9, slightly surpasses the birefringence of $BaTiS_3$, which is up to 0.76. $Sr_{9/8}TiS_3$ and other $Sr_{1+x}TiS_3$, however, distort $TiS_6$ chains in an incommensurate manner, periodically introducing rotational distortion to $TiS_6$ polyhedron. The presence of localized Ti *d*-states, commensurate with the excess Sr, significantly increases the birefringence of $Sr_{9/8}TiS_3$ to a much higher region, up to 2.1 (more details related to structural modulation in $Sr_{9/8}TiS_3$ can be found in the following sections).

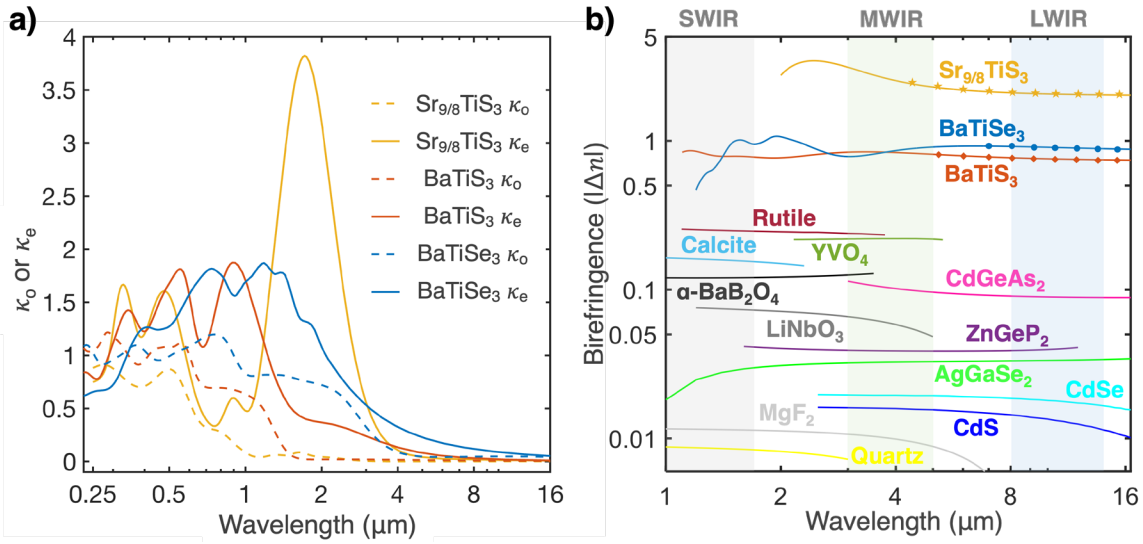


**Figure 3.23:** Comparison of the refractive index of $A_{1+x}TiX_3$ ($A$ = Sr, Ba; $X$ = S, Se). **(a)** Extinction coefficients, $\kappa_o$ and $\kappa_e$, of $Sr_{9/8}TiS_3$, $BaTiS_3$ and $BaTiSe_3$. **(b)** The absolute birefringence value of a variety of IR birefringent crystals (from the literature[94–104]), quasi-1D perovskite chalcogenides $Sr_{9/8}TiS_3$, $BaTiS_3$, and $BaTiSe_3$ extends the largest birefringence to ~0.7 - 2.1. The symbols indicate low-loss regions of $BaTiSe_3$, $BaTiS_3$, and $Sr_{9/8}TiS_3$. Figure adapted from Ref[69].

## 3.3 Origins of the substantial optical anisotropy in $A_{1+x}BX_3$

### 3.3.1 atomic-scale structural modulation in $Sr_{9/8}TiS_3$

$Sr_{1+x}TiS_3$ falls in a broad category of $BaNiO_3$-related structures[105,106], with quasi-1D chains of face-shared $BX_6$ octahedra that are aligned along a 6-fold rotational axis (commonly the *c*-axis) with *A* cations filling the inter-chain interstitials. Its chemical composition was determined to be off-stoichiometric using energy dispersive analytical X-ray spectroscopy (EDS) as reported in a previous work[107]. Although $A_{1+x}BX_3$ compounds are commonly stoichiometric (i.e., $x = 0$), certain non-stoichiometric crystalline structures, such as $Sr_{9/8}TiS_3$ and $Sr_{8/7}TiS_3$, have been reported to be more thermodynamically stable[108,109]; in these structures, excess Sr atoms periodically compress the Sr-lattice while introducing a stacking sequence of distorted $TiS_6$ polyhedral and displaced Sr atoms along the *c*-axis, expressed as structural modulation[105,108,109].

We evaluated the thermodynamic stability of both stoichiometric $SrTiS_3$ ($P2_1$) and modulated $Sr_{9/8}TiS_3$ ($R3c$) by constructing the convex hull with respect to the formation energy of their possible decomposition products. The convex hull connects phases that have a formation energy lower than any other phase or linear combination of phases at the respective compositions. If a phase has a formation energy above the hull, $E_{hull}$, it is considered metastable, as the system can lower its energy (by $E_{hull}$) by decomposing into products that are on the hull[110]. For the Sr-Ti-S system, we calculated the total energy ($E_{total}$) of all the thermodynamically stable

phases ($E_{\text{hull}}$ = 0) available in the Materials Project[111]. With all phases listed in the Table 3.6 being considered, we constructed the convex hull through the grand canonical linear programming (GCLP) method[112]. The GCLP minimizes the free energy of a mixture at a given composition in the Sr-Ti-S phase space to identify the combination of thermodynamically equilibrium phases:

$$\Delta G = \sum_i f_i \Delta E_f^i \qquad (3.3)$$

where, $\Delta G$ is the free energy of the compound with the desired composition, $f_i$ is the molar fraction of competing phases, $\Delta E_f^i$ is the formation energy of competing phases. We calculated $\Delta E_f^i$ of each phase using:

$$\Delta E_f^i = E_{\text{Sr}_x\text{Ti}_y\text{S}_z} - xE_{\text{Sr}} - yE_{\text{Ti}} - zE_{\text{S}} \qquad (3.4)$$

where $E_{\text{Sr}_x\text{Ti}_y\text{S}_z}$, $E_{\text{Sr}}$, $E_{\text{Ti}}$ and $E_{\text{S}}$ are the total energy of each phase from DFT calculations; while *x*, *y* and *z* are atomic fraction of each element in the compounds.

For $SrTiS_3$ and $Sr_{9/8}TiS_3$, we find the decomposition products that minimize the total energy are:

$$SrTiS_3 \rightarrow SrS + TiS_2$$

$$Sr_9Ti_8S_{24} \rightarrow 9SrS + 4.5TiS_2 + 0.5Ti_7S_{12}$$

As shown in the tabulated dataset Table 3.6 for the Sr-Ti-S system, modulated $Sr_{9/8}TiS_3$ is thermodynamically stable with formation energy on the hull ($E_{\text{hull}}$ = 0),

while stoichiometric $SrTiS_3$ is metastable having formation energy above hull ($E_{hull}$ = 44.975 meV/atom).

**Table 3.6:** Database for convex hull construction

| Formula | Space group | $E_{total}$/eV | Atoms/unit | $\Delta E_f$ (eV/atom) | $E_{hull}$ (meV/atom) |
|---|---|---|---|---|---|
| Sr | *R*-3*m* | -5.017 | 3 | 0 | |
| Ti | *P*6/*mmm* | -16.578 | 3 | 0 | |
| S | *P*2/*c* | -132.103 | 32 | 0 | |
| SrS | *Fm*-3*m* | -10.113 | 2 | -2.156 | |
| $SrS_3$ | *Aba*2 | -36.283 | 8 | -1.021 | |
| $Ti_2S$ | *Pnnm* | -218.902 | 36 | -1.020 | |
| $Ti_2S_3$ | *C*2/*m* | -61.002 | 10 | -1.413 | |
| $Ti_5S_8$ | *C*2/*m* | -79.046 | 13 | -1.415 | |
| $Ti_7S_{12}$ | *P*-1 | -229.359 | 38 | -1.393 | |
| TiS | *P*-6*m*2 | -12.506 | 2 | -1.426 | |
| $TiS_2$ | *P*-3*m*1 | -17.849 | 3 | -1.355 | |
| $TiS_3$ | $P2_1/m$ | -43.744 | 8 | -0.990 | |
| $SrTiS_3$ | $P2_1$ | -55.474 | 10 | -1.631 | 44.975 |
| $Sr_{9/8}TiS_3$ | *R*3c | -457.439 | 82 | -1.717 | 0 |

The crystal structure of $Sr_{9/8}TiS_3$ was resolved using single-crystal X-ray diffraction (SC-XRD). The resulting $Sr_{54}Ti_{48}S_{144}$ structure of *R*3*c* and $Sr_{1.125}TiS_3$ structure of $R\bar{3}m(00g)0s$[113] space groups reveal a similar modulated structure (visualized in Figure 3.24), which is consistent with the previously reported *R*3*m*(00g)0*s* $Sr_{9/8}TiS_3$ structure[108,109,114–116].

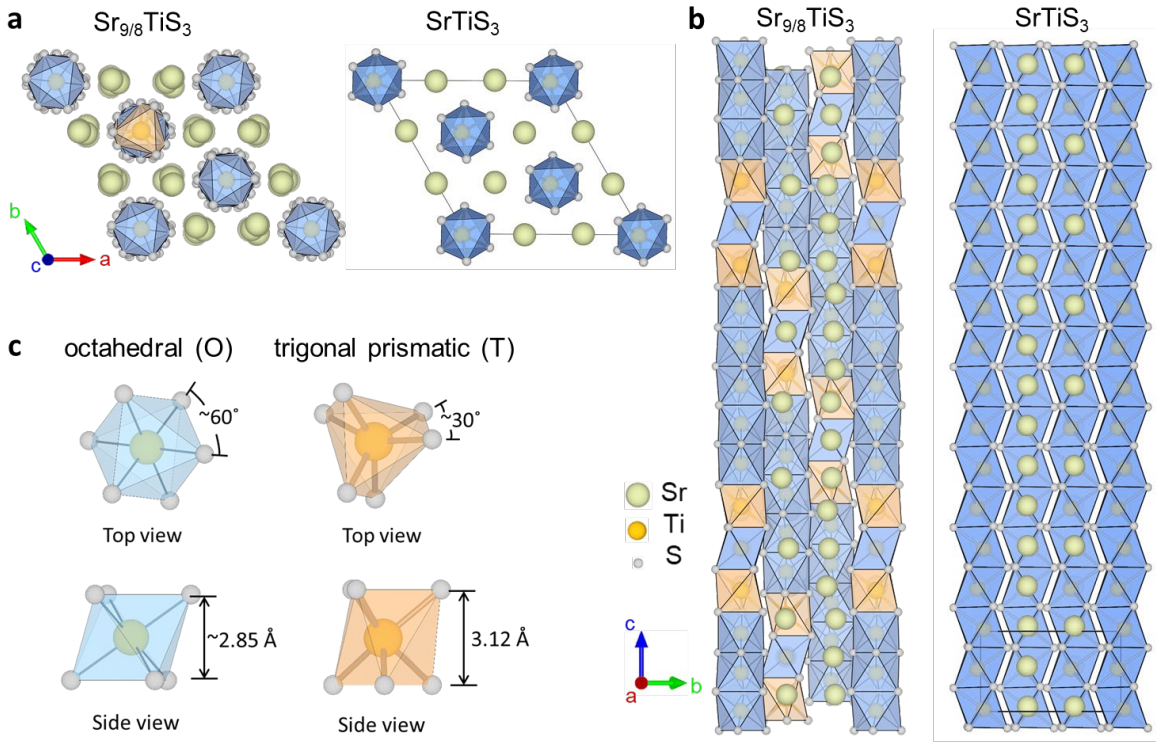


**Figure 3.24:** Crystal structure of $Sr_{9/8}TiS_3$ and hypothetical stoichiometric $SrTiS_3$. Schematics representing the modulated $Sr_{9/8}TiS_3$ (*R*3*c*) lattice, resolved from single-crystal XRD (SC-XRD), and viewed along the [001] axis in **(a)**, and [100] axis in **(b)**. The octahedral (O) and pseudo-trigonal prismatic (T) $TiS_6$ units are highlighted in blue and orange, respectively. Schematic representing lower-symmetry $P2_1$-$SrTiS_3$ viewed from [001] axis in a (right) and [100] axis in b (right), where the $TiS_6$ units form face-sharing octahedral chains running along the *c*-axis. **(c)** Schematic representing building blocks for modulated $Sr_{9/8}TiS_3$ with top and side views. Face-sharing octahedra (O) are highlighted in blue, and pseudo-trigonal prismatic (T) units are represented in orange. $TiS_6$ units undergo a twist distortion, ~30˚ rotation of S3 triangles around the *c*-axis from octahedral to trigonal-prismatic polyhedra, with elongated Ti–S bonds. Figure adapted from Ref[70].

In contrast to the hypothetical stoichiometric counterpart $SrTiS_3$, the $Sr_{9/8}TiS_3$ lattice has structural modulations consisting of blocks of face-shared octahedra (referred as 'O') that are separated by pseudo-trigonal-prismatic $TiS_6$ units (referred as 'T') along

the *c*-axis as shown in Fig. 3.24(b). The structural modulation of $Sr_{9/8}TiS_3$ arises from an overall trigonal twist distortion compared to the average unmodulated structure of $SrTiS_3$. To accommodate excess Sr in the lattice along the *c*-axis, Sr atoms undergo displacements within the *a*-*b* plane, resulting in the triangular-shaped projection in Fig. 3.24(a). The Sr displacements are accompanied by twist distortion of $TiS_6$ units from octahedral to trigonal-prismatic polyhedra. These different polyhedral units have different Ti–Ti distances along the *c*-axis. By counting the stacking sequence of building blocks (structurally classified as O and T), $TiS_6$ chains with periodic $[-(T-O-T)-(O)_5-]_2$ succession can be used to define the modulation periodicity of 16 units of $TiS_6$ within every 18 Sr layers in the $Sr_{9/8}TiS_3$ lattice [Fig. 3.24(b)].

Fig. 3.24(c) shows two building blocks of the modulated $Sr_{9/8}TiS_3$ lattice. Compared to face-shared octahedral $TiS_6$ units (O) represented in blue, the pseudo-trigonal prismatic units (T) in orange have elongated Ti–S bonds and have a ~30 ° rotation of $S_3$ triangles around the *c*-axis. As shown in Fig. 3.25, Sr atoms show displacive modulation about the average position along both *c*-axis and *a*-*b* plane, which leads to the twist distortion of $TiS_6$ units accompanied with altered Ti–Ti distances along the *c*-axis. When projected along the [100] zone axis, Ti atoms periodically overlap with Sr as highlighted with dashed ellipses in Figure 3.25.

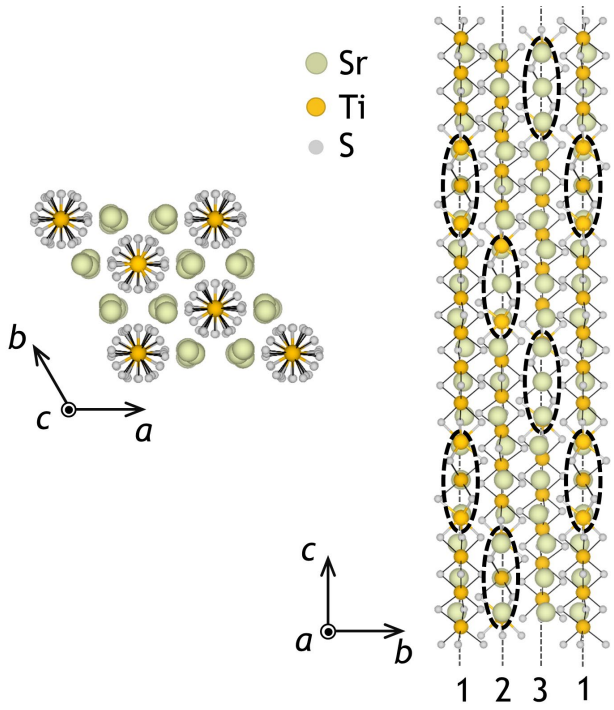


**Figure 3.25:** Structural modulations in $Sr_{9/8}TiS_3$. Schematic representing modulated $Sr_{9/8}TiS_3$. Three identical $TiS_6$ chains (1, 2, 3) are shown. They have a commensurate stacking sequence of $[-(T-O-T)-(O)_5-]_2$, which defines the modulation periodicity. The dashed ellipses indicate the periodic (T–O–T) segments, where Ti atoms overlap with Sr atoms, when projected along [100] zone axis. Figure adapted from Ref[70].

To directly visualize the subtle structural modulations in $Sr_{9/8}TiS_3$, we performed atomically resolved imaging using an aberration-corrected scanning transmission electron microscope (STEM). Large field-of-view, high-angle annular dark-field (HAADF) images of the $Sr_{9/8}TiS_3$ crystal viewed along the [001] and [100] zone axis are shown in Fig. 3.26. In this imaging mode, the intensity of the atomic columns is approximately proportional to the square of the effective atomic number of the column ($Z^2$)[117]. Along the [001] zone axis, the Sr atomic columns appear as triangles due to their staggered arrangement along the *c*-axis [Fig. 3.26(a)], which match well

with the structural features in Fig. 3.24(a). Along the [100] orientation, the Ti and Sr columns overlap within the triple blocks of – (T–O–T) –, and therefore, they appear as bright triplets in the HAADF images as they have higher intensity than the Sr-only atomic columns within the block of five octahedral units $-(O)_5-$ [Fig. 3.26(b, c)]. We also observe periodic distortions of the Sr atomic columns in the form of contraction and dilation of the Sr–Sr distance between neighboring chains. A comparison of the intensity and spacing between atomic columns in the experimental and the simulated HAADF images, as shown in Fig. 3.26(d), shows excellent agreement, and corroborates the modulation periodicity.

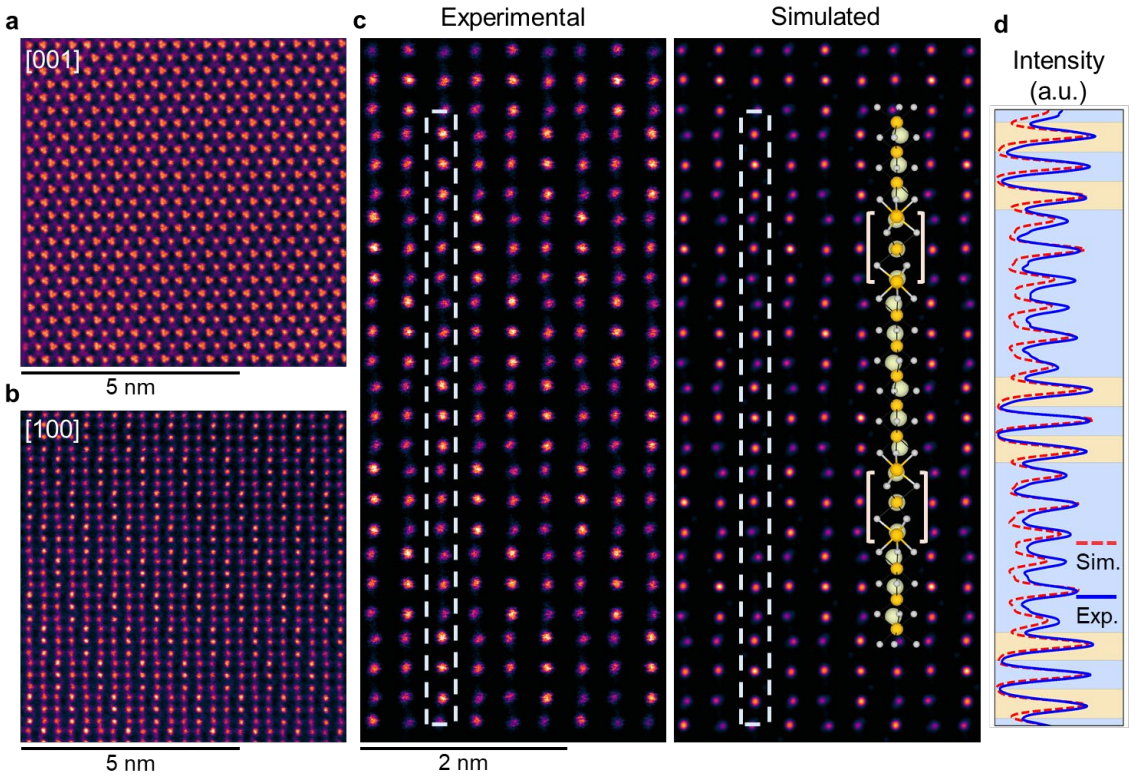


**Figure 3.26:** Direct observation of structural modulations in $Sr_{9/8}TiS_3$ crystals. Atomic-resolution HAADF-STEM images of a $Sr_{9/8}TiS_3$ crystal along the [001] axis in **(a)**, and [100]

axis in **(b)**. **(c)** High-magnification HAADF-STEM image (left panel) and simulated image (right panel) of $Sr_{9/8}TiS_3$ view along the [100] axis. A schematic of one column of atoms is overlayed on the simulated image. A repeating pattern of three bright atomic columns, where the Ti and Sr atoms overlap along the viewing direction, can be observed in these HAADF images. These triplet atomic columns are highlighted with square brackets in the atomic model. d. Line profiles across the experimental and simulated STEM images (white dashed boxes) comparing the intensity variation across a single atomic column. Figure adapted from Ref[70].

The displacive modulation of Sr resulting from structural modulations has been confirmed by measuring horizontal offsets of neighboring Sr atoms along *c*-axis in the HAADF-STEM images viewed along the [100] zone axis, as shown in Fig. 3.27. The position of Sr atomic columns were determined by applying a 2D Gaussian peak fitting alogrithm[118]. The Sr configuration in the experimental HAADF image shows good match with that in the simulated image obtained using the refined $Sr_{9/8}TiS_3$ lattice, which verifies the modulation periodicity of $Sr_{9/8}TiS_3$ resolved by SC-XRD.

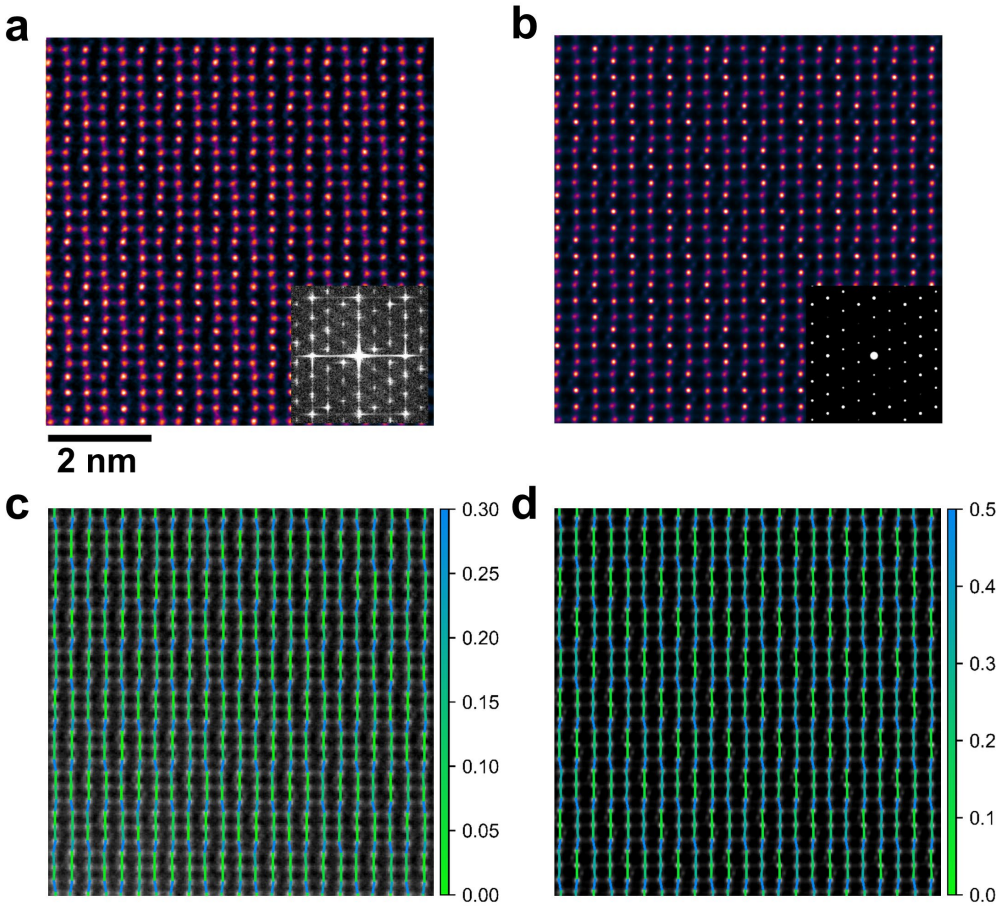


**Figure 3.27:** Experimental and simulated HAADF-STEM images of modulated $Sr_{9/8}TiS_3$. **(a)** Direct experimental observation of modulations in $Sr_{9/8}TiS_3$ viewed along [100] zone axis from a large field of view HAADF image. The inset is the corresponding fast Fourier transform (FFT) pattern. **(b)** Simulated HAADF-STEM image of modulated $Sr_{9/8}TiS_3$. The inset shows the simulated electron diffraction pattern. **(c, d)** Maps of structural modulation periodicity along the *c*-axis by measuring horizontal offsets of the neighboring atomic columns from **(a, b)**. The color of connecting lines represents the magnitude of deviation along the horizontal direction between neighboring atoms. The length scale of the color bar is in the units of Å. Figure adapted from Ref[70].

To reveal the origin of the giant optical anisotropy in $Sr_{9/8}TiS_3$ and its relationship with structural modulations, we performed first-principles density-functional theory

(DFT) calculations. We calculated the electronic structures of $Sr_{9/8}TiS_3$ and $SrTiS_3$ to understand the effect of modulations on the optical properties. Both $SrTiS_3$ and $Sr_{9/8}TiS_3$ are computed to possess an indirect bandgap. $SrTiS_3$ has an indirect bandgap between valence band maximum (VBM) at Γ point and conduction band minimum (CBM) at A point. The topmost valence band and bottom of the conduction band of $SrTiS_3$ show a relatively flat behavior along all the paths in the Brillouin zone, except for the Γ−Z direction, which in the reciprocal space corresponds to the direction parallel to the *c*-axis where the neighboring $TiS_6$ octahedra have face-sharing connectivity, while octahedral connectivity is broken along the *ab*-plane[119,120]. Compared with $SrTiS_3$, $Sr_{9/8}TiS_3$ shows similarly flat bands. The topmost valence bands and bottom conduction bands arise from *d*-states, and form the indirect bandgap between VBM at Γ and CBM at T.

In $Sr_{9/8}TiS_3$, the electrons introduced by excess $Sr^{2+}$ cations occupy the nominally empty Ti *d* states. Using DFT + Hubbard *U* calculations[121], with a $U$ = 3.0 eV for the Ti atoms, we checked for different magnetic orderings of the moments and found the paramagnetic configuration to be the most stable. As shown in the calculated band structure of $Sr_{9/8}TiS_3$ in Fig. 3.28(b), the additional valence electrons preferentially occupy $3d_{z^2}$ states (highlighted in red) of Ti atoms in $Sr_{9/8}TiS_3$. Compared to the pseudo-trigonal prismatic $TiS_6$ units (T), octahedral $TiS_6$ units (O) have shorter Ti-Ti distance, resulting in $3d_{z^2}$ states that are lower in energy. Thus, the Ti atoms in the O block preferentially accept the additional electrons. This also opens up a band gap

between the occupied $3d_{z^2}$ states of the octahedrally coordinated Ti atoms and the unoccupied Ti-$3d_{z^2}$ states of the Ti atoms with trigonal-prismatic coordination. The character of the edge states in modulated $Sr_{9/8}TiS_3$ is in sharp contrast to that of $SrTiS_3$ wherein the band gap is between the S-3$p$ states in the valence band and Ti-$3d_{z^2}$ states in the conduction band [Fig. 3.28(a)].

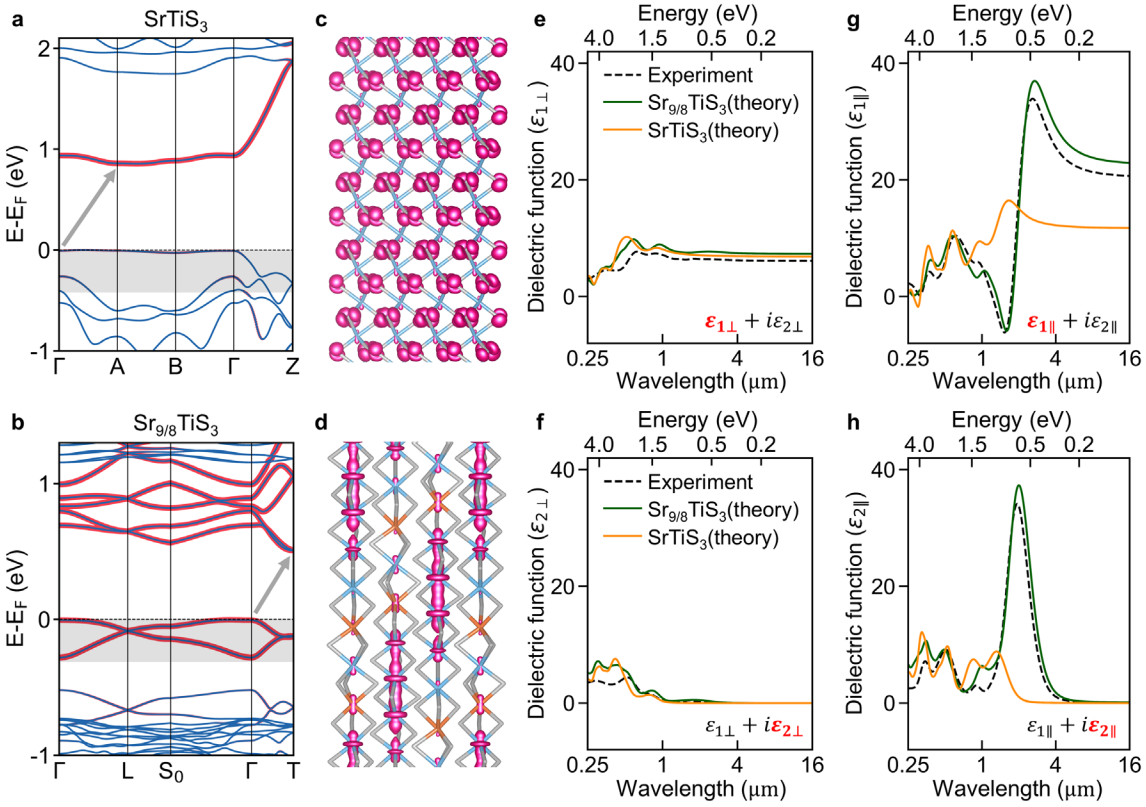


**Figure 3.28:** Electronic structure and optical properties of modulated $Sr_{9/8}TiS_3$. **(a, b)** Orbital-projected band structures for hypothetical stoichiometric $SrTiS_3$ in **(a)**, and modulated $Sr_{9/8}TiS_3$ in **(b)**. The thicker lines highlighted in red correspond to the contribution from Ti-$3d_{z^2}$ states. The Fermi energy is set to 0 eV. **(c, d)** Spatial distribution of the valence electrons below the Fermi energy (shaded in gray in **(a, b)**), showing **(c)** S-3$p$ character in $SrTiS_3$ and **(d)** Ti-$3d_{z^2}$ character in $Sr_{9/8}TiS_3$. The isosurface is set to an electron density of 0.004 e/Å$^3$. **(e-h)** Calculated complex dielectric function for polarization perpendicular ($\varepsilon_{i\perp}$) and parallel ($\varepsilon_{i||}$) to the $c$-axis of the hypothetical stoichiometric $SrTiS_3$ and modulated

$Sr_{9/8}TiS_3$, compared to the experimental results (black dashed line). The index $i$ = 1 represents the real part of the dielectric function and 2 represents the imaginary part. Figure adapted from Ref[70].

With the electronic ground states computed, we then calculated the complex dielectric function $\varepsilon_{\parallel/\perp}(\omega) = \varepsilon_{1\parallel/\perp}(\omega) + i\varepsilon_{2\parallel/\perp}(\omega)$ for electric fields along ($||$) and perpendicular to ($\perp$) the *c*-axis. The imaginary part $\varepsilon_2(\omega)$ is obtained by calculating the direct transitions between occupied and unoccupied states[122]. The real part $\varepsilon_1(\omega)$ is then extracted by a Kramers-Kronig transformation[64]:

$$\varepsilon_1(\omega) = 1 + \frac{2}{\pi} P \int_0^\infty \frac{\omega' \varepsilon_2(\omega')}{\omega'^2 - \omega^2} d\omega' \qquad (3.5)$$

$$\varepsilon_2(\omega) = -\frac{2\omega}{\pi} P \int_0^\infty \frac{\varepsilon_1(\omega') - 1}{\omega'^2 - \omega^2} d\omega' \qquad (3.6)$$

where $P$ is the "principal part". Based on the computed frequency-dependent dielectric function, optical properties, such as the real part of the refractive index, $n(\omega)$, and the extinction coefficient, $\kappa(\omega)$, can be obtained in terms of the real part, $\varepsilon_1(\omega)$, and imaginary part of the dielectric function, $\varepsilon_2(\omega)$:

$$\mathrm{n}(\omega) = \frac{\sqrt{2}}{2}\left[\sqrt{\varepsilon_1(\omega)^2 + \varepsilon_2(\omega)^2} + \varepsilon_1(\omega)\right]^{1/2} \qquad (3.7)$$

$$\kappa(\omega) = \frac{\sqrt{2}}{2}\left[\sqrt{\varepsilon_1(\omega)^2 + \varepsilon_2(\omega)^2} - \varepsilon_1(\omega)\right]^{1/2} \qquad (3.8)$$

Fig. 3.28(e, f) show the frequency-dependent dielectric functions of the hypothetical stoichiometric $SrTiS_3$ and the modulated $Sr_{9/8}TiS_3$, with very similar results perpendicular to the *c*-axis ($\varepsilon_{1\perp}$), but dramatic enhancement of the dielectric function

parallel to the *c*-axis ($\varepsilon_{1\parallel}$). The enhancement is a consequence of the selective occupation of $d_{z^2}$ states at the $(O)_5$ segments in modulated $Sr_{9/8}TiS_3$, which we show in real space by using an isosurface plot of the charge density arising from the occupied $3d_{z^2}$ band [Fig. 3.28(d)]. The occupied $3d_{z^2}$ electrons form a highly oriented blob and result in additional polarizability along the optic axis ($\varepsilon_{1\parallel}$). In contrast, the electrons from the valence band states in stoichiometric $SrTiS_3$ have an isotropic character and are localized on the S atoms [Fig. 3.28(c)]. The unoccupied conduction band is at substantially higher energy compared to the $3d_{z^2}$ electrons, resulting in very few free carriers and therefore low free-carrier absorption.

While an experimental comparison between $Sr_{9/8}TiS_3$ and $SrTiS_3$ cannot be made due to the metastable nature of $SrTiS_3$, we did compare the optical properties of $Sr_{9/8}TiS_3$ to $BaTiS_3$, and to hypothetical $SrTiS_3$ which is isostructural to $BaTiS_3$ in Fig. 3.29.

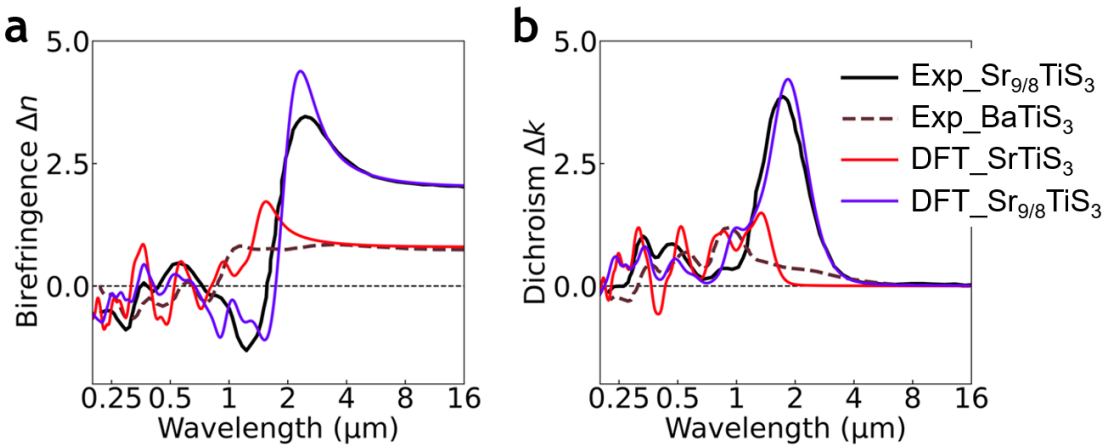


**Figure 3.29:** Comparison of optical anisotropy. **(a, b)** Birefringence and dichroism comparison between experimental measurements for $Sr_{9/8}TiS_3$ (in black solid), $BaTiS_3$ (in black dash) and DFT calculations for $Sr_{9/8}TiS_3$ (in blue solid) and $SrTiS_3$ (in red solid). All DFT

calculations were performed at the GGA+$U$ level ($U$ = 3 eV for Ti atoms). The hypothetical stoichiometric $SrTiS_3$ has a similar optical anisotropy as $BaTiS_3$. Figure adapted from Ref[70].

We account for strong correlation effects within the localized $d$ states of Ti by using the GGA + Hubbard $U$ method[121]. The Hubbard $U$ value was selected to be 3 eV as it was found to best match the experimental results, as shown in Fig. 3.30.

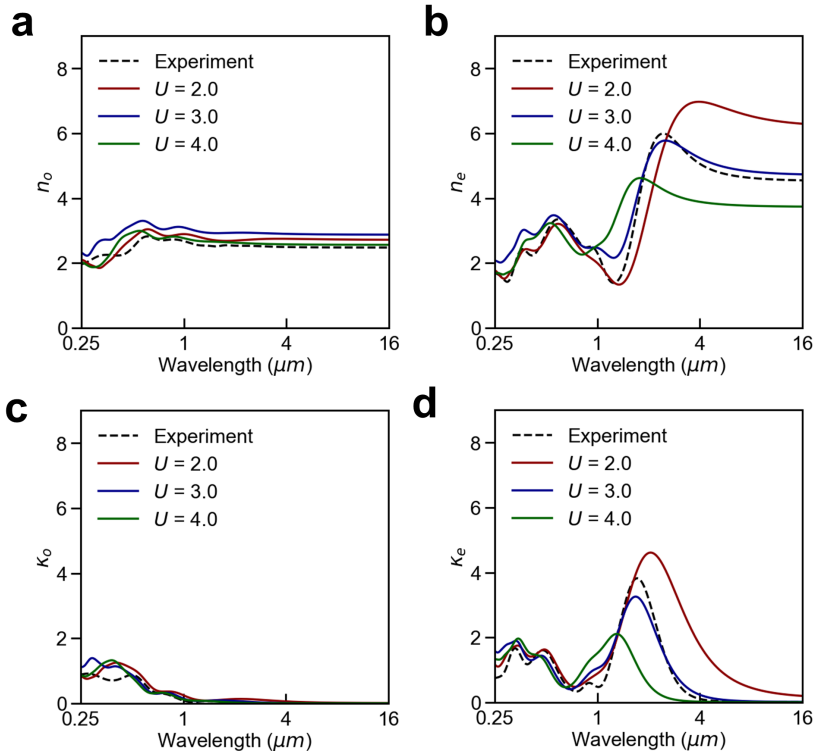


**Figure 3.30:** The effect of Hubbard $U$ on calculated optical properties of $Sr_{9/8}TiS_3$. **(a, b)** Real part of complex refractive index along the ordinary axis ($n_o$) and the extraordinary axis ($n_e$). **(c, d)** Imaginary part of the complex refractive index along the ordinary axis ($\kappa_o$), and the extraordinary axis ($\kappa_e$). Figure adapted from Ref[70].

In this section, we demonstrate how subtle atomic-scale structural modulations of a bulk crystal can dramatically change its optical properties. We synthesized and

studied single-crystal plates of modulated quasi-1D chalcogenide $Sr_{9/8}TiS_3$, a uniaxial material which we found to possess a record birefringence ($\Delta n > 2.1$) in a broadband low-loss spectral region between $\lambda = 6$ μm and at least 17 μm, with the optic axis in plane of the samples. Compared to stoichiometric unmodulated $SrTiS_3$, which is expected to have $\Delta n \lesssim 1$, the extra Sr in $Sr_{9/8}TiS_3$ results in additional electrons that selectively occupy localized anisotropic states (Ti-3 $d_{z^2}$), greatly enhancing the polarizability of the material along the optic axis, and thus resulting in a degree of optical anisotropy far larger than has been demonstrated in any bulk material. The atomic-scale structural features of $Sr_{9/8}TiS_3$ were resolved using single-crystal X-ray diffraction and directly observed with HAADF-STEM imaging, and the resulting structural information was used to perform DFT calculations that clarified the physical mechanism leading to the experimentally observed colossal optical anisotropy. We anticipate that structural modulation in nonstoichiometric crystals will be a new tool in realizing materials with large degrees of optical and optoelectronic anisotropy. Furthermore, the connection between subtle structural modulations and large changes in the refractive index may enable a new class of optical materials that can be tuned with an applied stimulus.

## 3.3.2 In-plane displacements in $BaTiS_3$/$BaTiSe_3$

### 3.3.2.1 $BaTiS_3$

Single crystals of $BaTiS_3$ were reported to crystallize in $P6_3mc$ space group and the unit cell is visualized in Figure 3.31(a), whose face-shared $TiS_6$-octahedra form quasi-1D chains along the *c*-axis.

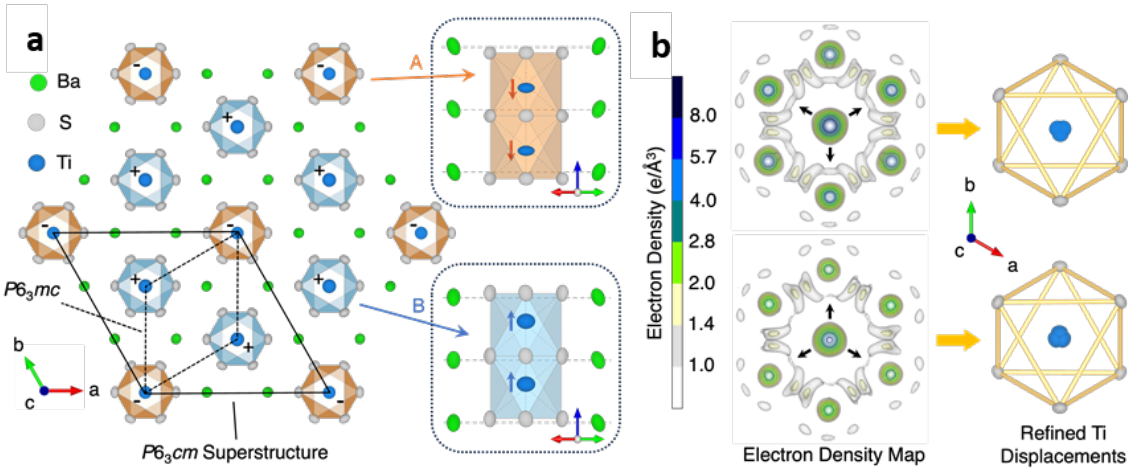


**Figure 3.31: (a)** Schematic of the $BaTiS_3$ crystal structure projected onto the *a*-*b* plane from the refined diffraction results. The ellipsoids used to show Ba, Ti, and S atoms reflect their refined atomic displacement parameters (ADPs). The trimerized $\sqrt{3} \times \sqrt{3} \times 1$ superstructure of $TiS_6$ chains leads to a lower symmetry $P6_3cm$ space group, which is the result of antiparallel displacements along the *c*-axis. The insets on the right visualize the positions of $TiS_6$ chains A (brown) and B (blue) with respect to adjacent Ba atoms. Chain A displaces down while chain B displaces up from a "fixed" Ba lattice. Moreover, Ti atoms also move away from the centroid of the $S_6$ octahedron antiparallelly between chain A and chain B. **(b)** Electron density maps, and displacement analysis for Ti01 (in chain A) and Ti02 (in chain B) along the *a*-*b* plane. Electron density below 1 e/Å$^3$ is comparable with the noise level and thus whitened. An anharmonic core electron distribution for Ti reveals disordered non-thermal Ti *a*-*b* plane displacements towards S atoms. Figure adapted from Ref[67].

The measured giant optical anisotropy was qualitatively explained in terms of the anisotropic distribution of elements with large differences in electronic polarizability[103]; however, the theoretically predicted and experimentally observed values of optical anisotropy were not in agreement[66,103,107]. First-principles, density-functional theory (DFT) calculations of $\Delta n$ for $BaTiS_3$ with $P6_3mc$ space group show that it is moderately birefringent (Figure 3.32), on the same level as other birefringent crystals such as rutile (~0.25), but much lower than the experimentally measured values for $BaTiS_3$ (~0.76).

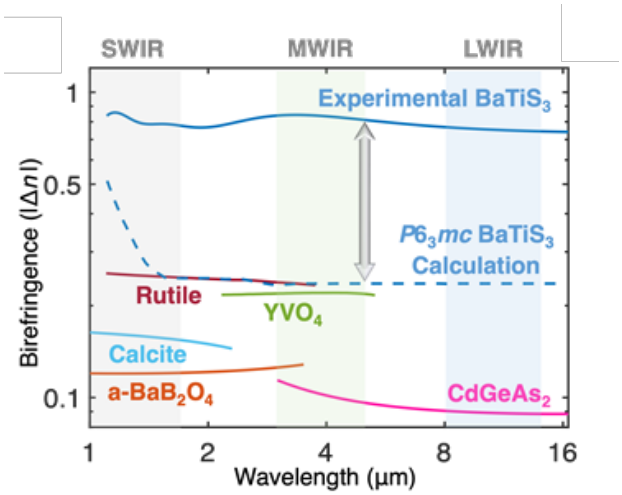


**Figure 3.32:** Comparison of the birefringence of $BaTiS_3$, which was experimentally measured[103] (blue solid line) and theoretically calculated from first-principles using the previously reported $P6_3mc$ space group (dashed blue line) against other birefringent crystals. The disagreement in the birefringence of $BaTiS_3$ between experiment and theory is evident. Figure adapted from Ref[67].

Therefore, this inconsistency motivated us to revisit the experimentally reported structure of $BaTiS_3$. Synchrotron single crystal X-ray diffraction (SC-XRD) studies

were performed on crystalline $BaTiS_3$ samples — that were synthesized using a previously reported CVT method[66,103]. We observe weak Bragg reflections suggesting a lower symmetry than $P6_3mc$. Even though the previously assigned $P6_3mc$ space group[66,103] captures the main reflections, we observe weaker symmetric superlattice reflections corresponding to a $\sqrt{3} \times \sqrt{3} \times 1$ trimerized translational symmetry over the $P6_3mc$ lattice. By including these superlattice reflections, we could figure out the formerly unassigned lattice disorder [103,123], which was referred to as potential $P6_3mc$ domain anomalies, to be refined as periodic atomic displacements in a $P6_3cm$ space group of a $\sqrt{3} \times \sqrt{3} \times 1$ unit cell. The resulting $P6_3cm$-$BaTiS_3$ structure projected onto the *a*-*b* plane is shown in Figure 3.31(a). The previously degenerate $TiS_6$-chains are now split into two types, each occupying different positions [right insets of Figure 3.31(a)] along the *c*-axis and with antiparallel Ti off-centering along the *c*-axis. They are labeled as $TiS_6$-chain A at the edges of the unit cell and $TiS_6$-chain B inside the unit cell; each unit cell thus has one chain A and two chains B. The Ti atoms are also displaced along the *c*-axis from the $S_6$ centroid, downwards by 0.167 Å in chain A and upwards by 0.147 Å in chain B. These antiparallel off-center displacements result in a ferrielectric ordering, as opposed to the ferroelectric ordering proposed for the $P6_3mc$ space group [123]. Figure 3.31(b) shows the electron density maps projected onto the *a*-*b* plane about the refined Ti A and Ti B sites, which highlights the small but definite deviations in the partial occupancy of Ti away from the centroid of the two types of $TiS_6$ chains.

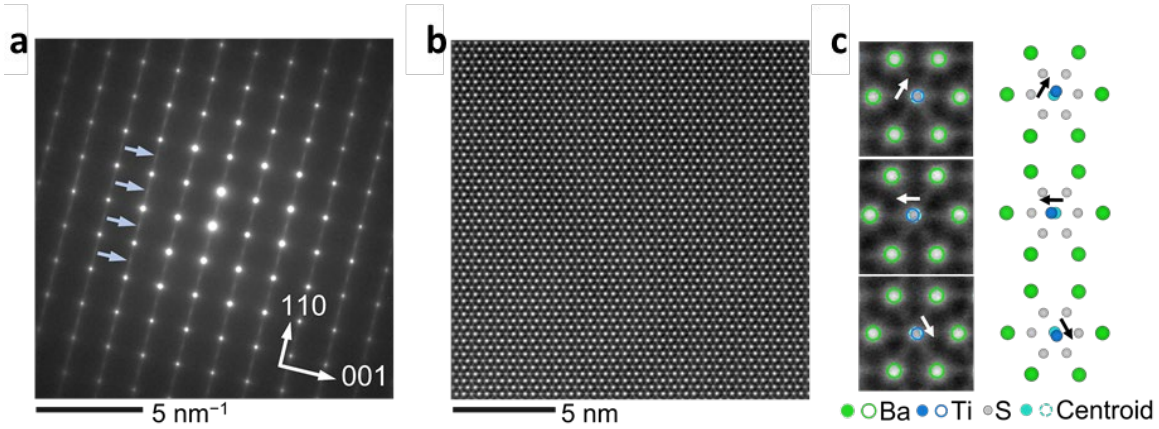


**Figure 3.33: (a)** TEM diffraction pattern viewed along the [1$\bar{1}$0] zone axis. Diffuse streaks specifically extend along the [110] direction, while sharp Bragg peaks exist along the [001] direction. **(b)** Representative HAADF-STEM image showing the atomic structure of $BaTiS_3$ along the *a*-*b* plane projection. **(c)** Local structural motifs from the HAADF image in **b** showing Ti *a*-*b* plane displacement towards adjacent S atoms. Ti displacements are determined from the centroid of the surrounding hexagonal Ba sublattice. Figure adapted from Ref[67].

To check the local ordering of these displacements, we carried out electron diffraction and imaging studies. Figure 3.33(a) shows a diffraction pattern viewed along the [1$\bar{1}$0]-zone axis obtained using a transmission electron microscope (TEM). Between the Bragg spots, we observe diffuse scattering rods (highlighted by blue arrows) that are specifically oriented along the 110-direction in reciprocal space. These streaks suggest the presence of strain or disorder normal to the (110)-planes. We do not observe any streaks between the Bragg reflections along 001. These diffraction patterns suggest that the observed Ti *a*-*b* plane displacements could possess short-range ordering.

To directly visualize the local ordering of these *a*-*b* plane displacements, we performed atomic scale imaging using an aberration-corrected scanning transmission electron microscope (STEM). Figure 3.33(b) shows a high-angle annular dark field (HAADF) STEM image of $BaTiS_3$ viewed along the [001]-zone axis. In this imaging mode, the intensity is proportional to the square of the average atomic number ($Z^2$) of the columns [124]. Thus, the heavier Ba atomic columns appear brighter than the lighter Ti columns, while the lightest S columns are almost invisible due to the dynamic-range constraints of the detector. We extracted the position of the atomic columns by fitting 2D Gaussians as shown in the small field-of-view HAADF images of three representative regions in Figure 3.33(c). We observe that the Ti atomic columns are displaced away from the centroid position defined by the six adjacent Ba columns.

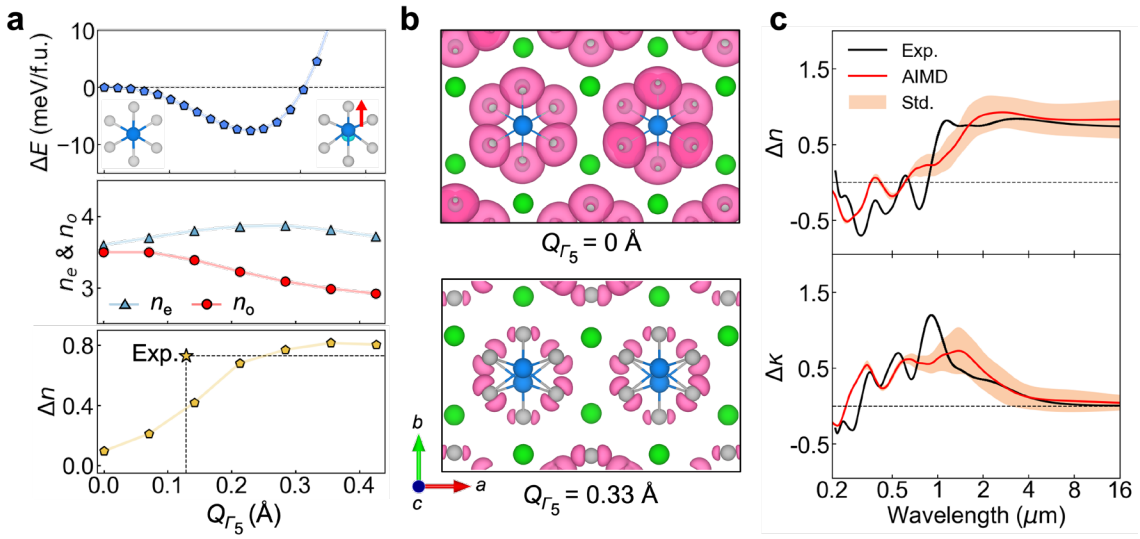


**Figure 3.34:** Optical anisotropy enhanced by Ti *a*-*b* plane displacements. **(a)** Top panel: Energy of $BaTiS_3$ as a function of the $\Gamma_5$ distortion mode associated with ordered *a*-*b* plane

displacements of Ti, as shown in atomic models in the inset. Middle and bottom panels: Real part of refractive index along the ordinary ( $n_o$ ) and extraordinary ( $n_e$ ) axes, and birefringence ( $\Delta n = n_e - n_o$ ) of $BaTiS_3$ (averaged between 4-16 μm wavelengths) as a function of average Ti *a-b* plane displacements. **(b)** Spatial distribution of electrons within 0.5 eV below the Fermi energy projected onto the *a-b* plane (top panel) without and (bottom panel) with Ti *a-b* plane displacements. Ti *a-b* plane displacements significantly decrease the charge distribution within the *a-b* plane, which is the reason for the decrease in $n_o$ shown in the middle panel of **(a)**. Isosurface in **(b)** set to an electron density of 0.0025 e/Å$^3$. **(c)** Birefringence ($\Delta n$) and dichroism spectra ($\Delta \kappa$) of the structure obtained by averaging 8 snapshots from an *ab*-initio molecular dynamics run of $BaTiS_3$ equilibrated at 800 K. The averaged structure has randomized Ti *a-b* plane displacements. The standard deviation (Std.) of the 8 structures is shaded in orange and centered around the average shown by the red solid line. The black solid line shows the experimentally measured anisotropy. Figure adapted from Ref[67].

To gain insights into the effect of the Ti *a-b* plane displacements on the optical properties, we then performed first-principles DFT calculations [125]. As mentioned before, the $P6_3cm$ structure does not have any *a-b* plane displacement of Ti atoms. A group symmetry analysis shows that freezing the $\Gamma_5$ distortion mode in the $P6_3cm$ structure leads to the off-centering of Ti atoms along the *a-b* plane. Freezing the $\Gamma_5$ distortion mode lowers the energy of the system, as shown in Figure 3.34(a), which explains the presence of *a-b* plane displacements in the experiments. We then calculated the complex dielectric function, ( $n + i\kappa$ ), of $BaTiS_3$ with different amplitudes of the $\Gamma_5$ distortion mode frozen to the $P6_3cm$ structure, as shown in Figure 3.35.

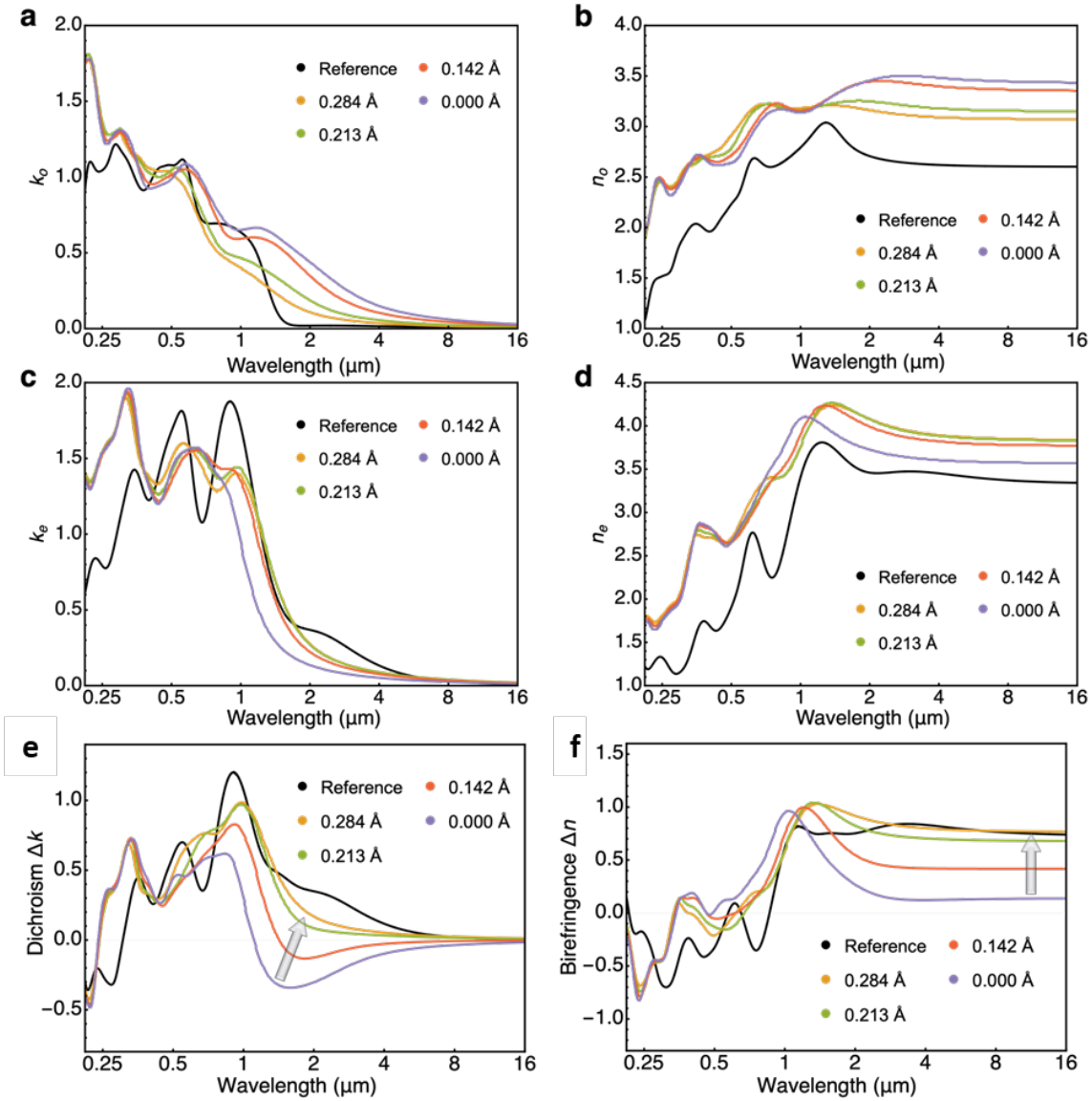


**Figure 3.35:** Real and imaginary parts of the refractive index of $BaTiS_3$ with different magnitudes of ordered Ti *a*-*b* plane displacements obtained by freezing the $\Gamma_5$ distortion mode. **(a-d)** The subscripts *o* and *e* correspond to the ordinary (along the *a*-axis of the structure) and extraordinary axes (along the *c*-axis), respectively. **(e)** Dichroism and **(f)** birefringence of $BaTiS_3$ as a function of Ti displacement in the *a*-*b* plane obtained by freezing the $\Gamma_5$ distortion mode with different magnitudes. Figure adapted from Ref[67].

The dielectric function was calculated along the *c*-axis, which we refer to as the extraordinary axis, and perpendicular to it, which are the ordinary axes. The real parts of the ordinary ($n_o$) and the extraordinary ($n_e$) refractive indices calculated in the transparent range of $BaTiS_3$ for photon energies smaller than 0.3 eV (light wavelength > 4 μm); and their difference, which is the birefringence ($\Delta n = n_e - n_o$), as a function of the average Ti displacement in the *a*-*b* plane is presented in the middle and bottom panels of Figure 3.34(a), respectively. We find that $\Delta n$ increases with increasing Ti *a*-*b* plane displacements until it plateaus for displacements > 0.3 Å. We also find that $n_e$ remains almost unchanged with increasing Ti *a*-*b* plane displacements. So, the dominant contribution to the increase in $\Delta n$ comes from a decrease in the magnitude of $n_o$ with increasing Ti *a*-*b* plane displacements. These trends are also observed for the wavelength-dependent $\Delta n$ [Figure 3.35(e)] and dichroism ($\Delta\kappa = \kappa_e - \kappa_o$), [Figure 3.35(f)] with varying displacements.

To identify the electronic origin of the enhancement in $\Delta n$ with Ti *a*-*b* plane displacements, we investigated the evolution of the occupied electronic states. $\Delta n$ in a crystal arises from the distribution and orientation of valence electrons near the Fermi energy[104,126]. Thus, electron redistribution near the Fermi energy introduced by the *a*-*b* plane Ti displacements can be expected to change the anisotropic optical response of $BaTiS_3$. Ti displacements in the *a*-*b* plane result in a decrease in the density of electrons that are oriented along the *a*-*b* plane and located within 0.5 eV

below the Fermi energy, as shown in the integrated electron density plots in Figure 3.34(b).

Finally, we have investigated the effect of the experimentally observed disordered Ti *a*-*b* plane displacements on $\Delta n$, as opposed to the ordered Ti displacements simulated by freezing the $\Gamma_5$ distortion mode. We performed *ab initio* molecular dynamics (AIMD) simulations starting with $BaTiS_3$ with ordered $\Gamma_5$ distortions and equilibrated the structure at 800 K for 5 ps to randomize the Ti displacements. We then used 8 randomly selected snapshots and calculated their dielectric function, $\Delta n$ and $\Delta \kappa$. The average values and standard deviations (Std.) of the calculated $\Delta n$ and $\Delta \kappa$ as a function of wavelength are shown in Figure 3.34(c). These results are in excellent agreement with the experimental results, which show that the hybridization of Ti and S states is, by large, determined by the local octahedral distortions, and is less sensitive to the Ti and S atoms in adjacent $TiS_6$-chains. Furthermore, we observe that the magnitude of Ti *a*-*b* plane displacements correlates extremely well with charge redistribution and the optical anisotropy in $BaTiS_3$.

In conclusion, $BaTiS_3$ shows correlated disorder at room temperature. These off-center Ti displacements within the *a*-*b* plane have long-range disorder but are ordered along the *c*-axis. The ordinary ($n_o$) refractive index in the partial (1.5 – 5 μm) and fully transparent region (> 5 μm) decreases while the extraordinary refractive index ($n_e$) remains almost unchanged with increasing Ti *a*-*b* plane displacements. Our results suggest that the refractive index tensor of $BaTiS_3$ is highly sensitive to the

magnitude of the Ti displacements, regardless of whether the displacements are ordered or disordered.

The magnitude of Ti displacements can potentially be tuned *via* external stimuli, such as temperature, strain, or electric field, in a manner of "ferroic" switching between different correlated Ti displacement modes. Therefore, the potential for reversible symmetry breaking by *a*-*b* plane Ti displacements in the $TiS_6$ octahedra in $BaTiS_3$ and related perovskite chalcogenides makes them a good platform to achieve tunable anisotropy, large non-linearity, and coupled phenomena such as opto-elastic and electro-optic effects. The adjustable refractive indices in $BaTiS_3$ can facilitate miniaturized controlled retarders and variable waveplates for polarization manipulation, and electro-optic modulators towards a broad range of mid-infrared photonic applications.

#### 3.3.2.2 $BaTiSe_3$

Similar to $BaTiS_3$, $BaTiSe_3$ possesses similar superstructure and Ti in-plane displacements. Figure 3.36(a) visualizes the resulting supercell-ordering of the antiparallel $TiS_6$ chain displacements, whose $P31c$ unit cell is highlighted (solid line) in comparison with $P6_3/mmc$ (dotted line). $TiSe_6$ chains are colored red (-$\boldsymbol{c}$) and blue (+$\boldsymbol{c}$) corresponding to the direction of chain displacement to the Ba atoms around them along the *c*-axis, illustrated in Figure 3.36(b). On top of the chain displacements,

Ti atoms also displace away from the centroid of $TiSe_6$ octahedra, thus leaving behind antiparallel $TiSe_6$ dipoles along the *c*-axis.

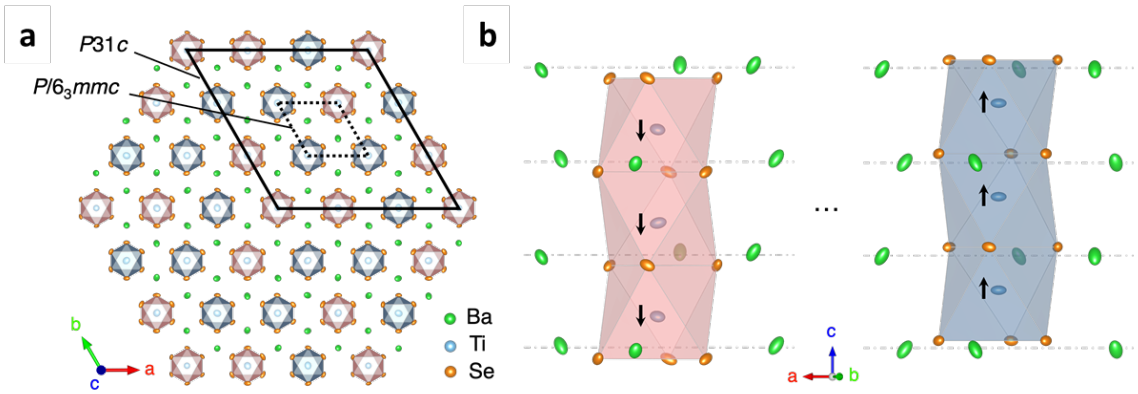


**Figure 3.36: (a)** $BaTiSe_3$ is refined as a *P*31*c* space group in a $2\sqrt{3}\times2\sqrt{3}\times1$ supercell of the *P*6$_3$/*mmc* along the *a*-*b* plane. **(b)** In *P*31*c*, $TiS_6$ chains are displaced along the *c*-axis in opposite directions, colored in red (downwards along the *c*-axis) and blue (upwards along the *c*-axis). Besides, Ti atoms also move away from the centroid of $Se_6$ octahedra along the *c*-axis. This is analogous but of different periodicity compared to $BaTiS_3$[67]. Figure adapted from Ref[69].

Electron density ($f_0$) of rod-shaped $BaTiSe_3$ crystals is extracted during the SC-XRD refinement. We observe anisotropic Ti off-centric electron distribution at all Ti atoms in $BaTiSe_3$. Figure 3.37 illustrates the *a*-*b* plane projection of the $TiSe_6$ chain electron density map of Ti01 and Ti02. We observed the same off-centric electron density distribution in $BaTiS_3$, which is a sign of disordered off-centric *a*-*b* plane Ti displacements. Such disorder is tested by first-principles calculations to give rise to enhanced optical anisotropy, especially the birefringence. The Ti *a*-*b* plane displacements in $BaTiSe_3$ are larger than $BaTiS_3$ and thus more obvious in the

electron density distribution as indicated by the arrows in Figure 3.37. This potentially contributes to the larger birefringence in $BaTiSe_3$.

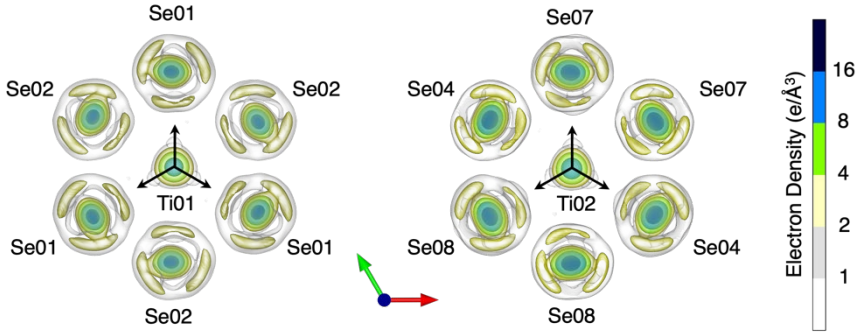


**Figure 3.37:** Electron density map of $BaTiSe_3$ near Ti01 and Ti02 projected along the *a*-*b* plane. The off-centric electron distribution of Ti is an indicator of disordered *a*-*b* plane Ti displacements towards the closest Se atoms. The average *a*-*b* plane off-centric displacements of Ti01 and Ti02 are refined as 0.155 Å and 0.166 Å towards the black arrows. This is larger than the ~ 0.12 Å in $BaTiS_3$[67]. Figure adapted from Ref[69].

Figure 3.38(a) shows the electron band structure of *P*31*c*-$BaTiSe_3$. Contrary to the predicted metal band structure of *P*6$_3$/*mmc*-$BaTiSe_3$ [127], *P*31*c* structure modulations split the conduction band minimum and valence band maximum and predict $BaTiSe_3$ as a semiconductor. The predicted complex refractive index in Figure 3.38(b) also adopts large birefringence and dichroism. This is a consistent trend with the experimental results. However, the sign of the dichroism ($\kappa_o$ - $\kappa_e$) at < 0.5 eV is opposite to the experimental measurement, which gives rise to a mismatch in the birefringence ($n_o$ – $n_e$) in Figure 3.38(c), at < 0.5 eV spectrum range. Such band structure disagreement near the Fermi level is majorly induced by the disordered *a*-*b* plane Ti displacements in $BaTiS_3$. Although the diffuse scattering resulting from

such *a*-*b* plane disorder is similar to $BaTiS_3$, the nature of such disorder in a larger unit cell of the *P*31*c* space group is distinctive and needs to be further resolved.

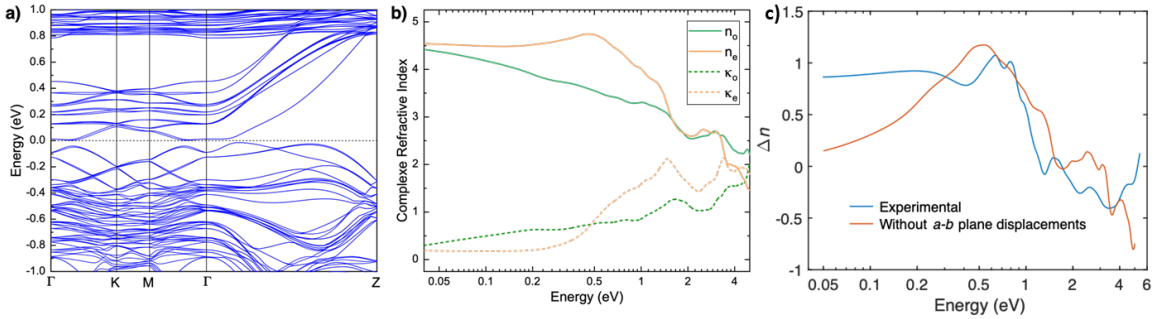


**Figure 3.38:** First principles calculation results on the *P*3*c*1-$BaTiSe_3$. **(a)** Electron band diagram of $BaTiSe_3$. **(b)** Complex refractive index as a function of energy. **(c)** Calculated birefringence of $BaTiSe_3$ in comparison with the experimental data. Figure adapted from Ref[69].

## 3.4 Applications

Materials with exceptional optical anisotropy, such as $Sr_{9/8}TiS_3$, $BaTiS_3$, and $BaTiSe_3$, open up extensive opportunities for the precise and effective manipulation and control of light—key attributes in the realm of advanced optical and photonic technologies. The pronounced birefringence of these materials is pivotal for efficiently creating polarized light, a fundamental requirement in devices like polarizers, wave plates, and other polarization-sensitive instruments. This heightened anisotropy facilitates a more efficient and precise control over the polarization state of light, allowing for the design of more compact and integrated devices. In this section, we explore two innovative applications of these anisotropic materials: an ultrathin waveplate and a narrowband polarized thermal emitter. Both

devices are currently under experimental testing, and the results in this section have not yet been published.

### 3.4.1 Ultrathin waveplate with designs of anti-reflection coating (ARC)

In the realm of materials with optical anisotropy, waveplates are often the first application to consider. We conducted a preliminary experiment featuring light transmission through two crossed polarizers with a 3.2 μm thick $Sr_{9/8}TiS_3$ waveplate positioned between them, as shown in Figure 3.39. As we rotate the sample, light transmission varies dramatically—from nearly 0% to approximately 90%—owing to the polarization rotation induced by the birefringent properties of the material.

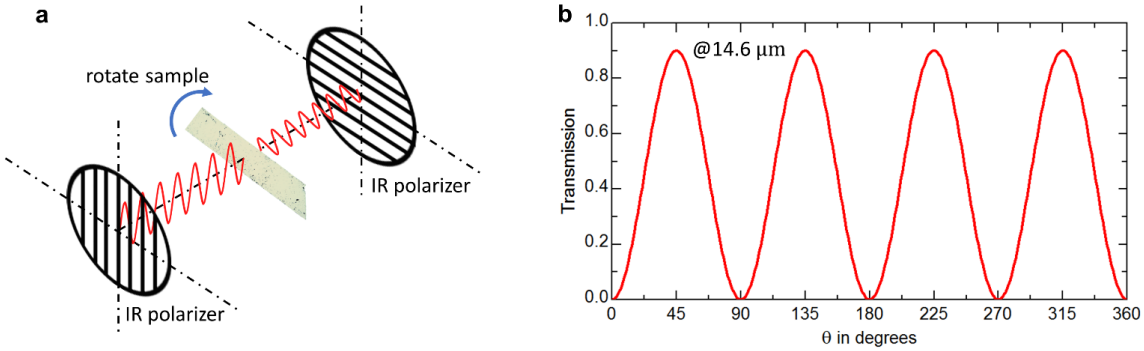


**Figure 3.39: (a)** Schematics of the measurement with two crossed IR polarizers and the $Sr_{9/8}TiS_3$ sample in between. **(b)** Transmission at 14.6 μm as a function of rotation angle of the sample. Figure adapted from Ref[70].

Table 3.7 presents the calculated thicknesses of $BaTiS_3$ and $Sr_{9/8}TiS_3$ required to function as 1/4 or 1/2 waveplates at an operational wavelength of 8 μm. Notably, for a 1/4 waveplate using $Sr_{9/8}TiS_3$, the necessary thickness is less than 1 μm, highlighting its ultrathin characteristic.

**Table 3.7:** Calculation of waveplate parameters based on $BaTiS_3$ and $Sr_{9/8}TiS_3$.

| $\Gamma = \frac{2\pi \cdot \Delta n \cdot d}{\lambda_0}$ | **$BaTiS_3$ $\Delta n = 0.76$ @8 $\mu m$** | **$Sr_{9/8}TiS_3$ $\Delta n = 2.11$ @8 $\mu m$** |
|---|---|---|
| **1/4 waveplate** $\Gamma = \frac{\pi}{2} + 2m\pi$ | $L = \left(m + \frac{1}{4}\right) \cdot \frac{\lambda}{0.76}$ $d_{min} = 2.63\ \mu m$ | $L = \left(m + \frac{1}{4}\right) \cdot \frac{\lambda}{2.11}$ $d_{min} = 0.95\ \mu m$ |
| **1/2 waveplate** $\Gamma = \pi + 2m\pi$ | $L = \left(m + \frac{1}{2}\right) \cdot \frac{\lambda}{0.76}$ $d_{min} = 5.26\ \mu m$ | $L = \left(m + \frac{1}{2}\right) \cdot \frac{\lambda}{2.11}$ $d_{min} = 1.90\ \mu m$ |

However, for practical applications of the waveplate, an anti-reflection coating (ARC) is essential. Reflections from both the top and bottom surfaces can lead to undesirable Fabry-Pérot fringes, as shown in Figure 3.40. Properly designing the ARC can significantly enhance the performance and efficiency of the waveplate. The ultimate goal of ARC design is to minimize reflection and achieve unity transmission. In the following sections, two designs of ARC are proposed.

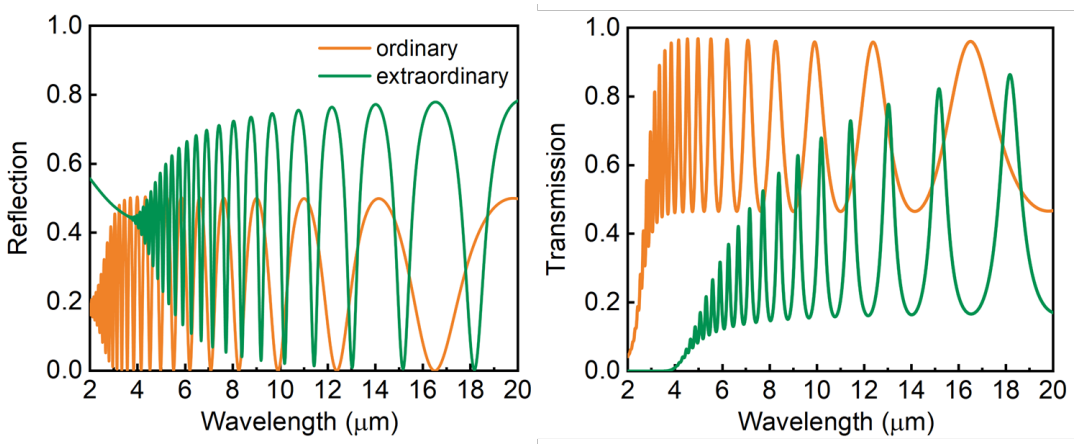


**Figure 3.40:** Calculated reflection and transmission spectra of a 10 μm thick $Sr_{9/8}TiS_3$ waveplate, showing the inevitable Fabry–Pérot fringes due to the top and back reflections.

### 3.4.1.1 Design I: single-layer ridges

The simplest interference anti-reflective coating (ARC) is composed of a single thin layer of transparent material, whose refractive index is the square root of the substrate's refractive index. In air, this configuration theoretically results in zero reflectance for light with a wavelength (within the coating) equal to four times the coating's thickness. This also reduces reflectance for wavelengths across a broad spectrum around this central value. A layer with a thickness equivalent to a quarter of a designated wavelength is referred to as a “quarter-wave layer.” For anisotropic substrates like $Sr_{9/8}TiS_3$, the single layer must meet the "quarter-wave condition" for both the ordinary and extraordinary axes simultaneously, while maintaining a uniform thickness. However, such anisotropic single layer with the desired anisotropic refractive index is not feasible for the design of ARC for these materials $Sr_{9/8}TiS_3$, $BaTiS_3$, and $BaTiSe_3$ with giant birefringence. Instead, one might consider

employing structure-induced anisotropy, such as optical anisotropy created by ridges. According to the effective medium theory (EMT) for ridges, parameters such as the thickness, duty cycle, and refractive index of the ridges can be strategically calculated.

$$\tilde{n}_{\parallel} = [(1-D)\tilde{n}_1^2 + D\tilde{n}_2^2]^{1/2} \quad (3.9)$$

$$\tilde{n}_{\perp} = \frac{\tilde{n}_1 \cdot \tilde{n}_2}{[D\tilde{n}_1^2 + (1-D)\tilde{n}_2^2]^{1/2}} \quad (3.10)$$

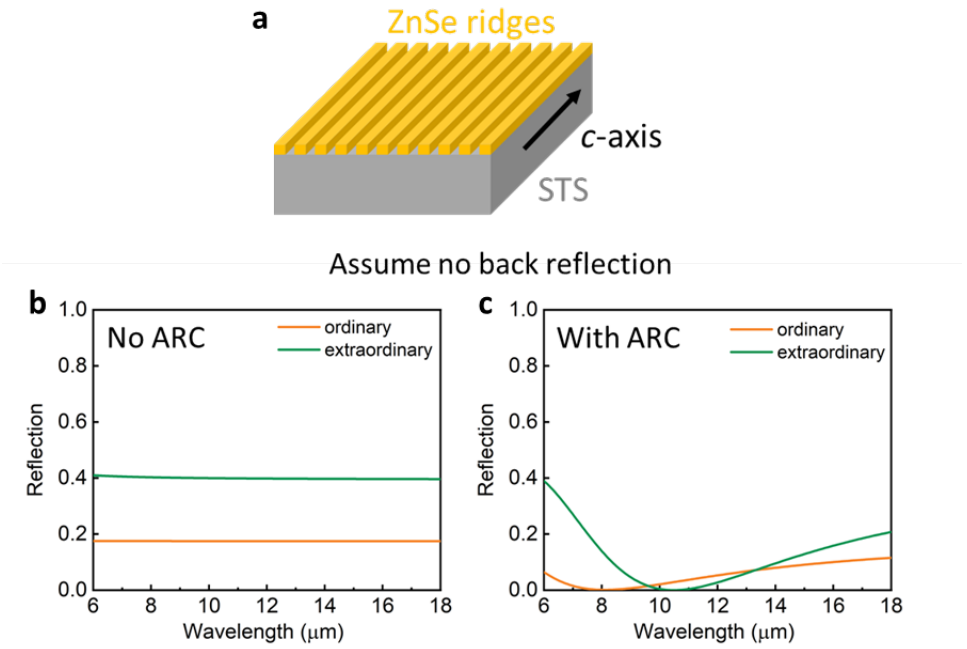


**Figure 3.41: (a)** Schematics of single-layer ZnSe ridges on top of a semi-infinite $Sr_{9/8}TiS_3$ substrate. Thickness, duty cycle and material index are calculated using effective medium theory. **(b, c)** Reflection spectra with and without the ARC in **(a)** for both ordinary and extraordinary directions.

According to calculations using EMT, a combination of air and zinc selenide (ZnSe, $n$~2.4) with a duty cycle of $D = 0.714$ and a thickness of 1.35 μm effectively

suppresses reflections from an $Sr_{9/8}TiS_3$ substrate around the 10 μm wavelength, as illustrated in Figure 3.41(a). Figures 3.41(b) and 3.41(c) display the reflection spectra for both ordinary and extraordinary axes with and without the anti-reflection coating composed of ZnSe ridges. These graphs demonstrate the ARC's impressive performance across both axes.

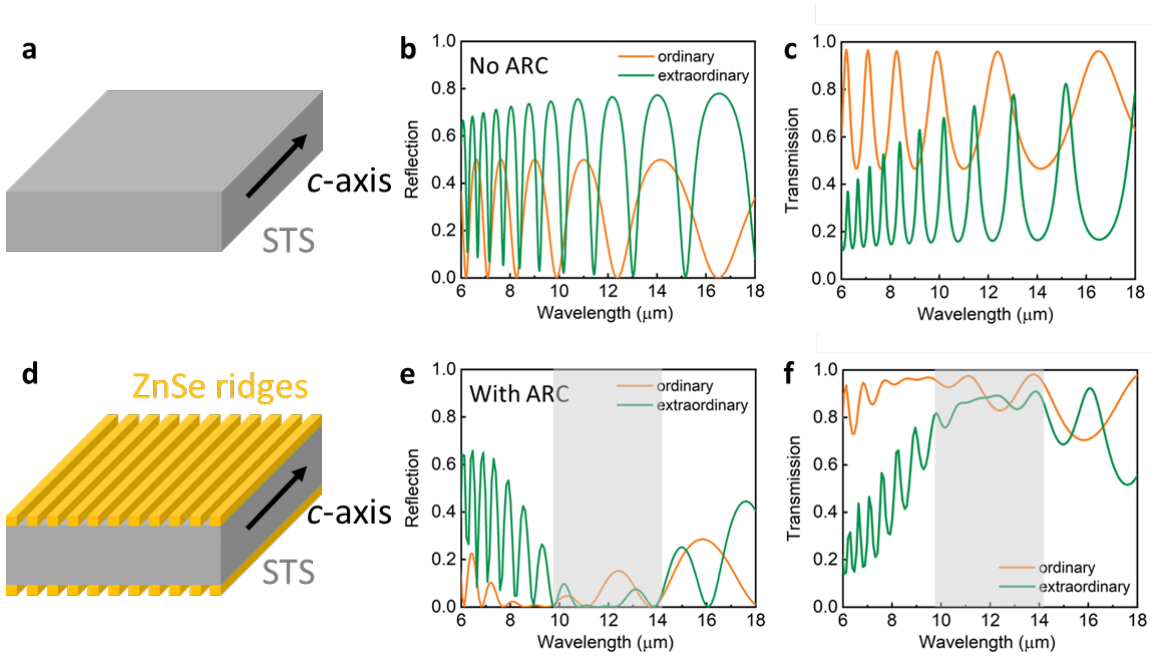


**Figure 3.42:** Considering back reflection with a finite thickness of the anisotropic material $Sr_{9/8}TiS_3$. Reflection **(b, e)** and transmission **(c, f)** spectra with and without the ARC.

Figure 3.42 displays the reflection and transmission spectra for a 10 μm thick $Sr_{9/8}TiS_3$ waveplate with and without the ARC made from ZnSe ridges. It is evident that the ARC effectively suppresses Fabry–Pérot fringes and nearly achieves unity transmission for both the ordinary and extraordinary axes, thanks to the ZnSe ridges applied to both the top and bottom surfaces.

#### 3.4.1.2 Design II: double-layer planar thin films

In this section, we propose another design for anti-reflection coatings tailored for anisotropic materials like $Sr_{9/8}TiS_3$, utilizing double-layer planar thin films. Based on our calculations, we selected $YF_3$ ($n$~1.36) and ZnS ($n$~2.3) as the low-index and high-index materials, respectively. Although $YF_3$ ($n$~1.36) combined with ZnSe ($n$~2.4) is also a viable option, we opted for ZnS due to the greater availability of deposition tools.

Our design incorporates a 1.74 μm thick layer of $YF_3$ and a 0.98 μm thick layer of ZnS, achieving effective reflection suppression for both the ordinary and extraordinary axes of $Sr_{9/8}TiS_3$, as depicted in Figures 3.43(b) and 3.43(c). Additionally, we assessed the reflectance at oblique angles of incidence beyond the normal, as illustrated in Figures 3.43(d) and 3.43(e). We found that this double-layer planar thin film configuration offers robust performance against varying angles of incidence.

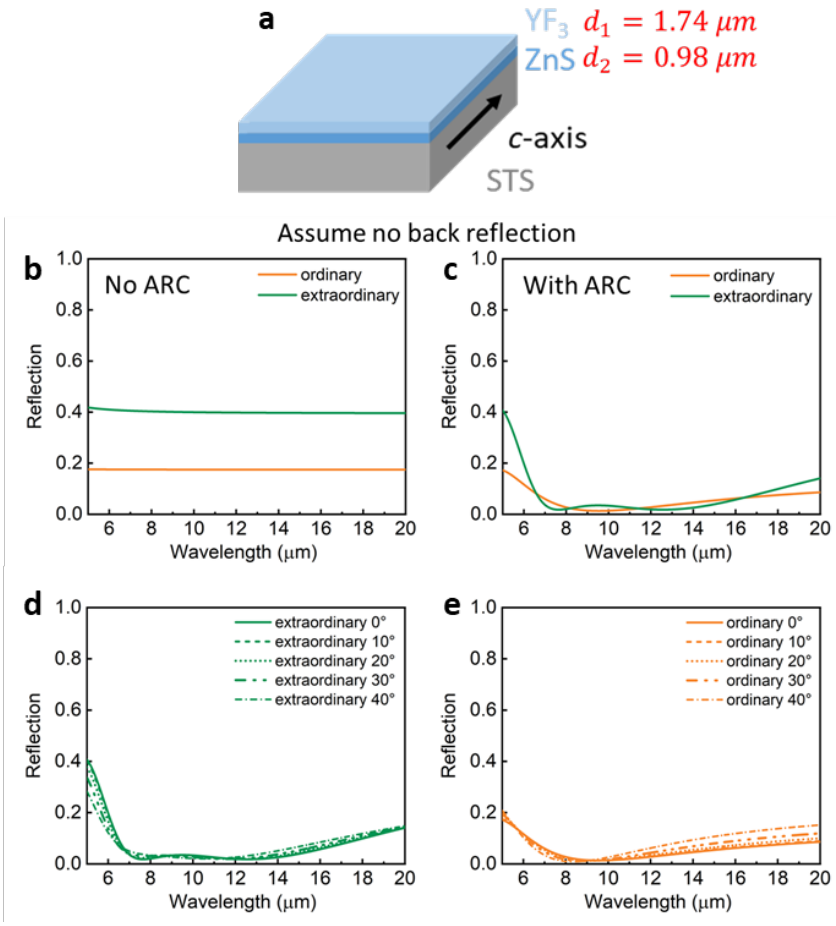


**Figure 3.43: (a)** Schematics of double-layer ARC consisting of planar $YF_3$ and ZnS thin films. **(b, c)** Reflection spectra with and without the ARC in **(a)**. **(d, e)** Angle dependence.

Figure 3.44 illustrates the reflection and transmission spectra for a 10 μm thick $Sr_{9/8}TiS_3$ waveplate, both with and without an ARC composed of $YF_3$/ZnS double-layer planar thin films. The ARC significantly reduces the Fabry–Pérot fringes and achieves near-perfect transmission for both the ordinary and extraordinary axes by applying the ARC to both top and bottom surfaces. Figures 3.45 display the reflectance and transmittance of this 10 μm thick $Sr_{9/8}TiS_3$ waveplate with double-

layer planar thin film configuration in Figure 3.44(d) under oblique angles of incidence, showing excellent robust performance against varying angles of incidence.

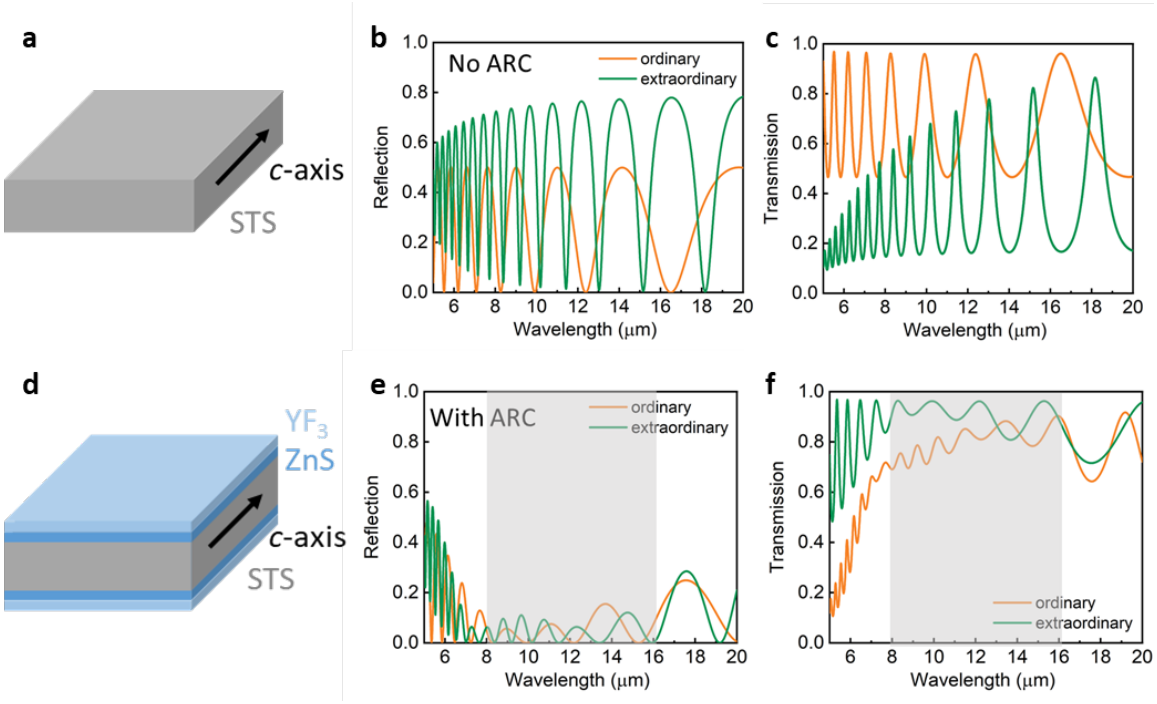


**Figure 3.44:** Considering back reflection with a finite thickness of the anisotropic material $Sr_{9/8}TiS_3$. Reflection **(b, e)** and transmission **(c, f)** spectra with and without the ARC.

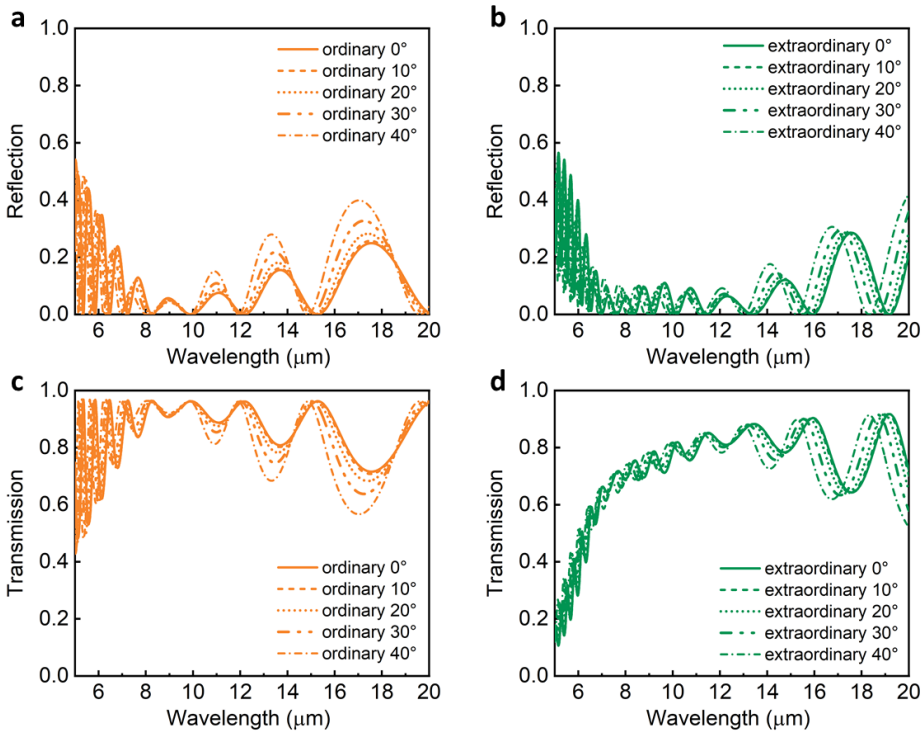


**Figure 3.45:** Angle dependence of the double-layer ARC (ZnS and $YF_3$) as shown in **Figure 3.44(d)**.

## 3.4.2 Planar polarized narrowband thermal emitters

The capacity to manipulate, control and engineering the spectrum, direction, and polarization of thermal emission plays a pivotal role in a variety of applications. These include infrared sources, which are essential for night vision and thermal imaging[14,17]; thermal camouflage[29,30], which can mask heat signatures from detection; radiative cooling[28], where excess heat is dissipated without energy consumption; and energy conversion systems, like those converting heat to electricity[39,40,128]. Notably, the generation of spectrally narrowband IR emission has garnered extensive attention in

the literature, underscoring its importance in enhancing the efficiency and specificity of these technologies.

While many designs rely on in-plane patterning and the use of multiple layers to achieve reduced emission bandwidth[129], here we propose to use these birefringent materials with the inherently giant anisotropy in a simple Salisbury screen configuration[130,131], which involves a three-layer structure consisting of an emitter, a dielectric spacer, and a back reflector, creates a Fabry–Pérot cavity. With careful design of the resonance wavelength of this cavity, strong narrowband emission is achievable. We also demonstrate an even simpler structure with only two layers, a birefringent material and a metal back reflector, that can achieve relatively narrowband emission with large degree of polarization.

This approach offers several advantages. Planar structures like these are generally easier and more cost-effective to manufacture compared to architectures requiring complex three-dimensional patterning or a multitude of layers. They also tend to be more scalable and compatible with existing manufacturing processes. Additionally, the planar configuration maximizes the use of material properties and facilitates integration with other electronic and photonic components, making it a versatile choice for a wide range of applications.

### 3.4.2.1 Design I: anisotropic material as the emitter

Here, we present a streamlined design for a planar polarized thermal emitter that incorporates a metal back reflector on $Sr_{9/8}TiS_3$, as depicted in Figure 3.46(a). In this configuration, $Sr_{9/8}TiS_3$ serves as the emitter. By adjusting the thickness of $Sr_{9/8}TiS_3$, we can precisely control the central emission wavelength and modulate the bandwidth, as shown in Figure 3.46(b). The results, illustrated in Figures 3.46(c-e), demonstrate a high degree of polarization (>0.9), indicating a significant contrast between the two polarizations. Figure 3.47 shows the emissivity of a 0.47 μm thick $Sr_{9/8}TiS_3$ with a metal back reflector, as observed in Fig. 3.46(d), across various angles of incidence, revealing that the $p$-polarized emissivity remains robust over a wide range of angles. Additionally, Figure 3.48 displays the 3D emission profile of a 0.47 μm thick $Sr_{9/8}TiS_3$ with a metal back reflector, as in Fig. 3.46(d), at a wavelength of 3.5 μm, showcasing its directionality and the marked contrast between different polarizations.

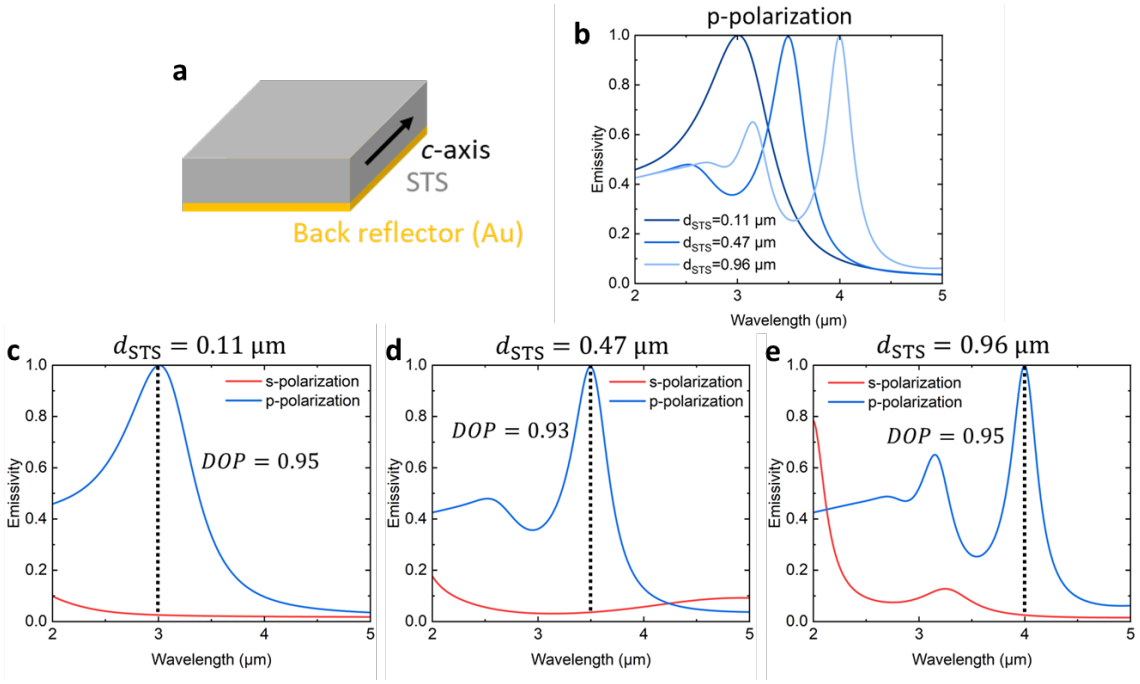


**Figure 3.46: (a)** Schematics of a simple emitter design with a $Sr_{9/8}TiS_3$ and a metal back reflector. **(b)** Calculated $p$-polarized emissivity with varying thicknesses of $Sr_{9/8}TiS_3$, showing tunable central emission wavelength. **(c-e)** $p$- and $s$-polarized emissivity with varying thicknesses of $Sr_{9/8}TiS_3$, showing large degree of polarization.

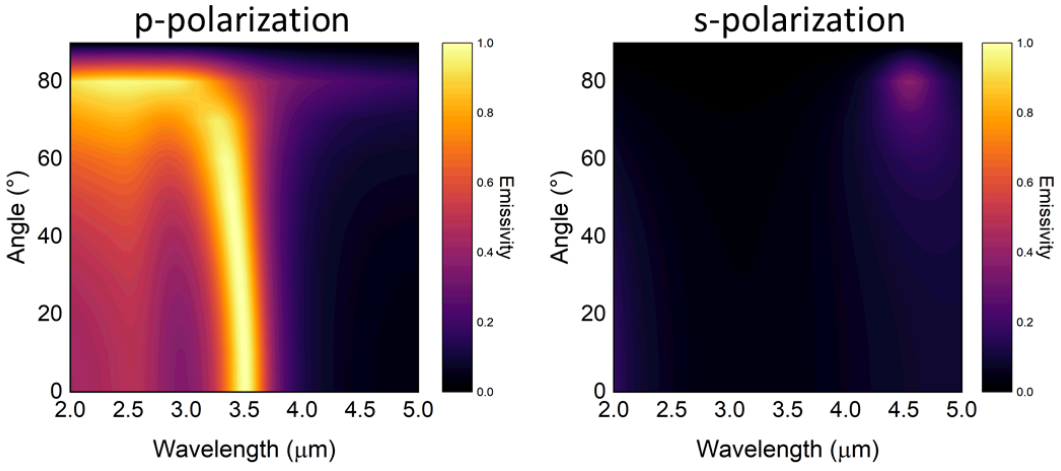


**Figure 3.47:** Calculated $p$- and $s$-polarized emissivity of a 0.47 μm thick $Sr_{9/8}TiS_3$ with a metal back reflector in **Figure 3.46(d)** with varying angles of incidence. $p$-polarized emissivity is robust within a broad angle range.

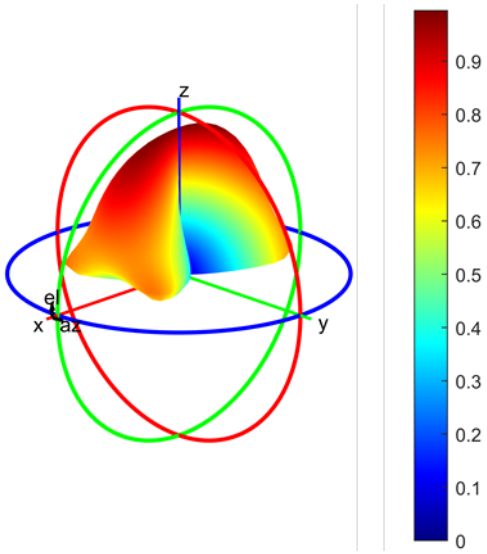


**Figure 3.48:** 3D emission profile of a 0.47 μm thick $Sr_{9/8}TiS_3$ with a metal back reflector in **Figure 3.46(d)** at wavelength of 3.5 μm, showing directional and polarized emission.

### 3.4.2.2 Design II: anisotropic material as the spacer

In this section, we utilize the Salisbury screen configuration [130,131] to develop a narrowband polarized emitter, consisting of an emitter, $Sr_{9/8}TiS_3$ as an anisotropic spacer, and a metal back reflector. Leveraging the strong surface phonon polaritons (SPhPs) inherent to SiC[129], known for their naturally narrowband resonances due to a high material quality factor, we have integrated a thin SiC layer acting as an emitter atop the $Sr_{9/8}TiS_3$ and the metal back reflector, as depicted in Figure 3.49(a). The results, shown in Figures 3.49(b-d), highlight narrowband emission with a high quality factor ($Q$~200) in $s$-polarization, and a substantial degree of polarization (>0.9), revealing a stark contrast between two different polarizations. Figure 3.50 illustrates the emissivity of a configuration comprising a 50 nm thick SiC and a 2.8 μm thick $Sr_{9/8}TiS_3$ with a metal back reflector, as seen in Figure 3.49(c), across various

angles of incidence, demonstrating that $s$-polarized emissivity remains robust over a wide angle range. Furthermore, Figure 3.51 shows the 3D emission profile and a slice under normal incidence for the same structures at a wavelength of 12.5 μm, showcasing the directionality and pronounced contrast between the two polarizations.

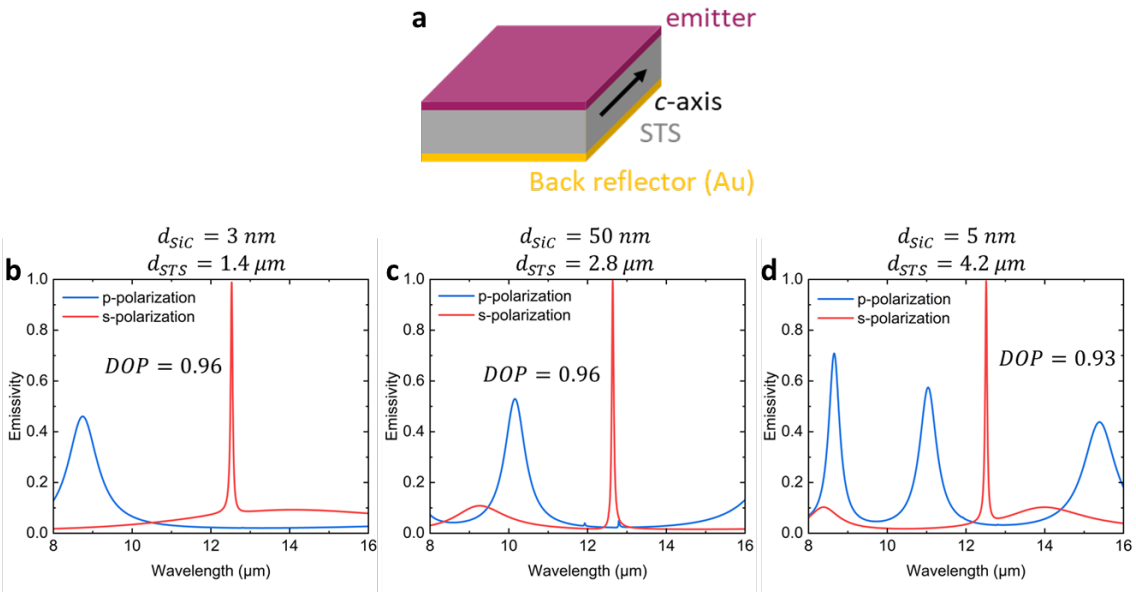


**Figure 3.49: (a)** Schematics of an emitter design based on Salisbury screen configuration, with SiC as an emitter, $Sr_{9/8}TiS_3$ as an anisotropic spacer, and a metal back reflector. **(b-d)** Calculated $p$- and $s$-polarized emissivity with varying thicknesses of SiC and $Sr_{9/8}TiS_3$, showing narrow bandwidth and large degree of polarization.

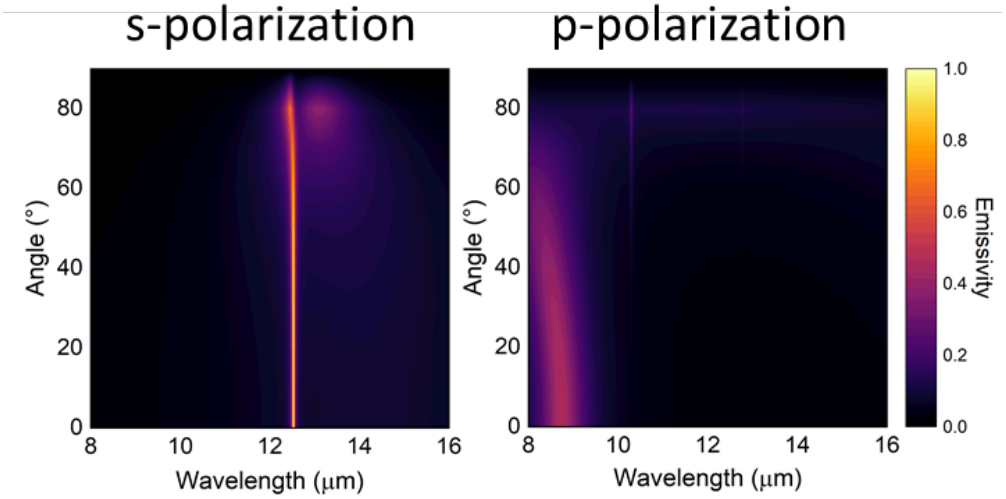


**Figure 3.50:** Calculated *s*- and *p*-polarized emissivity of a 50 nm thick SiC and a 2.8 μm thick $Sr_{9/8}TiS_3$ with a metal back reflector in **Figure 3.49(c)** with varying angles of incidence. *s*-polarized emissivity is robust within a broad angle range.

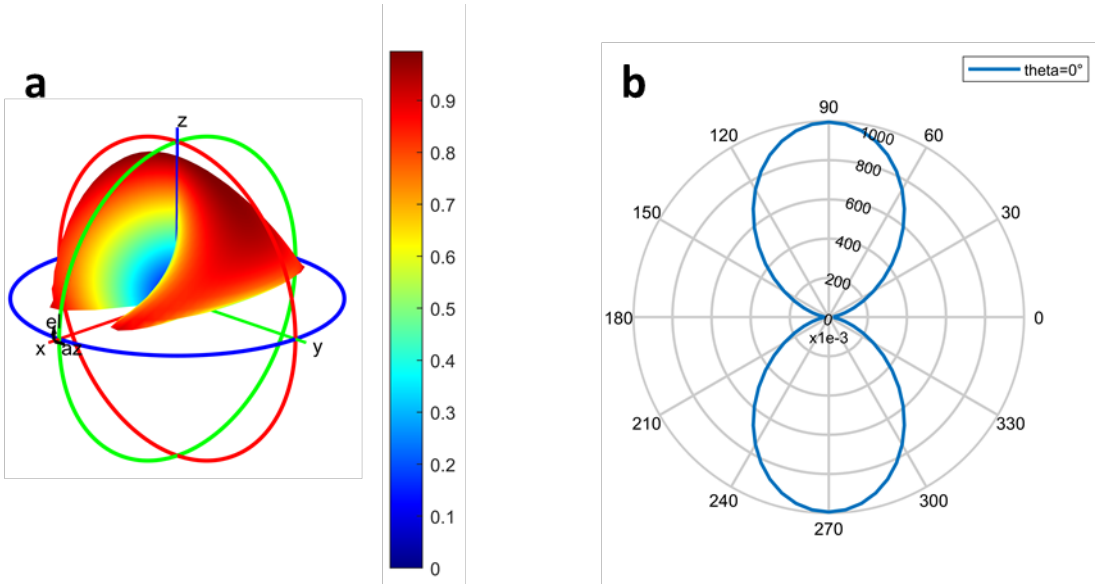


**Figure 3.51: (a)** 3D emission profile of a 50 nm thick SiC and a 2.8 μm thick $Sr_{9/8}TiS_3$ with a metal back reflector in **Figure 3.49(c)** at wavelength of 12.5 μm, showing directional and polarized emission. **(b)** Slice of emission profile at normal incidence $\theta = 0°$.

# Chapter 4

# Local modulation of material properties using FIB

The work presented in this chapter was in collaboration with Prof. Carsten Ronning's group at Friedrich Schiller University Jena in Germany, and Prof. Shriram Ramanathan at Purdue University (now at Rutgers University). Figures and text in this section are adapted from our publication in *Nanophotonics*[132] and *Advanced Photonics Research*[133].

## 4.1 Introduction

Modulating material properties, particularly the refractive index, is crucial for advancing technologies in optics, photonics, electronics, and telecommunications. Tailoring the refractive index enables the development of specialized tunable optical components for imaging, waveguiding, and filtering, which are essential for applications ranging from simple optical devices to complex photonic systems.

Conventional methods for spatial modulation of material properties, like control of doping or defect density, typically involve using high-voltage ion accelerators with lithographically defined masks, requiring complex cleanroom fabrication processes. These methods often struggle with applying varied levels of modulation across different regions due to the intricate alignment needed for multiple lithographic patterns. Thus, a straightforward direct writing technique emerges as a more effective solution, simplifying the process and enhancing precision in modifying material properties.

Focused ion beam (FIB) is a well-established technique for high-resolution area-selective milling, deposition, and imaging [134–138]. For example, FIB-assisted deposition and milling has been broadly used for applications such as TEM specimen preparation [139], fabrication of electronic and photonic nanostructures [138,140–142], failure analysis [143], and mask repair [144]. Compared to photolithography and e-beam lithography, FIB is a resist-free technique that enables direct etching or deposition of materials with lateral resolution comparable to e-beam lithography (i.e., on the scale of 10 – 100 nm). In this study, we advance the use of a commercial FIB system to locally modulate the optical properties via doping or defect engineering.

Here, we extend the use of the FIB to (a) modify the carrier concentration of zinc oxide (ZnO), a wide-bandgap semiconducting oxide, by area-selective doping, and (b) defect-engineer vanadium dioxide ($VO_2$), a prototypical insulator-to-metal transition (IMT) material. The ability to tune the carrier density and phase change behavior via

focused ion beam irradiation can enable local patterning of function in nanostructures with high resolution.

## 4.2 Tunable carrier concentration in FIB-doped ZnO

The carrier concentration in most semiconductors can be tuned by orders of magnitude via *in-situ* or *ex-situ* doping processes, resulting in plasma wavelengths from near infrared to far infrared [145–149]. Doping can be performed *in-situ* (i.e., during material growth) by tailoring the conditions to introduce dopants during growth processes such as sputtering [150], laser ablation [151], evaporation [152], chemical-vapor deposition [153], etc. In contrast, in *ex-situ* doping techniques, dopants are introduced after material growth, for example via diffusion doping [154,155], or ion implantation [156]. One advantage of ion implantation is that dopants can be introduced area-selectively, such as by implantation through lithographically defined masks, enabling designer structures, e.g., with plasmonic resonances. For example, our group has used this technique to locally tune the optical properties of silicon to realize all-silicon monolithic Fresnel zone plates and frequency-selective surfaces in the mid and far infrared [145]. In this section, we replace the conventional process of lithography and ion implantation with a FIB-based doping process, realizing mask-free area-selective doping.

We chose zinc oxide (ZnO) as the host material for FIB irradiation. Intrinsic ZnO is transparent from the visible to the mid infrared, and can also be *n*-type doped using

gallium (Ga) [149], which is a common ion source in commercial FIB systems. Ga-doped ZnO has been demonstrated as a promising plasmonic material for infrared nanophotonics such as subwavelength waveguides [128,157,158], light-emitting diodes [159,160], and optical metasurfaces [161–163].

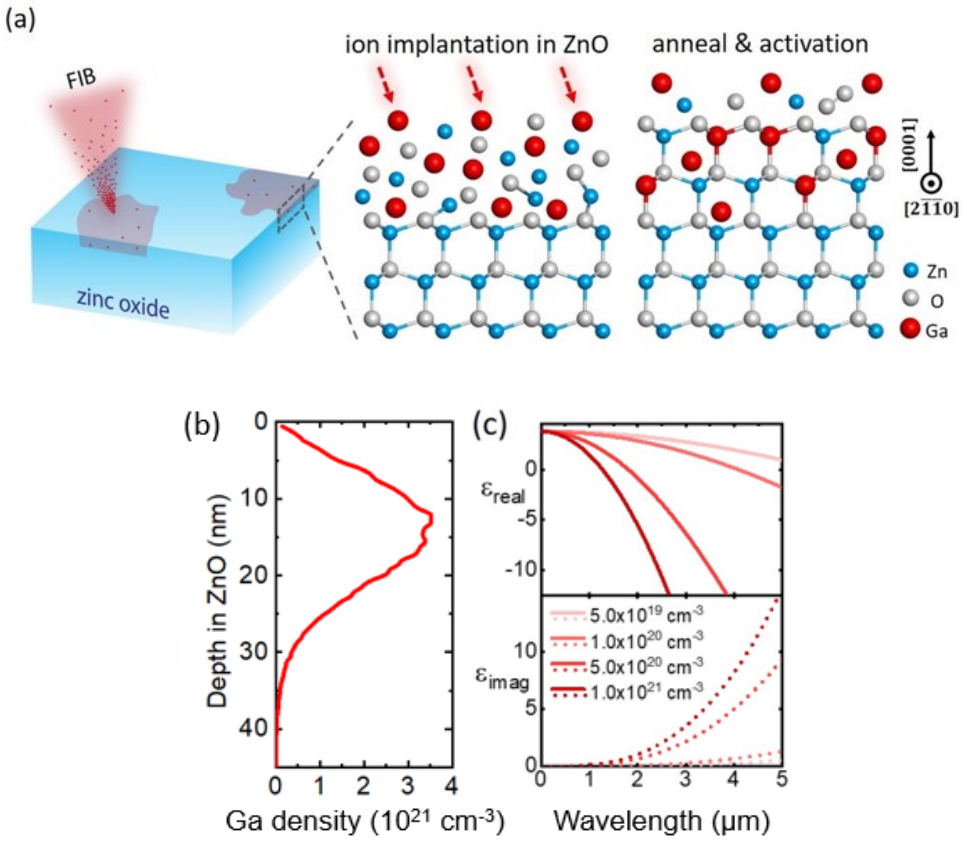


**Figure 4.1: (a)** Schematic of FIB-assisted doping process: The surface of a single-crystalline ZnO substrate can be doped using a FIB implantation and subsequent high-temperature annealing for activation. **(b)** Depth profile of 30-keV Ga ions impinging into crystalline ZnO, simulated using TRIM. **(c)** Calculated real and imaginary parts of the complex permittivity of Ga-doped ZnO with varying carrier concentrations. Adapted from Ref[132].

The schematic of our FIB-assisted doping process is shown in Fig. 4.1(a): the ZnO wafer is bombarded by a 30-keV focused Ga ion beam, resulting in the implantation of Ga atoms into the top ~30 nm of the ZnO lattice, but also resulting in lattice damage. A subsequent high-temperature annealing process is necessary for healing the damaged lattice and activating the dopants. As a result, an *n*-type Ga-doped ZnO layer is formed. The penetration depth profile of Ga ions into ZnO [Fig. 4.1(b)] was estimated using the Monte Carlo code, Transport of Ions in Matter (TRIM) [164], and verified in our samples using X-ray photoelectron spectroscopy depth profiling and Auger electron spectroscopy.

The XPS survey scan of the as-implanted Ga:ZnO surface is shown in Fig. 4.2, in which peaks of Zn, O, C and Ga were detected. The spectrum shows nontrivial surface contamination with C and O due to the long exposure in air.

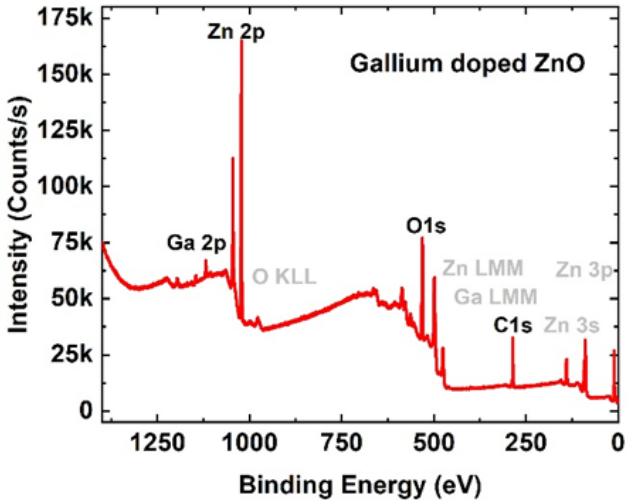


**Figure 4.2:** XPS survey scan of as-implanted Ga:ZnO sample surface with binding energies for several peaks. Adapted from Ref[132].

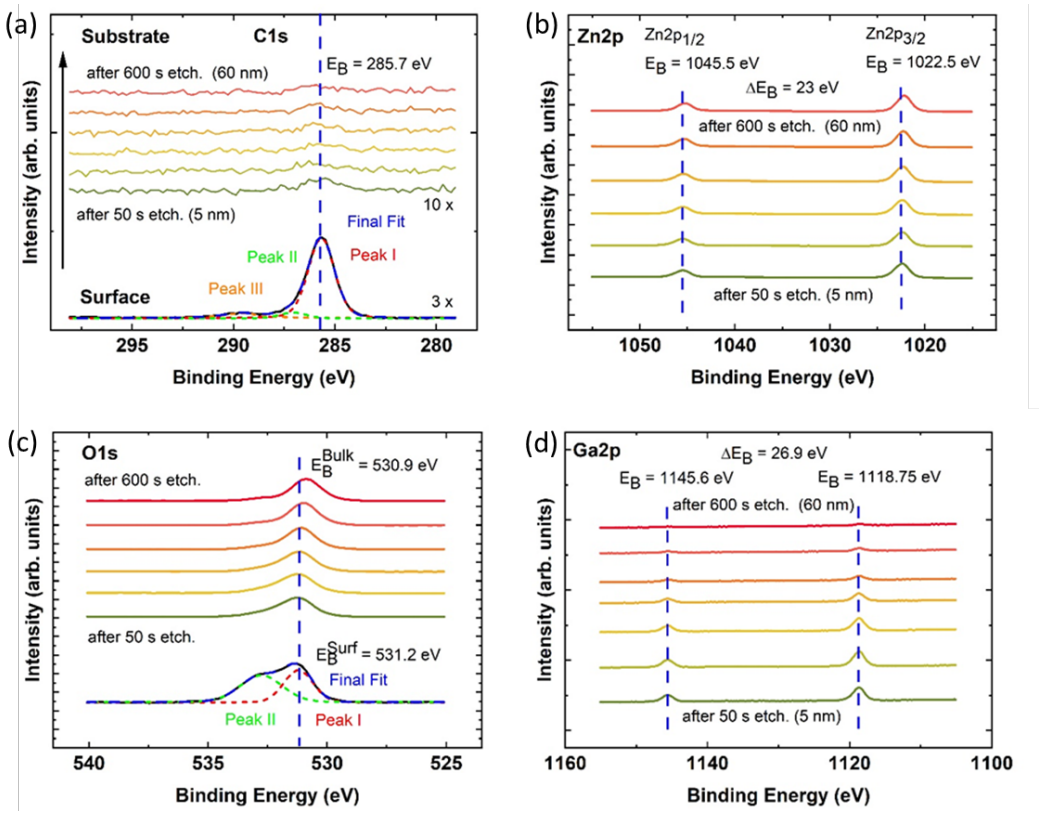


**Figure 4.3: (a)** Surface and depth profile of C1s spectra of the as-implanted Ga:ZnO sample. The depth profile (green-to-red lines) is a series of highly resolved XPS spectra measured in a sequence of 100-second etchings. For a better view the C1s spectra are scaled up. **(b)** Depth profile of Zn2p spectra of the unannealed Ga:ZnO substrate. **(c)** Surface and depth profile of O1s spectra for the as-implanted Ga:ZnO. **(d)** Depth profile of Ga2p spectra of the as-implanted Ga:ZnO. Adapted from Ref[132].

Fig. 4.4 plots the concentration of Ga as a function of depth for the as-implanted Ga:ZnO and the samples annealed at 900 °C and 1000 °C. In general, the Ga concentration in the annealed samples were found to be lower than that of the as-implanted sample, indicating the thermal diffusion of Ga from the surface into the bulk ZnO during the annealing process. Furthermore, such diffusion is highly

dependent on the annealing temperature, as we found that the Ga concentration left at the surface region in the sample annealed at 1000 °C (blue curve) is much less than that of the sample annealed at 900 °C (red curve). We also observed several subpeaks of Ga concentration in the annealed samples (two in the red curves and one in the blue curve), indicating a re-accumulation process of Ga that is also depending on annealing conditions (i.e., temperature and time). Though the dynamic of such re-accumulation has not been fully understood, we believe it can be avoided by a more-sufficient annealing treatment (i.e., annealing with either sufficiently high temperature or sufficiently long time).

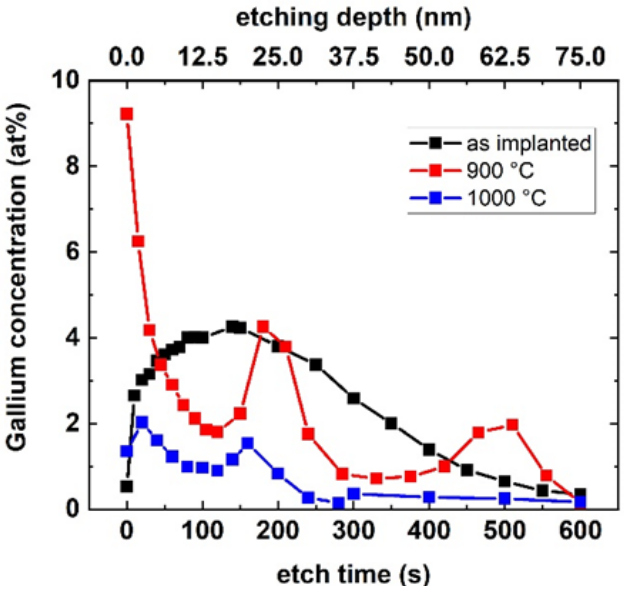


**Figure 4.4:** Depth profiles of Ga concentration for the as-implanted Ga:ZnO and Ga:ZnO samples annealed at 900 °C and 1000 °C for 40 minutes. Adapted from Ref[132].

We also performed Auger Electron Spectroscopy (AES) measurements (Varian Inc.) on the same as-implanted Ga:ZnO to confirm the depth profile of the Ga concentration,

by comparing the results to those of the TRIM simulation and the XPS measurements. The depth profiling was done via a stepwise etching process using krypton (Kr). The total etching process resulted in a removal of 68-nm material. The etching rate was 0.12 nm/s with the step size of 30 seconds.

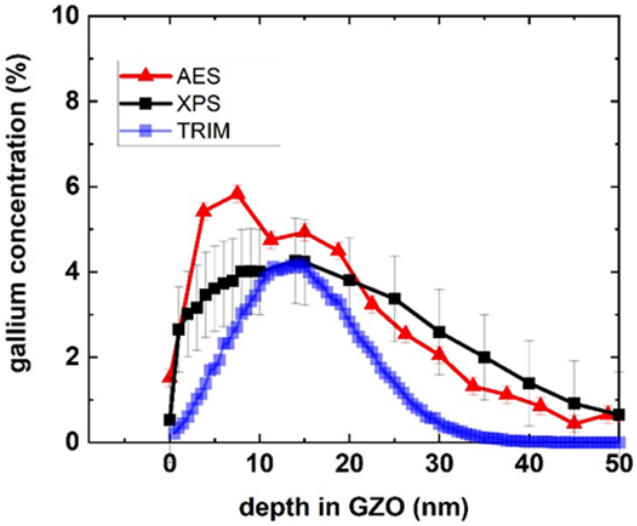


**Figure 4.5:** Comparison between AES, XPS, and TRIM results of the depth profiling of Ga concentration in the as-implanted Ga:ZnO sample that was implanted by 30-keV Ga ions with a fluence of $6\times10^{15}$ $cm^{-2}$. Adapted from Ref[132].

Comparison among the results of AES, XPS, and TRIM simulation is summarized in Fig. 4.5. TRIM simulation predicts a Gaussian-like depth profile of the Ga distribution with the peak concentration, $c_{Ga}$, of ~5.2 at.%, which matches well with that of the XPS measurements. The measured depth profiles by XPS or AES featured broader Ga distribution ranges than that of the TRIM simulation which is probably due to slight thermal diffusion of Ga caused by the generated heat during the implantation.

We estimated the total amount of implanted Ga by calculating area under the concentration curves. For the TRIM simulation, the total implanted Ga concentration, $c_{Ga,}$ is $6 \times 10^{22}$ cm$^{-3}$. For the experiments, we got $c_{Ga}$ of $1.23 \times 10^{23}$ cm$^{-3}$ from AES results and $1.18 \times 10^{23}$ cm$^{-3}$ from XPS results, which agree well with each other.

The optical properties of metals and metal-like materials can often be approximated using the Drude model [165]. For Ga-doped ZnO, we anticipate that the Drude model should work well in the near-to-mid infrared, with the exception of wavelengths ~20-25 μm, where there is a strong vibrational resonance [166]. In the Drude model, the complex permittivity ($\tilde{\varepsilon}$) is given by

$$\tilde{\varepsilon}(\omega) = \varepsilon_{real} + i\varepsilon_{imag} = \varepsilon_{\infty}\left(1 - \frac{\omega_p^2}{\omega^2 + i\frac{\omega}{\tau}}\right) \quad (4.1)$$

$$\omega_p^2 = \frac{n_e q^2}{m^* \varepsilon_0 \varepsilon_{\infty}}, \quad \lambda_p = \frac{2\pi c}{\omega_p}, \quad \mu = \frac{\tau q}{m^*} \quad (4.2)$$

where $\varepsilon_{\infty}$ is the high-frequency permittivity, $\omega_p$ is the screened plasma frequency, which also corresponds to a plasma wavelength ($\lambda_p$), $n_e$ is the carrier concentration and $\mu$ is the carrier mobility determined by the scattering rate ($\tau$), the effective mass of the free carriers ($m^*$), and the unit charge ($q$). The plasma wavelength is the wavelength at which the real part of the permittivity approaches zero, resulting in metal-like behavior at longer wavelengths. As shown in Fig. 4.1(c), we used the Drude model [Eqs. (4.1) and (4.2)] to calculate the complex permittivity ($\tilde{\varepsilon}$) of the Ga-doped ZnO for carrier concentrations from $5 \times 10^{19}$ to $1 \times 10^{21}$ cm$^{-3}$, in which the plasma

wavelength is blue-shifted toward the near infrared as the carrier concentration increases as shown in Fig. 4.1(c).

We irradiated several single-crystalline (0001) ZnO substrates ( $10 \times 10$ $mm^2$, CrysTec GmbH) with 30-keV Ga ions at room temperature using a commercial FIB system (FEI 600i nanoLab). On each sample, five 200-by-200-μm areas were homogenously implanted with ion fluences of $3.6\times10^{14}$, $6\times10^{14}$, $1.2\times10^{15}$, $3.6\times10^{15}$, and $6\times10^{15}$ $cm^{-2}$ (corresponding to Ga peak concentrations of 0.31, 0.52, 1, 3.1, and 5.2 at.%, respectively), which are close to and above the solid solubility limit of Ga in ZnO [167–169]. Note that we irradiated 200-by-200-μm areas to enable far-field optical characterization; in principle, nanometer-scale (10 – 100 nm) lateral resolution can be achieved for the implantation process in a commercial FIB system if diffusion can be avoided. To heal the damaged lattice and activate the Ga dopants, we then performed 40-minute thermal annealing treatments in air of the irradiated samples. Each sample was annealed at a different temperature ranging from 600 to 1000 °C, respectively.

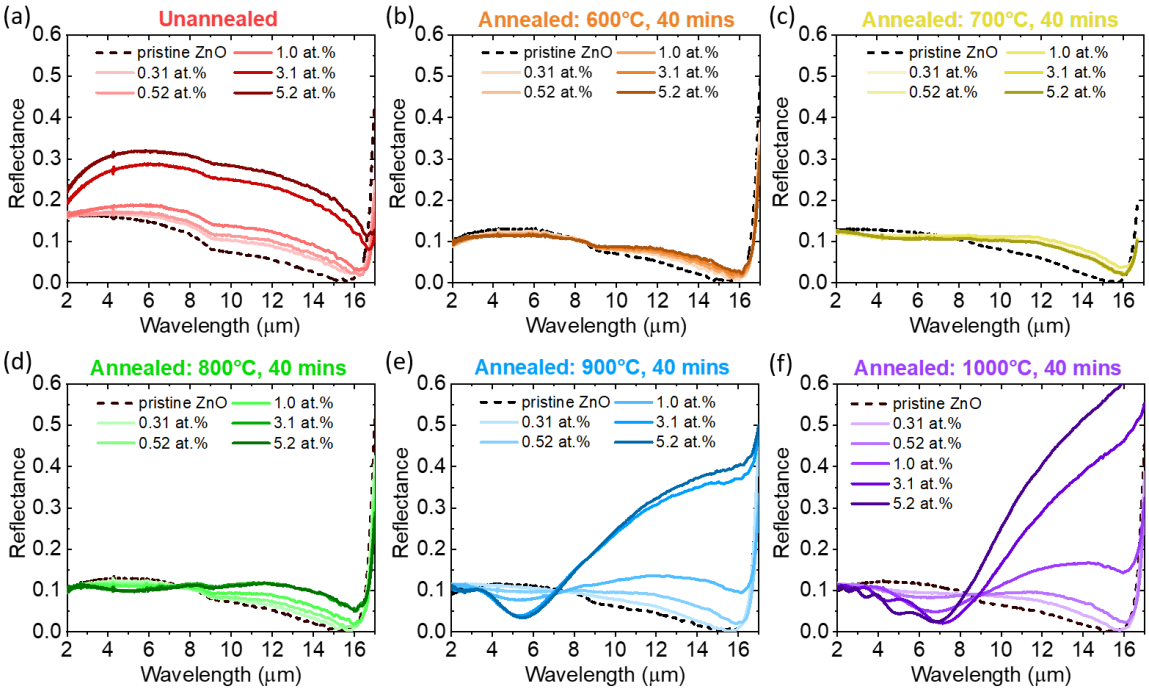


**Figure 4.6:** Measured near-normal-incidence reflectance for undoped ZnO, and areas irradiated with different ion fluences followed by **(a)** no annealing treatment, **(b-f)** annealing in air for 40 minutes at temperatures of 600, 700, 800, 900, and 1000 °C, respectively. Adapted from Ref[132].

To study the changes in optical properties caused by various doping concentrations and annealing treatments at different temperatures, we performed reflectance measurements on each of these FIB-ZnO regions using a Fourier-transform infrared (FTIR) spectrometer (Bruker Vertex 70) outfitted with an infrared microscope (Hyperion 2000). For the unannealed Ga:ZnO samples [Fig. 4.6(a)], we observed increasing reflectance with respect to increasing Ga ion fluence, which we attribute to the partial activation of Ga dopants even without an annealing treatment. Our assumption is supported by a comparison with ZnO substrates that were implanted with Kr ions.

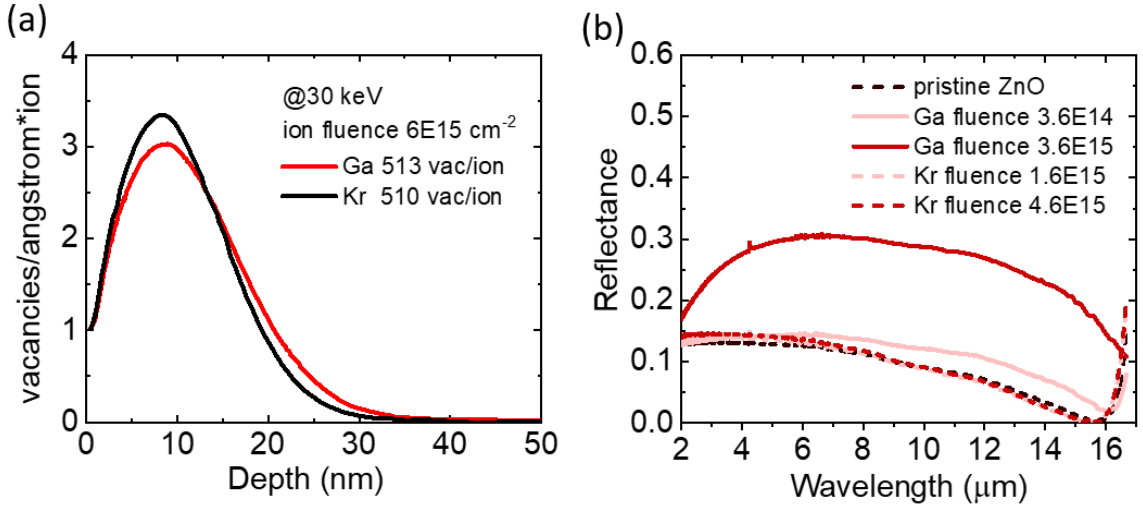


**Figure 4.7: (a)** TRIM-calculated vacancy distribution of Ga and Kr implantation at 30 keV, both with an ion fluence of $6 \times 10^{15}$ $cm^{-2}$. **(b)** Reflectance of Kr-implanted single-crystalline ZnO and Ga-implanted single-crystalline ZnO, both without annealing. Adapted from Ref[132].

Figure 4.7(b) presents the FTIR reflectance of ZnO implanted with Kr and Ga ions using similar implantation conditions. The reflectance of the Kr-implanted ZnO is close to that of the pristine ZnO, indicating that any implantation-induced defects do not affect the optical properties. In contrast, the reflectance of ZnO significantly increased after the Ga implantation, which we attributed to some Ga dopant activation even without annealing, resulting in a thin layer of highly doped Ga:ZnO.

As observed in Fig. 4.6, the increase of the reflectance versus doping concentration at longer wavelengths (> 8 μm) is as expected due to the activation of dopants. The reduction of the reflectance at shorter wavelengths is likely due to the diffusion of Ga during the annealing treatments which can result in μm-thick doped layers, causing Fabry–Pérot (F-P) fringes at shorter wavelengths (< 8 μm) [Fig. 4.6(d-f)].

To quantitatively extract physical properties such as carrier concentration and mobility, we performed spectroscopic ellipsometry analysis, which requires centimeter-scale irradiation areas. Therefore, we prepared another set of ZnO substrates irradiated by comparable ion fluences and identical ion energy of 30 keV using an ion implanter, enabling us to homogeneously implant an entire 1-by-1-cm ZnO substrate. Then, we performed spectroscopic ellipsometry (IR-VASE Mark II, J. A. Woollam Co.) measurements for wavelengths from 2 to 20 μm and built a model using ellipsometry analysis software (WVASE, J. A. Woollam Co.) to fit the data.

Infrared ellipsometry measurements on Ga:ZnO samples were performed for incident angles of 50°, 60°, and 70°. First, we characterized optical properties of the pristine ZnO substrate using a series of Gaussian oscillators (Table 4.1 and Fig. 4.8) expressed as:

$$\varepsilon_{Gaus} = \varepsilon_1 + i\varepsilon_2 \qquad (4.3)$$

$$\varepsilon_2 = A_n e^{\left(\frac{E-E_n}{\sigma}\right)^2} - A_n e^{-\left(\frac{E+E_n}{\sigma}\right)^2} \qquad (4.4)$$

$$\varepsilon_1 = \frac{2}{\pi} P \int_0^{\infty} \frac{\xi \varepsilon_2(\xi)}{\xi^2 - E^2} d\xi \qquad (4.5)$$

Where, $\sigma = \frac{Br_n}{2\sqrt{\ln(2)}}$, $Br_n$ = FWHM, P is the Cauchy Principal Value.

**Table 4.1:** Fitting parameters of Gaussian oscillators used for pristine ZnO substrate.

| Oscillator | Type | Amplitude $A_n$ | Center Energy $E_n$ (eV) | Broadening $Br_n$ (eV) |
|---|---|---|---|---|
| 1 | Gaussian | 85.165 | 0.0506 | 0.00210 |
| 2 | Gaussian | 16.737 | 0.05019 | 0.00610 |
| 3 | Gaussian | 0.32918 | 0.08231 | 0.03047 |
| 4 | Gaussian | 0.05138 | 0.17235 | 0.03051 |
| 5 | Gaussian | 0.21273 | 0.05917 | 0.01021 |
| 6 | Gaussian | 0.11585 | 0.19682 | 0.08180 |
| 7 | Gaussian | 0.03799 | 0.11703 | 0.01615 |

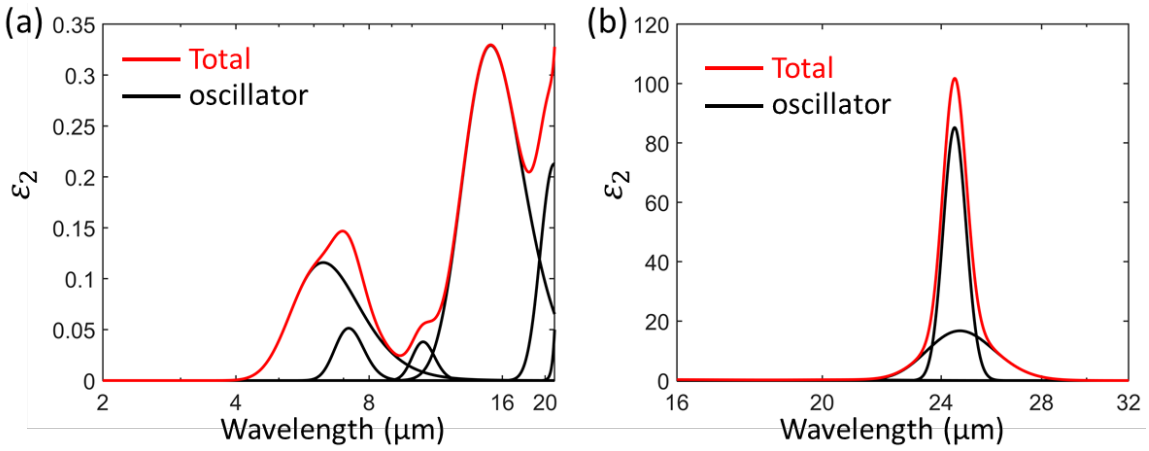


**Figure 4.8:** The fitting $\varepsilon_2$ values of the pristine ZnO substrate. The summed $\varepsilon_2$ function (red) and individual Gaussian oscillators (black) are plotted in **(a)** from 2 to 20 μm, and **(b)** from 16 to 32 μm. Adapted from Ref[132].

As shown in Fig. 4.9 (a, b) the measured (discrete points) and fitted (continuous curves) Ψ and Δ for the pristine ZnO are in good agreement. Our modeling was also verified by comparing the calculated reflection based on our ellipsometry model to

our FTIR reflectance measurements, as shown in Fig. 4.9(c). Fig. 4.9(d) plots the extracted complex refractive index of the pristine ZnO substrate.

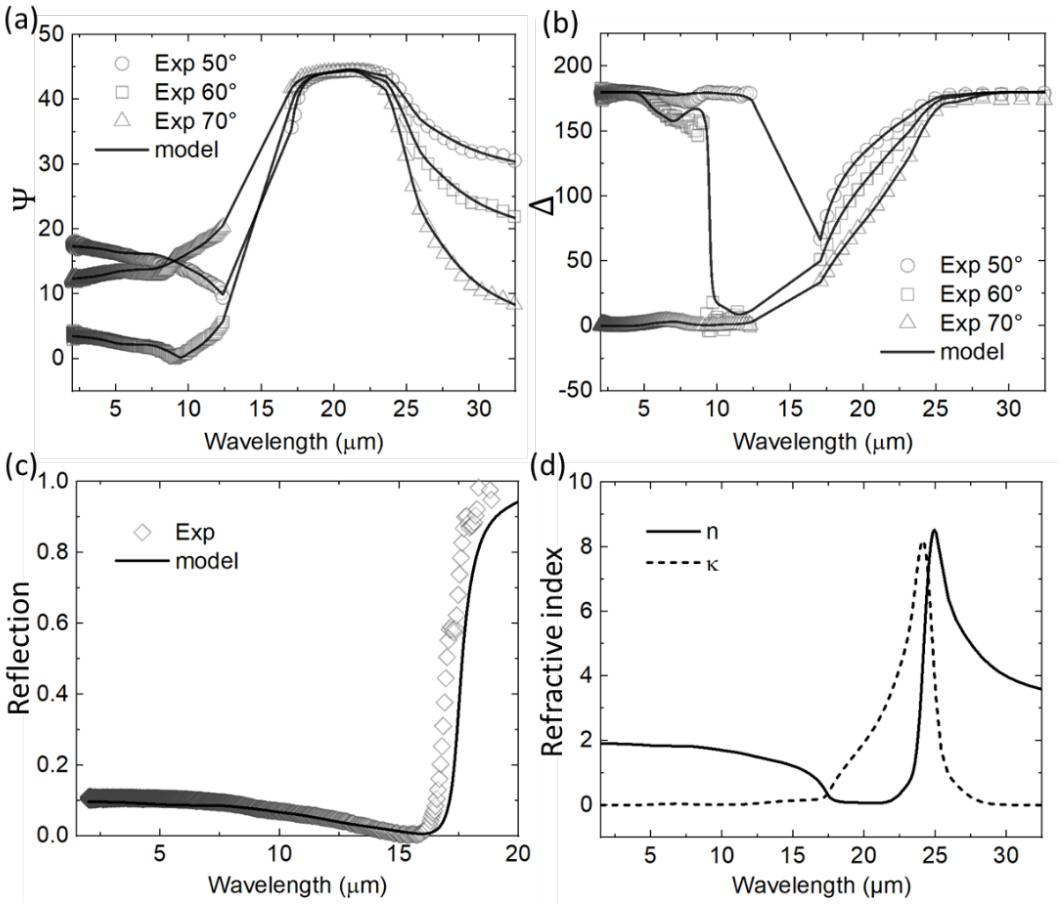


**Figure 4.9: (a, b)** Comparison between fitting (solid curves) and measured ellipsometry data of Ψ and Δ for the pristine ZnO substrate. **(c)** Comparison between calculated reflectance based on our ellipsometry fitting (solid curve) and FTIR measurements (diamond dots) for the pristine ZnO substrate. **(d)** Extracted complex refractive index of the pristine ZnO substrate. Adapted from Ref[132].

Then, we followed the same fitting procedures to extract the optical properties of Ga:ZnO samples. For the thermal annealed Ga:ZnO samples, according to the SIMS depth profile shown in Fig. 4.10, we found ~0.2 μm and ~1 μm plateaus in the 3.1-

at.% samples annealed at 800 °C and 900 °C, respectively, which are clear evidence of the diffusion of Ga dopants.

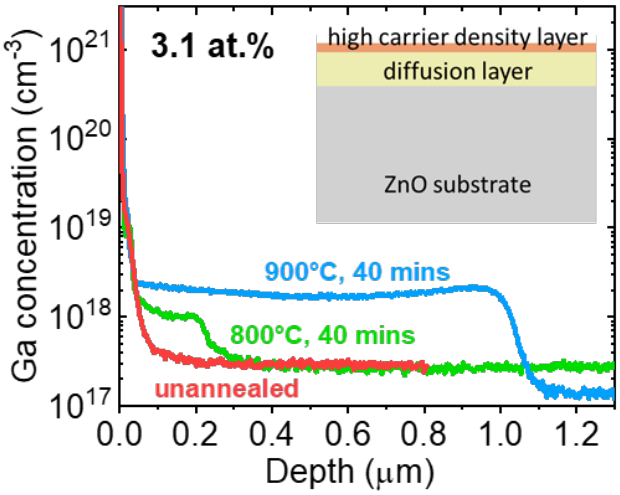


**Figure 4.10:** SIMS depth profiles of the Ga concentration in the samples implanted using an ion accelerator (not a FIB, to enable very large area implantation for infrared ellipsometry and SIMS). The ion energy was identically 30 keV and the peak doping concentration was chosen to be 3.1 at.%. The inset is the schematic showing the three-layer depth profile of thermal annealed FIB-ZnO. Adapted from Ref[132].

Therefore, we built two layers to model the top surface and the diffusion layer separately. Each layer includes an additional Drude function to account for the induced carrier concentration due to the FIB-assisted doping (note that the seven Gaussian oscillators are fixed, and only the Drude term was fitted.):

$$\varepsilon_{Drude} = \varepsilon_1 + i\varepsilon_2 = \frac{-\hbar^2}{\varepsilon_0 \rho_n (\tau_n \cdot E^2 + i\hbar E)} \quad (4.6)$$

$$\rho_n = \frac{m^*}{Nq^2\tau} = \frac{1}{q\mu N} \quad (4.7)$$

Where, $m^*$ is the effective mass, $\rho$ is the resistivity, and $\tau$ is the scattering time.

For the 3.1-at.% Ga-doped ZnO sample, we have six fitting parameters, including two sets of thickness, carrier concentration, and mobility: one set for the diffusion layer, and one set for the high carrier concentration layer. Fitting results and comparison between the measured and fitted Ψ and Δ have been shown in Fig. 4.11 and Table 4.2.

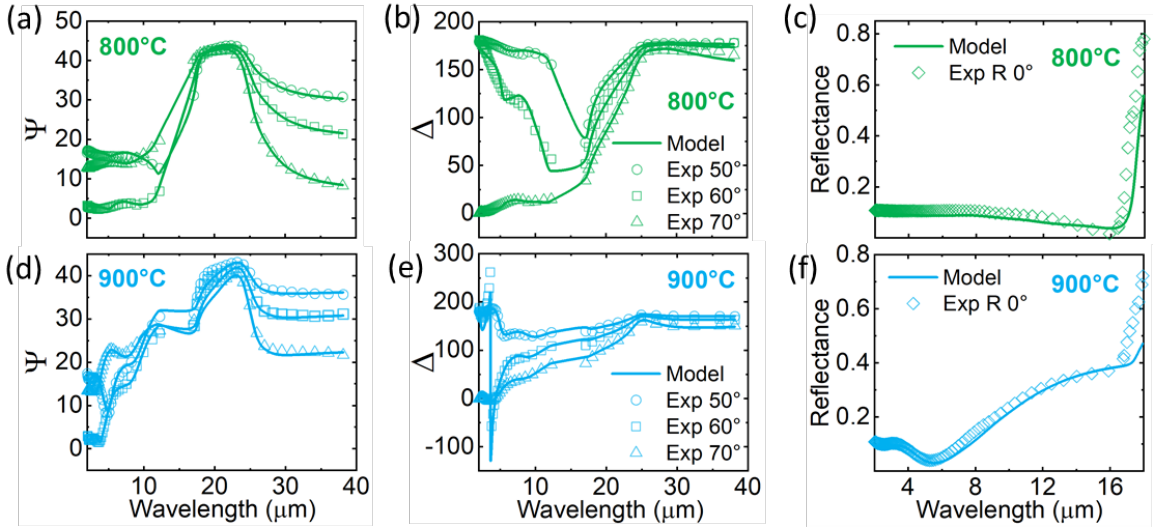


**Figure 4.11: (a-f)** The experimental (discrete points) and model fitted (solid curves) ellipsometric parameters (Ψ and Δ) and normal-incidence reflectance for the 3.1-at.% sample annealed at 800 °C **(a-c)** and for the other one annealed at 900 °C **(d-f)**. Adapted from Ref[132].

**Table 4.2:** Drude-fitting parameters of the two 3.1-at.% samples thermally annealed at 800 °C and 900 °C, respectively.

| 3.1 at.% Ga:ZnO | High carrier concentration layer | | | Diffusion layer | | |
|---|---|---|---|---|---|---|
| | Thickness | $n_e$ ($cm^{-3}$) | μ | Thickness | $n_e$ ($cm^{-3}$) | μ |
| **800°C** | 8.0 | $1.25\times10^{20}$ | 19.94 | 205.4 | $1.23\times10^{18}$ | 316.47 |
| **900°C** | 8.0 | $2.16\times10^{20}$ | 17.80 | 1008.3 | $2.40\times10^{18}$ | 232.59 |

The carrier concentration of the 3.1-at.% samples annealed at 800 °C and 900 °C reached $10^{20}$ $cm^{-3}$ in the top-surface layer, while the carrier concentrations in the

diffusion layers underneath are two orders of magnitude lower (Table 4.2). These fitting results agreed with our SIMS characterizations that the Ga dopants were diffusing from the implantation profile during the annealing process, resulting in a much thicker diffusion layer with a much lower carrier concentration. For most applications, such diffusion layers are unwanted since they trade off patterning resolutions and optical contrast between FIB-irradiated and pristine regions. Since the diffusion layer is highly correlated to the annealing conditions (i.e., annealing temperature and annealing time), decreasing the annealing time such as flash lamp annealing [170,171] and laser annealing [172–174] could be useful for suppressing the diffusion.

And then we performed laser annealing instead of thermal annealing and achieved higher carrier concentration beyond the solid-solubility limit (SSL) for doping in ZnO.

Figure 4.12(a) depicts the SSL for the three *n*-type dopants in ZnO, Ga, Al, and In, as a function of temperature[167,168,175]. Ga has the highest SSL over a wide temperature range, which makes it the most promising dopant for ZnO plasmonics. This is mainly connected to the small tetrahedral covalent radius and the low formation energy of $Ga_2O_3$ compared to those of $Al_2O_3$ and $In_2O_3$[176].

Beyond the choice of the dopant for ion implantation, the annealing time is another key factor. The annealing time must be shorter than or at least similar to the thermal response time (time of a material to react to a sudden temperature change) of ZnO in

order to achieve hyper-doping, so that the dopant diffusion length is less than the average distance between dopants at a given temperature to avoiding clustering[170]. Figure 4.12(b) displays the dopant diffusion length $d_l$ versus annealing time of the three n-type dopants in ZnO at 900 °C. This diffusion length was calculated using:

$$D = D_0^{\text{eff}} \times e^{\left(-\frac{E_a}{kT}\right)} \quad (4.8)$$

$$d_l = \sqrt{D \times t_{\text{ann}}} \quad (4.9)$$

with the dopant diffusivity $D$, effective diffusion constant $D_0^{\text{eff}}$, activation energy $E_a$, Boltzmann constant $k$, temperature $T$, and annealing time $t_{\text{ann}}$. We extracted the values of $D_0^{\text{eff}}$and $E_a$ for the dopants Ga, Al, and In from references[167,169,177], where they modelled the dopant diffusion profiles at different annealing temperatures. Consequently, we used values of $D_0^{\text{eff}}$of 0.08 cm$^2$ s$^{-1}$ and $E_a$ of 3 ± 0.2 eV for Ga[169], $D_0^{\text{eff}}$= 0.04 cm$^2$ s$^{-1}$ and $E_a$ of 2.6 ± 0.2 eV for Al[167] and $D_0^{\text{eff}}$= 0.04 cm$^2$ s$^{-1}$ and $E_a$ of 2.2 ± 0.2 eV for In[177]. The dopant diffusivity $D$ versus annealing time in Figure 4.12(b) was then calculated using Eq. (4.8). Long-term annealing procedures, like furnace annealing (FA) with typical annealing times on the order of 10 minutes, result in diffusion lengths of $d_l$ (Ga) ≈ 280 nm. However, laser annealing (LA) with annealing times in the nanoseconds range strongly suppresses dopant diffusion, resulting in a calculated diffusion length below 0.001 nm, which is smaller than the lattice constants of ZnO. Therefore, we implanted Ga into ZnO and used subsequent laser annealing to

achieve heavy doping and plasma wavelengths close to the important telecommunication wavelength of 1.55 µm.

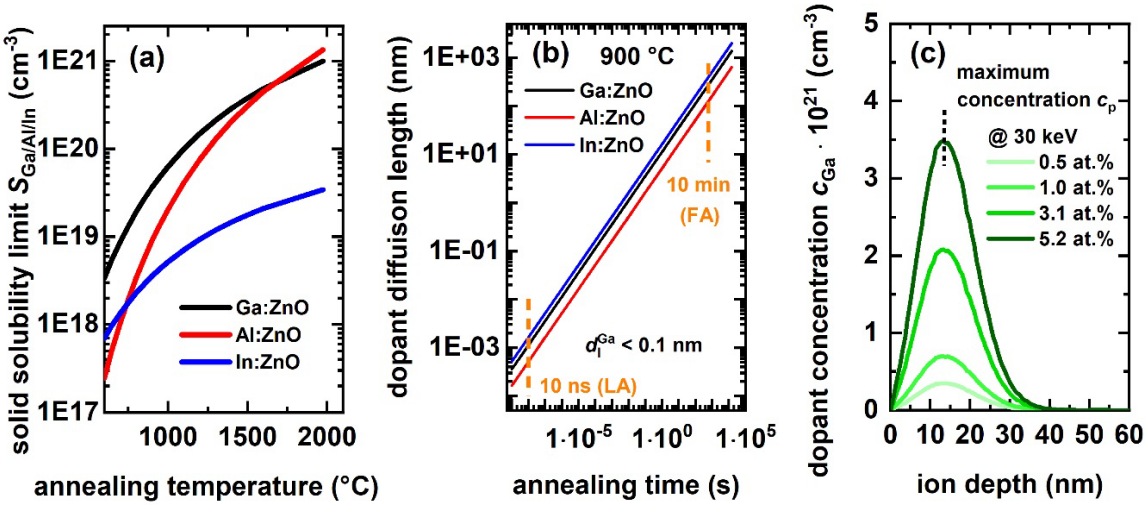


**Figure 4.12: (a)** Solid-solubility-limit as a function of temperature for n-type dopants (Ga, Al, In) in single-crystalline ZnO, using data taken from references. [22-24] **(b)** Dopant diffusion lengths for Ga, Al, and In in ZnO at 900 °C as a function of annealing time. [25,23,26] The dashed orange lines indicate typical annealing times for furnace annealing (FA) and laser annealing (LA). **(c)** Simulated Ga implantation profiles in ZnO using SRIM for an ion energy of 30 keV as a function of depth for different ion fluences, resulting into different gallium concentrations $c_{Ga}$. Adapted from Ref[133].

We irradiated single-crystalline <0001> ZnO substrates with 30 keV $Ga^+$ ions at room temperature using a commercial focused ion beam (FIB) system. The ZnO substrates are single side polished and were grown by a hydrothermal process at CrysTec® GmbH with a thickness of 0.5 mm and an area of 1 cm$^2$. Regions with sizes of 150 × 150 µm$^2$ were homogeneously irradiated. Figure 4.12(c) shows implantation profiles for different peak dopant concentrations $c_p$ as a function of depth, as simulated with

the Monte-Carlo code TRIM[178]. The projected mean ion range is ≈ 14 nm and the straggle ≈ 7 nm. Each sample was implanted with ion fluences ranging from $6 \times 10^{14}$ to $6 \times 10^{15}$ $cm^{-2}$, resulting in peak values of 0.5 to 5.2 at.% that correspond to Ga concentrations of $4.28 \times 10^{20}$ to $4.28 \times 10^{21}$ $cm^{-3}$, respectively[179].

Post-implantation annealing was performed with an INNOVAVENT VOLCANO® UV laser line beam system, which was powered by a TRUMPF TruMicro® 7370 laser with a peak laser power $P_{laser}$ of 180 W at 10 kHz, with a pulse width of 15 ns. The UV laser light ($\lambda_{laser}$ = 343 nm) was formed to a beam with a "line" cross-section, with full-width at half-maximum (FWHM) of 30 µm with Gaussian shape in the short axis and top-hat profile with a homogeneity better than 5 % (pulse peak-to-pulse peak) at a line length of 15 mm in the long axis. This line beam was scanned at a velocity of 30 mm/s over the sample surface with a 3 µm pitch, resulting in a consecutive laser spot area overlap of 90 %. The laser energy density could be set by a variable attenuator to energy densities of 100, 150, 200, 250, 300, and 350 mJ $cm^{-2}$ resulting in different annealing temperature profiles and peak annealing temperatures. The peak annealing temperatures were simulated to be about 570 °C (100 mJ $cm^{-2}$), 920 °C (150 mJ $cm^{-2}$), 1300 °C (200 mJ $cm^{-2}$), 1700 °C (250 mJ $cm^{-2}$). For laser energy densities above 250 mJ $cm^{-2}$, the peak annealing temperatures reaches the melting point of ZnO, which is 1975 °C. The onset of these destructive effects sets the maximum laser energy density for successful laser annealing of Ga-doped ZnO to about 250 mJ $cm^{-2}$. Regarding the surface quality of our Ga doped and laser annealed ZnO samples we

performed atomic force microscopy (AFM) measurements after the ion implantation and laser annealing and verify the surfaces can be still considered as of good quality with a surface roughness ~1.8 nm.

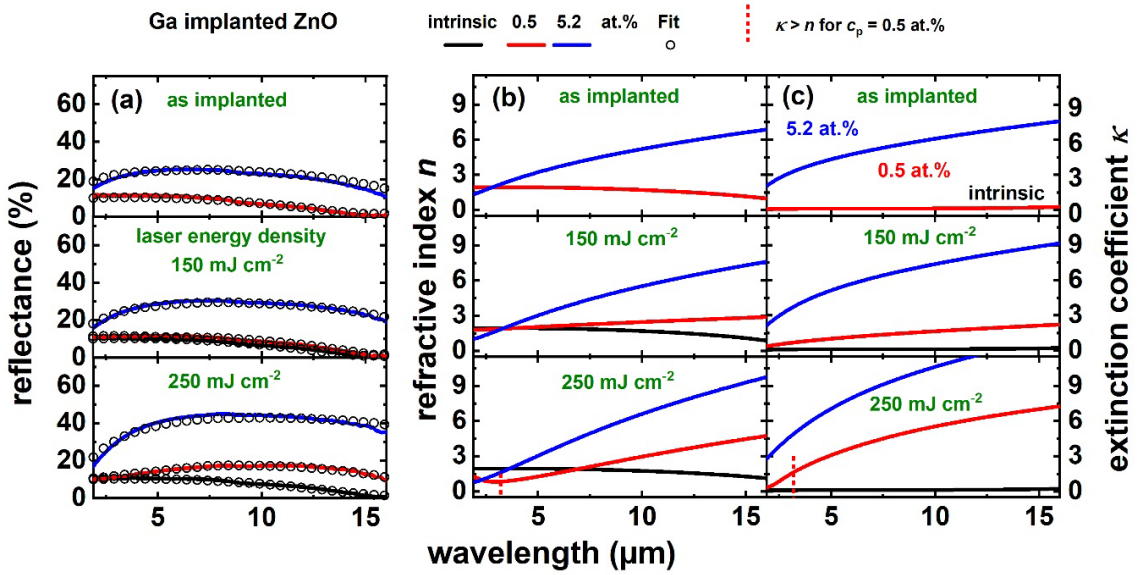


**Figure 4.13: (a)** Measured (solid lines) and fitted (dotted lines) reflectance spectra of intrinsic (black) and Ga-implanted ZnO (red, blue) in the unannealed state and after laser annealing with different laser energy densities (150 and 250 mJ cm$^{-2}$). **(b, c)** Real part ($n$) and imaginary part ($\kappa$) of the complex refractive index $\tilde{n}$ extracted from Drude-Lorentz fits to the experimental reflectance spectra from **(a)** for the gallium-implanted top layer. The perpendicular red dashed line in **(b, c)** indicates the plasma wavelengths, where $\kappa$ starting to get bigger than n for Ga implanted ZnO with $c_p$ = 0.5 at.%, which corresponds to plasmonic behavior. Adapted from Ref[133].

Figure 4.13(a, top) shows reflectance spectra in the infrared regime obtained from two as-implanted and non-annealed samples with Ga peak concentrations $c_p$ of 0.5 and 5.2 at.%, measured using a Fourier-transform infrared (FTIR) spectrometer (Bruker Vertex 70) connected to an infrared microscope (Hyperion 2000) in

reflection mode. The spectrum of an intrinsic ZnO substrate is also shown for comparison (black), which is in top of Figure 4.13(a-c) similar to the reflectance of the sample with $c_p$ of 0.5 at.% (red). The reflectance increased with increasing Ga concentration in the as-implanted state (i.e., before laser annealing). This may be caused by various effects: the formation of Ga clusters at such high impurity concentrations[180,181] or implanted dopants are in substitutional position within the ZnO lattice without any annealing, which was experimentally observed for dopants in several references[182–187].

Figure 4.14(a, b) shows the plasma frequency $\omega_N$ and damping factor $\Gamma_D$ as a function of the ion fluence, where $\omega_N$ and $\Gamma_D$ were extracted from the fits to reflectance spectra in Figure 4.13. Increasing both the ion fluence and the laser energy density usually leads to an increase of $\omega_N$, and the highest plasma frequencies of 1-1.3 eV were obtained for a laser energy density of 250 mJ cm$^{-2}$ and an ion fluence range of 3.6 × $10^{15}$ – 6 × $10^{15}$ cm$^{-2}$ (equivalently, peak dopant concentration of 3.1 – 5.2 at.%). Degradation of the ZnO samples occurs beyond this value, as mentioned above. The damping factor is inversely proportional to the carrier mobility and Figure 4.14(b) indicates that higher dopant concentrations result into a lower mobility, which is consistent with increased electron-defect scattering.

Figure 4.14(c) depicts the dopant activation efficiency, which is the ratio of the achieved free-carrier concentration for a given averaged implanted Ga concentration across the thickness of 30 nm. Laser annealing with 150 mJ cm$^{-2}$ results in activation

of 95 % to 40 % of the incorporated Ga atoms with increasing ion fluence, whereas values of 100-50 % can be achieved by laser annealing using 250 mJ $cm^{-2}$. However, the activation efficiency also decreases with increasing dopant concentration, which is most probably limited by the temperature-dependent SSL of Ga in ZnO.

Furthermore, we extracted the activated dopant concentration from the fits and plotted in Figure 4.14(d) the respective plasma wavelength, defined as $\lambda_p = \omega_p/2\pi$, versus the used ion fluence range for all investigated ZnO:Ga layers. We obtained the highest carrier concentration of $(1.23 \pm 0.41) \times 10^{21}$ $cm^{-3}$ for an ion fluence of $6 \times 10^{15}$ $cm^{-2}$ and for laser annealing with a laser energy density of 250 mJ $cm^{-2}$. This value corresponds to a plasma wavelength of 1.02 ± 0.17 µm, which is below the telecommunication wavelength of 1.55 µm (blue dashed line in Figure 4.14(d)). This value translates also to an activation of $\sim 10^{21}$ $cm^{-3}$ Ga atoms in the ZnO lattice, which is close to the SSL of Ga at a temperature of 1975 °C (compare Figure 4.12(a)).

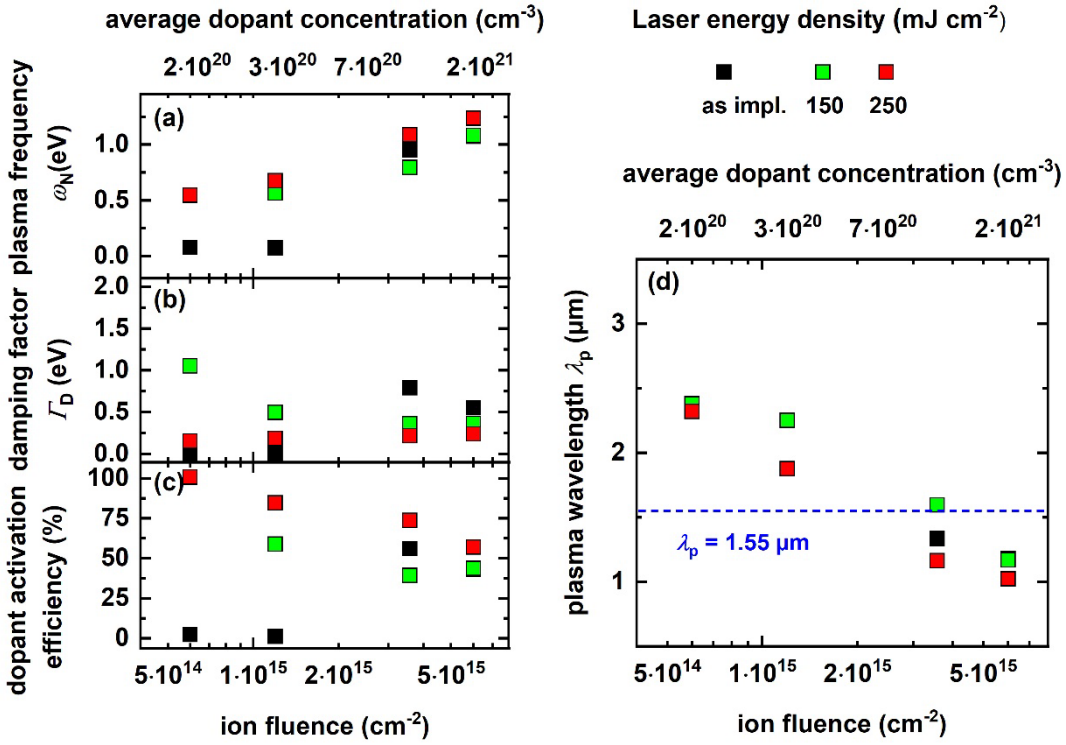


**Figure 4.14: (a)** Plasma frequency $\omega_N$ and **(b)** damping factor $\Gamma_D$ extracted from the fits shown in **Figure 4.13** as a function of the ion fluences for different laser energy densities. **(c)** Dopant activation efficiency, which is the ratio of activated free carriers to the averaged implanted Ga concentration across the thickness, versus ion fluences. **(d)** Plasma wavelength $\lambda_p$ versus ion fluence. The telecommunication wavelength is indicated with a blue dashed line. Adapted from Ref[133].

Figure 4.15 highlights the SSL of Ga compared to the activated dopant concentrations of our ZnO:Ga samples, irradiated with an ion fluence of 6 × $10^{15}$ $cm^{-2}$ ($c_p$ = 5.2 at.%), for the investigated temperature range. Here, the laser energy has been converted to a temperature using the material parameters of ZnO, the Beer-Lambert law, and the heat equation. For the laser energy density range of 150 mJ $cm^{-2}$ – 250 mJ $cm^{-2}$ we

achieved hyper-doped ZnO. Increasing the laser energy density towards the melting temperature of ZnO led to values close to the SSL of Ga in ZnO[168].

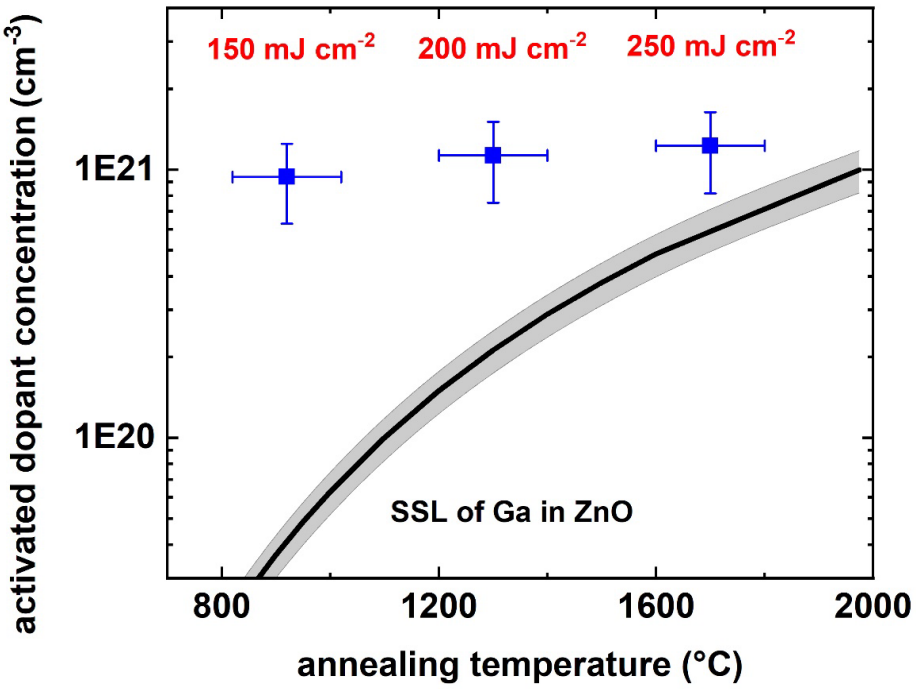


**Figure 4.15:** Comparison between activated free-carrier concentrations, from the Ga doped samples irradiated with an ion fluence of 6 × $10^{15}$ $cm^{-2}$ ($c_p$ = 5.2 at.%) and laser annealed in the laser energy density range 150 mJ $cm^{-2}$ – 250 mJ (corresponds to an annealing temperature range 920 °C and 1700 °C) and the temperature-dependent solid solubility limit of Ga in ZnO taken from the work of Sky et al [22], where the grey area around the black line displays an error of ± 18 % for the solid solubility limit. Adapted from Ref[133].

In conclusion, we are able to tune the optical properties of ZnO by ion implantation of gallium and subsequent nanosecond laser annealing. Using this approach, we achieved even plasma wavelengths in the near-infrared spectral region, including for wavelengths shorter than 1.55 µm. The highest achieved free-carrier concentration

in ZnO:Ga was $N_e \approx 1.23 \pm 0.41 \times 10^{21}$ cm$^{-3}$, corresponding to $\lambda_p = 1.02 \pm 0.17$ µm, which is 1.48 at. % substituted Gallium in the ZnO host lattice with a doping level of $2.16 \times 10^{21}$ cm$^{-3}$ (2.6 at. %) and a dopant activation efficiency of 57 %. In general, with this doping approach we are reaching dopant activation efficiencies in the range from 30 % up to 100 %. This is enabled by the combination of high concentration ion implantation and the high peak annealing temperatures during the short laser annealing in the nanosecond regime, where dopant diffusion is suppressed, which is advantageous for maintaining spatially localized distributions of dopants, resulting even in hyper-doping of ZnO under certain conditions.

Heavily or hyper-doped ZnO:Ga with plasma frequencies in the telecommunication range have a broad applicability. With a focused ion beam we are able to selective and gradually dope ZnO. Thus, it opens a wide field for lateral arrangements of sub-wavelength sized and spaced optical doped and un-doped regions with a high optical contrast, which are a promising approach for photonic or plasmonic applications in the infrared spectral range. Figure 4.16 showcases an example of applications based on FIB doped ZnO platform, which is a frequency-selective surface with frequency-selective transmittance and/or absorptivity/emissivity. By simply changing the geometry and doping concentration of the doped regions, one can realize tunable central wavelength and bandwidth.

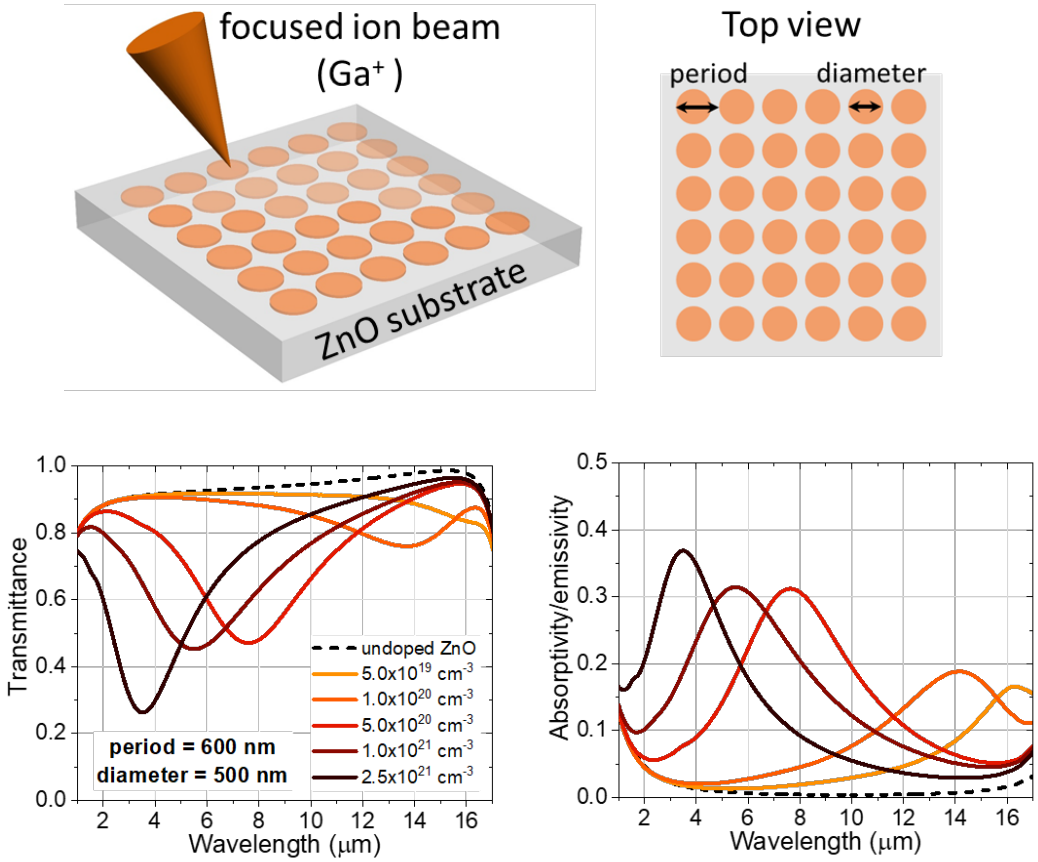


**Figure 4.16:** Frequency-selective surfaces based on FIB doped ZnO, enabling tunable frequency-selective transmittance and/or absorptivity/emissivity. Adapted from Ref[132].

## 4.3 Tunable phase-transition characteristics in FIB-engineered $VO_2$

In the previous section, we demonstrated that optical properties such as carrier density and mobility of an oxide semiconductor (e.g., ZnO) can be locally modified via a simple step of mask-free FIB-assisted ion implantation, followed by a thermal

annealing process. We can also use FIB implantation (without annealing) to intentionally introduce structural defects into a material, and the induced defect density can be continuously controlled by varying the ion fluence. Such defect-engineering techniques can be useful for modulating physical properties of materials, especially for strongly correlated electron systems in which electronic properties are very sensitive to changes in the lattice parameters [188–201]. In this section, we show that such FIB-assisted defect-engineering can be used to locally modulate the IMT temperature of thin-film $VO_2$, an electron-correlated material that undergoes an IMT at ~70 °C [202,203] and features an orders-of-magnitude change in carrier density. The IMT temperature of $VO_2$ is determined by the stability of the electron hybridization, which is very sensitive to the strain environment in the thin film [188,204–207]. We previously demonstrated that the IMT temperature can be tuned by introducing structural defects in the $VO_2$ film via high-energy ion irradiation performed using an ion accelerator, where we found the change in optical properties and IMT temperature of $VO_2$ depend on the density of generated defects, but not on the particular ion species (Ar or Cs), and the generated defects introduce more strain to the surrounding and lower the IMT temperature [188].

Here, we show that high-resolution mask-free defect engineering can also be accomplished using a commercial FIB system. Similar to the FIB irradiation of ZnO (before annealing), here structural defects are introduced by the collision cascades of impinging ions and lattice atoms (V and O) [Fig. 4.17(a)], causing changes in the strain

environment in the film and thus the IMT temperature is expected to be modulated to different extents depending on the ion fluence.

We deposited a ~50-nm $VO_2$ film on *c*-plane sapphire via magnetron sputtering [203,208]. Then, twelve 200-by-200-μm regions were irradiated using focused 30-keV Ga ions at room temperature with varying ion fluences up to $2 \times 10^{14}$ $cm^{-2}$, as shown in Fig. 4.17(b). The density of induced structural defects is proportional to the density of Ga ions implanted into the $VO_2$ film, which we estimated using TRIM simulations [Fig. 4.17(c)].

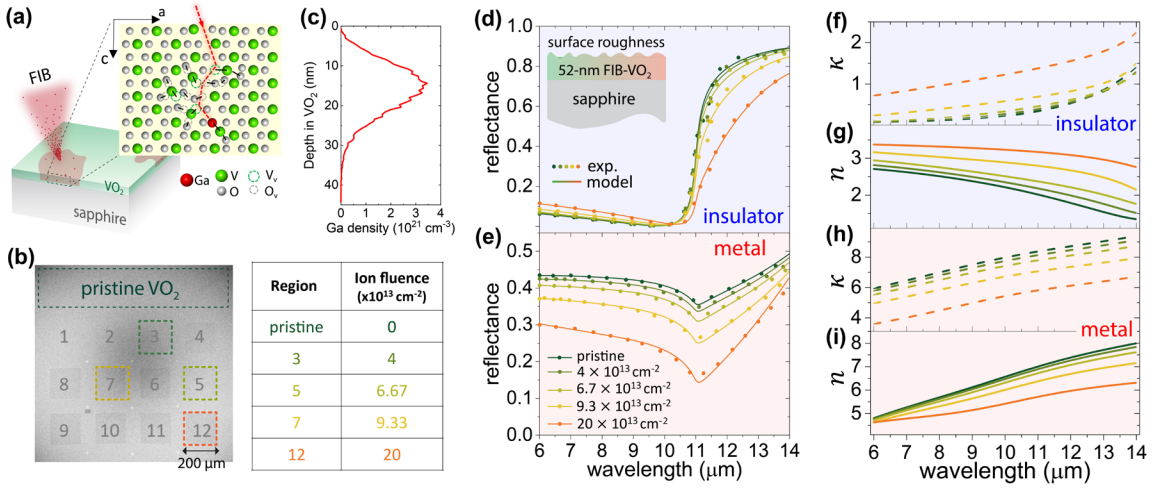


| Region | Ion fluence (x$10^{13}$ $cm^{-2}$) |
|---|---|
| pristine | 0 |
| 3 | 4 |
| 5 | 6.67 |
| 7 | 9.33 |
| 12 | 20 |

**Figure 4.17: (a)** Ion irradiation of $VO_2$ using a FIB system, with an inset schematic of the defect-engineering process, showing a collision cascade in the $VO_2$ lattice initiated by an energetic Ga ion. **(b)** SEM image of the FIB-irradiated $VO_2$ regions with the corresponding ion fluences listed. **(c)** Simulated depth profile of 30-keV Ga ions into a $VO_2$ thin film using TRIM. **(d, e)** The symbols are FTIR reflectance measurements on pristine $VO_2$ and regions irradiated with ion fluences of 4 x $10^{13}$, 6.7 x $10^{13}$, 9.3 x $10^{13}$, 20 x $10^{13}$ $cm^{-2}$, for temperatures at 25 °C (all regions in pure insulating phases) and 100 °C (all regions in pure metallic phases), respectively. The solid curves are the model fits to the FTIR measurements, where the

underlying model was created based on ellipsometry of pristine $VO_2$. The insulator-phase **(f, g)** and metal-phase **(h, i)** refractive indices extracted from the fittings shown in (d) and (e). Adapted from Ref[132].

To investigate the irradiation-induced changes in the optical properties of the pure insulator- and metal-phase $VO_2$, we first performed reflectance measurements on each of these FIB-irradiated $VO_2$ regions using our FTIR spectrometer with microscope, for temperatures of 25 °C (i.e., $VO_2$ in the pure insulating phase for all the irradiated regions) and 100 °C (i.e., $VO_2$ in the pure metallic phase for all the irradiated regions), as shown in Fig. 4.17(d, e). Then, we fitted the measured reflectance by adjusting the parameters of a model that we previously built to characterize refractive indices of intrinsic thin-film $VO_2$ [203]. As shown in the inset of Fig. 4.17(d), the model consisted of a semi-infinite anisotropic *c*-plane sapphire [203], a $VO_2$ layer, and surface roughness (50% air + 50% of the material underneath). For the insulating phase, the dielectric function of the $VO_2$ layer is a series of Lorentzian oscillators. For the metallic phase, we also used Drude functions to capture the contribution of the free carriers (more details can be found in ref. [203]). The thicknesses of $VO_2$ and surface roughness were set to 52 nm and 5 nm, respectively, based on SEM imaging of the cross section (Fig. 4.18). We were able to fit our reflectance measurements [Fig. 4.17(d, e)] by only adjusting the line shapes, amplitudes, and spectral positions of the Lorentz and Drude functions. Therefore, the complex refractive indices of $VO_2$ for different ion fluences can be extracted.

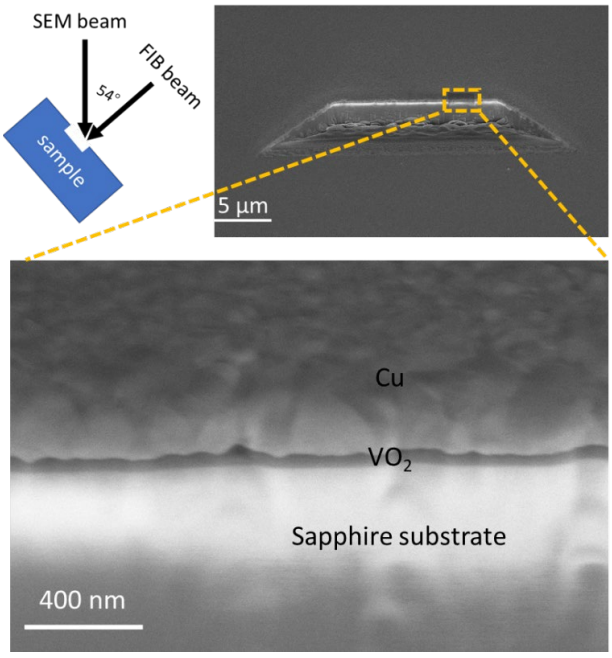


**Figure 4.18:** Schematic of FIB-milling-assisted cross-section imaging of the FIB-$VO_2$ sample. The measured thickness of $VO_2$ is (52±5) nm. Adapted from Ref[132].

Then, we investigated FIB-induced modulation of the IMT temperature and width by a combination of temperature-dependent FTIR reflectance measurements and effective-medium theory, as schematically shown in Fig. 4.19(a). FTIR reflectance measurements were performed on all irradiated regions for temperatures increasing from 10 to 120 °C, in steps of 2 °C. We observed that the phase transition shifted to lower temperatures as the ion fluence increased, which agrees with our previous observations for defect-engineered $VO_2$ irradiated using an ion accelerator [188]. To quantitatively study the changes of IMT characteristics with respect to the FIB fluence, we used the Looyenga effective-medium theory formalism[174] to approximate the refractive indices of the irradiated $VO_2$ at intermediate temperatures [203,209]:

$$\tilde{\varepsilon}_{eff}{}^{1/3} = (1-f)\tilde{\varepsilon}_i{}^{1/3} + f\tilde{\varepsilon}_m{}^{1/3} \qquad (4.10)$$

where $\tilde{\varepsilon} = \tilde{n}^2 = (n+i\kappa)^2$ is the complex dielectric function of $VO_2$ and $f$ is the temperature-dependent volume fraction of the metal-phase $VO_2$ domains within the film. The co-existence of insulating and metallic domains can be understood as a first-order equilibrium distribution, and therefore $f(T)$ can be expressed as [188,210]:

$$f(T) = \frac{1}{1+\exp\left[{}^{E}/_{k_B}\left({}^{1}/_{T} - {}^{1}/_{T_{IMT}}\right)\right]} \qquad (4.11)$$

where $E$ is an energy scale that determines the sharpness of the IMT (i.e., inversely proportional to the IMT width). $T_{IMT}$ is the temperature where 50% of $VO_2$ transformed to the metallic phase in a heating process.

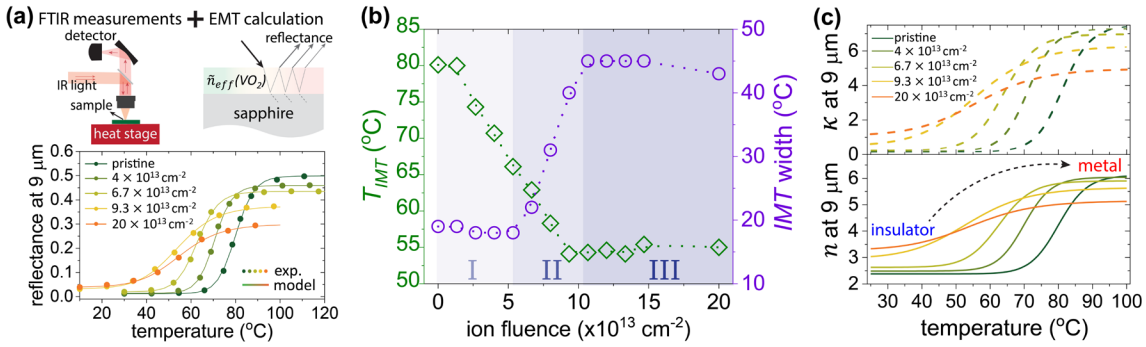


**Figure 4.19: (a)** Temperature-dependent optical characterization of the FIB-irradiated $VO_2$. First, we measured temperature-dependent reflectance across the IMT for each irradiated region. Then, we applied effective-medium theory to approximate the refractive indices at intermediate temperatures and calculate the temperature-dependent reflectance. By sweeping the parameters of $T_{IMT}$ and $E$—which determine the IMT width and temperature, respectively—in Eq. (4.11), we found the best fit between the FTIR measurements and calculation, enabling us to extract the IMT temperature and width for each irradiation ion fluence, as plotted in **(b)**. **(c)** Extracted temperature-dependent refractive indices of the

defect-engineered $VO_2$ irradiated by different ion fluences. Here we plot the results for a single wavelength of 9 μm to clearly show the evolution of refractive-index values versus temperature and ion fluence. Adapted from Ref[132].

For given $E$ and $T_{IMT}$, we used Eq. (4.10) and (4.11) to obtain the temperature-dependent refractive indices and then calculated the optical reflectance of each irradiated region using the transfer-matrix method. As shown in Fig. 4.19(a), by sweeping $E$ and $T_{IMT}$, we achieved good agreement between the calculation (solid curves) and FTIR measurements (dotted lines). The fitted IMT temperature and width as a function of ion fluence are shown in Fig. 4.19(b). The IMT width is defined to be the temperature interval between where 3% of $VO_2$ is in the metallic phase and where 97% of $VO_2$ is in the metallic phase. Note that due to the hysteresis in $VO_2$, the value of $T_{IMT}$ is different for heating and cooling [203,211]. Once $f(T)$ was determined, we were able to obtain the temperature-dependent refractive indices across the IMT for each irradiated region, as shown in Fig. 4.19(c). Here, we only plot the results for a single wavelength (λ = 9 μm) to better show the evolution of the refractive indices with respect to both the temperature and the FIB fluence. The full dataset for wavelengths from 6 to 14 μm are plotted in Fig. 4.20.

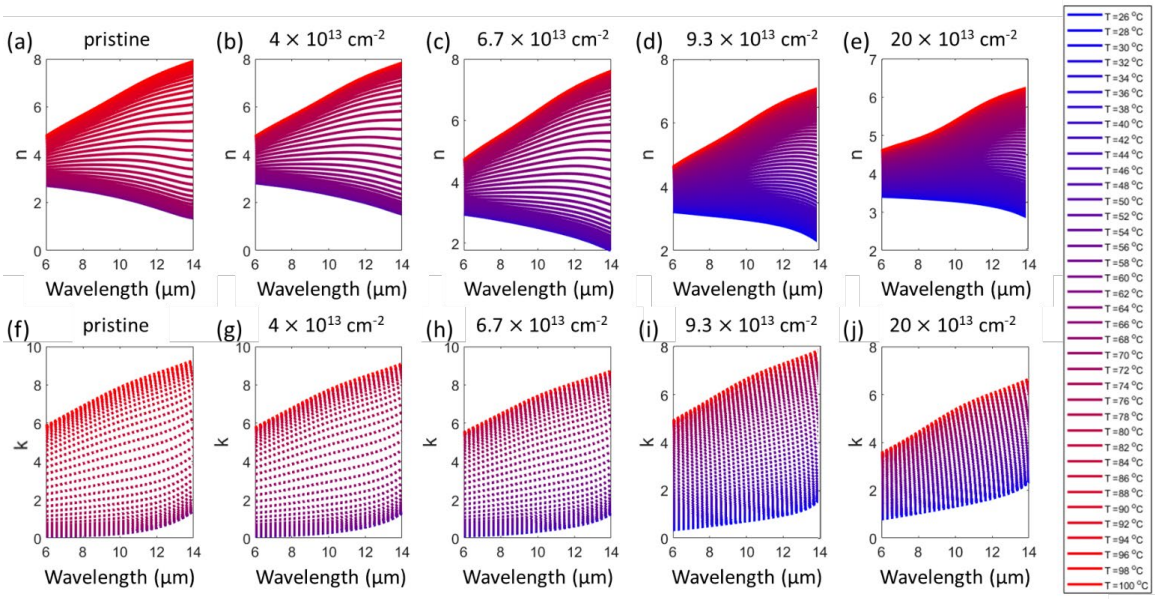


**Figure 4.20:** Full dataset of **(a-e)** real and **(f-j)** imaginary parts of temperature-dependent refractive indices of $VO_2$ irradiated with different ion fluences as indicated on top of each figure, for wavelengths from 6 to 14 μm. Adapted from Ref[132].

As shown in Fig. 4.19(b), there are three distinct ion fluence regimes (labeled in the figure as I, II, and III), in which the IMT characteristics evolve differently. For ion fluences < 5 $\times 10^{13}$ cm$^{-2}$, the IMT temperature gradually decreases with fluence, with a reduction of ~15 °C for 5 $\times 10^{13}$ cm$^{-2}$ and no substantial changes in either the refractive index of the two pure phases or in the IMT width. At higher ion fluences between 5 $\times 10^{13}$ and 1.1 $\times 10^{14}$ cm$^{-2}$, we observed that the IMT temperature could be further shifted to lower temperatures, but the shift was accompanied by a significant broadening in the IMT width and a reduction in the refractive-index contrast between the two pure phases [Fig. 4.19(c)].

We attribute such distinct phenomena to the different defect morphologies induced by different levels of ion fluence. At low ion fluences, the impinging ions mostly cause point defects that can reduce the transition temperature due to local compressive strain [188,207]. Such point defects are in much smaller than the probing wavelengths of our FTIR measurements. The strain induced by the point defects can be redistributed and partially relaxed at room temperature after irradiation [212,213], resulting in a homogeneous strain environment in the film. This understanding is consistent with the lack of broadening in the IMT width in the low-fluence irradiation regions in Fig. 4.19. As the ion influence increases, point defects are expected to accumulate and form nanometer-sized defect complexes that can affect the IMT temperature in microscopic scales, thus resulting in apparent broadening of the IMT in regions irradiated with high fluence.

When the ion fluence surpasses $\sim 1.1 \times 10^{14}$ cm$^{-2}$, both the IMT temperature and width became constant versus the increasing ion fluence, likely due to the limited penetration depth of the 30-keV Ga ions in the $VO_2$ film. At these high ion fluences, we expect the density of the induced structural defects complexes to saturate (*i.e.,* complete amorphization occurs [188]) within the depth of ~30 nm from the $VO_2$ surface, while leaving a less-affected $VO_2$ layer underneath, as shown in our TRIM simulation [Fig. 4.17(c)].

We took SEM images of the FIB-$VO_2$ sample. As shown in Fig. 4.21, FIB-irradiated regions have a contrast compared to pristine regions, but there is no obvious change

of the morphology caused by the FIB irradiation in comparison with the pristine $VO_2$ region, as seen in the high-resolution SEM Figure 4.21(e).

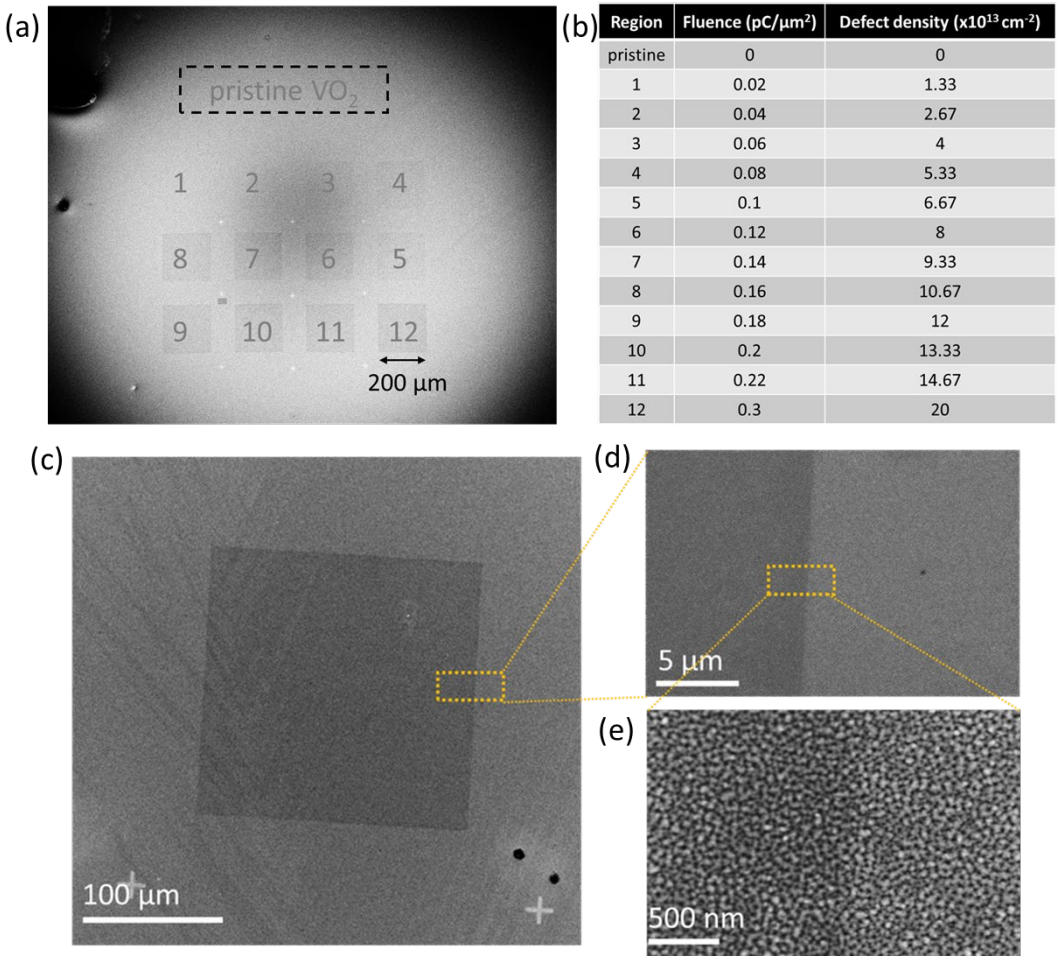


| Region | Fluence (pC/µm²) | Defect density (x10¹³ cm⁻²) |
|---|---|---|
| pristine | 0 | 0 |
| 1 | 0.02 | 1.33 |
| 2 | 0.04 | 2.67 |
| 3 | 0.06 | 4 |
| 4 | 0.08 | 5.33 |
| 5 | 0.1 | 6.67 |
| 6 | 0.12 | 8 |
| 7 | 0.14 | 9.33 |
| 8 | 0.16 | 10.67 |
| 9 | 0.18 | 12 |
| 10 | 0.2 | 13.33 |
| 11 | 0.22 | 14.67 |
| 12 | 0.3 | 20 |

**Figure 4.21: (a,b)** SEM image of the top surface of the FIB-$VO_2$ sample with the corresponding ion fluences given in the table. **(c-e)** SEM images of the FIB-irradiated $VO_2$ region #12 with an ion fluence of 2 ×14 $cm^{-2}$. Adapted from Ref[132].

We performed Raman mapping to show that FIB is able to locally modulate the IMT of $VO_2$ within sub-micrometer areas. We used an excitation laser of 532 nm with a step size of 1 µm of a 5-by-40-µm rectangular region that included both pristine and

irradiated regions. As shown in Fig. 4.22, the irradiated $VO_2$ region was transformed to the metallic phase at 50 °C, featuring no Raman mode at 610 $cm^{-1}$, while the pristine region was still in its insulating phase, with a strong Raman mode at 610 $cm^{-1}$.

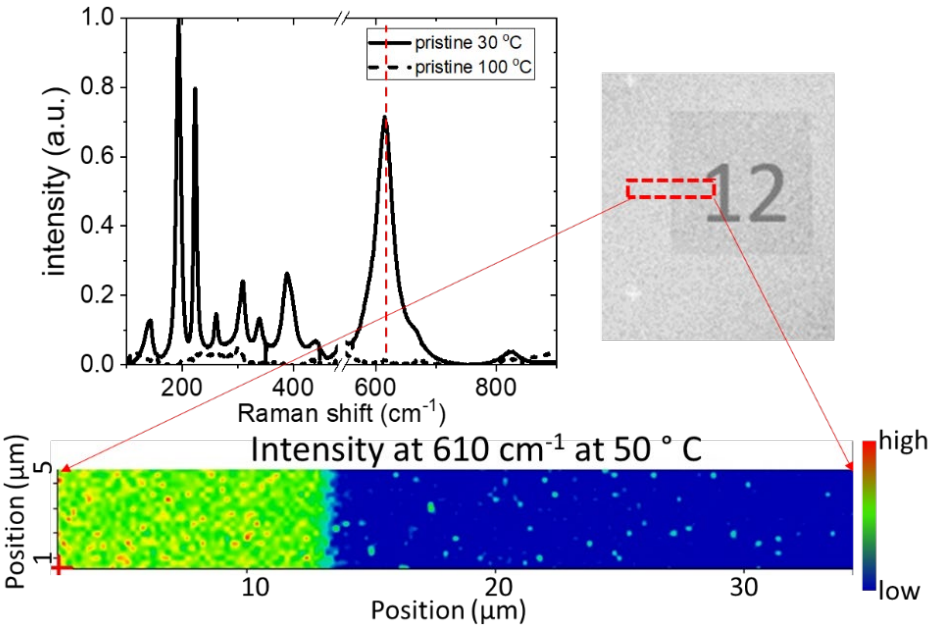


**Figure 4.22:** Raman mapping across the boundary between a pristine region and a region irradiated with fluence of 2 × 14 $cm^{-2}$. Adapted from Ref[132].

To check the stability of the hysteresis curves after multiple thermal cycles, we ran temperature-dependent FTIR reflectance measurements on region #6 (irradiated with the ion fluence of 8×13 $cm^{-2}$) of our FIB-$VO_2$ sample for 3 cycles of heating and cooling, as shown in Figure 4.23 below. Our results show that the hysteresis and IMT temperature is stable with multiple thermal cycles between room temperature and 90 °C.

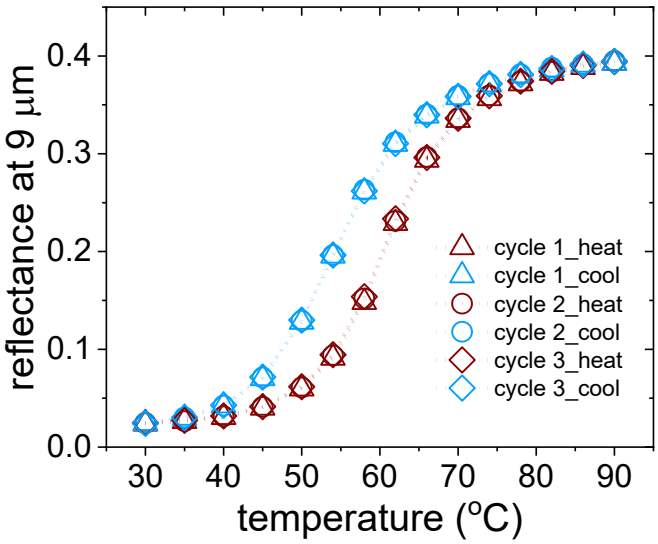


**Figure 4.23:** FTIR reflectance measurements on FIB-$VO_2$ for 3 cycles of heating and cooling between room temperature and 90 °C. Adapted from Ref[132].

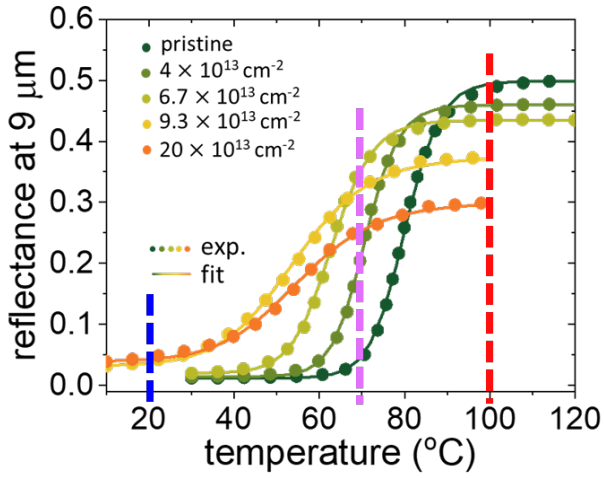


**Figure 4.24:** Temperature-dependent reflectance at 9 µm across the IMT for different levels of defect engineering (ion fluences).

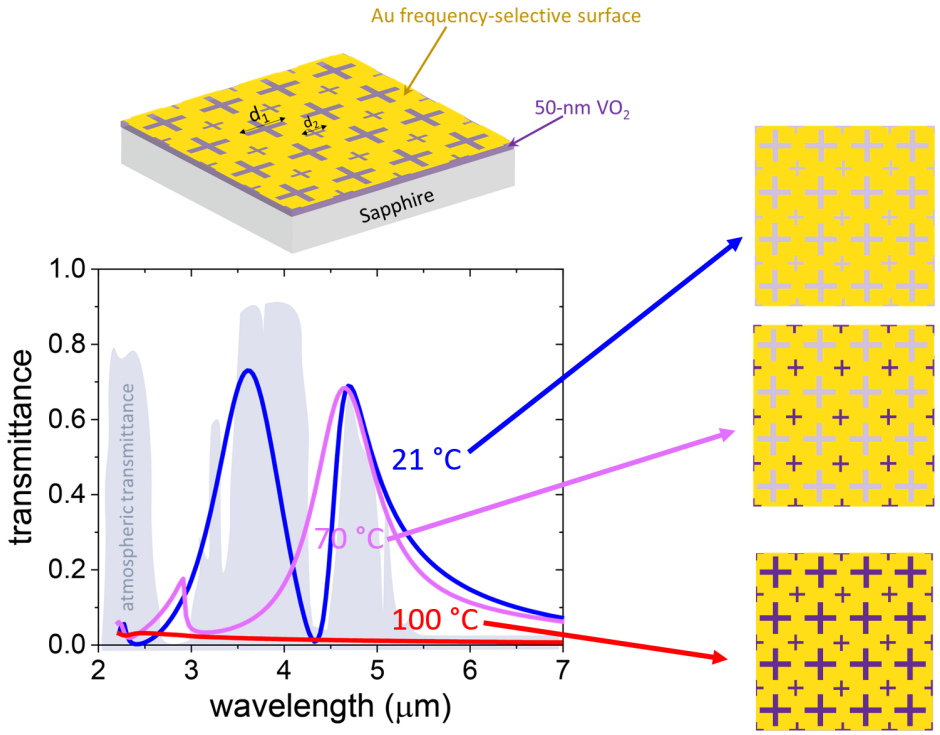


**Figure 4.25:** Design of a tunable dual-band transmission filter based on FIB-$VO_2$. *Unpublished data*

Here, we showcased an example of potential applicational uses of FIB-defected $VO_2$, which is a dual-band transmission filter with a gold frequency-selective surface on top of the thin film $VO_2$. In particular, we can have two different sets of gold apertures corresponding to two resonant central wavelengths. This design can give us two separate transparent windows when the $VO_2$ is in the insulating phase, for example, at 21 °C. When the $VO_2$ is transformed to the metallic phase, for example, at 100 °C, the transmission goes down to zero for all wavelength ranges. And we can use FIB to modify the phase transition of $VO_2$ through one of the two sets of apertures such that we can have a temperature (for example, at 70 °C) to allow one of the two apertures

in insulating phase and the other in metallic phase, which gives us a single transparent window in the spectrum. With FIB direct writing, one can make the $VO_2$ has different phase transition temperatures in different regions within one sample, providing more degrees of freedom for the design of tunable optical devices.

In conclusion, we have shown that the optical properties of two oxide materials, zinc oxide (ZnO) and vanadium dioxide ($VO_2$), can be locally modulated by doping or defect engineering using a commercial focused ion beam (FIB) with gallium ions. Using the FIB, we modified the carrier concentrations in initially undoped ZnO, reaching carrier concentrations as high as $10^{20}$ $cm^{-3}$, and reduced the temperature of the insulator-to-metal transition (IMT) in $VO_2$ by as much as ~25 °C. The FIB process does not require any lithography or masking, and only requires one additional annealing step in the case of doping. Due to the versatility of commercial FIBs, this technique can be used to modify and engineer materials with high resolution even for the case of irregularly shaped materials where conventional lithography is challenging. The ability to dope and defect-engineer certain oxides using a commercial FIB provides functionalities beyond the more-common FIB milling and deposition, and may enable the direct fabrication of a broader range of infrared devices based on semiconducting oxides.

# Chapter 5

## Summary and outlook

During my PhD, I developing novel characterization techniques and discovered new materials with enhanced optical properties. We have successfully integrated advanced spectroscopic methods to characterize and engineer materials within the infrared spectrum, leading to innovations in ultrathin optical devices and complex optical structures.

The research presented here employed FTIR systems and spectroscopic ellipsometry to understand and manipulate the optical interactions of new infrared materials, specifically the $A_{1+x}BX_3$ series, demonstrating substantial birefringence. This facilitated the development of novel polarization optics and provided insights into the mechanisms behind optical anisotropy, which are essential for designing next-generation materials.

By leveraging focused ion beam technology for selective material modulation, we demonstrated the ability to engineer sophisticated functionalities into semiconductor materials such as ZnO and $VO_2$. These capabilities allow for the precise control of

material properties without conventional lithographic techniques, opening up possibilities for more efficient and versatile optical components.

Looking forward, the potential for expanding these technologies is immense. Future research should focus on refining these characterization and fabrication techniques, exploring further the properties of new optical materials, and expanding their applications. The integration of these advanced materials into existing systems promises to drive innovations in various technology sectors, potentially revolutionizing optical devices, telecommunications, and beyond. This work lays a strong foundation for the continued exploration and expansion of optical material sciences.

# Bibliography


1. Burton, H. E. The Optics of Euclid1. *J. Opt. Soc. Am., JOSA* **35**, 357–372 (1945).
2. Ptolemy & Smith, A. M. *Ptolemy's Theory of Visual Perception: An English Translation of the Optics*. (American Philosophical Society, 1996).
3. Alhazen. *The Optics of Ibn Al-Haytham: Books I-III : On Direct Vision*. (Warburg Institute, University of London, 1989).
4. Kepler, J., 1571-1630. *Optics : Paralipomena to Witelo & Optical Part of Astronomy / Johannes Kepler ; Translated by William H. Donahue*. (Santa Fe, N.M. : Green Lion Press, 2000., 2000).
5. Newton, I. *Opticks:: Or, a Treatise of the Reflexions, Refractions, Inflexions and Colours of Light. Also Two Treatises of the Species and Magnitude of Curvilinear Figures.*. (Sam. Smith, and Benj. Walford, printers to the Royal Society, at the Prince's Arms in St. Paul's Church-yard., 1704).
6. Young, T. & Kelland, P. *A Course of Lectures on Natural Philosophy and the Mechanical Arts*. (Taylor and Walton, 1845).
7. Fresnel, A. Note sur le calcul des teintes que la polarisation développe dans les lames cristallisées. *Annales de chimie et physique* **17**, 101–112 (1821).
8. Maxwell, J. C. A Dynamical Theory of the Electromagnetic Field. *Philosophical Transactions of the Royal Society of London* **155**, 459–512 (1865).
9. Einstein, A. Über einen die Erzeugung und Verwandlung des Lichtes betreffenden heuristischen Gesichtspunkt. *Annalen der Physik* **322**, 132–148 (1905).
10. Bohr, N. I. On the constitution of atoms and molecules. *The London, Edinburgh, and Dublin Philosophical Magazine and Journal of Science* **26**, 1–25 (1913).

11. The Electromagnetic Spectrum Video Series & Companion Book. https://science.nasa.gov/ems/.

12. Cozzolino, D. *Infrared Spectroscopy for Environmental Monitoring*. (Elsevier Science, 2022).

13. Ring, E. F. J. & Ammer, K. The technique of infrared imaging in medicine. in *Infrared Imaging: A casebook in clinical medicine* (IOP Publishing, 2015). doi:10.1088/978-0-7503-1143-4ch1.

14. Infrared Thermal Imaging: Fundamentals, Research and Applications, 2nd Edition | Wiley. *Wiley.com* https://www.wiley.com/en-us/Infrared+Thermal+Imaging%3A+Fundamentals%2C+Research+and+Applications%2C+2nd+Edition-p-9783527413515.

15. Kahn, J. M. & Barry, J. R. Wireless infrared communications. *Proceedings of the IEEE* **85**, 265–298 (1997).

16. Infrared Astronomy. *Webb* https://webbtelescope.org/home/webb-science/the-observatory/infrared-astronomy.

17. Lloyd, J. M. *Thermal Imaging Systems*. (Springer US, 2013).

18. Gade, R. & Moeslund, T. B. Thermal cameras and applications: a survey. *Machine Vision and Applications* **25**, 245–262 (2014).

19. Xiao, Y. *et al.* Precision Measurements of Temperature-Dependent and Nonequilibrium Thermal Emitters. *Laser and Photonics Reviews* **14**, 1–17 (2020).

20. Yao, C. *et al.* Correcting thermal-emission-induced detector saturation in infrared spectroscopy. *Opt. Express, OE* **30**, 38458–38467 (2022).

21. Smith, J. G. *Organic Chemistry*. (McGraw-Hill Education, 2019).

22. Harris, D. C. & Bertolucci, M. D. *Symmetry and Spectroscopy: An Introduction to Vibrational and Electronic Spectroscopy*. (Dover Publications, 1989).

23. Hollas, J. M. *Modern Spectroscopy*. (Wiley, 2013).

24. Ritter, E. *et al.* Time-resolved infrared spectroscopic techniques as applied to channelrhodopsin. *Front. Mol. Biosci.* **2**, (2015).

25. White, R. *Chromatography/Fourier Transform Infrared Spectroscopy and Its Applications*. (Taylor & Francis, 1989).

26. Bierman, D. M. *et al.* Enhanced photovoltaic energy conversion using thermally based spectral shaping. *Nat Energy* **1**, 1–7 (2016).

27. Ilic, O. *et al.* Tailoring high-temperature radiation and the resurrection of the incandescent source. *Nature Nanotech* **11**, 320–324 (2016).

28. Raman, A. P., Anoma, M. A., Zhu, L., Rephaeli, E. & Fan, S. Passive radiative cooling below ambient air temperature under direct sunlight. *Nature* **515**, 540–544 (2014).

29. Shahsafi, A. *et al.* Temperature-independent thermal radiation. *Proceedings of the National Academy of Sciences* **116**, 26402–26406 (2019).

30. Kats, M. A. *et al.* Vanadium dioxide as a natural disordered metamaterial: perfect thermal emission and large broadband negative differential thermal emittance. *Physical Review X* **3**, 041004 (2013).

31. Baranov, D. G. *et al.* Nanophotonic engineering of far-field thermal emitters. *Nat. Mater.* **18**, 920–930 (2019).

32. Planck, M. Ueber das Gesetz der Energieverteilung im Normalspectrum. *Annalen der Physik* **309**, 553–563 (1901).

33. Kirchhoff, G. Über das Verhältnis zwischen dem Emissionsvermögen und dem Absorptionsvermögen der Körper für Wärme und Licht. in *Von Kirchhoff bis Planck: Theorie der Wärmestrahlung in historisch-kritischer Darstellung* (ed. Schöpf, H.-G.) 131–151 (Vieweg+Teubner Verlag, Wiesbaden, 1978). doi:10.1007/978-3-663-13885-3_10.

34. Hadad, Y., Soric, J. C. & Alu, A. Breaking temporal symmetries for emission and absorption. *Proceedings of the National Academy of Sciences* **113**, 3471–3475 (2016).

35. Zhu, L. & Fan, S. Near-complete violation of detailed balance in thermal radiation. *Phys. Rev. B* **90**, 220301 (2014).

36. Tsang, L., Njoku, E. & Kong, J. A. Microwave thermal emission from a stratified medium with nonuniform temperature distribution. *Journal of Applied Physics* **46**, 5127–5133 (1975).

37. Xiao, Y., Charipar, N. A., Salman, J., Piqué, A. & Kats, M. A. Nanosecond mid-infrared pulse generation via modulated thermal emissivity. *Light Sci Appl* **8**, 51 (2019).

38. Xiao, Y. *et al.* Measuring Thermal Emission Near Room Temperature Using Fourier-Transform Infrared Spectroscopy. *Phys. Rev. Appl.* **11**, 014026 (2019).

39. Seyf, H. R. & Henry, A. Thermophotovoltaics: a potential pathway to high efficiency concentrated solar power. *Energy Environ. Sci.* **9**, 2654–2665 (2016).

40. Bermel, P. *et al.* Design and global optimization of high-efficiency thermophotovoltaic systems. *Opt. Express, OE* **18**, A314–A334 (2010).

41. Yeng, Y. X. *et al.* Enabling high-temperature nanophotonics for energy applications. *Proceedings of the National Academy of Sciences* **109**, 2280–2285 (2012).

42. Revercomb, H. E. *et al.* Radiometric calibration of IR Fourier transform spectrometers: solution to a problem with the High-Resolution Interferometer Sounder. *Appl. Opt., AO* **27**, 3210–3218 (1988).

43. Lindermeir, E., Haschberger, P., Tank, V. & Dietl, H. Calibration of a Fourier transform spectrometer using three blackbody sources. *Appl. Opt., AO* **31**, 4527–4533 (1992).

44. Clausen, S., Morgenstjerne, A. & Rathmann, O. Measurement of surface temperature and emissivity by a multitemperature method for Fourier-transform infrared spectrometers. *Appl. Opt., AO* **35**, 5683–5691 (1996).

45. Mizuno, K. *et al.* A black body absorber from vertically aligned single-walled carbon nanotubes. *Proceedings of the National Academy of Sciences* **106**, 6044–6047 (2009).

46. Rozenbaum, O., Meneses, D. D. S., Auger, Y., Chermanne, S. & Echegut, P. A spectroscopic method to measure the spectral emissivity of semi-transparent materials up to high temperature. *Review of Scientific Instruments* **70**, 4020–4025 (1999).

47. Minami, Y., Yogi, T. & Sakai, K. Thermal phonon resonance in solid glass. *Japanese journal of applied physics* **45**, 4469 (2006).

48. Ballard, J., Remedios, J. J. & Roscoe, H. K. The effect of sample emission on measurements of spectral parameters using a fourier transform absorption spectrometer. *Journal of Quantitative Spectroscopy and Radiative Transfer* **48**, 733–741 (1992).

49. Tripp, C. P. & McFarlane, R. A. Discussion of the Stray Light Rejection Efficiency of FT-IR Spectrometers: The Effects of Sample Emission on FT-IR Spectra. *Applied spectroscopy* **48**, 1138–1142 (1994).

50. Richardson Jr, R. L., Yang, H. & Griffiths, P. R. Effects of detector nonlinearity on spectra measured on three commercial FT-IR spectrometers. *Applied spectroscopy* **52**, 572–578 (1998).

51. Fiedler, L., Newman, S. & Bakan, S. Correction of detector nonlinearity in Fourier transform spectroscopy with a low-temperature blackbody. *Applied optics* **44**, 5332–5340 (2005).

52. Rahimi, N., Patadia, A., Babic, D., Grubisic, D. & Kunsch, J. P1.3 - Characterization of the Linearity of InGaAs Photodetectors Using Series Resistance. *Tagungsband* 519–523 (2016) doi:10.5162/sensoren2016/P1.3.

53. Hoefler, J. J. & Taylor, R. E. Effects of infrared detector nonlinearity on thermal diffusivity measurements using the flash method. *Int J Thermophys* **11**, 1099–1110 (1990).

54. Kempfert, K. D., Jiang, E. Y., Oas, S. & Coffin, J. Detectors for Fourier transform spectroscopy. *AN-00125* (2001).

55. Bowie, B. T. & Griffiths, P. R. Measurement of the sensitivity and photometric accuracy of FT-IR spectrometers. *Applied Spectroscopy* **54**, 1192–1202 (2000).

56. Shao, L. & Griffiths, P. R. Correcting nonlinear response of mercury cadmium telluride detectors in open path Fourier transform infrared spectrometry. *Analytical chemistry* **80**, 5219–5224 (2008).

57. Sova, R. M., Linevsky, M. J., Thomas, M. E. & Mark, F. F. High-temperature infrared properties of sapphire, AlON, fused silica, yttria, and spinel. *Infrared physics & technology* **39**, 251–261 (1998).

58. Bode, H. W. & Shannon, C. E. A simplified derivation of linear least square smoothing and prediction theory. *Proceedings of the IRE* **38**, 417–425 (1950).

59. Huang, T., Dong, S., Quo, X., Xiao, L. & Jia, S. Signal-to-noise ratio improvement of photon counting using wavelength modulation spectroscopy. *Applied Physics Letters* **89**, (2006).

60. Fujiwara, H. *Spectroscopic Ellipsometry: Principles and Applications*. (Wiley, 2007).

61. Tiwald, T. E. Measurement of free carriers in silicon and silicon carbide using infrared ellipsometry. *ETD collection for University of Nebraska - Lincoln* 1–87 (1999).

62. *Guide to Using WVASE 32: Spectroscopic Ellipsometry Data Acquisition and Analysis Software*. (J. A. Woollam Company, Incorporated, 2008).

63. Woollam, J. Guide to Using WVASE 32: Spectroscopic Ellipsometry Data Acquisition and Analysis Software. *JA Woollam Company, Lincoln, NE, USA* (2012).

64. Peiponen, K.-E. & Vartiainen, E. M. Kramers-Kronig relations in optical data inversion. *Phys. Rev. B* **44**, 8301–8303 (1991).

65. Johs, B. *et al.* Overview of variable-angle spectroscopic ellipsometry (VASE): II. Advanced applications. in *Optical Metrology: A Critical Review* vol. 10294 1029404 (International Society for Optics and Photonics, 1999).

66. Zhao, B. *et al.* Orientation-controlled anisotropy in single crystals of quasi-1D $BaTiS_3$. *Chem. Mater.* **34**, 5680–5689 (2022).

67. Zhao, B. *et al.* Giant Modulation of Refractive Index from Picoscale Atomic Displacements. *Advanced Materials* **n/a**, 2311559.

68. Chen, H. *et al.* Molten flux growth of single crystals of quasi-1D hexagonal chalcogenide BaTiS3. Preprint at https://doi.org/10.48550/arXiv.2403.05869 (2024).

69. Zhao, B. *et al.* Infrared Optical Anisotropy in Quasi-1D Hexagonal Chalcogenide BaTiSe3. *arXiv.org* https://arxiv.org/abs/2402.02323v1 (2024).

70. Mei, H. *et al.* Colossal Optical Anisotropy from Atomic-Scale Modulations. *Advanced Materials* **35**, 2303588 (2023).

71. Weber, M. F., Stover, C. A., Gilbert, L. R., Nevitt, T. J. & Ouderkirk, A. J. Giant birefringent optics in multilayer polymer mirrors. *Science* **287**, 2451–2456 (2000).

72. Yasuno, Y., Makita, S., Sutoh, Y., Itoh, M. & Yatagai, T. Birefringence imaging of human skin by polarization-sensitive spectral interferometric optical coherence tomography. *Opt. Lett.* **27**, 1803–1805 (2002).

73. Oka, K. & Kaneko, T. Compact complete imaging polarimeter using birefringent wedge prisms. *Opt. Express* **11**, 1510–1519 (2003).

74. Nicholls, L. H. *et al.* Ultrafast synthesis and switching of light polarization in nonlinear anisotropic metamaterials. *Nat. Photon.* **11**, 628–633 (2017).

75. Wu, C. *et al.* Giant optical anisotropy in the UV-transparent 2D nonlinear optical material $Sc(IO_3)_2(NO_3)$. *Angewandte Chemie* **133**, 3506–3510 (2021).

76. de Dood, M. J. A., Irvine, W. T. M. & Bouwmeester, D. Nonlinear Photonic Crystals as a Source of Entangled Photons. *Phys. Rev. Lett.* **93**, 040504 (2004).

77. Riccardi, M. & Martin, O. J. F. Electromagnetic forces and torques: from dielectrophoresis to optical tweezers. *Chem. Rev.* (2023).

78. Dyakonov, M. New type of electromagnetic wave propagating at an interface. *J. Exp. Theor. Phys.* **94**, 119 (1988).

79. Ma, W. *et al.* In-plane anisotropic and ultra-low-loss polaritons in a natural van der Waals crystal. *Nature* **562**, 557–562 (2018).

80. Chaudhary, K. *et al.* Engineering phonon polaritons in van der Waals heterostructures to enhance in-plane optical anisotropy. *Sci. Adv.* **5**, eaau7171 (2019).

81. Ma, W. *et al.* Ghost hyperbolic surface polaritons in bulk anisotropic crystals. *Nature* **596**, 362–366 (2021).

82. Bartholin, R. *Experimenta Crystalli Islandici disdiaclastici, quibus mira et insolita refractio detegitur*. (1669).

83. Fresnel, A. Extrait d'un Mémoire sur la double réfraction. *Annales de chimie et physique* **28**, 263–279 (1825).

84. Bragg, W. L. The refractive indices of calcite and aragonite. *Proceedings of the Royal Society of London. Series A, Containing Papers of a Mathematical and Physical Character* **105**, 370–386 (1924).

85. Bragg, W. L. *Atomic Structure of Minerals*. (Cornell University Press, 1937).

86. Lawless, W. N. & Devries, R. C. Oxygen polarizability and point-dipole theory in the carbonate minerals. *J. Phys. Chem. Solids.* **25**, 1119–1124 (1964).

87. Isherwood, B. J. & James, J. A. Structural dependence of the optical birefringence of crystals with calcite and aragonite type structures. *Acta Cryst. A* **32**, 340–341 (1976).

88. Segura, A. *et al.* Natural optical anisotropy of h-BN: Highest giant birefringence in a bulk crystal through the mid-infrared to ultraviolet range. *Phys. Rev. Mater.* **2**, 024001 (2018).

89. Ermolaev, G. A. *et al.* Giant optical anisotropy in transition metal dichalcogenides for next-generation photonics. *Nat. Commun.* **12**, 854 (2021).

90. Wang, Q. H., Kalantar-Zadeh, K., Kis, A., Coleman, J. N. & Strano, M. S. Electronics and optoelectronics of two-dimensional transition metal dichalcogenides. *Nat. Nanotech.* **7**, 699–712 (2012).

91. Álvarez-Pérez, G. *et al.* Infrared permittivity of the biaxial van der Waals semiconductor α-$MoO_3$ from near- and far-field correlative studies. *Adv. Mater.* **32**, 1908176 (2020).

92. Taboada-Gutiérrez, J. *et al.* Broad spectral tuning of ultra-low-loss polaritons in a van der Waals crystal by intercalation. *Nat. Mater.* **19**, 964–968 (2020).

93. Niu, S. *et al.* Giant optical anisotropy in a quasi-one-dimensional crystal. *Nat. Photon.* **12**, 392–396 (2018).

94. Sinton, W. M. Birefringence of rutile in the infrared. *J. Opt. Soc. Am.* **51**, 1309_1 (1961).

95. Ghosh, G. Dispersion-equation coefficients for the refractive index and birefringence of calcite and quartz crystals. *Optics Communications* **163**, 95–102 (1999).

96. Zelmon, D. E., Small, D. L. & Jundt, D. Infrared corrected Sellmeier coefficients for congruently grown lithium niobate and 5 mol% magnesium oxide –doped lithium niobate. *J. Opt. Soc. Am. B* **14**, 3319 (1997).

97. Luo, H. T., Tkaczyk, T., Dereniak, E. L., Oka, K. & Sampson, R. High birefringence of the yttrium vanadate crystal in the middle wavelength infrared. *Opt. Lett.* **31**, 616 (2006).

98. Segura, A. *et al.* Natural optical anisotropy of h-BN: Highest giant birefringence in a bulk crystal through the mid-infrared to ultraviolet range. *Phys. Rev. Materials* **2**, 024001 (2018).

99. Guoqing, Z. *et al.* Growth and spectrum of a novel birefringent α-BaB2O4 crystal. *Journal of Crystal Growth* **191**, 517–519 (1998).

100. Chenault, D. B. & Chipman, R. A. Infrared birefringence spectra for cadmium sulfide and cadmium selenide. *Appl. Opt.* **32**, 4223 (1993).

101. Dodge, M. J. Refractive properties of magnesium fluoride. *Appl. Opt.* **23**, 1980 (1984).

102. Nikogosi͡an, D. N. *Nonlinear Optical Crystals: A Complete Survey*. (Springer-Science, New York, 2005).

103. Niu, S. *et al.* Giant optical anisotropy in a quasi-one-dimensional crystal. *Nat. Photon.* **12**, 392–396 (2018).

104. Mei, H. *et al.* Colossal optical anisotropy from atomic-scale modulations. *Advanced Materials* 2303588 (2023).

105. Tranchitella, L. J., Fettinger, J. C., Dorhout, P. K., Van Calcar, P. M. & Eichhorn, B. W. Commensurate columnar composite compounds: synthesis and structure of $Ba_{15}Zr_{14}Se_{42}$ and $Sr_{21}Ti_{19}Se_{57}$. *J. Am. Chem. Soc.* **120**, 7639–7640 (1998).

106. Loye, H.-C. zur, Zhao, Q., E. Bugaris, D. & Michael Chance, W. 2*H*-perovskite related oxides: Synthesis, structures, and predictions. *CrystEngComm* **14**, 23–39 (2012).

107. Niu, S. *et al.* Mid-wave and long-wave infrared linear dichroism in a hexagonal perovskite chalcogenide. *Chem. Mater.* **30**, 4897–4901 (2018).

108. Gourdon, O., Petricek, V. & Evain, M. A new structure type in the hexagonal perovskite family; structure determination of the modulated misfit compound $Sr_{9/8}TiS_3$. *Acta Cryst. B* **56**, 409–418 (2000).

109. Gourdon, O. *et al.* Influence of the metal–metal sigma bonding on the structures and physical properties of the hexagonal perovskite-type sulfides $Sr_{9/8}TiS_3$, $Sr_{8/7}TiS_3$, and $Sr_{8/7}[Ti_{6/7}Fe_{1/7}]S_3$. *J. Solid State Chem.* **162**, 103–112 (2001).

110. Sun, W. *et al.* The thermodynamic scale of inorganic crystalline metastability. *Sci. Adv.* **2**, e1600225 (2016).

111. Jain, A. *et al.* Commentary: The Materials Project: A materials genome approach to accelerating materials innovation. *APL Materials* **1**, 011002 (2013).

112. R. Akbarzadeh, A., Ozoliņš, V. & Wolverton, C. First-Principles Determination of Multicomponent Hydride Phase Diagrams: Application to the Li-Mg-N-H System. *Advanced Materials* **19**, 3233–3239 (2007).

113. Yamamoto, A. Crystallography of quasiperiodic crystals. *Acta Cryst. A* **52**, 509–560 (1996).

114. Onoda, M., Saeki, M., Yamamoto, A. & Kato, K. Structure refinement of the incommensurate composite crystal $Sr_{1.145}TiS_3$ through the Rietveld analysis process. *Acta Cryst. B* **49**, 929–936 (1993).

115. International Tables for Crystallography. *urn:isbn:978-1-4020-4969-9* https://it.iucr.org/ doi:10.1107/97809553602060000001.

116. Stokes, H. T., Campbell, B. J. & van Smaalen, S. Generation of (3 + *d*)-dimensional superspace groups for describing the symmetry of modulated crystalline structures. *Acta Cryst. A* **67**, 45–55 (2011).

117. Pennycook, S. J. & Jesson, D. E. High-resolution Z-contrast imaging of crystals. *Ultramicroscopy* **37**, 14–38 (1991).

118. Mukherjee, D., Miao, L., Stone, G. & Alem, N. mpfit: a robust method for fitting atomic resolution images with multiple Gaussian peaks. *Adv. Struct. Chem.* **6**, 1 (2020).

119. Thind, A. S., Huang, X., Sun, J. & Mishra, R. First-principles prediction of a stable hexagonal phase of $CH_3NH_3PbI_3$. *Chem. Mater.* **29**, 6003–6011 (2017).

120. Wagner, N., Seshadri, R. & Rondinelli, J. M. Property control from polyhedral connectivity in $ABO_3$ oxides. *Phys. Rev. B* **100**, 064101 (2019).

121. Dudarev, S. L., Botton, G. A., Savrasov, S. Y., Humphreys, C. J. & Sutton, A. P. Electron-energy-loss spectra and the structural stability of nickel oxide: An LSDA+U study. *Phys. Rev. B* **57**, 1505–1509 (1998).

122. Gajdoš, M., Hummer, K., Kresse, G., Furthmüller, J. & Bechstedt, F. Linear optical properties in the projector-augmented wave methodology. *Phys. Rev. B* **73**, 045112 (2006).

123. Sun, B. *et al.* High frequency atomic tunneling yields ultralow and glass-like thermal conductivity in chalcogenide single crystals. *Nat Commun* **11**, 6039 (2020).

124. Pennycook, S. J. & Jesson, D. E. High-resolution Z-contrast imaging of crystals. *Ultramicroscopy* **37**, 14–38 (1991).

125. Gajdoš, M., Hummer, K., Kresse, G., Furthmüller, J. & Bechstedt, F. Linear optical properties in the projector-augmented wave methodology. *Phys. Rev. B* **73**, 045112 (2006).

126. Maslen, E. N., Streltsov, V. A., Streltsova, N. R. & Ishizawa, N. Electron density and optical anisotropy in rhombohedral carbonates. III. Synchrotron X-ray studies of $CaCO_3$, $MgCO_3$ and $MnCO_3$. *Acta Crystallogr B Struct Sci* **51**, 929–939 (1995).

127. Mathew, T., Rahul K, S., Joseph, S. & Mathew, V. Density functional study of structural, electronic and optical properties of quasi-one-dimensional compounds $BaTiX_3$ ( X = S , Se ). *Superlattices and Microstructures* **153**, 106859 (2021).

128. Chen, F. R., Xu, Z. G. & Wang, Y. T. Near-field radiative heat transfer enhancement in the thermophotovoltaic system using hyperbolic waveguides. *International Journal of Thermal Sciences* **166**, 106978 (2021).

129. Caldwell, J. D. *et al.* Low-loss, infrared and terahertz nanophotonics using surface phonon polaritons. *Nanophotonics* **4**, 44–68 (2015).

130. Fante, R. L. & McCormack, M. T. Reflection properties of the Salisbury screen. *IEEE Transactions on Antennas and Propagation* **36**, 1443–1454 (1988).

131. Salisbury, W. W. Absorbent body for electromagnetic waves. (1952).

132. Mei, H. *et al.* Tuning carrier density and phase transitions in oxide semiconductors using focused ion beams. *Nanophotonics* **11**, 3923–3932 (2022).

133. Koch, A. *et al.* Heavily Doped Zinc Oxide with Plasma Frequencies in the Telecommunication Wavelength Range. *Advanced Photonics Research* **4**, 2200181 (2023).

134. Giannuzzi, L. A. & Stevie, F. A. A review of focused ion beam milling techniques for TEM specimen preparation. *Micron* **30**, 197–204 (1999).

135. Melngailis, J. Focused ion beam technology and applications. *Journal of Vacuum Science & Technology B: Microelectronics Processing and Phenomena* **5**, 469–495 (1987).

136. Reyntjens, S. & Puers, R. A review of focused ion beam applications in microsystem technology. *Journal of micromechanics and microengineering* **11**, 287 (2001).

137. Volkert, C. A. & Minor, A. M. Focused Ion Beam Microscopy and Micromachining. *MRS Bulletin* **32**, 389–399 (2007).

138. Matsui, S. & Ochiai, Y. Focused ion beam applications to solid state devices. *Nanotechnology* **7**, 247–258 (1996).

139. Mayer, J., Giannuzzi, L. A., Kamino, T. & Michael, J. TEM Sample Preparation and FIB-Induced Damage. *MRS Bulletin* **32**, 400–407 (2007).

140. Karre, P. S. K., Bergstrom, P. L., Mallick, G. & Karna, S. P. Room temperature operational single electron transistor fabricated by focused ion beam deposition. *Journal of Applied Physics* **102**, 024316 (2007).

141. Lanyon, Y. H. *et al.* Fabrication of Nanopore Array Electrodes by Focused Ion Beam Milling. *Anal. Chem.* **79**, 3048–3055 (2007).

142. Kim, Y. K., Danner, A. J., Raftery, J. J. & Choquette, K. D. Focused Ion Beam Nanopatterning for Optoelectronic Device Fabrication. *IEEE Journal of Selected Topics in Quantum Electronics* **11**, 1292–1298 (2005).

143. Nikawa, K. Applications of focused ion beam technique to failure analysis of very large scale integrations: A review. *Journal of Vacuum Science & Technology B: Microelectronics and Nanometer Structures Processing, Measurement, and Phenomena* **9**, 2566–2577 (1991).

144. Stewart, D. K., Morgan, J. A. & Ward, B. Focused ion beam induced deposition of tungsten on vertical sidewalls. *Journal of Vacuum Science & Technology B: Microelectronics and Nanometer Structures Processing, Measurement, and Phenomena* **9**, 2670–2674 (1991).

145. Salman, J. *et al.* Flat Optical and Plasmonic Devices Using Area-Selective Ion-Beam Doping of Silicon. *Advanced Optical Materials* **6**, 1701027 (2018).

146. Look, D. C. & Leedy, K. D. ZnO plasmonics for telecommunications. *Appl. Phys. Lett.* **102**, 182107 (2013).

147. Kesim, Y. E., Battal, E. & Okyay, A. K. Plasmonic materials based on ZnO films and their potential for developing broadband middle-infrared absorbers. *AIP Advances* **4**, 077106 (2014).

148. Kim, J. *et al.* Optical Properties of Gallium-Doped Zinc Oxide---A Low-Loss Plasmonic Material: First-Principles Theory and Experiment. *Phys. Rev. X* **3**, 041037 (2013).

149. Naik, G. V., Shalaev, V. M. & Boltasseva, A. Alternative Plasmonic Materials: Beyond Gold and Silver. *Advanced Materials* **25**, 3264–3294 (2013).

150. Chen, L.-Y., Chen, W.-H., Wang, J.-J., Hong, F. C.-N. & Su, Y.-K. Hydrogen-doped high conductivity ZnO films deposited by radio-frequency magnetron sputtering. *Appl. Phys. Lett.* **85**, 5628–5630 (2004).

151. Henley, S. J., Ashfold, M. N. R. & Cherns, D. The growth of transparent conducting ZnO films by pulsed laser ablation. *Surface and Coatings Technology* **177–178**, 271–276 (2004).

152. Bae, S. Y., Na, C. W., Kang, J. H. & Park, J. Comparative Structure and Optical Properties of Ga-, In-, and Sn-Doped ZnO Nanowires Synthesized via Thermal Evaporation. *J. Phys. Chem. B* **109**, 2526–2531 (2005).

153. Ataev, B. M., Bagamadova, A. M., Djabrailov, A. M., Mamedov, V. V. & Rabadanov, R. A. Highly conductive and transparent Ga-doped epitaxial ZnO films on sapphire by CVD. *Thin Solid Films* **260**, (1995).

154. Fahey, P. M., Griffin, P. B. & Plummer, J. D. Point defects and dopant diffusion in silicon. *Rev. Mod. Phys.* **61**, 289–384 (1989).

155. Baumann, I. *et al.* Erbium incorporation in LiNbO3 by diffusion-doping. *Appl Phys A* **64**, 33–44 (1996).

156. Williams, J. S. Ion implantation of semiconductors. *Materials Science and Engineering: A* **253**, 8–15 (1998).

157. Letizia, R. & Pinto, D. Analysis of Nitrides- and TCOs-Based Plasmonic Waveguides for Slow-Wave and Negative Index Sub-Wavelength Propagation. *Journal of Lightwave Technology* **32**, 1578–1584 (2014).

158. Xu, F. & Sun, Y. Efficient second harmonic generation between photonic and plasmonic modes in a tunable transparent conducting oxide waveguide. *Chin. Opt. Lett., COL* **14**, 031901 (2016).

159. Pandey, S. K. *et al.* Band alignment and photon extraction studies of Na-doped MgZnO/Ga-doped ZnO heterojunction for light-emitter applications. *Journal of Applied Physics* **118**, 165301 (2015).

160. Singh, K., Bandyopadhyay, A. & Sengupta, A. Low-Loss Metallic Waveguide for Terahertz Applications. 5.

161. Kim, J. *et al.* Controlling the Polarization State of Light with Plasmonic Metal Oxide Metasurface. *ACS Nano* **10**, 9326–9333 (2016).

162. Kim, J. *et al.* GZO/ZnO multilayered nanodisk metasurface to engineer the plasma frequency. in *2014 Conference on Lasers and Electro-Optics (CLEO) - Laser Science to Photonic Applications* 1–2 (2014).

163. Kim, J. Plasmonic devices based on transparent conducting oxides for near infrared applications. (Purdue University, United States -- Indiana).

164. Ziegler, J. F. & Biersack, J. P. The stopping and range of ions in matter. in *Treatise on heavy-ion science* 93–129 (Springer, 1985).

165. Zhong, Y., Malagari, S. D., Hamilton, T. & Wasserman, D. M. Review of mid-infrared plasmonic materials. *JNP* **9**, 093791 (2015).

166. Zamiri, R. *et al.* Far-infrared optical constants of ZnO and ZnO/Ag nanostructures. *RSC Adv.* **4**, 20902–20908 (2014).

167. Johansen, K. M., Vines, L., Bjørheim, T. S., Schifano, R. & Svensson, B. G. Aluminum Migration and Intrinsic Defect Interaction in Single-Crystal Zinc Oxide. *Phys. Rev. Applied* **3**, 024003 (2015).

168. Sky, T. N., Johansen, K. M., Riise, H. N., Svensson, B. G. & Vines, L. Gallium diffusion in zinc oxide via the paired dopant-vacancy mechanism. *Journal of Applied Physics* **123**, 055701 (2018).

169. Nakagawa, T. *et al.* Diffusion Model of Gallium in Single-Crystal ZnO Proposed from Analysis of Concentration-Dependent Profiles Based on the Fermi-Level Effect. *Jpn. J. Appl. Phys.* **46**, 4099 (2007).

170. Prucnal, S., Rebohle, L. & Skorupa, W. Doping by flash lamp annealing. *Materials Science in Semiconductor Processing* **62**, 115–127 (2017).

171. Lindberg, P. F. *et al.* The effect of millisecond flash lamp annealing on electrical and structural properties of ZnO: Al/Si structures. *Journal of Applied Physics* **119**, 185305 (2016).

172. Hsiao, W.-T. *et al.* Effect on structural, optical and electrical properties of aluminum-doped zinc oxide films using diode laser annealing. *Optics & Laser Technology* **68**, 41–47 (2015).

173. Cranton, W. *et al.* Enhanced electrical and optical properties of room temperature deposited Aluminium doped Zinc Oxide (AZO) thin films by excimer laser annealing. *Optics and Lasers in Engineering* **80**, 45–51 (2016).

174. Ding, C.-F., Hsiao, W.-T. & Young, H.-T. Effect on the electro-optical properties of transparent conducting aluminum doped zinc oxide thin films using low temperature ultraviolet laser annealing. *Journal of Materials Science: Materials in Electronics* **28**, 15647–15656 (2017).

175. Sky, T. N. *et al.* Diffusion of indium in single crystal zinc oxide: a comparison between group III donors. *Semicond. Sci. Technol.* **34**, 025011 (2019).

176. Ellmer, K. & Bikowski, A. Intrinsic and extrinsic doping of ZnO and ZnO alloys. *J. Phys. D: Appl. Phys.* **49**, 413002 (2016).

177. Nakagawa, T. *et al.* Analysis of Indium Diffusion Profiles Based on the Fermi-Level Effect in Single-Crystal Zinc Oxide. *Jpn. J. Appl. Phys.* **47**, 7848 (2008).

178. Ziegler, J. F., Ziegler, M. D. & Biersack, J. P. SRIM – The stopping and range of ions in matter (2010). *Nuclear Instruments and Methods in Physics Research Section B: Beam Interactions with Materials and Atoms* **268**, 1818–1823 (2010).

179. Komatsu, M., Ohashi, N., Sakaguchi, I., Hishita, S. & Haneda, H. Ga, N solubility limit in co-implanted ZnO measured by secondary ion mass spectrometry. *Applied Surface Science* **189**, 349–352 (2002).

180. McCluskey, M. D. & Jokela, S. J. Defects in ZnO. *Journal of Applied Physics* **106**, 071101 (2009).

181. Kohan, A. F., Ceder, G., Morgan, D. & Van de Walle, C. G. First-principles study of native point defects in ZnO. *Phys. Rev. B* **61**, 15019–15027 (2000).

182. Rita, E. *et al.* Lattice location and thermal stability of implanted Fe in ZnO. *Applied Physics Letters* **85**, 4899–4901 (2004).

183. Wahl, U. *et al.* Lattice location and stability of implanted Cu in ZnO. *Phys. Rev. B* **69**, 012102 (2004).

184. Rita, E. *et al.* Lattice site and stability of implanted Ag in ZnO. *Physica B: Condensed Matter* **340–342**, 240–244 (2003).

185. Alves, E. *et al.* Lattice site location and optical activity of Er implanted ZnO. *Nuclear Instruments and Methods in Physics Research Section B: Beam Interactions with Materials and Atoms* **206**, 1047–1051 (2003).

186. Wahl, U. *et al.* Implantation site of rare earths in single-crystalline ZnO. *Applied Physics Letters* **82**, 1173–1175 (2003).

187. Rita, E. *et al.* Optical doping of ZnO with Tm by ion implantation. *Physica B: Condensed Matter* **340–342**, 235–239 (2003).

188. Rensberg, J. *et al.* Active optical metasurfaces based on defect-engineered phase-transition materials. *Nano letters* **16**, 1050–1055 (2016).

189. Zhou, Y. *et al.* Strongly correlated perovskite fuel cells. *Nature* **534**, 231–234 (2016).

190. Wu, T. S. *et al.* Correlation between oxygen vacancies and magnetism in Mn-doped Y2O3 nanocrystals investigated by defect engineering techniques. *Appl. Phys. Lett.* **101**, 022408 (2012).

191. Yi, J. B. *et al.* Ferromagnetism in Dilute Magnetic Semiconductors through Defect Engineering: Li-Doped ZnO. *Phys. Rev. Lett.* **104**, 137201 (2010).

192. Brahlek, M. *et al.* Opportunities in vanadium-based strongly correlated electron systems. *MRS Communications* **7**, 27–52 (2017).

193. Li, Z., Wu, Q. & Wu, C. Surface/Interface Chemistry Engineering of Correlated-Electron Materials: From Conducting Solids, Phase Transitions to External-Field Response. *Advanced Science* **8**, 2002807 (2021).

194. He, Z. *et al.* Defect Engineering in Single-Layer MoS2 Using Heavy Ion Irradiation. *ACS Appl. Mater. Interfaces* **10**, 42524–42533 (2018).

195. Liang, Q., Zhang, Q., Zhao, X., Liu, M. & Wee, A. T. S. Defect Engineering of Two-Dimensional Transition-Metal Dichalcogenides: Applications, Challenges, and Opportunities. *ACS Nano* **15**, 2165–2181 (2021).

196. Lin, Z. *et al.* Defect engineering of two-dimensional transition metal dichalcogenides. *2D Mater.* **3**, 022002 (2016).

197. Runnerstrom, E. L. *et al.* Defect Engineering in Plasmonic Metal Oxide Nanocrystals. *Nano Lett.* **16**, 3390–3398 (2016).

198. Wang, F. *et al.* Defect-mediated ferromagnetism in correlated two-dimensional transition metal phosphorus trisulfides. *Science Advances* **7**, eabj4086.

199. Li, Z., Xiao, C., Zhu, H. & Xie, Y. Defect Chemistry for Thermoelectric Materials. *J. Am. Chem. Soc.* **138**, 14810–14819 (2016).

200. Kimerling, L. C. Defect Engineering. *MRS Bulletin* **16**, 42–47 (1991).

201. Feng, J. *et al.* Defect Engineering in Semiconductors: Manipulating Nonstoichiometric Defects and Understanding Their Impact in Oxynitrides for Solar Energy Conversion. *Advanced Functional Materials* **29**, 1808389 (2019).

202. Yang, Z., Ko, C. & Ramanathan, S. Oxide Electronics Utilizing Ultrafast Metal-Insulator Transitions. *Annu. Rev. Mater. Res.* **41**, 337–367 (2011).

203. Wan, C. *et al.* On the Optical Properties of Thin-Film Vanadium Dioxide from the Visible to the Far Infrared. *Annalen der Physik* **531**, 1900188 (2019).

204. Rensberg, J. Defect engineering of phase transition materials to create optical metasurfaces. (2018). doi:10.22032/dbt.34411.

205. Park, J. H. *et al.* Measurement of a solid-state triple point at the metal-insulator transition in VO 2. *Nature* **500**, 431–434 (2013).

206. Aetukuri, N. B. *et al.* Control of the metal–insulator transition in vanadium dioxide by modifying orbital occupancy. *Nature Phys* **9**, 661–666 (2013).

207. Cao, J. *et al.* Strain engineering and one-dimensional organization of metal–insulator domains in single-crystal vanadium dioxide beams. *Nature Nanotechnology* **4**, 732–737 (2009).

208. Wan, C. *et al.* Ultrathin Broadband Reflective Optical Limiter. *Laser and Photonics Reviews* **15**, 2100001 (2021).

209. Looyenga, H. Dielectric constants of heterogeneous mixtures. *Physica* **31**, 401–406 (1965).

210. Qazilbash, M. *et al.* Infrared spectroscopy and nano-imaging of the insulator-to-metal transition in vanadium dioxide. *Physical Review B* **79**, 075107 (2009).

211. Gurvitch, M., Luryi, S., Polyakov, A. & Shabalov, A. Nonhysteretic behavior inside the hysteresis loop of VO2 and its possible application in infrared imaging. *Journal of Applied Physics* **106**, 104504 (2009).

212. Liu, M. *et al.* Symmetry breaking and geometric confinement in VO2: Results from a three-dimensional infrared nano-imaging. *Appl. Phys. Lett.* **104**, 121905 (2014).

213. Cao, J. *et al.* Extended Mapping and Exploration of the Vanadium Dioxide Stress-Temperature Phase Diagram. *Nano Lett.* **10**, 2667–2673 (2010).